Solar Spectral Irradiance - Measurement and Application in Photovoltaics

by

Michal Krawczynski

Doctoral Thesis
Submitted in partial fulfilment of the requirements
for the award of

Doctor of Philosophy of Loughborough University

July 1, 2014

Abstract

This thesis presents the outcome of investigations undertaken in the field of terrestrial spectral solar irradiance characterisation and its impact on photovoltaics. Spectral irradiance has not previously been widely researched in the context of photovoltaic applications. Long term, natural environment spectral irradiance observations are practically non-existent with availability very limited in terms of covered period, temporal resolution and site location. The work presented here concentrates on four main aspects of spectral irradiance:

- spectroradiometer calibration
- spectral irradiance calibration transfer standards
- natural spectral irradiance variability and its impact on photovoltaic device efficiency
- impact of reference sensor spectral mismatch on accuracy of reference irradiance measurements

Spectral irradiance measurements allow for an accurate calculation of the field efficiency of a photovoltaic device. This investigation shows that the calibration accuracy of spectroradiometers is a serious issue. The lack of standards in this domain promotes persistency of such a state of affairs. Two methods for spectroradiometer sensitivity calibration were compared: indoor - FEL standard bulb based and outdoor - Langley plots. Wavelength calibration was done with use of a spectral line lamp.

Spectral radiance transfer FEL bulbs were recognised as a main source of an uncertainty in the spectroradiometer calibration process. Properties of FEL bulbs are discussed in detail. As a result a simplified

technique for FEL bulb characterisation is defined, based on measurements of bulb temperature and active area of the filament. Additionally, degradation and long term output stability of FEL bulbs has been analysed. It was proven that stable output from the FEL bulb can not be guaranteed without an active feedback measurement.

Efficiency of a photovoltaic device is valid only for the standard test conditions under which it is determined. The impact of realistic spectral irradiance distribution on the field efficiency of a variety of photovoltaic devices is investigated. Relations between device efficiency, air mass and clearness index are established. Differences between the standard AM1.5 spectrum and the observed long term average spectral irradiance are presented and discussed. Seasonal variations of the observed spectral irradiance are also analysed.

Spectral mismatch between reference sensor and photovoltaic devices adds an excessive systematic error to the measurements. Impact of spectral irradiance variations on mismatch, caused by changes in the composition of the atmosphere, is analysed through the use of the established SMARTS model to generate spectral irradiance for various levels of aerosol turbidity, aerosol models, precipitable water, ozone, zonal albedo and atmospheric pollution.

Acknowledgements

The present thesis would never have materialized without the support I received from the amazing people I had the chance, luck and honour to meet on my way.

First and foremost, I would like to sincerely thank Professor Ralph Gottschalg and Dr. Thomas Betts for their kind supervision, inspiring advice, invaluable moral and financial support, and inexhaustible patience. Without them this work would have been impossible.

I would like to acknowledge Dr. Matthias Strobel for all his help with installing meteorological equipment on the top of the legendary "W" building (most of the time in adverse weather conditions).

My appreciation also goes to Brian Goss, Noel Bristow and Dr. Martin Bliss for their terrific input into the PVPMS project. Their work indirectly enabled the financing of the meteorological equipment I used during the course of my research.

Special thanks are due to present and former PhD students of the Applied Photovoltaics group in CREST including: Mike Parker, Ian Cole, Foteini Plyta, Hassan Qasem, Dr.Chris Hibberd, Jyotirmoy Roy, Ira Sara, Jiang Zhu, Dr. Sheryl Williams, Dr. Pongpan Vorasayan, Dr. Christos Monokroussos.

I would like to thank to Maciej Matachowski for his selfless friendship.

I owe my deepest gratitude to my parents, Jolanta and Jerzy, my grandmother Zofia Stachura, and my brother Maciej. They gave me my wings and taught me how to fly. Without them I might have never had enough courage to chase my dreams.

Finally I want to thank my sweetheart Edyta Karpicka for her encouragement and for looking after me during the different stages of my studies.

Contents

List of Figures

List of Tables

Nomenclature

Constants

C	coefficient, decimal number
c	speed of light in vacuum
c_1	first radiation constant $c_1 = 2\pi hc^2$
c_2	second radiation constant $c_2 = hc/k$
h	Planck constant
k	Boltzmann constant
m	integer
n	integer, quantum number
R	Sun-Earth distance in astronomical units

Physical parameters

λ	wavelength of electromagnetic radiation
A	area
d	length
E	energy
m	mass

N	concentration
q	electric charge
T	body temperature in Kelvins
v	frequency

Photovoltaic cell parameters

α	current temperature coefficient
β	voltage temperature coefficient
τ	minority carrier lifetime
CP	collection probability
D	minority carrier diffusivity
E_G	material band-gap
EQE_λ	spectral external quantum efficiency
FF	fill factor
G	generation rate of electron-hole pairs
I	cell circuit (output) current
I_0	saturation current
I_D	diode current
I_L	illuminated current
I_{MPP}	cell output current at the maximum power point
I_{R_p}	leakage current
I_{SC}	cell short circuit current
IQE_λ	spectral internal quantum efficiency

J_L	photocurrent density
L	minority carrier diffusion length
n	ideality factor
n_0	concentration of electrons at equilibrium
n_i	intrinsic carrier concentration
p_0	concentration of holes at equilibrium
R	recombination rate
V_D	diode voltage
V_{bi}	built-in potential
V_{MPP}	cell output voltage at the maximum power point
V_{OC}	cell open circuit voltage
W	depletion region width
R_P	parallel (shunt) resistance
R_S	serial resistance

Atmospheric optics parameters

α	Angstrom exponent
β	aerosols load (optical depth at 1 μ m)
τ	optical depth
θ	solar zenith angle
AM	relative air mass
AM'	atmospheric pressure corrected relative air mass
DU	Dobson unit

k_c	instantaneous clear sky index
k_d	instantaneous diffuse fraction
K_T	clearness index
k_t	instantaneous clearness index
$k_{t'}$	zenith angle-independent clearness index
p	atmospheric pressure
p_0	standard atmospheric pressure
RH	relative humidity

Radiometric parameters

ϵ	emissivity coefficient
ϵ_λ	spectral emissivity coefficient
η_G	spectral efficiency of a current generation
η_J	photocurrent generation efficiency of the incident radiation
μ	attenuation coefficient
μ_λ	spectral attenuation coefficient
$\phi_{e,\lambda}$	spectral photon flux
ϕ_e	photon flux
$E_{e,0}$	solar irradiance at the edge of the atmosphere
$E_{e,\lambda}$	spectral irradiance
$E_{e,C}$	solar constant equal to 1367W/m2
E_e	total irradiance
R_λ	spectral reflectance

T transmittance

T_λ spectral transmittance

Detector parameters

δM relative mismatch difference

$M_{AM1.5}$ detector response mismatch for standard AM1.5 conditions

M_{norm} normalised detector response mismatch

$M_{specific}$ reference irradiance detector mismatch for the specific irradiance

S_d output signal from the photovoltaic device

S_s output signal from the reference detector

$s_{\lambda,r}$ radiometer sensitivity

$SR_{\lambda,detector}$ spectral response of the detector

SR_{device} spectral response of the device

$v_{\lambda,r}$ detector signal magnitude

Photovoltaic System parameters

$E_{e,STC}$ standard test condition irradiance

E_{elec} electric energy generated by the system over a given time interval

H_e irradiation received in a given time interval

P_0 system power rated for standard test conditions

PR performance ratio

Y_f final yield

Y_r reference yield

Uncertainty parameters

ΔX	absolute measurement error value
δX	relative measurement error
$\hat{y}$	mean value
$\partial x_i, \partial x_j$	partial derivatives
σ	unbiased standard deviation
f	functional dependency between measured quantities
k	coverage factor
RSD	relative standard deviation
SNR	signal to noise ratio
U	expanded uncertainty
$u(y)$	uncertainty of a measurement
X	uncorrected result of the measurement
x_1, x_2	measured quantities
X_t	true value
y_i	value of a single measurement

Acronyms

$AERONET$	Aerosol Robotic Network
$ANSI$	American National Standards Institute
AOI	Angle of incidence
APE	Average Photon Energy
$ASTM$	American Society for Testing and Materials
$CREST$	Centre for Renewable Energy Systems Technology

$DSLR$ Digital single-lens reflex camera

$ESTI$ European Solar Test Installation

ETL Extract, Transform and Load

ISO International Organization for Standardization

$MODIS$ Moderate Resolution Imaging Spectroradiometer

$NIST$ National Institute of Standards and Technology

$OLAP$ Online Analytical Processing

$SMARTS$ Simple Model of the Atmospheric Radiative Transfer of Sunshine

SQL Structured Query Language

WMO World Meteorological Organization

WRC World Radiation Center

WSG World Standard Group

BCE Before the Christian Era

BOS Balance of System

CPV Concentrating photovoltaics

EU European Union

IEA International Energy Agency

TCO Transparent Conductive Oxide

IR Infrared radiation

UV Ultraviolet radiation

VIS Visible radiation

Chapter 1

Introduction

1.1 Motivation

Throughout the last century, electrical energy has proven its benefits in millions of households. Around 25% of total energy consumed by EU households is electrical. Even though only 25% of total energy demand is electrical, electricity accounts for 40% of global CO_2 emissions [8]. The reasons for this are: significant dependency on fossil fuels for electricity production (coal 42%; gas 21%; petroleum 6%)[8], low generation efficiency (ranging from 28% in India to 43% in Denmark with a world average of 34%) [9], old and overloaded electricity transmission networks.

Global consumption of energy is predicted to grow by 53% from 2008 to 2035 with the maximum rate of 83% in developing countries [10]. According to IEA [11] it is estimated that 18% of the global population (1.28 billion people) are still living without electricity. World electricity demand is expected to grow with a rate greater than demand for any other form of energy [12]. With limited reserves and rapidly growing demand, long term trends of fossil fuel prices (including coal, natural gas, petroleum) are expected to rise in the future. The impact of hydraulic fracturing on fossil fuels market is not easy to predict (environmental pollution, enormous water usage). Severe damage of several nuclear reactors caused by the massive earthquake in Japan 2011 reawakened public fears (Three Mile Island, Chernobyl) making the future of the nuclear energy sector uncertain. The influence of increased concentration of greenhouse gases (CO_2

- 36% , CH_4 - 150% , N_2O -16% in relation to preindustrial age) and resulting global warming is predicted to have an adverse impact on societies (coastal flooding, land desertification, thermal comfort) and ecosystems (decreasing diversity of species, acidification of the oceans). Regardless of the ongoing discussion about the human influence on global warming, it is indisputable that a higher level of utilisation of renewable sources of energy in the global energy mix must be achieved in order to satisfy future energy demand without risk of detrimental environmental and economic changes.

The Sun is the most abundant source of energy in our environment. All renewable sources of energy (wind, solar thermal, photovoltaic, hydro, biofuels, solid biomass, biogas) directly or indirectly relate to the Sun. Depending on location, the Earth's surface receives from 800kWh/m^2 to 2200kWh/m^2 of radiant energy per year. The possibility of a direct transformation of the solar radiation into electric current not only gives a simple way of reducing the carbon footprint in developed countries, but it also makes it possible to bring electricity to unelectrified regions within a short time frame.

Generation of electric current under the influence of the light (also known as the photovoltaic effect), has been known to mankind since 1839 [13]. Significant progress in photovoltaics has been made since 1954 with the development of the first modern photovoltaic cell. Since then, photovoltaic devices have been through a long development process driven by performance and economical optimisation. Since 2006, photovoltaics have started to become one of the leading renewable technologies in the EU. Only in 2013, newly-added photovoltaics capacity around the globe reached a record level of at least 38.4GWp, increasing world cumulative installed capacity to 138.8GWp [14]. The European market success of photovoltaics has been achieved with substantial support in form of feed-in tariffs.

Regardless of a drastic price drop for modules and balance of system (BOS) components, photovoltaic technology is still more expensive in comparison to its competitors (photovoltaics 141$/MWh wind - 82$/MWh, hydro - 77$/MWh [15]). Further reduction of costs for photovoltaic installations, without a technological leap, is going to be harder to achieve. In such a scenario, profit margins from investments made in photovoltaics become smaller. It is important to assure

a high level of system performance over the system life time. Accurate supervisory monitoring of a photovoltaic installation is an essential tool for ensuring profitability and reducing financial risk of an investment.

1.2 Context of the problem

The performance of a photovoltaic system is a complex function of many parameters such as: system design (array orientation, shading, building integrated/free standing), module technology (crystalline, thin film, CPV), exposure history (UV irradiation, thermal stress, electrical and mechanical loads), environmental conditions (irradiance, temperature, solar spectrum, windspeed and direction, humidity) and BOS elements (inverters, storage, cabling). Accurate performance estimation of a photovoltaic system is not a trivial task. This process requires a collection of precise meteorological and operational data from various sensors and detailed information about the particular system design.

Photovoltaic systems scale from single kWp[1] domestic installations to hundreds of MWp power plants. According to [14], European cumulative capacity segmentation of system types varies significantly between countries (e.g. Denmark - residential, Romania - ground mounted , Switzerland - domination of industrial rooftop applications , Slovakia - commercial rooftop applications). The level of system complexity naturally increases with the size of the installation. In effect, requirements for supervisory monitoring systems vary. In the case of residential installations, most often the only performance check is done by a comparison of energy yield with historical data or data from closest neighbours. Advanced monitoring solutions are economically inefficient for such a small installations. Higher prices that residential installation owners get per kWh of generated electricity offset to some extent losses caused by lack of precise monitoring. The UK market is dominated by ground mounted and commercial rooftop applications. In case of large commercial, industrial or ground mounted systems, small profitability margins push investors towards more sophisticated monitoring solutions.

[1]kWp -kilowatt-peak ; a unit used for description of nominal power of the photovoltaic module at standard test conditions (STC): irradiance equal to $1000[W/m^2]$, temperature of 25^0C, standard terrestrial solar spectrum for the air mass 1.5

1.3 Key challenges to be addressed in this thesis

The performance of photovoltaic systems can suddenly degrade. If relevant supervisory measurements of environmental and operational conditions are not recorded, a photovoltaic system may under-perform for prolonged periods of time. Quality of reference measurements may be affected also by the type of detectors used. This thesis discusses requirements which should be fulfilled in order to achieve precise and accurate reference solar radiation measurements for use in photovoltaic system performance monitoring. Sensor technologies commonly used for reference irradiance measurements are discussed. Special attention has been paid to the radiometer uncertainty, application of spectroradiometers, analysis of spectral irradiance variations and variability of the performance of different cell technologies under realistic atmospheric conditions. A variety of experimental setups, models and analytical data processing techniques are used to support the work undertaken. Figure 1.1 presents the structural layout of this thesis.

The reference irradiance is a key factor influencing the accuracy of a supervisory monitoring system. The importance of dedicated reference irradiance measurements is often underestimated by photovoltaic system designers. Irradiance sensors are very rarely found in domestic systems. Even if a reference irradiance sensor is included in the system (e.g. solar farm), quality assessment and interpretation of results is problematic for the personnel maintaining the system. The increasing number of currently available and continuously emerging photovoltaic cell technologies causes ongoing diversification of cell spectral response characteristics. This makes an accurate measurement of a reference irradiance for a specific cell technology an even more complex task. Moreover, some photovoltaic cell technologies exhibit higher level of sensitivity to variations of spectral irradiance than others (e.g. multi-junctions, where the efficiency is limited by the worst performing junction at the time). Spectral irradiance measurements constitute an ultimate measure of available resource for photovoltaic technology. Regardless of this fact the level of utilisation of spectral irradiance measurements in photovoltaics is very limited (even in the scientific world) due to expensive in-

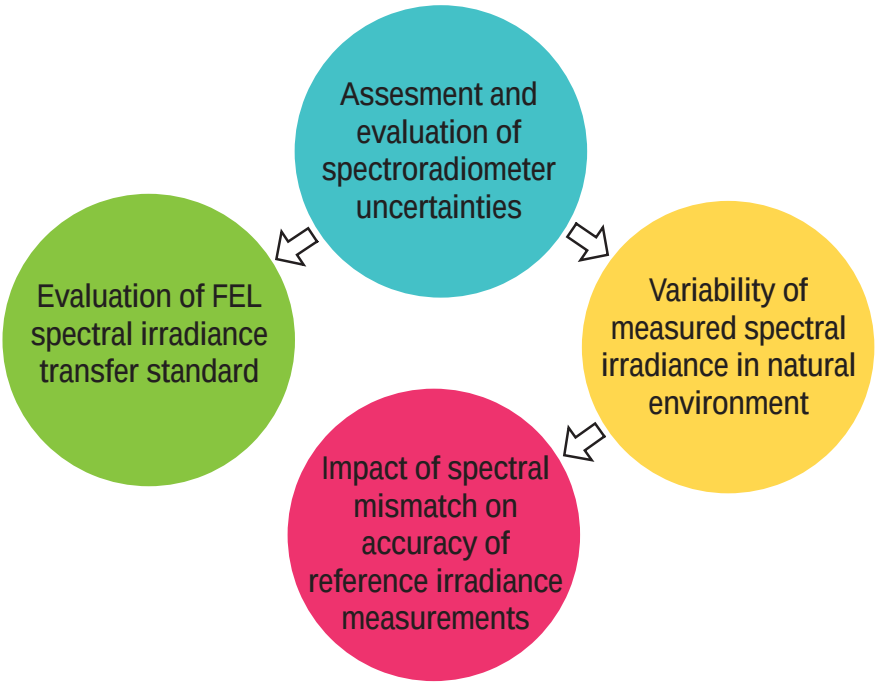

Figure 1.1: Thesis structure

strumentation and complex metrological methodology. It is of great importance for the photovoltaic industry to develop advanced standards of reference irradiance measurements. In this thesis, the author investigates whether the application of spectroradiometers can improve the accuracy of reference yield calculations for photovoltaic systems.

Chapter 2

Photovoltaics - theories and concepts

2.1 Optical radiation

The nature of light has intrigued the modern human for more than two millennia. The earliest documented work in this domain comes from fourth century BCE [16]. The debate on the character of optical radiation intensified in the middle of the seventeenth century. Over the following two centuries, the main contributors to this debate (René Descartes, Christiaan Huygens, Willebroad Snell, Isaac Newton, Thomas Young, Leonhard Euler, Augustin Fresnel to name a few) contributed significantly to the level of knowledge on optical radiation. A significant progress was achieved in the middle of the nineteenth century, Clerk Maxwell postulated that the light is a form of electromagnetic radiation[1] [17]. Maxwell's electromagnetic wave theory, however, did not explain all the phenomena involving interaction of the light with matter (e.g. photoelectric effect). The first complete description of optical radiation was given in twentieth century by Albert

[1] electromagnetic radiation - synchronised oscillation of electric and magnetic fields. It is parameterised by two orthogonal vectors of electric (E) and magnetic (M) fields and so called wave vector (k). Electromagnetic radiation propagates in the direction of the wave vector. Electric and magnetic fields exchange energy between themselves with a frequency f. For optical radiation the frequency ranges from $0.3THz$ up to $30THz$. Often, term of a wavelength ($\lambda = \frac{1}{f}$) is used instead of frequency. Optical radiation undergoes interference, supporting its electromagnetic wave nature.

Einstein with use of quantum mechanics. The foundation of quantum mechanics was created by Max Planck [18], as an effect of his earlier work in the field of a black body radiation [19]. Planck postulated that the energy of atomic oscillators is quantised.

$$E = nhv \tag{2.1}$$

where:

n - quantum number

h - Planck constant

v - frequency of the oscillator

Planck's assumption revolutionised modern physics. For the first time, the description of the macroscopic phenomenon of black body spectral radiation was given with the use of quantum theory.

$$E_{e,\lambda,B} = \frac{2hc^2}{\lambda^5} \frac{1}{e^{\frac{hc}{kT}} - 1} \tag{2.2}$$

where:

c - speed of light in vacuum

λ - wavelength of the electromagnetic radiation

k - Boltzmann constant

T - body temperature in Kelvins

In 1905, Albert Einstein extended Planck's quantum theory. He postulated that not only the vibration of the source of radiation, but also the vibration of radiation itself is quantised. Electromagnetic radiation is transmitted as a bundle of energy called quantum. In effect, the energy of electromagnetic radiation emitted by an atomic oscillator must be quantised (see equation 2.3). Since 1926 a quantum of optical radiation has been given the name of 'photon' [20].

$$E = \frac{h \cdot c}{\lambda} \tag{2.3}$$

The emission spectrum of realistic bodies depends on their chemical composition and geometrical structure of the emitting surface. The ability of a body to emit thermal radiation is called emissivity. One of the best known natural thermal sources of optical radiation is the Sun. Optical radiation covers only a part of the electromagnetic spectrum. Three sub-bands are specified: UV (10-380nm), VIS (380nm-780nm) and IR (780nm-1mm) [21]. Energy of photons rises with frequency. Therefore, spectral flux[1] is a function of photon count at the respective wavelength. In meteorology, instead of spectral flux, a term of spectral irradiance[2] is used more often. The spectral irradiance integrated over the range of wavelengths is called total irradiance.

$$E_e = \int_{\lambda_1}^{\lambda_2} E_{e,\lambda} \, \mathrm{d}\lambda \tag{2.4}$$

where:

E_e - total irradiance

λ_1, λ_2 - integration boundaries

$E_{e,\lambda}$ - spectral irradiance

Due to its relatively low energy, optical radiation is mostly not capable of ionisation (apart from deep ultraviolet), however it can effectively destroy chemical bonds causing material defects and degradation.

While the optical radiation passes through the medium it can be attenuated. Attenuation may be caused by two processes: scattering and absorption. Scattering of the optical radiation can be inelastic (Brillouin, Raman) and elastic (Rayleigh, Mie). For elastic scattering, the direction of propagation of optical radiation is changed while its energy stays invariant. During inelastic scattering, a photon changes its direction of propagation as well as its energy. In absorption processes, the energy of the optical radiation is taken up by matter (atoms, electrons, molecules) and re-emitted in another form. Absorption is described by the Lambert-Beer law.

$$T = e^{-ANd} = e^{-\mu d} \tag{2.5}$$

[1] spectral flux - radiant flux per unit wavelength

[2] irradiance - radiant flux received per unit area.

where:

T - transmittance

A - light absorption cross section

d - path length

N - concentration of absorbing particles

μ - attenuation coefficient

The Lambert-Beer law can be used to describe attenuation of the solar direct beam irradiance in the atmosphere.

$$E_{e,T} = R^{-2} \cdot E_{e,C} \cdot e^{-AM(\tau_w+\tau_a+\tau_r+\tau_g+\tau_{NO_2}+\tau_{O_3})} \tag{2.6}$$

where:

$E_{e,T}$ - transmitted irradiance

R - Earth-Sun distance coefficient

$E_{e,C}$ - solar constant

AM - relative air mass

τ_w - optical depth introduced by atmospheric water vapour

τ_a - optical depth introduced by aerosols

τ_r - optical depth introduced by Rayleigh scattering

τ_g - optical depth introduced by uniformly mixed gases

τ_{NO_2} - optical depth introduced by nitrogen dioxide

τ_{O_3} - optical depth introduced by ozone

2.2 Photovoltaic devices

The fundamental operational principle of photovoltaic devices is the internal photovoltaic effect. The photovoltaic effect was demonstrated for the first time by Becquerel [13]. Becquerel used two platinum electrodes separated by a thin membrane immersed in an acidic solution (see Figure 2.1) to generate light induced

voltage. Over the next century, Becquerel's invention was followed by a number of modifications [22–26]. The efficiency of the best selenium photovoltaic cells at this stage reached 1%-2%. Soon after discovery of the PN (positive-negative) junction [27] the first design of the modern silicon photovoltaic cell was proposed and patented [28].

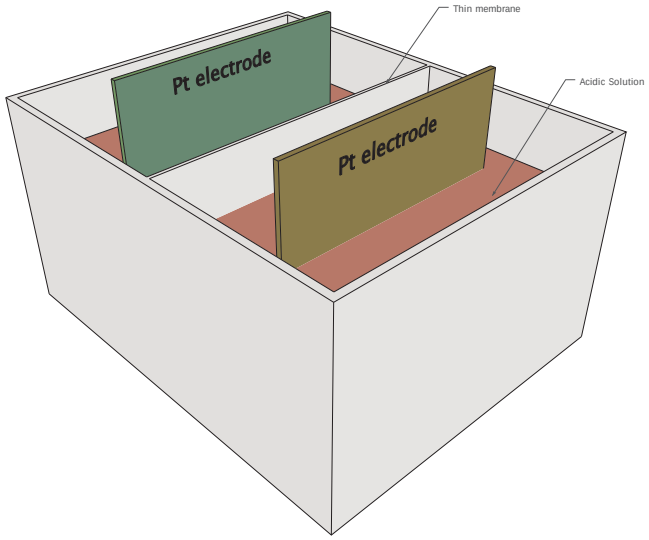

Figure 2.1: Becquerel device

2.2.1 Principles of operation

A solar cell is a device composed from p-type (donor doped) and n-type (acceptor doped) layers of semiconductor. When n-doped and p-doped semiconductor layers are brought together, electrons from the n-area diffuse into the p-area leaving exposed positive ion atomic cores. Holes from the p-area diffuse into the n-area leaving exposed negative ion atomic cores. Charges on dopant atoms are fixed in the lattice. An electric field is formed between positively and negatively charged doping atoms which stops further diffusion of the carriers, and the PN junction comes to an equilibrium state. Figure 2.2 presents a PN junction in equilibrium with charge density, electric field and voltage plots across the junction.

The potential difference formed across the junction, without an externally applied voltage is called the built-in potential. Its value depends on temperature,

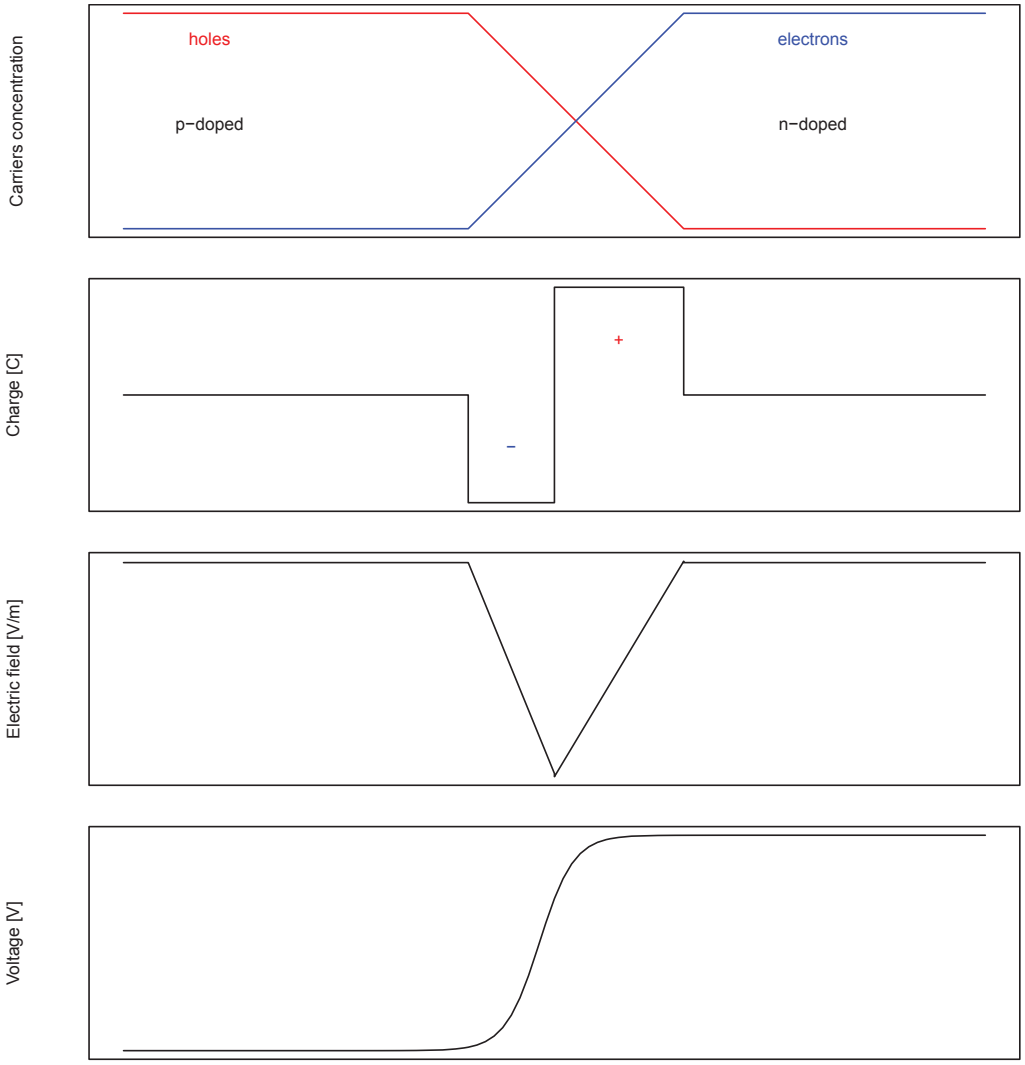

Figure 2.2: PN junction in equilibrium

concentration of free charges and concentration of donors and acceptors from dopants. The value of the built-in potential can be calculated from equation 2.7.

$$V_{bi} = \frac{kT}{q} \ln\left(\frac{N_A N_D}{p_0 n_0}\right) \tag{2.7}$$

where:

V_{bi} - built-in potential

N_A - concentration of acceptors

N_D - concentration of donors

p_0 - concentration of holes at equilibrium

n_0 - concentration of electrons at equilibrium

Radiation incident on the surface of the solar cell can be reflected from the front side of the cell surface. To reduce reflection losses, antireflective coatings are used. Photons, which are not reflected, can be transmitted through, or absorbed in the material. If the photon energy is lower than the material's band-gap[1], the photon will be transmitted through the material. Absorption of photons is possible if the photon's energy is at least equal to or greater than the band-gap of the material. Figure 2.3 presents band-gaps of common materials used for solar cells.

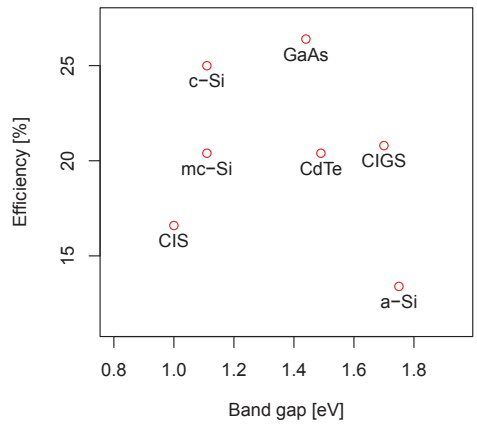

Figure 2.3: Band gaps of common materials used for solar cells vs. record reported efficiencies [1]

The absorption coefficient of a material is a function of the wavelength, e.g. for silicon, the absorption coefficient is greater for short wavelengths. Light flux transmitted through the material follows the Lambert-Beer law (2.5) and can be calculated from equation 2.8:

$$\phi_{e,\lambda,T}(d) = \phi_{e,\lambda,0} \cdot e^{-\mu_\lambda d} \tag{2.8}$$

[1]band-gap - energy difference between the top of the valence band and the bottom of the conduction band in semiconductors isolators

where:

$\phi_{e,\lambda,T}$ - transmitted spectral flux

$\phi_{e,\lambda,0}$ - incident spectral flux

μ_λ - spectral attenuation coefficient

d - path length

The amount of carriers generated at given point across the solar cell is given by derivative of Lambert-Beer law and is called the generation rate.

$$G_\lambda(d) = \frac{\partial \phi_{e,\lambda,T}(d)}{\partial d} = \mu_\lambda \cdot \phi_{e,\lambda,0} \cdot e^{-\mu_\lambda d} \tag{2.9}$$

where:

G_λ - spectral generation rate of electron-hole pairs

Carriers can be generated throughout the volume of the material. The probability of carrier collection varies across the device. Collection probability specifies a chance by which a minority carrier generated at the specific point in a device will reach the region of the PN junction. Collection probability is equal to 1 in the region of the PN junction and it gradually decreases towards the front side and the back side of the cell. The pace at which collection probability decreases depends on material recombination rate and surface recombination rate.

Rate of recombination depends on minority carrier diffusion length. Minority carrier diffusion length (L) is defined as an average distance that a carrier can move after generation until it recombines (see equation 2.10).

$$L = \sqrt{D\tau} \tag{2.10}$$

where:

L - minority carrier diffusion length

D - minority carrier diffusivity

τ - minority carrier lifetime

Minority carrier lifetime (τ) is an average time between generation and recombination of the electron-hole pair (see equation 2.11).

$$\tau = \frac{\Delta n}{R} \tag{2.11}$$

where:

τ - minority carrier lifetime

Δn - excess minority carriers concentration

R - recombination rate

Recombination is mainly promoted by defects and impurities of the material (in bulk and on the surface). To minimise surface recombination, the surface can be passivated to reduce the number of dangling bonds[1]. Long-wavelength light may not be fully absorbed by the solar cell, even if the energy of photons is greater than the material's band gap. This causes transmission losses. To avoid transmission losses, the back of the cell is covered by a reflector (e.g. aluminium). In the case of a silicon solar cell, the aluminium layer also passivates[2] the silicon surface and is used as a back contact.

Minority carriers (electrons in p-region and holes in n-region) reaching the area of the PN junction are pulled by the electric field of a junction towards n-region (electrons) or p-region (holes), where they become majority carriers. Electrons and holes are then carried by diffusion, respectively through the n-region and p-region, towards cell contacts.

The number of carriers generated by the cell normalised to the cell surface area is called photocurrent density (J_L). It is one of the main cell parameters. The photocurrent density depends mainly on the generation rate and minority carrier diffusion length. Assuming a constant generation rate across the device, the photocurrent can be expressed by equation 2.12.

$$J_L = q \cdot (L_n + L_p + W) \cdot \int_{\lambda_1}^{\lambda_2} G_\lambda \, \mathrm{d}\lambda \tag{2.12}$$

[1]dangling bond - unsatisfied chemical bond associated with an atom in the surface layer of a solid

[2]passivation - a process of reduction of the number of dangling bonds by growing a passivation layer at the surface of a solid

where:

J_L - illuminated current density

L_n - electrons carrier diffusion length

L_p - holes carrier diffusion length

W - depletion region width

λ_1, λ_2 - material sensitivity boundaries

If the generation rate is not constant, the photocurrent density is calculated from equation 2.13

$$J_L = q \int_{\lambda_1}^{\lambda_2} \int_0^d G_\lambda(d) \cdot CP(d)\, \mathrm{d}d\, \mathrm{d}\lambda \tag{2.13}$$

where:

d - effective thickness of the device

CP - collection probability

It was shown above that the amount of generated photocurrent is a complex function of incident radiation (spectral distribution, intensity), physical properties of the solar cell material (band gap, defects, impurities) and construction of the cell (passivation, antireflective coating, electric contacts). All these aspects must be considered for accurate modelling of performance of the cell.

2.2.2 Solar cell technologies

Crystalline silicon: At present, the predominant type of solar cell used in the industry is based on crystalline silicon. Crystalline silicon cells have a market share of 80-90%. This type of cell is manufactured from a crystalline silicon wafer (p-type[1] or n-type[2]). The surface of the wafer is doped to change its conductivity type. This process creates a PN junction. A layer of a TCO is created to passivate the front surface of the cell and to support finger electrodes in collection of the

[1] p-type semiconductor - intrinsic semiconductor doped with acceptor impurities.
[2] n-type semiconductor - intrinsic semiconductor doped with donor impurities.

charge from the front side of the cell. An aluminium layer is deposited on the back of the wafer to collect the charge and to reflect back transmitted radiation. A simplified structural model of a silicon solar cell is presented in Figure 2.4.

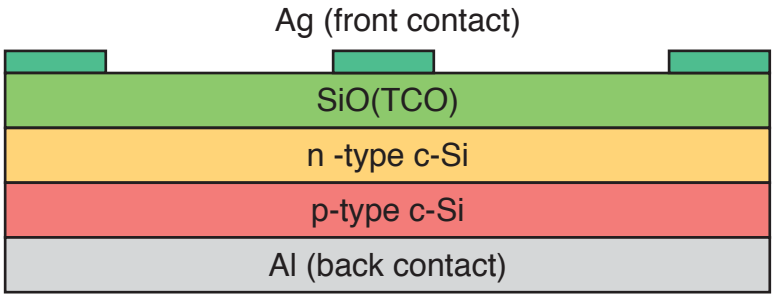

Figure 2.4: Simplified structure of silicon photovoltaic cell

Major progress in manufacturing of silicon solar cells was achieved through an implementation of the Czochralski process [29, 30] for mono-crystalline silicon growth and through implementation of high temperature diffusion of dopants into the silicon surface. Mono-crystalline silicon solar cells within a few months of introduction in 1954, reached the efficiency of 6%, tripling that of already known selenium solar cells[31]. At the beginning the of the 1960's the efficiency of silicon solar cells reached 15%. Due to their high cost, the main application of silicon solar cells was limited to the space industry. Over the years, the design of silicon solar cells went through a set of improvements (surface texturing[1], antireflective coating, surface passivation, contacts optimisation, back contact doping, screen printing). The technology of silicon solar cells benefited largely from achievements of the semiconductor industry. With increasing interest in the application of the solar cell in commercial products, reduction of costs became a major goal. As a result, simpler to manufacture multi-crystalline silicon was proposed as an alternative to mono-crystalline technology. The current laboratory record efficiency for a mono-crystalline silicon solar cell was set at 25% in 1998 [32] and for multi-crystalline cell at 20.4% in 2004 [33]. Record efficiency for the mass-manufactured mono-crystalline silicon module (21.5%) belongs to Sunpower X-Series (third-generation Maxeon cells). Record efficiency for multi-crystalline silicon module (17%) belongs to Phono Solar PS330P-24/T.

[1]surface texturing - process of roughening of the surface of the cell to reduce the chance of losses through the reflection

Thin films: Historically the first thin film solar cell was created in 1883 [23], much earlier than silicon solar cells. However, thin film technology did not progress significantly until the introduction of CdTe, initially proposed as a solar cell material in 1956 [34]. The high absorption coefficient of CdTe promised high conversion efficiencies. Application of CdTe was however limited because the behaviour of dopants was not understood until 1959 [35]. Over the next ten years, CdTe-based cells reached efficiency exceeding 6%. Figure 2.5 presents a simplified model of a CdTe solar cell.

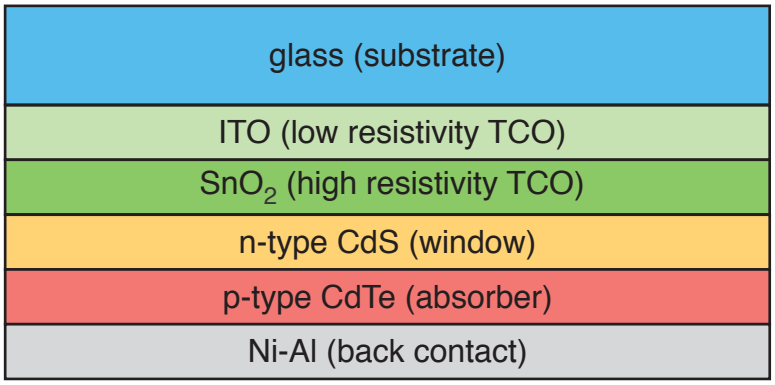

Figure 2.5: Simplified structure of CdTe photovoltaic cell

The cell structure is deposited on top of a 3-4mm thick glass substrate. At first, a layer of transparent conductive oxide is created. Next two layers: CdS (cadmium sulphide; n-doped semiconductor) and CdTe (cadmium telluride; p-doped semiconductor) create the PN junction. Finally a metallic back contact is deposited on top of CdTe layer.

In 1974, over twenty years after the first synthesis [36], $CuInSe_2$ was proposed for solar cell application [37]. In 1976, the first amorphous silicon photovoltaic cell was made [38] reaching an efficiency of 1.1%. Figure 2.6 presents a simplified model of a CIS/CIGS solar cell.

Optimistic predictions of achievable efficiencies as well as expected low manufacturing costs of new thin film solar cells stimulated intensive research since the 1970's. After almost forty years of further development, thin film modules achieved efficiencies of 6%-9% (a-Si, μa-Si) 9%-11% (CdTe) and 10%-12% (CIGS) and record market share of 16.5% in 2009. Significant decrease in crystalline sili-

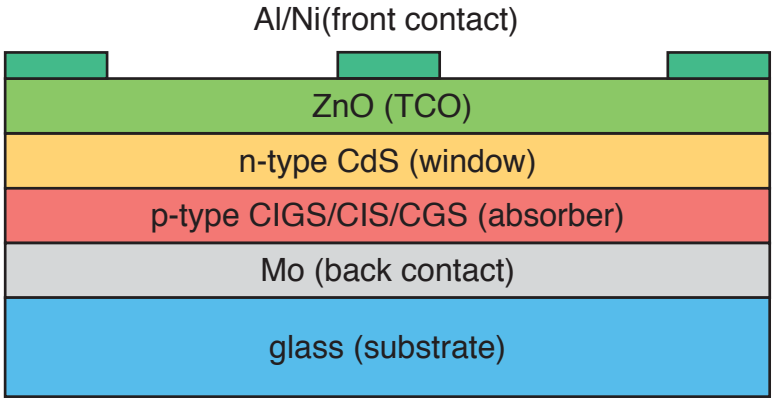

Figure 2.6: Construction of CIGS/CIS/CGS photovoltaic cell

con module prices caused by overproduction led to a reduction of thin film market share to 11% in 2011. It is expected that thin film technologies' market share will increase to 33% by 2020 [39]. In 2015, the dominating thin film technology is CdTe.

Figure 2.7 presents a simplified model of an a-Si solar cell.

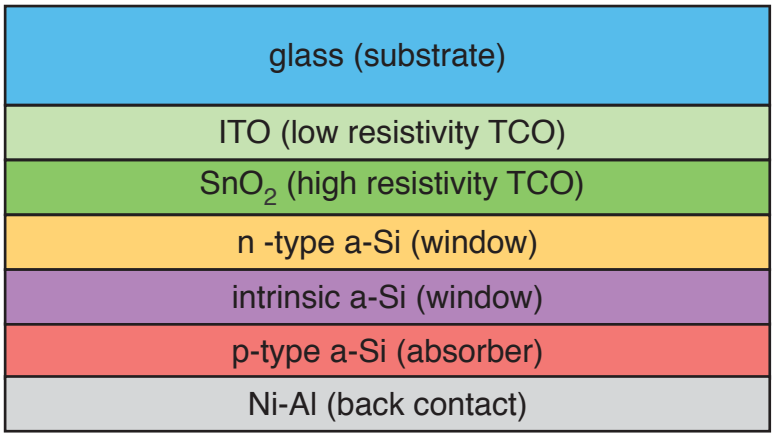

Figure 2.7: Simplified structure of a-Si photovoltaic cell

Future technologies Regardless of the current strong dominance of crystalline silicon in the market share, it is clear that diversification of solar cell technologies will increase in the future. It is of great importance, that photovoltaic system monitoring will take into account subtle differences between a cell's optical and

electrical properties (specifically quantum efficiency). Emerging multi-junction solar cells promise >40% efficiencies. Such types of solar cells are increasingly sensitive to spectral distribution of solar irradiance. For this reason, the application of a spectroradiometer is going to be essential to improve quality of reference irradiation measurements.

2.2.3 Characterisation of solar cells

Solar cell equivalent circuit: In terms of electrical properties, a solar cell can be represented by a diode. The ideal diode current (I_D) is given by Shockley's formula (see equation 2.14), which primarily determines the shape of the I-V characteristic of a solar cell. According to equation 2.14, the diode current is a function of diode voltage (V_D) and temperature (T).

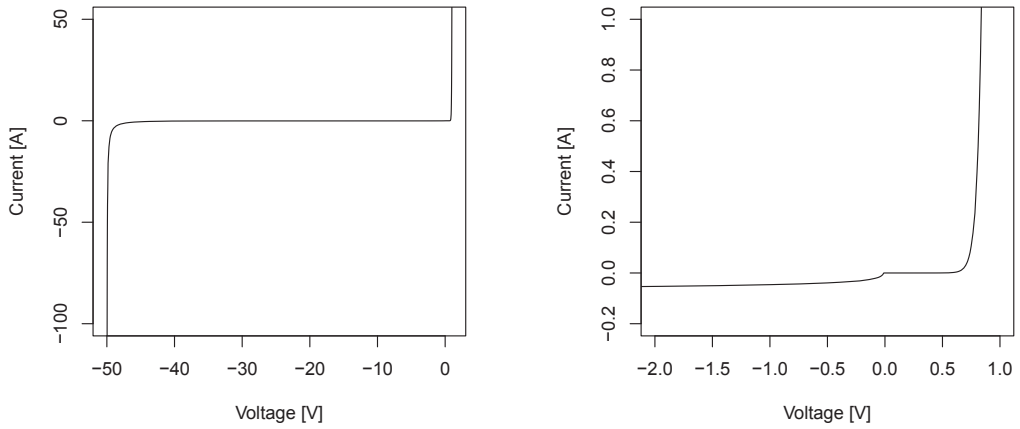

Figure 2.8: Typical diode I-V curve

$$I_D = I_0 \cdot \left[exp\left(\frac{qV_D}{nkT}\right) - 1 \right] \tag{2.14}$$

where:

I_D - ideal diode current

I_0 - saturation current

V_D - diode voltage

n - ideality factor

The saturation current depends on solar cell material properties (see equation 2.15)

$$I_0 = q\sigma \left(\sqrt{\frac{D_p}{\tau_p}} \cdot \frac{n_i^2}{N_D} + \sqrt{\frac{D_n}{\tau_n}} \cdot \frac{n_i^2}{N_A} \right) \tag{2.15}$$

where:

σ - cross section area

D_p, D_n - diffusivity of holes and electrons

τ_p, τ_n - lifetime the holes and electrons

n_i - intrinsic carrier concentration

N_D, N_A - donor and acceptor concentrations

If the diode is exposed to irradiance, incident photons generate photocurrent (I_L). Equation 2.16 describes the current (I) for an illuminated diode. Light generated current shifts the diode characteristic towards the fourth quadrant of the $I - V$ plot (negative current, positive voltage), where the diode starts to generate energy.

$$I = I_L - I_D \tag{2.16}$$

where:

I - cell circuit current

I_L - illuminated current

I_D - diode current

In practice, the standard electric representation of a solar cell is given by the one diode model (see fig 2.9). The one diode model considers the solar cell as a non-ideal current source with series resistance (R_S), parallel resistance (R_P) and parallel reverse biased diode.

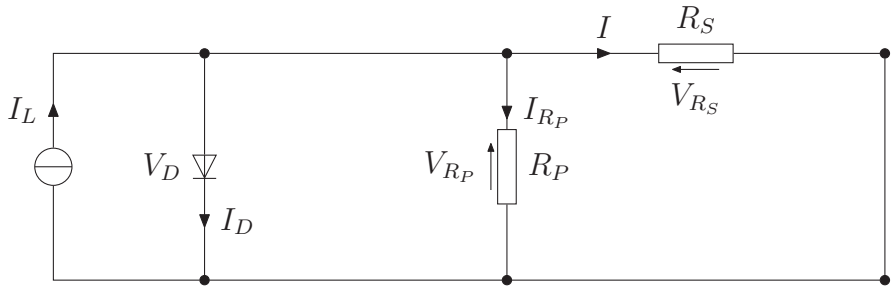

Figure 2.9: One diode solar cell model

Series resistance is usually quite low (in the range of $m\Omega$) and it represents resistance of the electrical contacts. Parallel resistance inhibits leakage current[1] and is usually high ($> 100k\Omega$). Non-ideal series and parallel resistances cause flattening of the $I-V$ characteristic of the solar cell, which has a negative influence on cell efficiency. From Kirchhoff's current law applied to fig 2.9, equation 2.17 and 2.18 can be derived.

$$I = I_L - I_D - \frac{V_D}{R_P} \tag{2.17}$$

where:

V_D - diode voltage

R_P - cell parallel resistance

$$V = V_D - I \cdot R_S \tag{2.18}$$

where:

V - cell circuit voltage

I - cell circuit current

V_D - diode voltage

R_S - cell series resistance

[1]leakage current - electric current flowing from one cell terminal to the other due to poor insulation

After substitution, the final equation for I-V characteristic can be given (see equation 2.19)

$$I = I_L - I_0 \cdot \left[exp\left(\frac{q \cdot (V + I \cdot R_S)}{nkT} \right) - 1 \right] - \frac{V + I \cdot R_S}{R_P} \tag{2.19}$$

The standard I-V characteristic of a solar cell is presented as a flipped fourth quadrant of total I-V curve (see Figure 2.10). The main parameters that can be defined from the I-V curve are: short circuit current (I_{SC}), open circuit voltage (V_{OC}), current at maximum power point (I_{MPP}), voltage at maximum power point (V_{MPP}) , power at maximum power point (P_{MPP}), fill factor (FF), series (R_S) and parallel (R_P) resistance. Fill factor is defined as the ratio between the area limited by the I_{MPP} and V_{MPP} points and the area limited by the I_{SC} and V_{OC} points (see equation 2.20)

$$FF = \frac{I_{MPP} \cdot V_{MPP}}{I_{SC} \cdot V_{OC}} \tag{2.20}$$

where:

FF - fill factor

I_{MPP} - cell output current at the maximum power point

V_{MPP} - cell output voltage at the maximum power point

I_{SC} - cell short circuit current

V_{OC} - cell open circuit voltage

For simple comparison between different cells, the efficiency coefficient is used (see equation 2.21).

$$\eta = \frac{FF \cdot I_{SC} \cdot V_{OC}}{E_{e,in}} \tag{2.21}$$

where:

FF - fill factor

$E_{e,in}$ - irradiance incident on the surface of the cell

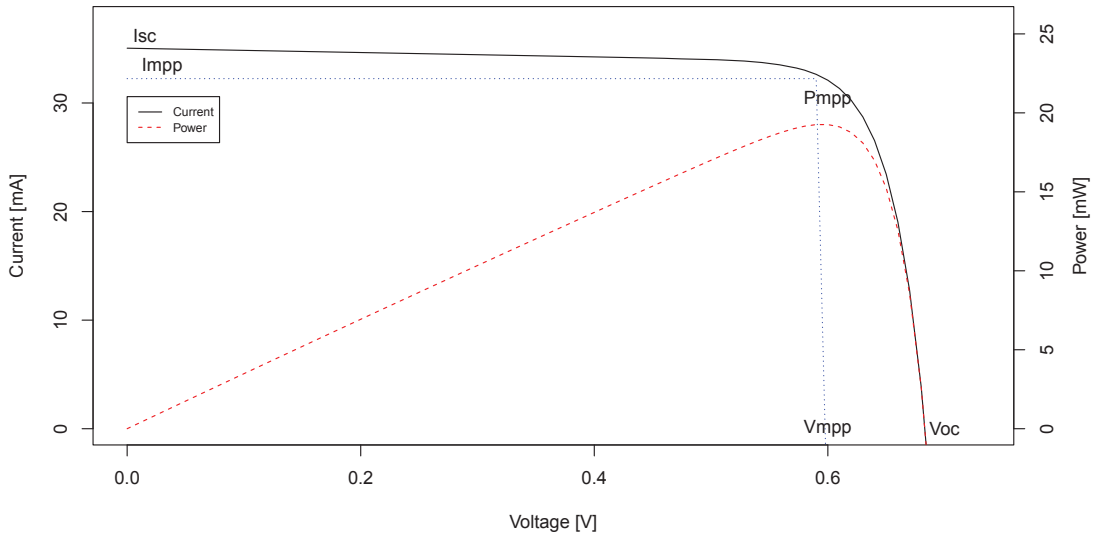

Figure 2.10: Standard solar cell I-V characteristic

Irradiance effects: Irradiance intensity impacts the amount of energy generated by the solar cell the most. Irradiance intensity variations influence the short circuit current of the solar cell. As a first approximation, there is a linear dependency between irradiance intensity and short circuit current (assuming constant spectral distribution of incident radiation; see Figure 2.11). For this reason a solar cell can be used to measure the irradiance intensity.

Figure 2.12 illustrates the influence of solar radiation intensity on the $I - V$ characteristic of a solar cell.

If the series resistance of a cell is low, it can be assumed that the short circuit current density(J_{SC}) is almost equal to the illuminated current density (J_L). It was shown in equation 2.13 that the current density is a complex function of many parameters. A simplified way of characterising the response of the solar cell to the incident photons is achieved with use of quantum efficiency (QE), also called as photon to electron conversion efficiency. The quantum efficiency depends on the wavelength of the incident light. It is defined as a ratio between the number of carriers generated by the solar cell to the number of photons of specific energy interacting with the cell. There are two measures of quantum efficiency : internal (IQE) and external(EQE). Internal quantum efficiency (see

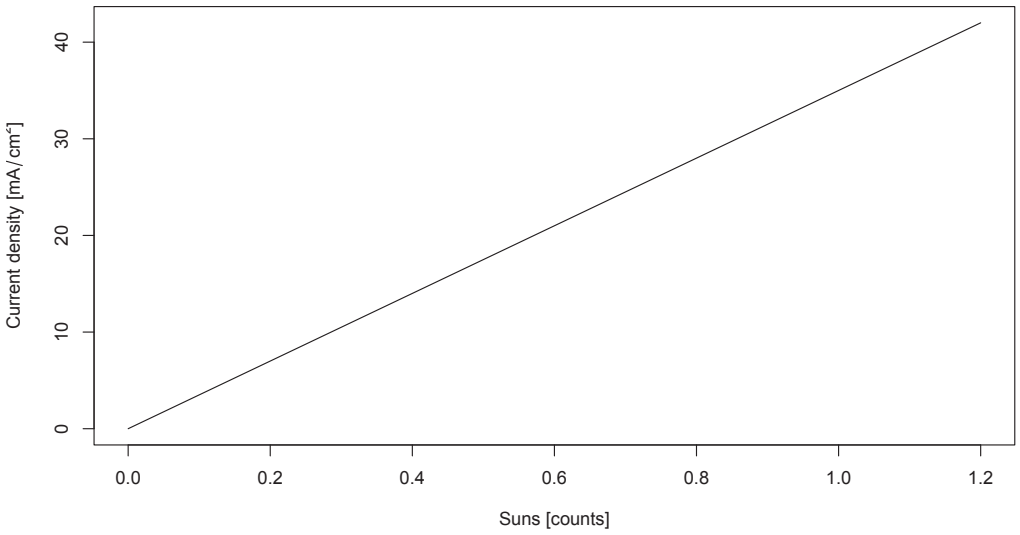

Figure 2.11: Influence of irradiance on short circuit current density. The irradiance is expressed in Suns, where one Sun equals $1000W/m^2$. The current density represents the amount of current generated under given irradiance for each cm^2 of the photovoltaic device.

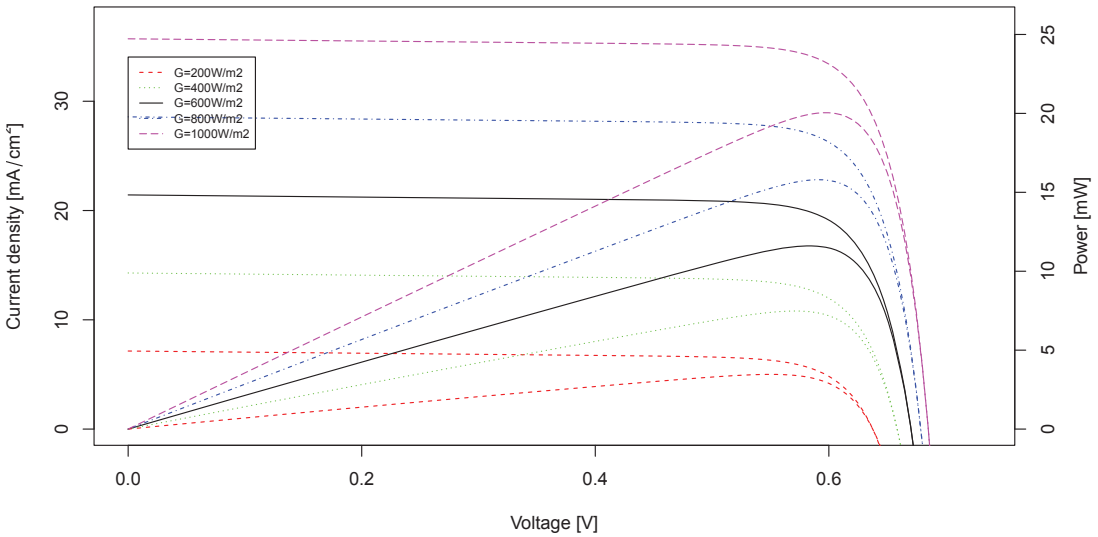

Figure 2.12: Influence of irradiance on I-V curve

equation 2.23) specifies effectiveness of carrier generation and collection process inside the cell while external quantum efficiency (see equation 2.22) also accounts

for reflection and transmission loses.

$$EQE_\lambda = \frac{J_{\lambda,L}}{\phi_{e,\lambda}} \tag{2.22}$$

where:

EQE_λ - spectral external quantum efficiency

$\phi_{e,\lambda}$ - spectral photon flux

$J_{\lambda,L}$ - spectral illuminated current density

$$IQE_\lambda = \frac{EQE_\lambda}{1 - R_\lambda - T_\lambda} \tag{2.23}$$

where:

IQE_λ - spectral internal quantum efficiency

T_λ - spectral transmittance

R_λ - spectral reflectance

Figure 2.13 presents external quantum efficiency of different solar cell technologies.

External and internal quantum efficiency can be measured in laboratory conditions. Once the external quantum efficiency is known, the illuminated current density can be calculated from the photon flux (see equation 2.24).

$$J_L = q \int_{\lambda_1}^{\lambda_2} EQE_\lambda \cdot \phi_{e,\lambda} \, \mathrm{d}\lambda \tag{2.24}$$

where:

J_L - total illuminated current density

The solar cell's short circuit current (I_{SC}) can then be calculated from cell's surface (A) and illuminated current density (J_L) (see equation 2.25)

$$I_{SC} \approx I_L = A \cdot J_L \tag{2.25}$$

where:

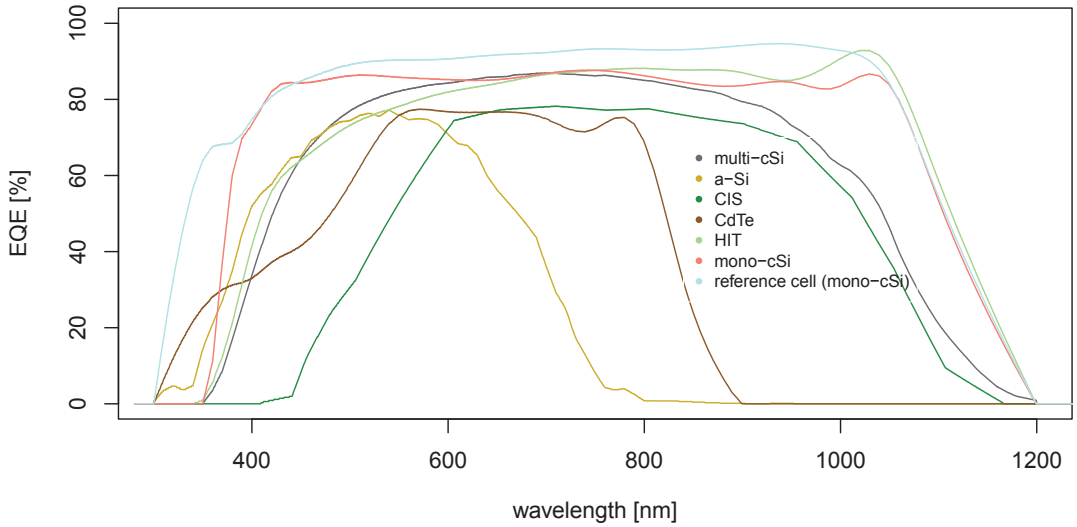

Figure 2.13: External quantum efficiency of a different solar cell technologies

A - area of the cell

Irradiance intensity influences also open circuit voltage. By setting the diode current (I_D) to zero, the open circuit voltage of an illuminated solar cell can be derived (see equation 2.26).

$$V_{OC} = \frac{nkT}{q} \ln\left(\frac{I_L}{I_0}\right) \tag{2.26}$$

The light generated current is almost equal to short circuit current. Then the dependency between open circuit voltage and short circuit current can be derived (see equation 2.27). The light generated current was expressed as multiplication of short circuit current (I_{SC}).

$$V_{OC}(m) = \frac{nkT}{q} \ln\left(\frac{m \cdot I_{SC}}{I_0}\right) = V_{OC} + \frac{nkT}{q} \ln(m) \tag{2.27}$$

where:

$V_{OC}(m)$ - open circuit voltage under concentration factor m

m - concentration factor of an incident irradiance

Variations in open circuit voltage must be taken into account in case of concentrator systems (increase in performance for high concentration) but also for non-concentrating systems (decrease in performance in low light conditions). There is a logarithmic dependency between open circuit voltage and light generated current (see Figure 2.14).

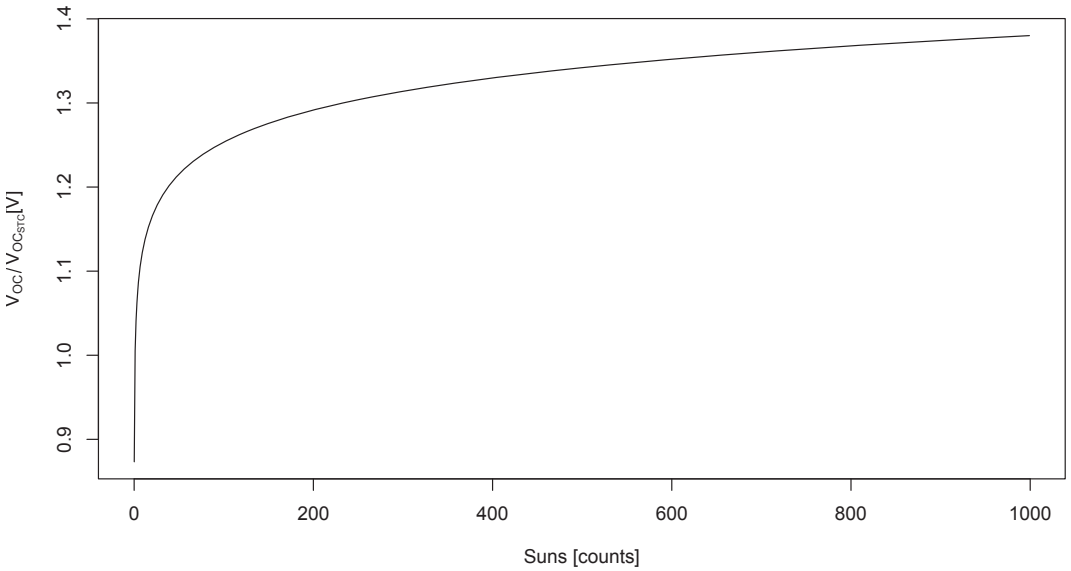

Figure 2.14: Influence of irradiance on open circuit voltage

Temperature effects: Temperature influences the generation rate and recombination rate of the solar cell material. Both short circuit current and open circuit voltage of the solar cell are affected. An increase of temperature will result in an apparent reduction of the band gap of the material (see equation 2.28 and Figure 2.15).

$$E_G(T) = E_G(0) - \frac{C_\alpha \cdot T^2}{T + C_\beta} \tag{2.28}$$

where:

$E_G(T)$ - material band-gap at temperature T

C_α, C_β - material dependent constants

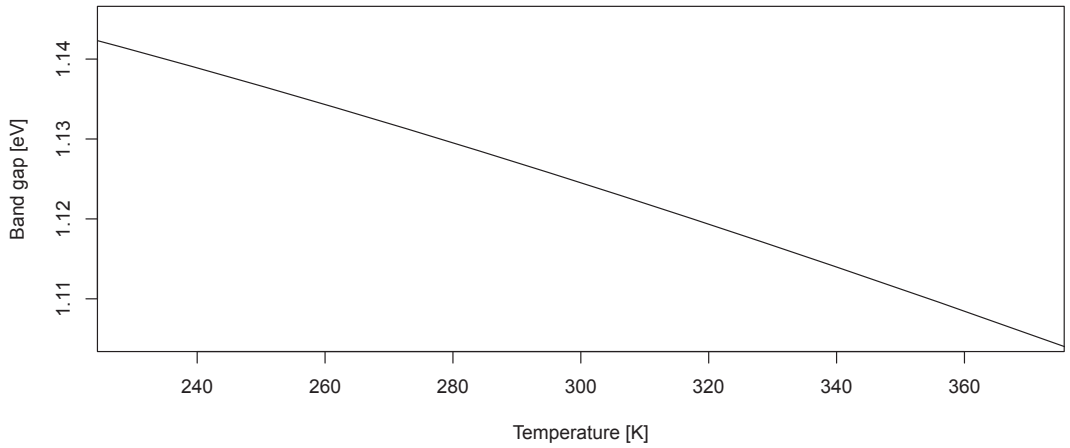

Figure 2.15: Influence of temperature on the apparent band gap of silicon

Lower band gaps result in increased intrinsic carriers concentration (n_i) (see Figure 2.16), which further causes an increase of the saturation current (I_0) (see equation 2.15 and 2.29).

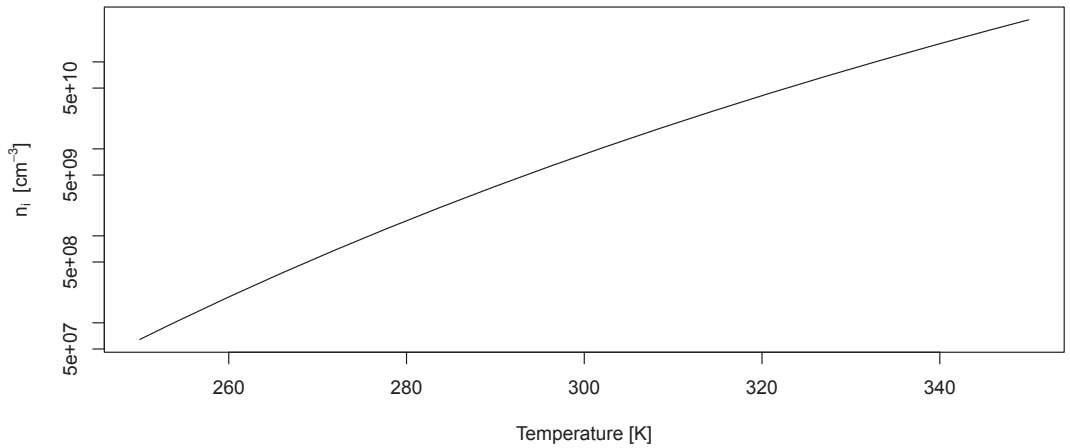

Figure 2.16: Influence of temperature on intrinsic carrier concentration for silicon

$$I_0(T) = C_B T^{C_\zeta} \cdot exp\left(-\frac{qE_G(0)}{kT}\right) \tag{2.29}$$

where:

$I_0(T)$ - saturation current at temperature T

C_B - temperature independent constant

C_ζ - constant reflecting possible temperature dependency of other than intrinsic carrier concentration material parameters

Increase of the saturation current causes a minor increase of the short circuit current. Temperature has the strongest impact on open circuit voltage (V_{OC}) of the cell. The open circuit voltage of the cell is reduced (see equation 2.30 and 2.31).

$$\frac{dV_{OC}}{dT} = -\frac{E_G(0) - V_{OC} + \zeta\frac{kT}{q}}{T} \tag{2.30}$$

$$V_{OC} = \frac{1}{q}E_G(0) - \frac{kT}{q}ln\left(\frac{BT^\zeta}{I_{SC}}\right) \tag{2.31}$$

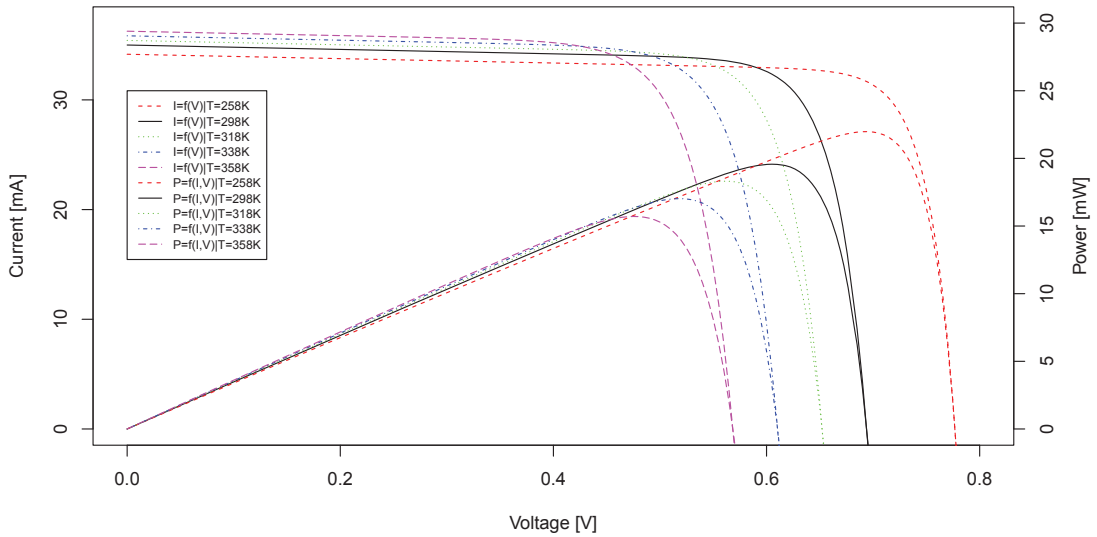

Figure 2.17: Influence of temperature on I-V curve

Solar cell efficiency is defined at standard test conditions[1]. Standard test conditions are not satisfied for the most of the operational time of the photovoltaic cell. Environmental parameters vary, which affects cell performance. The $I-V$ characteristic can be corrected with respect to temperature if the temperature coefficients of solar the cell are known. Current standards [40] specify empirical temperature coefficients for short circuit current (α), open circuit voltage (β) and maximum power point (δ). Coefficients are obtained by fitting linear function to thermal variations of the I_{SC}, V_{OC}, P_{MPP} for a given temperature range ($E_{e,STC} = 1000W/m^2\ AM1.5$). Temperature coefficients can be determined in natural solar irradiance or in the laboratory, under simulated solar irradiance. The parameters obtained are valid only for the same intensity and type of irradiance as used during the test procedure. Temperature coefficients for short circuit current and open circuit voltage are defined in equations 2.32 and2.33 respectively.

$$\alpha = \frac{I_{SC2} - I_{SC1}}{T_2 - T_1} \mid_{E_{e,STC}=1000W/m^2,AM1.5} \tag{2.32}$$

where:

I_{SC2} - short circuit current at temperature T_2 and irradiance $E_{e,STC}$

I_{SC1} - short circuit current at temperature T_1 and irradiance $E_{e,STC}$

T_1, T_2 - temperatures

α - current temperature coefficient

$$\beta = \frac{V_{OC2} - V_{OC1}}{T_2 - T_1} \mid_{E_{e,STC}=1000W/m^2,AM1.5} \tag{2.33}$$

where:

V_{OC2} - open circuit voltage at temperature T_2 and irradiance $E_{e,STC}$

V_{OC1} - open circuit voltage at temperature T_1 and irradiance $E_{e,STC}$

T_1, T_2 - temperatures

β - voltage temperature coefficient

[1] STC - Standard Test Conditions; irradiance $E_{e,STC} = 1000W/m^2$ at $AM1.5$ spectrum, device temperature $T = 25^0C$

2.2.4 Degradation

Long-term exposure of a device to different environments changes device behaviour. Most often observed changes are caused by degradation of cell materials and structure. Such a changes in solar cell can be reversible (meta-stable) or permanent. Long term variation of solar cell performance, caused by changes to the solar cell/module, is referred to as degradation. Degradation effects are caused by: long term illumination (light soaking), electric current flow, temperature (thermal mechanical cycling, ions diffusion), mechanical stress, electric bias or even electrostatic potentials [41–44]. Impact differs depending on cell technology.

Most solar cells reveal variations of performance after long term exposure to light (light soaking). Light soaking effects can be reversible (meta-stable) or permanent. Nearly all photovoltaic technologies exhibit changes in device performance under extended illumination, although the magnitude of these changes is much greater for some technologies than others. Such changes include reversible meta-stable phenomena, in which the photovoltaic device performance can alternate between different states depending on the history of illumination, electrical bias, and temperature, as well as long-term effects in which the device performance is fundamentally altered.

Temperature variations cause mechanical stress to the solar cells (thermal cycling). Temperature is also partially responsible for seasonal performance variations of some photovoltaic cells (thermal annealing) [45]

2.3 Photovoltaic system performance

2.3.1 System performance monitoring

The high level of complexity of photovoltaic systems and wide variety of the environmental conditions under which a system is working cause difficulties in system performance rating. Performance rating is required for appropriate system maintenance, which allows maximising the amount of yielded energy. Many companies offer proprietary monitoring solutions applicable for photovoltaics. Due to the lack of precise guidelines however, offered monitoring systems are designed differently (use different sensors, data acquisition, analytical processing). Com-

mercially available photovoltaics monitoring systems struggle to provide operational data results with defined levels of uncertainty. This situation brings up the question of how well different monitoring systems compare. As there is no precise guidance on the evaluation of uncertainty of measurements, a certain level of inconsistency between different systems is expected. It is of great importance to establish standards for adequate quality assessment of measurements and data processing. Standardised monitoring guidelines [46] initialised a process of unification in the field of methodology of measurements, which should be made for appropriate system performance calculations. Further development must be undertaken in the field of monitoring application and integration with existing/oncoming energy management systems.

2.3.2 System performance parameters

Three main standard parameters are used to define the overall performance of a photovoltaic system: final system yield, reference yield, and performance ratio [46] [47]. The final system yield (Y_f) (see equation 2.34) represents a number of equivalent hours, for which photovoltaic system would have to operate at standard test conditions, to generate the same amount of energy as it was transmitted by the system to the load, over the given time interval. The final yield normalises produced energy with respect to system size. It allows for comparison of the energy produced by systems of different size.

$$Y_f = \frac{E_{elec}}{P_0} \tag{2.34}$$

where:

Y_f - final yield

E_{elec} - electric energy generated by the system over a given time interval

P_0 - system power rated for standard test conditions

Reference yield represents solar radiation resources theoretically available to the photovoltaic system in a given period of time. It is defined as total in-plane irradiation normalised by standard test condition irradiance $E_{e,STC} = 1000W/m^2$.

Reference yield is a function of the location, orientation of the PV array, and month-to-month and year-to-year weather variability (see equation 2.35)

$$Y_r = \frac{H_e}{E_{e,STC}} \tag{2.35}$$

where:

Y_r - reference yield

H_e - irradiation received during given time interval

$E_{e,STC}$ - standard test condition irradiance

By combining the final yield and the reference yield, the performance ratio of photovoltaic system can be calculated. The performance ratio is considered as not biased by system size nor system location. However, due to imperfectness of reference measurements (e.g. irradiance), location specific environmental conditions may have an impact on a value of performance ratio. The performance ratio indicates the overall losses in the system due to temperature, incomplete utilisation of irradiance, system component inefficiencies, component failures, wiring losses, inverter inefficiency, mismatch or system down-time (see Figure 2.36).

$$PR = \frac{Y_f}{Y_r} \tag{2.36}$$

where:

Y_f - final yield

Y_r - reference yield

PR - performance ratio

The performance ratio coefficient is the most common way of evaluating of the overall performance of a photovoltaic system. While the performance ratio can be useful for small photovoltaic systems, giving clear indication of major failures, the level of detail is often not suitable for in-depth investigation of performance problems in large installations. For that reason, more specific performance efficiency indicators such as: array capture loses (L_C), array yield (Y_A), BOS losses (L_{BOS}), net energy from array, net energy from/to storage, net energy from backup, net

energy to load, net energy from/to utility grid were proposed [46]. Derivation of the parameters listed above requires the implementation of a detailed metrological system (sensors, data acquisition, data processing and historical storage). Present guidelines for performance monitoring of photovoltaic systems [46] specify required minimal levels of accuracy of given metrological parameters and recommendation for data processing workflow. Due to its moderate complexity they are applicable in practice. One major shortcoming in monitoring guidelines for photovoltaic systems is the uncertainty assessment. Further chapters of this thesis air to rise the level of knowledge in the field of metrological uncertainty of environmental parameters used in photovoltaic monitoring systems, in particular spectral irradiance.

2.4 Solar radiation

Solar radiation has an enormous influence on every aspect of human existence. The great majority of currently known and utilised sources of energy relate to the sun. To understand the nature of the solar radiation reaching the surface of the earth it is required to investigate how the solar energy is created and which factors influence its transmission on its way down to the earth's surface.

2.4.1 Extraterrestrial solar radiation

The sun is a plasmatic body composed mainly of hydrogen. It is the closest star to the earth. Energy released by the sun comes from a nuclear fusion process. Two nuclei of hydrogen join together to create one helium nuclei. The difference in mass between the substrates and products is converted into energy in accordance with Einstein's mass-energy equivalence formula [48] (see equation 2.37). As a result, highly energetic photons and neutrinos are emitted.

$$E = mc^2 \tag{2.37}$$

The nuclear fusion process happens in the core part of the sun, where the temperature exceeds $15 \cdot 10^6 K$. The generated photons are rapidly absorbed

by the solar plasma and remitted. The process of absorption and remission of photons starts in the core and continues through the radiation zone, convective zone up to the photosphere. Due to dependencies between temperature and pressure gradient, there is no convective heat transport in the radiation zone. Convection becomes possible in the outer parts of the sun. The structure of the sun is schematically shown in Figure 2.18.

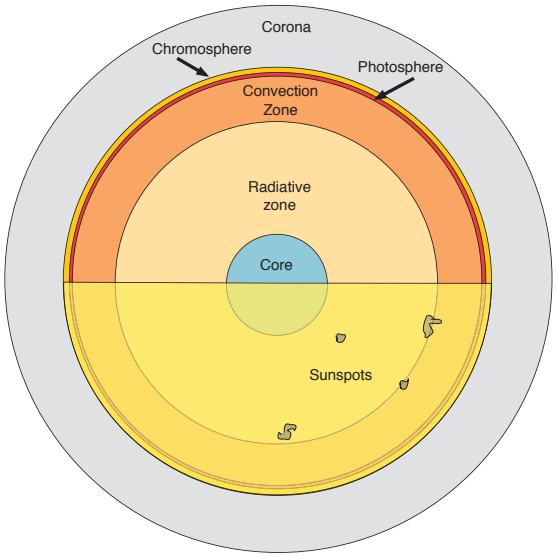

Figure 2.18: Structure of the sun according to NASA [2]

The spectral distribution of the radiation leaving the sun is mainly formed by the photosphere, where temperature lowers to around 5777K. Due to that fact, the spectrum of solar radiation observed on the edge of earth's atmosphere can be (in its first approximation) described by Planck's blackbody theory. In reality, the solar spectrum slightly varies from Planck's black body theory. Differences between the black body model and standardised extraterrestrial specta are shown in Figure 2.19

These differences are caused by non-uniform temperature and thickness of the photosphere and selective absorption of photosphere radiation in the solar atmosphere (corona). ASTM[1] E-490 [49] and WMO[2] Standard Extraterrestrial

[1]ASTM - American Society for Testing and Materials
[2]WMO - World Meteorological Organization

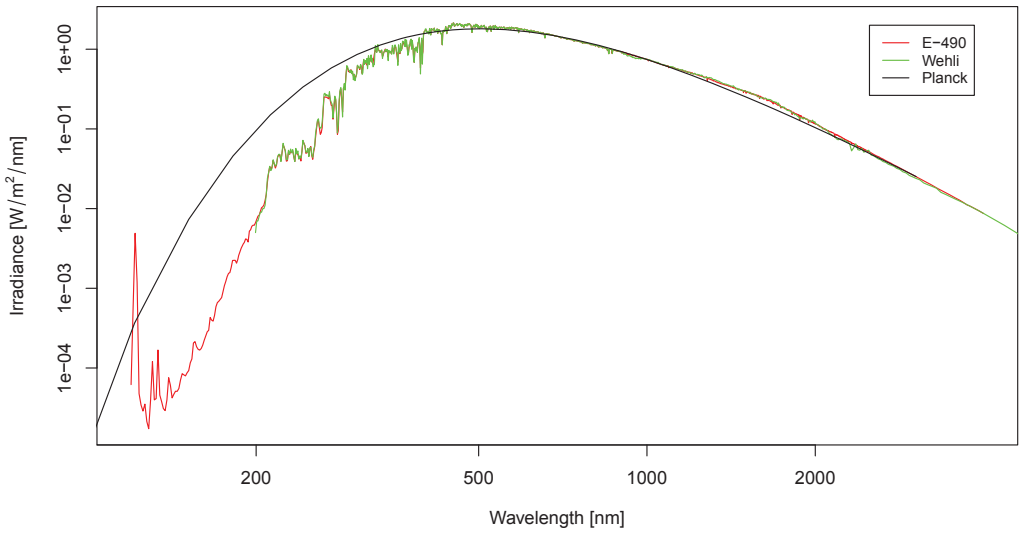

Figure 2.19: Standardised extraterrestrial spectral solar radiation ASTM E-490 [49] and Wehrli Standard Extraterrestrial Solar Irradiance Spectrum[50] vs. black body spectral radiation at temperature of 5777K (Planck)

Solar Irradiance Spectrum [50] are widely recognised as reference extraterrestrial solar spectra.

The solar constant describes the total integrated spectral radiant power received from the sun by a horizontal plane on the edge of the earth's atmosphere. Its value depends on the standard used ($1353W/m^2 \pm 1.6\%$ for ASTM E-490 and $1367W/m^2 \pm 1\%$ for WMO). Extraterrestrial solar spectra were obtained from measurements taken under moderate sun activity. Solar variation[1] is considered negligible for the purpose of this work and will not be further discussed. Variations of sun to earth distance influence radiant power coming to the earth significantly ($\pm 3.3\%$), thus an appropriate correction is required (see 2.38).

$$E_{e,0} = E_{e,C} + E_{e,C} \cdot 0.033 \cdot cos\left(\frac{360(n_{day} - 2)}{365}\right) \tag{2.38}$$

where:

$E_{e,0}$ - solar irradiance at the edge of the atmosphere

$E_{e,C}$ - solar constant equal to 1367W/m2

[1] solar variation - change of radiation emitted by the Sun mainly due to sunspots

Figure 2.20 presents the solar constant radiation variation as a function of day of the year.

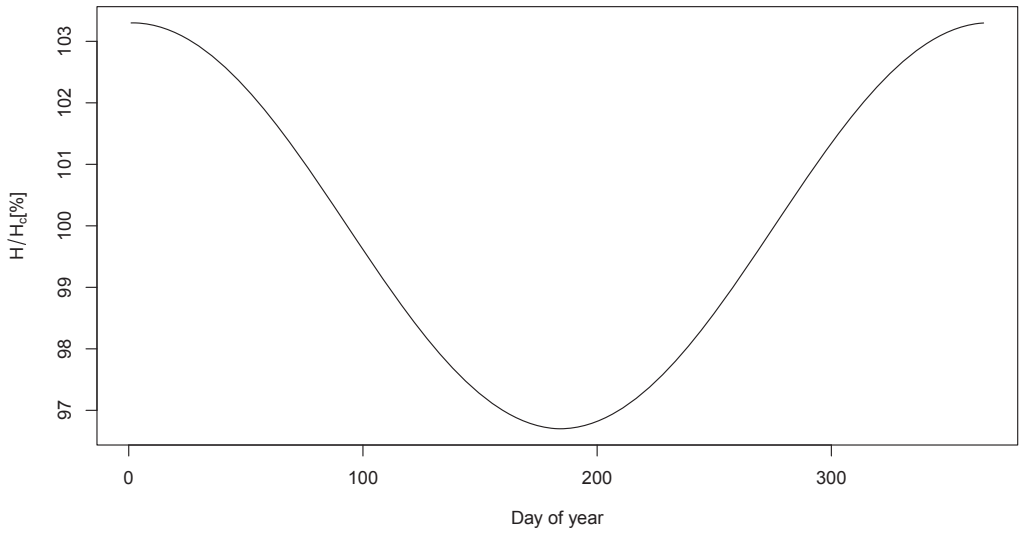

Figure 2.20: Variation of irradiance due to sun-earth distance

96.68% ($1322W/m^2$) of overall solar radiant power is transmitted with a wavelengths less than 2500nm. None of the currently available photovoltaic cells exceed this range. For these two reasons further analysis takes into account only spectral radiation below 2500nm.

2.4.2 Solar radiation on the earth's surface

While solar radiation passes through the atmosphere it can be transmitted, absorbed (then re-emitted), reflected (specularly or diffusively) and scattered[1]. The type and magnitude of occurring effects depends on the physical properties of the matter constituting the atmosphere at the time the solar radiation is interacting

[1]scattering - change of a direction of propagation of the electromagnetic radiation caused by the interaction of the electromagnetic radiation with an atom, molecule or particulate matter. The process of scattering can be elastic (Rayleigh, Mie: the energy of the electromagnetic radiation is conserved) or inelastic (Raman: the energy of the electromagnetic radiation is not conserved). Rayleigh scattering happens from the particle much smaller than the wavelength of the radiation. Mie scattering happens from the particle similar to, or larger than the wavelength of the radiation

with it. As a result, quantitative and qualitative properties of solar radiation are affected. Figure 2.21 presents a simple model of radiative transfer in the earth's atmosphere.

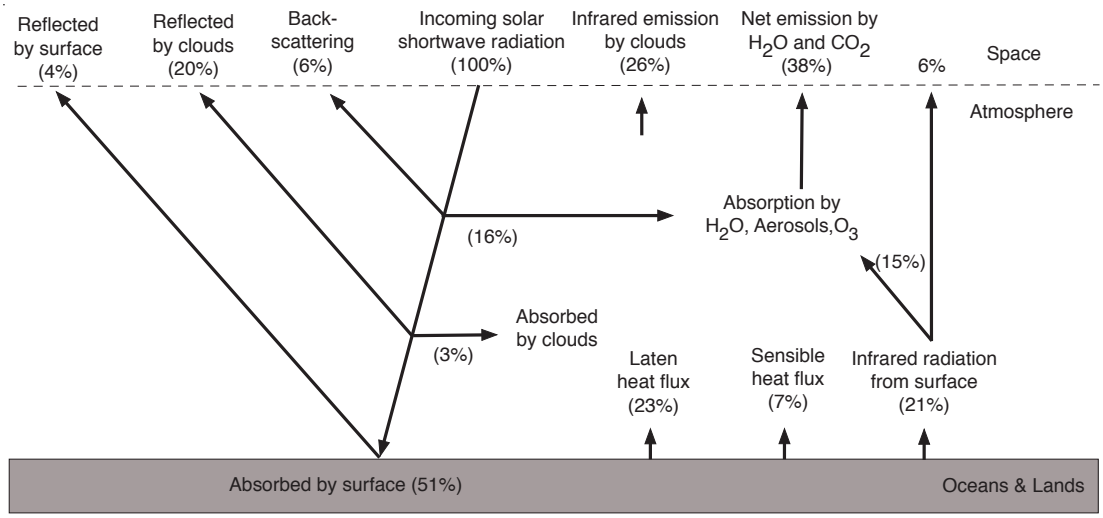

Figure 2.21: Simple model of radiative transfer in the earth atmosphere. Latent heat (water evaporation). Sensible heat (warm air)

The total radiative transfer between space and the earth equalises to zero. All shortwave radiation absorbed by the atmosphere or by the earth's surface is re-emitted in the form of long-wave (far infrared) radiation back to the space[1].

Earth's atmosphere is a highly complex, concentric, multilayer structure composed of variable chemical elements. Physical conditions (temperature, pressure, particle concentration, state of aggregation) vary significantly across the atmosphere layers. Several atmospheric layers are distinguished based on temperature differences (starting from the outermost): exosphere, thermosphere, mesosphere, stratosphere and troposphere. Figure 2.22 presents atmosphere cross-section with temperature and pressure variations overlaid.

The outermost layer of the atmosphere, still gravitationally linked to the earth, reaches up to 100 000km from the earth surface. However atmospheric gases at heights above 80km (mainly atomic H, He, O, N) are extremely diluted and so

[1]This simplified schematic does not include photosynthesis, which is the only process capable of converting shortwave radiation into chemical energy. Photosynthesis efficiency is very low. Globally less than 1% of solar energy is effectively converted by the plants into chemical energy.

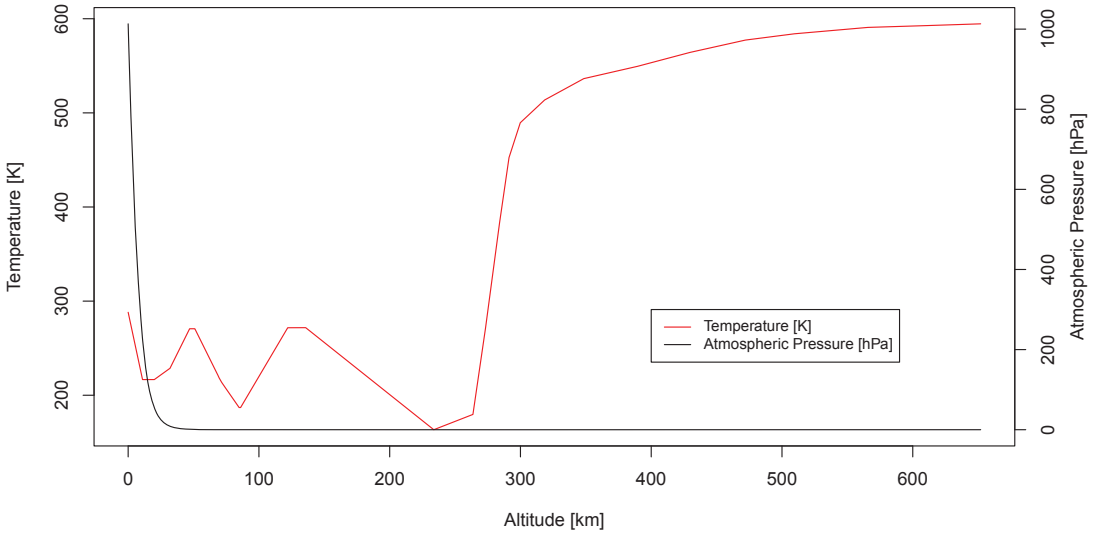

Figure 2.22: Partial atmosphere cross-section temperature and pressure [3]

attenuation of solar radiation is insignificant. The major part of atmospheric mass is found at heights less than 80km (99.995%) and 80% are at less than 15km in the troposphere only. Moreover, the troposphere is the place where the highest variations of atmospheric constituents are observed. The composition of the atmosphere manifests itself through the complex shape of the atmospheric transmittance spectrum. Figure 2.23 presents the spectral transmittance of solar radiation in the atmosphere under clear sky conditions.

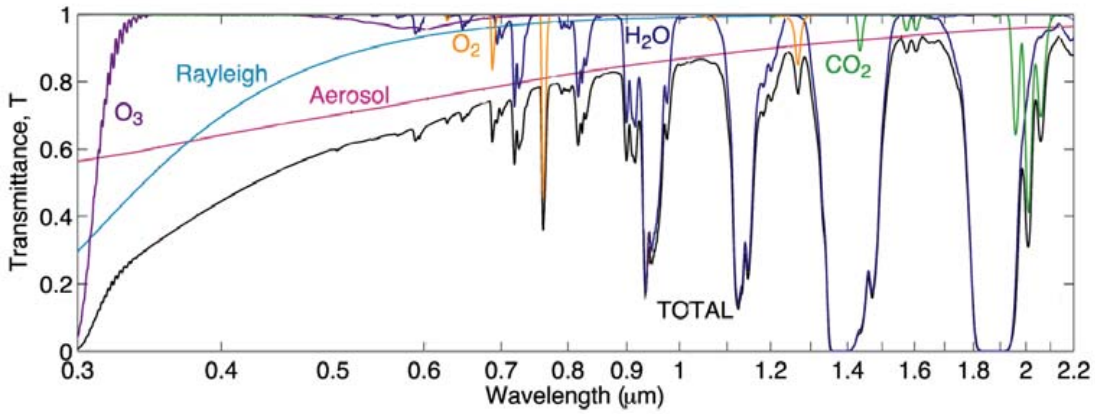

Figure 2.23: Spectral transmittance of the earth atmosphere [4]

Atmospheric constituents can be divided in three groups: dry air molecules, water vapour and aerosols. Each group of the atmospheric constituents contributes to the overall atmospheric transmittance. Because of the atmospheric scattering, part of the solar radiation reaches the surface of the earth as a diffused irradiance[1]. The ratio between the diffuse and the direct beam solar irradiance, on the surface of the Earth, depends on the state of the atmosphere.

Air mass is the most influential parameter affecting spectral irradiance on the surface of the earth under clear sky conditions. It scales the magnitude of all other atmospheric solar radiation attenuation effects. Most often relative air mass is used instead of absolute. Figure 2.24 presents: (a) simplified geometrical definition of the relative airmass and (b) the impact of the atmospheric refraction on the airmass.

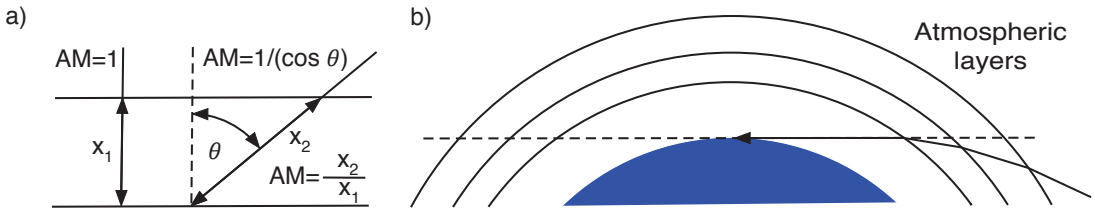

Figure 2.24: Geometric representation of the: a) air mass b) atmospheric refraction refraction

The approximate value of the air mass can be calculated from sun zenith angle according to equation 2.39.

$$AM \approx \frac{1}{cos(\theta)} \tag{2.39}$$

where:

AM - relative air mass

θ - solar zenith angle

In reality, the true value of the air mass is limited for the zenith angle $\geq 90\circ$. Due to the refractive properties of the atmosphere, the maximal value of the air mass is greater than the one defined by the line tangent to the surface of the earth

[1]diffuse irradiance - a fraction of the solar irradiance which reached the surface of the Earth after being scattered by the atmospheric constituents

and the edge of the atmosphere. Various air mass models have been developed over the years [51–53]. These models mainly improve air mass calculation at very low sun altitude. Only a small fraction of solar irradiation is being received by photovoltaic modules under such conditions however, so therefore there is no potential gain in terms of overall yield accuracy. For the purpose of this thesis the Kasten model[54] was used. Equation 2.40 presents Kasten's formula for air mass calculations.

$$AM = \frac{1}{cos(\theta) + 0.50572 \cdot (96.07995 - \theta)^{-1.6364}} \tag{2.40}$$

A dry and clean atmosphere contains N_2 (78,08%) , O_2 (20.95%), Ar(0.93%) and other trace gases(0.04%). Dry air molecules are distributed throughout all of the layers of the atmosphere. The ratio between the main constituents (O_2, N_2) are reasonably constant up to a height of 90km. Above this height molecular oxygen becomes dissociated and its share in atmosphere starts to grow. Dry air molecules are responsible for most of the Rayleigh scattering and some narrow-band absorption bands in the UV region (O_3) VIS region (O_2) and IR region (CO_2). More details about dry air molecules can be found in the Appendix A)

Atmospheric aerosols are solid or liquid substances mainly of terrestrial origin, which remain suspended in the air for a given period of time. The main sources of aerosols are presented in the Appendix A) Aerosols, depending on the distribution of particle size, can cause Raleigh and Mie scattering. Aerosol particles, depending on their origin (particulate matter from the earth, ocean salt, smoke, ground dust) vary in size from 2nm to 2μm. The wavelength dependency of scattering caused by aerosols is weaker than that caused by dry air molecules due to the fact that Mie scattering becomes dominant.

Atmospheric water vapour represents 0.25% of the atmosphere mass. Its content varies from 0% in polar to 4% in tropical climatic zones. The amount of water vapour in the atmosphere has a tremendous influence on the climate and life on the earth surface. Under standard atmospheric conditions (1013.25hPa, 20^0C) the mean free path for atmospheric particles is 68nm, which is two orders of magnitude greater than the sizes of an atomic nuclei of a N and O. On the nuclear level, the atmosphere can be then considered as an almost empty space. As

a result, the presence of dry particles does not affect the maximal water vapour content in the atmosphere. The theoretical maximum water vapour content in the atmosphere is defined by equilibrium state between evaporation and condensation processes. The rate of evaporation is a function of the energy required by a particle to overcome intermolecular forces and leave the liquid phase. This energy, called evaporation heat, needs to be provided to the particles to enable the evaporation process. Evaporation energy depends on the kind of the particle. Different chemical substances have different evaporation heat. Evaporation heat also depends on the shape of the interface from which the particles are evaporating. Clouds can contain droplets which are made of only a few water particles. In the case that the evaporation interface becomes spherical, bounding interactions between particles weaken and evaporation heat decreases. The saturation vapour pressure is defined for the case of planar interface between liquid and vapour phases. For that reason saturation water vapour pressure in the clouds can be over 100% of the saturation water vapour pressure over the water surface. This state is called supersaturation. Saturation water vapour pressure depends only on temperature (see Figure 2.25).

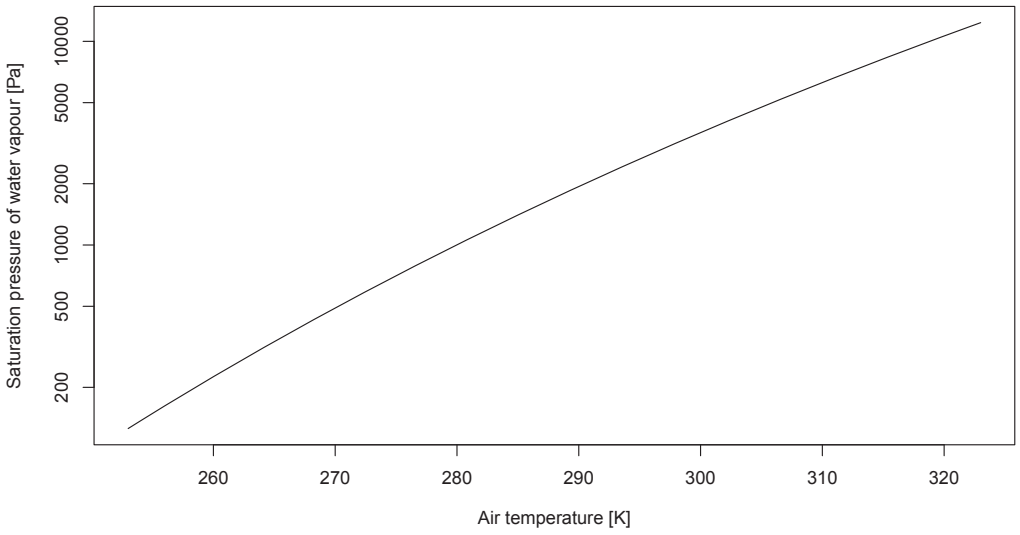

Figure 2.25: Saturation water vapour pressure as a function of a temperature [5].

The ratio between the absolute water vapour pressure and the saturation

water vapour pressure is called the relative humidity.

$$RH = \frac{p_{H_2O}}{p_{H_2O_{sat}}} \tag{2.41}$$

where:

RH - relative humidity

p_{H_2O} - water vapour pressure

$p_{H_2O_{sat}}$ - water vapour saturation pressure

Water evaporates to the atmosphere from the oceans, rivers, lakes and ground. Molecules of water are lighter than molecules of nitrogen and oxygen and therefore are partially responsible for the air lift. While warm, humid air rises, atmospheric pressure decreases (see 2.22), which causes a temperature drop. At lower temperature, the saturation water vapour pressure lowers, and water vapour starts to condensate into droplets which then form clouds. Formation of water drops is promoted by aerosol particles, which act as condensation nuclei. As a result, water vapour has a significant influence on aerosol particles in the atmosphere. Water vapour is the main absorber in the infrared. Molecular water is comparable in size to dry air molecules, but as it can cluster into droplets of much greater sizes, it can cause both Rayleigh and Mie scattering. More information on water vapour can be found in the Appendix A).

Cloud coverage is the most variable and the most influential stochastic metrological parameter which determines the amount of solar radiation reaching the surface of the Earth. Over the years, multiple methods of the overcast classification were proposed. The simplest one (by Barbaro) values cloudiness based on sight, at regular time intervals, in eights or tenths of overcast sky (see Table 2.1).

Table 2.1: Classification of day type by Barbaro [6].

Day Type	Octas	Tenths
Clear day	0-2	0-3
Partially cloudy day	3-5	4-7
Cloudy day	6-8	8-10

Barnabo's method requires taking frequent sky observations by personnel. Moreover, achieved results are susceptible to subjective judgement.

The impact of the atmosphere on terrestrial global horizontal irradiance is described by the clearness index. Instantaneous clearness index (k_t) is a ratio between the terrestrial solar global horizontal irradiance and the corresponding extraterrestrial solar irradiance (see equation 2.42).

$$k_t = \frac{E_{e,GHI}}{E_{e,0}} \tag{2.42}$$

where:

k_t - instantaneous clearness index

$E_{e,GHI}$ - terrestrial solar global horizontal irradiance

$E_{e,0}$ - solar irradiance at the edge of the atmosphere

Iqbal[7] proposed, that the type of the day can be determined based on daily clearness index K_T[1] (see Table 2.2). The method proposed by Iqbal does not require any additional measurements to be taken. In addition it is applicable to the retrospective datasets if only the time and the geographical location of the meteorological site is known.

Table 2.2: Classification of day type by Iqbal [7].

Day Type	K_T
Clear day	$0.7 \leqslant K_T < 0.9$
Partially cloudy day	$0.3 \leqslant K_T < 0.7$
Cloudy day	$0.0 \leqslant K_T < 0.3$

Under real skies (varying cloud coverage, turbidity, air mass), solar global horizontal irradiance can be respectively enhanced or reduced. In some specific cases, the same value of the clearness may be observed under various combinations of atmospheric conditions (e.g. cloud-enhanced irradiance observed under high air mass can produce clearness index equal to the one observed under cloudless

[1] K_T -daily clearness index defined as the ratio between daily horizontal global solar irradiation observed on the surface of the Earth and corresponding extraterrestrial solar irradiation

sky and low air mass). Part of these variations has a deterministic character, and therefore can be predicted with the use of various clear sky models [55–60].

Once the clear sky irradiance is known, a clear sky index can be calculated (see equation 2.43).

$$k_c = \frac{E_{e,GHI}}{E_{e,GHI_C}} \tag{2.43}$$

where:

k_c - instantaneous clear sky index

$E_{e,GHI}$ - solar global horizontal irradiance

E_{e,GHI_c} - modelled solar global horizontal irradiance

By using a simple direct irradiance attenuation model, Perez [61] proposed a zenith angle-independent clearness index formulation (see equation 2.44).

$$k_{t'} = \frac{k_t}{1.031 \cdot exp(\frac{-1.4}{0.9+\frac{9.4}{AM}})) + 0.1} \tag{2.44}$$

where:

$k_{t'}$ - zenith angle-independent clearness index

In the context of sky type classification, the quality of the clear sky index depends on the accuracy of the clear sky model. It has to be noted here, that parameters used in clear sky models, to some extent, undergo stochastic variations too. For example, an increase of aerosols or water vapour concentration may lead to a turbid sky. In such a case, the diffuse fraction (k) provides the method of differentiation (see equation 2.45).

$$k_d = \frac{E_{e,GHI}}{E_{e,DHI}} \tag{2.45}$$

where:

k_d - instantaneous diffuse fraction

$E_{e,DHI}$ - solar diffuse horizontal irradiance

According to Thevenard[62], the sky should be classified as clear when the diffuse fraction k lays between 0.2 and 0.4. Use of the diffuse fraction requires measurements of diffuse irradiance. Such measurements are not frequently available, which significantly constrains the application of classification methods based on diffuse fraction.

In the case that high temporal resolution data is available, the Ineichen[63] method can be applied for clear sky classification. In this method, conditions defined in equation 2.46 and 2.47 have to be met.

$$E_{e,GHI} > 0.9 \cdot E_{e,GHI_C} \tag{2.46}$$

where:

$$E_{GHI_C} = E_0 \cdot exp(\frac{-2 \cdot AM}{(9.4+0.9 \cdot AM)})$$

$$|\Delta E_{e,GHI} - \Delta E_{e,GHI_C}| < 10\% \tag{2.47}$$

where:

$$\Delta E_{e,GHI} = \frac{E_{e,GHI}(t-1) - E_{e,GHI}(t+1)}{E_{e,GHI}(t)}$$
$$\Delta E_{e,GHI_c} = \frac{E_{e,GHI_c}(t-1) - E_{e,GHI_c}(t+1)}{E_{e,GHI_c}(t)}$$

A comprehensive overview and evaluation of the existing clear-sky classification procedures and models was given by Younes and Muneer[64]. The authors also proposed a new approach for identification of clear sky based on clearness index, diffuse ratio, turbidity and cloud-cover limits. Relevant limits were calculated via the cloud-cover cumulative frequency distribution and the associated clearness index and diffuse ratio cumulative frequencies.

Atmospheric pressure directly influences attenuation of solar radiation in the atmosphere. Variations of atmospheric pressure are caused by the appearance of such processes as rising air, air density variation or air mass variations. Atmospheric pressure is commonly used as a parameter in radiative transfer models.

To account for the atmospheric pressure variation pressure corrected relative air mass can be calculated from the equation 2.48.

$$AM' = \frac{p}{p_0} \cdot AM \tag{2.48}$$

where:

AM' - atmospheric pressure corrected relative air mass

p - atmospheric pressure

p_0 - standard atmospheric pressure

2.4.3 Solar radiation measurements

Solar radiation is the most important as well as the most complex of all environmental observations. Three main groups of solar radiation detector types can be specified (thermopile, black body cavity, solid state). Black body cavity radiometers are the ultimate metrological devices for solar radiation measurements. Due to limitations in real life applications (they can be used only on clear days) and extremely high costs, absolute cavity radiometers are considered not applicable to photovoltaics and are not studied in this thesis. Only thermopile and semiconductor sensors are discussed. With respect to spectral response, a given type of detector can be used for broadband or spectrally selective measurements. The accuracy of spectrally selective measurements is usually worse than broadband measurements. It happens due to the higher optical and mechanical complexity of the radiometer (interference filters, diffractive slit, grating plate), lower signal to noise ratio of output signals, elongated time required for measurement. In most of the cases (including photovoltaics), the spectral distribution of solar radiation is neglected, and broadband solar radiation is used instead. Solar radiation measurements are available from many meteorological stations worldwide, however only 64 of them comply with restrictive BSRN[1] regulations [65]. The majority of the meteorological stations measure only global solar radiation on a horizontal plane. In accordance to WMO [66] and ISO standards [67] the global

[1]BSRN - Baseline Surface Radiation Network

solar radiation sensor must comply with a set of parameters (angular response of 2π, spectral range of $300nm$-$3000nm$, daily totals uncertainty of 5%, long term stability) to be accepted as a reliable source of network data.

Global solar radiation reaching the Earth's surface can be decomposed into direct and diffuse components. Under clear sky conditions, the ratio between direct and diffuse solar spectral radiation can be calculated for a given location and time from atmospheric radiation transfer models. For a tilted plane and standard atmosphere state around 87% of global solar radiation reaches the earth surface as the direct component. The remaining 23% comes as diffuse. This relation is dramatically differed by clouds. The share of the diffuse irradiance component in global irradiance increases with increasing precipitable water amount. Direct solar radiation is partially reflected/backscattered from the top of the cloud back to the space. The remaining part of the solar direct radiation is scattered and absorbed by water particles as it traverses the cloud. Under cloudy sky conditions, diffuse irradiance can reach 100% of global irradiance. The ratio between diffuse and direct solar radiation affects the level of energy losses caused by reflections from the photovoltaic module surface. As only direct radiation is capable of casting shadows shading effects are strongly dependent on global solar radiation components shares.

Under partially cloudy sky conditions, temporal variation of solar irradiance can easily reach hundreds of Watts per square meter per second. Moreover, under specific conditions, clouds can reflect solar radiation towards the ground causing localised radiation enhancement. It has been reported [68] that such an irradiance enhancement may not be utilised by photovoltaic installations because of too low sizing factor of the inverters. Moreover, overloading may cause the inverter to shutdown and increases probability of failure. It is impossible to avoid transient irradiance states in photovoltaic systems. Variation of the reference irradiance should then be considered as a factor, which influences the accuracy of performance monitoring of a photovoltaic system. Sub-second irradiance measurements are required for more detailed assessment of the effects of transient reference irradiance. Thermopile pyranometers, because of relatively long response time (5-18s) are not suitable for such applications.

Chapter 3

Uncertainty of spectral irradiance measurements

3.1 Introduction

The uncertainty of reference solar radiation measurements is a predominant factor defining the quality of a photovoltaics monitoring system. Reference solar radiation sensors have proven their usefulness in applied photovoltaics by enabling performance monitoring. Regardless of this, only a few experiments have been conducted to investigate the statistical distribution of outdoor spectral solar radiation and its impact on instantaneous and long-term performance of photovoltaic cells [69]. The AM 1.5 spectrum defined in ISO [70] and ASTM [71] standards was adopted in photovoltaics [72] as a representative standard test condition for characterisation of electrical and optical properties of photovoltaic cells. The main aim of this chapter is to evaluate the impact of using various instrumentation for reference solar radiation measurements in photovoltaics. A comparison of spectroradiometers to other solar radiation sensors commonly used in photovoltaics is made along with an explanation of experimental setup, calibration methodology and discussion of achieved results. Differences between standardised AM1.5 and outdoor measured spectral solar radiation characteristics are analysed. The influence of the angular response of the sensor under different radiation types (diffuse, direct, mixed) is also considered in relation to photovoltaic device performance

assessment.

Recommendations for measurements uncertainty are defined and normalised by the "Guide to the expression of uncertainty in measurement" [73]. The concept of uncertainty as a quantifiable attribute is relatively new in the history of measurement, although error and error analysis have long been a part of the practice of measurement science. It is now widely recognised that, when all of the known or suspected components of error have been evaluated and the appropriate corrections have been applied, there still remains an uncertainty about the correctness of the stated result, that is, a doubt about how well the result of the measurement represents the value of the quantity being measured.

Measurement is the process of quantification of the value of any measurable quantity. The "true" value of the measurable quantity remains unknown throughout. The measurement process leads to an uncorrected result, which is biased by the set of errors. Some of these errors are deterministic and can be eliminated by applying appropriate corrections. The corrected result of a measurement is the best possible approximation of the "true" value. Regardless of effort, not all of the sources of error can be identified. Unnoticed systematic errors and random errors are still present in the corrected result. The corrected result of a measurement is expressed by the following parameters: expected value, variance, distribution type and confidence factor. The concept of the measurement process is shown in Figure 3.1

If the distribution of the remaining error is normal, the true value of measurement lies within one standard deviation (1xSD) interval from the corrected result with a probability of 68.3%, within 2xSD interval with a probability of 95.4% and within 3xSD interval with a probability of 99.7%

The difference between the uncorrected result of a measurement (X) and the true value (X_t) is called the absolute error of measurement (ΔX) (see equation 3.1).

$$\Delta X = X - X_t \tag{3.1}$$

The unit of the absolute measurement error is the same as that of the measured

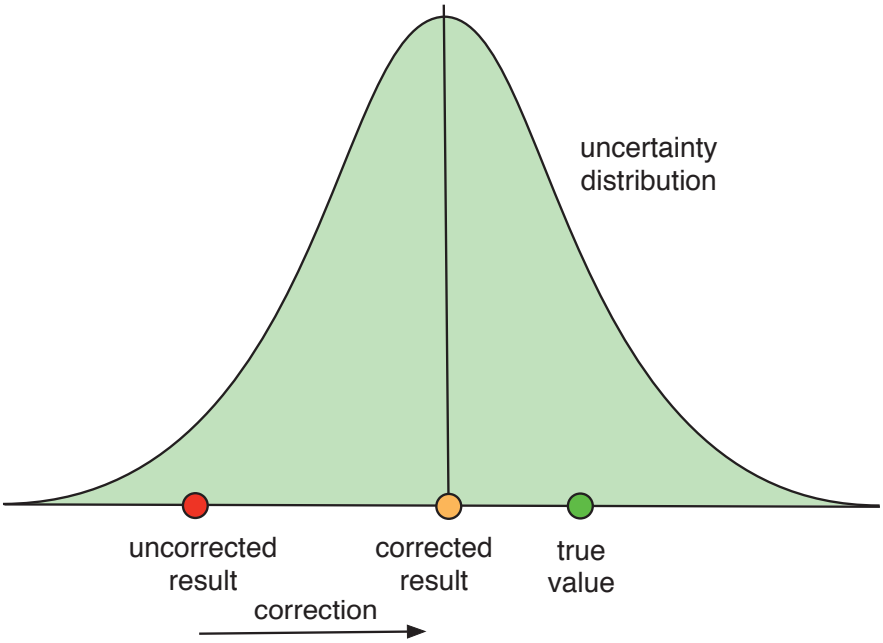

Figure 3.1: Concept of measurement process

parameter. The ratio of the absolute error of measurement and the true value of measurand(X_t) is called the relative error (δX) and is expressed as a percentage (see equation 3.2).

$$\delta X = \frac{\Delta X}{X_t} \tag{3.2}$$

Measurement errors can be divided into two main groups: systematic and random. Systematic error expresses the difference between the mean value resulting from repeated measurements and the true value of the measurand. Random errors express the difference between the value of a single measurement and its mean resulting from measurement repetition (given that the conditions of the measurements are unchanged). Figure 3.2 illustrates the difference between systematic and random error.

Standard uncertainty (u) of the result of measurement is expressed as an

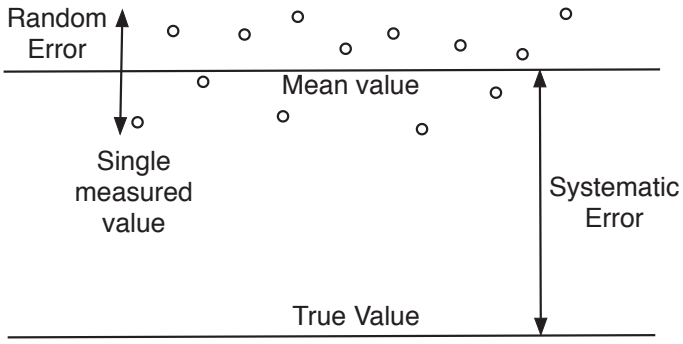

Figure 3.2: Classification of measurement errors for a repeated measurement of a constant value

estimated standard deviation (σ) associated with the result.

$$u(y) = \sigma = \sqrt{\frac{1}{N-1}\sum_{i=1}^{N}(y_i - \hat{y})^2} \tag{3.3}$$

where:

$u(y)$ - uncertainty of a measurement

N - number of measurements

y_i - value of a single measurement

$\hat{y}$ - mean value

The distribution of standard uncertainty is most often Gaussian. Assuming this is so, 68% of the distribution lies within 1xSD from the mean. To increase the level of trust in a result, the expanded uncertainty is used.

$$U = u(y) \cdot k \tag{3.4}$$

where:

U - expanded uncertainty

k - coverage factor

Expanded uncertainty takes into account a coverage factor. Coverage factor k=2 implies approximately 95% level of confidence and for k=3 level of confidence

comes up to 99.6%. Gaussian distributions with overlaid coverage factors are shown in Figure 3.3.

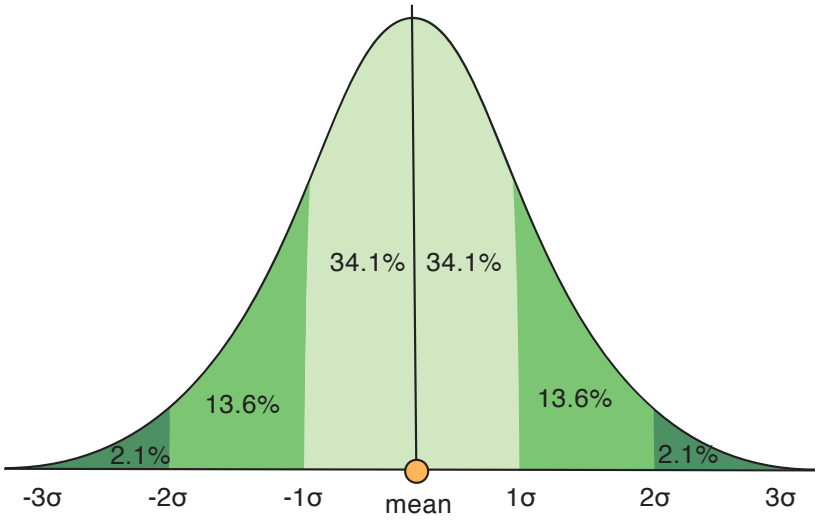

Figure 3.3: Expanded uncertainty coverage

The result of a measurement may be obtained from more than one functionally related quantity (as shown in equation 3.5).

$$y = f(x_1, x_2, x_3, ..., x_N) \tag{3.5}$$

where:

x_1, x_2 - measured quantities

f - functional dependency between measured quantities

y - resultant value

The standard uncertainty of a measurement is then expressed as combined standard uncertainty (u_c) and is calculated as the positive square root of the combined variance obtained from all variance and covariance components. The equation for combined standard uncertainty can be generalised by a first order

Taylor approximation (see equation 3.6).

$$u_c^2(y) = \sum_{i=1}^{N} \left(\frac{\partial f}{\partial x_i} \right)^2 u^2(x_i) + 2 \sum_{i=1}^{N-1} \sum_{j=i+1}^{N} \frac{\partial f}{\partial x_i} \frac{\partial f}{\partial x_j} u(x_i, x_j) \tag{3.6}$$

where:

x_1, x_2 - measured quantities

f - functional dependency between measured quantities

$\partial x_i, \partial x_j$ - partial derivatives

This equation is referred to as the law of propagation of uncertainty, and can be used for estimation of uncertainty of complex measurements.

Every measurement taken in a natural environment is uncertain and this uncertainty can be limited by the use of sophisticated metrological instrumentation and methodology. The most important part of metrology is the definition of base units (SI system), their standards and their uncertainties. Any measurable quantity and its uncertainty can be derived from the base units system and its standards. Metrological devices are usually calibrated against working standards (see Figure 3.4). If the result of a measurement can be compared to the primary standard (directly or through the chain of working/secondary standards) it is said that the result is traceable.

Figure 3.4: Hierarchy of standards

Extremely low levels of uncertainty can be achieved at the cost of reproducibility (advanced and prohibitively expensive equipment, sophisticated metrological

methods and extensive experimenter experience). It is of great importance that the measurement process can be easily reproduced. A low level of reproducibility makes the measurement process not applicable in a real life scenario, regardless of the benefits of lowered uncertainty. The uncertainty of a measurement cannot be taken as an ultimate descriptor of adequacy of a given metrological system. In many cases over-specified accuracy requirements become the reason of unjustified increase in metrological system cost without any significant improvements in the system usability for a given scenario.

3.2 Classification of radiometers

The majority of worldwide meteorological stations worldwide use thermopile radiometers for solar irradiance measurements. This type of sensors fulfils the WMO and ISO requirements at moderate expense. Photovoltaic systems are often not equipped with dedicated reference solar radiation sensors at all and measurements taken by local meteorological stations are the only available reference radiation data. Use of a local meteorological station data decreases the accuracy of instantaneous irradiance measurements due to the localised character of irradiance and the need for horizontal to in-plane irradiance translation algorithms.

The ubiquity of thermopile pyranometers in meteorology led them to be adopted for photovoltaic applications. While thermopile pyrometers are optimal for meteorological observations, some of their properties have a questionable influence on the accuracy of application specific reference radiation measurements. The hemispherical integrating dome gathers light differently to the flat surface of solar modules. Moreover reflections from flat vs. curved surfaces differ (especially for low sun positions). The wide spectral range of a thermopile pyranometer, invaluably important for investigation of radiative energy transfer, does not work to the advantage of photovoltaics applications. This is due to a fact that all currently available solar cells have relatively narrow spectral response in comparison to thermopile pyranometer. Finally, a thermopile pyranometer measures radiative power, while a photovoltaic cell is a quantum device and so it is sensitive to photon flux. Regardless of the problems listed above, due to its long-term stability and existent calibration standards, thermopile pyranometers can be used

to monitor long-term performance degradation of the photovoltaic modules. The possibility of continuous measurement of long-term performance degradation is important during evaluation studies of new cell/module technologies as well over the lifetime of a photovoltaic system.

Figure 3.5: Thermopile pyranometer

As shown in Figure 2.12 the short circuit current of a photovoltaic cell depends mainly on the intensity of solar radiation. It almost does not depend at all on temperature. These characteristics enabled for the construction of semiconductor radiometers and some of them have been accepted even by the WMO. In photovoltaics, use of the irradiance sensor made of the same semiconductor technology as the photovoltaic cells can be beneficial. Mismatch between the spectral responses of the solar radiation sensor and photovoltaic module is almost completely removed. The angular response of the reference semiconductor sensor matches that of the photovoltaic module. The reference cell works in shunt mode therefore its degradation due to thermal cycling and light exposure is much the same as degradation of the photovoltaic cells inside the module. As long as there is a known correlation between the degradation of the photovoltaic module and the reference irradiance sensor (e.g. same manufacturing technology), the lack of long-term stability of the irradiance sensor can be considered as not influential for its accuracy.

For these reasons, reference cells with the same exposure history as the module

should provide the most relevant measure for performance estimation. The same exposure history cannot always be guaranteed due to various scenarios of solar system lifetime (e.g. required replacement of reference sensor/part of photovoltaic array). Problems arising from the lack of long-term stability of the reference semiconductor irradiance sensors can be resolved by an appropriate calibration method.

Outdoor solar spectral radiation measurements are often considered as an unimportant, secondary order factor in applied photovoltaics. The reason for this lies in the complicated metrological instrumentation required to take spectral measurements, the extensive specialist knowledge required to interpret spectral measurements data, questionable quality of available spectroradiometers, assumed low impact of solar spectral radiation variation on total sums of generated energy. With current trends focused on multi-junction and thin film photovoltaic cells, the characterisation of spectral solar radiation under realistic atmospheric conditions should be taken into detailed consideration as its importance greatly increases for such kinds of devices. Moreover, spectroradiometers are capable of providing spectrally correct reference measurements for multiple solar cell technologies. Additional important application of spectroradiometers other than outdoor monitoring is for indoor photovoltaic module characterisation. Lack of continuous spectral characterisation of the radiation emitted by solar simulators is one of the main sources of uncertainty in indoor photovoltaic devices characterisation processes.

3.3 Radiometers calibration standards

The main application of optical radiometry on the earth's surface relates to solar energy use. The global solar energy market is increasingly becoming an important part of the world economy. Photovoltaic modules are priced based on rated power. With similar technological advancement in manufacturing processes, the power rating of solar devices has become significant factor in product marketing. Regardless of the correctness of the standard test condition based approach of energy ratings, metrological procedures based on radiation should utilise radiometers calibrated in accordance to traceable standards. The standardisation

of radiometer calibration has its genesis in the U.S space program. Over the years, a set of radiometric standards has been developed by ISO and IEA/ASTM. Current radiometric measurements standards defined by ASTM are listed in Table 3.1.

Table 3.1: ASTM radiometric standards

Standard	Title
G130	Standard Test Method for Calibration of Narrow- and Broad-Band Ultraviolet Radiometers Using a Spectroradiometer
G138	Standard Test Method for Calibration of a Spectroradiometer Using a Standard Source of Irradiance
G183	Standard Practice for Field Use of Pyranometers, Pyrheliometers and UV Radiometers
G167	Standard Test Method for Calibration of a Pyranometer Using a Pyrheliometer
G173	Standard Tables for Reference Solar Spectral Irradiances: Direct Normal and Hemispherical on 37 Tilted Surface
G177	Standard Tables for Reference Solar Ultraviolet Spectral Distributions: Hemispherical on 37 Tilted Surface
G197	Standard Table for Reference Solar Spectral Distributions: Direct and Diffuse on 20 Tilted and Vertical Surfaces

Current radiometric standards defined by ISO/IEC were listed in Table 3.2.

Table 3.2: ISO/IEC radiometric standards

Standard	Title
ISO 9059:1990	Solar energy - Calibration of field pyrheliometers by comparison to a reference pyrheliometer
ISO 9060:1990	Solar energy - Specification and classification of instruments for measuring hemispherical solar and direct solar radiation
ISO 9845-1:1992	Solar energy - Reference solar spectral irradiance at the ground at different receiving conditions – Part 1: Direct normal and hemispherical solar irradiance for air mass 1,5
ISO 9846:1993	Solar energy - Calibration of a pyranometer using a pyrheliometer
ISO 9847:1992	Solar energy - Calibration of field pyranometers by comparison to a reference pyranometer
ISO/TR 9901:1990	Solar energy - Field pyranometers – Recommended practice for use

A review of the standards clearly shows that there are no ISO/IEC references for spectroradiometer calibration and the only existing standard in this domain

is ASTM G138. References to spectral characterisation of radiation are present in many photovoltaic normative documents, however the lack of standardised spectroradiometer calibration procedures is a source of excessive uncertainty in photovoltaic module power rating.

Radiometer calibration is usually realised by comparison to the radiance source or another radiometer (calibrated and traceable to international standards) under defined geometry.

3.4 Sources of radiometer uncertainty

Uncertainty analysis of any kind of measurement process can be divided into a set of separated steps. Firstly, a specific measurement equation should be derived. This defines the measurement and metrological setup used for achieving the measurement. The next step is to identify and to quantify all the sources of the uncertainty in the measurement. Once the uncertainty sources are identified and quantified, the probability density function of each of them should be established. This allows for calculation of combined uncertainty (in accordance to uncertainty propagation law) and expanded uncertainty (specific confidence interval). Once all of the above steps are completed, the result of a measurement and its uncertainty can be reported.

There is a great level of misunderstanding in interpretation of manufacturers' claimed uncertainties of radiometers in photovoltaics. For instance, the uncertainty of pyranometer measurements is defined specifically for radiant power, not the photon flux. Use of radiant power for system performance analysis leads to systematic error. Therefore manufacturer claimed uncertainty is not valid and should be recalculated specifically for photon flux. List of sources of radiometer uncertainty was shown in Table 3.3.

Consumer product calibration should be realised by direct comparison to a working irradiance standard lamp. The uncertainty of the working irradiance standard is a function of the uncertainty of primary standard characterisation followed by calibration transfer procedures. The cost of the lamps offered by NIST is often prohibitively high, especially given that the calibration of the lamp is valid only for 50h. As a result, commercial-grade working irradiance standard

Table 3.3: Sources of radiometer uncertainty

Radiation standard (sensitivity and wavelength)
stated calibration uncertainty of a transfer standards
reproducibility and stability of operational conditions (current, voltage)
structural stability (degradation,recrystallisation)
Calibration transfer
alignment of calibration rig
air temperature and humidity
interpolation algorithm
Radiometer (generic)
angular response
non-linearity of a detector
temperature drifts
long-term detector degradation
Radiometer (specific)
stray light
exposure time
dark current noise
optical element fluorescence

lamps are offered by various manufacturers (Newport, Gamma Scientific, Optronics Laboratories (Gooch&Housego)). To reduce the cost of products some manufacturers [74] transfer calibration form the NIST lamp to in-house prepared FEL lamp and use it as a working standard for further calibration. The uncertainty related to calibration transfer procedure is doubled, since two calibration transfer procedures are required. The irradiance uncertainty chain is shown in Figure 3.6.

It is clearly visible that the calibration of an irradiance standard can be easily degraded by an inappropriate calibration transfer procedure. Moreover, the lamp under test should be aged before calibration, as there is a significant reduction in emitted radiant power in the first hours of lamp lifetime. Assuming that the radiometer does not introduce any additional sources of uncertainty (which is not realistic), the minimum uncertainty of a radiometer sensitivity scale calibration cannot be lower than 3%. The electrical working parameters of the standard lamp must be precisely controlled. The radiometric power source must be calibrated

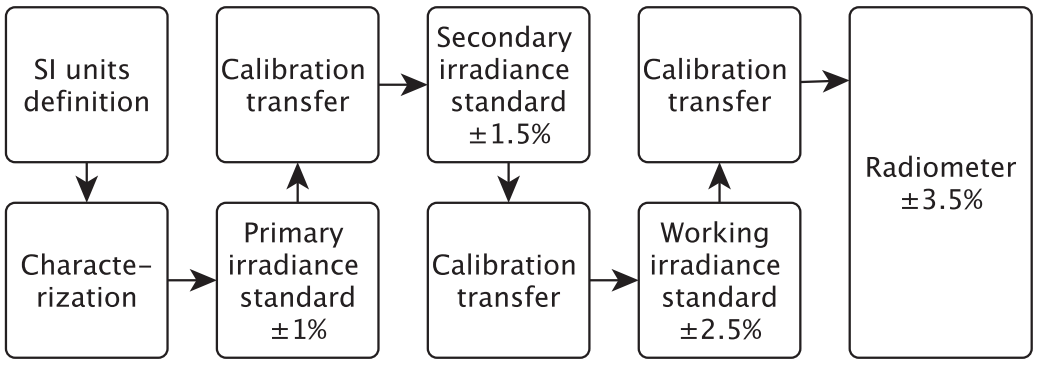

Figure 3.6: Standard lamp uncertainty traceability chain

against electric current and voltage standards, or the lamp calibration will be void. An inappropriate selection of power supply can become a significant source of uncertainty.

An example of combined uncertainty of spectroradiometer calibration for EKO MS-700 spectroradiometer was shown in Table 3.4.

Table 3.4: Combined uncertainty of spectroradiometer calibration

Source	**Uncertainty** [%]		
	350nm-450nm	450nm-900nm	900nm-1050nm
Combined uncertainty	**±10.89**	**±4.13**	**±4.06**

The high uncertainty value in the range 350nm-450nm is attributed to stray light.

3.5 Experimental evaluation of radiometers

Radiometers are complex metrological devices. Regardless of technical advances, the quality of achieved measurements can be compromised by poor calibration of the device. Accurate optical measurements are difficult to conduct, moreover metrological procedures are not standardised and are realised in different ways by different institutions. As a result, an additional significant source of uncertainty

arises. Validation of manufacturers calibration is the most important factor if a radiometer is going to be used for defining absolute measurand values. The calibration process can be realised in natural (outdoor) or artificial (indoor) environments.

3.5.1 Indoor calibration

Indoor calibration of radiometers has proven itself to be very useful for a number of reasons: the process can be followed at any time, metrological conditions can be precisely controlled, the uncertainty of achieved results can be traced back to the standards (if the equipment used held valid calibration certificates during the measurement process), the calibration setup can be recreated with ease in different locations. The uncertainty of an indoor calibration is determined by the calibration of equipment used, usually the modified FEL[1] quartz tungsten-halogen lamp. The extended calibration uncertainty (at 3σ) of a standard FEL lamp ranges from 2.5% at 250nm to 1% at 654.6nm to 6.5% at 2400nm [75] with respect to SI units. Commercially available calibration lamps were reported not to agree with the primary standards within manufacturer stated uncertainties [76], even though the calibration transfer process should add no more than 1% of uncertainty. Calibration of a standard lamp takes into account not only a transfer of radiant characteristic from working/primary standard. Lamps must be first prepared and tested in terms of long-term stability (less than 0.5% intensity variation at 654.6nm after 40h of annealing), filament symmetry (less than 1% intensity variation while lamp is rotated by 1deg in pitch and yaw from its aligned position) and other defects (envelope quartz glass colorisation, emission lines) [75]. If used correctly, an annealed tungsten-halogen lamp exhibits moderate level of variations in intensity and spectral distribution of emitted radiation over its lifetime. However, stability of the lamp parameters heavily depends on the halogen cycle, which is affected by the operating voltage. Either too high or too low an operating voltage significantly decreases the lifetime of the lamp [77]. The calibration of a standard lamp is not a trivial task and it can be compromised by inappropriate use of equipment. Detailed characterisation of standard lamp is not

[1] FEL - American National Standards Institute (ANSI) lamp code

the main focus of this chapter, but possible problems related to calibration of the standard lamp were expressed for the benefit of reader awareness of how standard lamp calibrations can be invalidated. The calibration process undertaken here took into consideration the calibration of spectrally selective radiometers. As a result, two calibration domains were defined: irradiance sensitivity scale and irradiance wavelength scale. For each domain a separate calibration setup was commissioned.

3.5.1.1 Wavelength scale calibration

The wavelength scale calibration process assigns specific mapping between wavelengths and pixels of the spectroradiometer detector. This type of calibration is realised with the use of mercury-argon spectral line lamp. Mercury-argon lamp emits a set of narrow band, intense optical radiation lines from the excitation of various rare gases and metal vapours. The calibration lamp emits radiation at wavelengths defined by quantum and molecular effects (transitions of electrons and molecules from higher energy states to lower ones). Therefore wavelengths of emission lines can be predicted from transition theory with very low uncertainty. Wavelength domain calibration is not considered to be a problematic process.

In general the wavelength scale of a spectroradiometer is defined as a polynomial function of a detector pixel number. This way scale nonlinearities can be appropriately expressed (see equation 3.7).

$$\lambda(n) = C_0 + n \cdot C_1 + n^2 \cdot C_2 + n^3 \cdot C_3 + n^4 \cdot C_4 \tag{3.7}$$

where:

$\lambda(n)$ - wavelength relevant for n^{th} channel

$C_0 - C_4$ - calibration coefficients

n - number of the pixel

For wavelength scale calibration, a Newport 6035 mercury-argon spectral pencil lamp was used. The lamp was powered by a Newport 6061 DC power source capable of providing 6mA to 20mA DC current. The emitted radiation spectrum

varies with the supply current. Supply current variations do not affect the location of the emission lines, only the presence and amplitude of the lines. The power supply was adjusted to the nominal mercury-argon lamp current of 18mA. The lamp was located in a distance of 0.1m from the surface of the detector. Such a close distance reflects low intensity of a radiant power emitted by the mercury-argon lamp. The lamp envelope was covered by a Newport 6040 large aperture shield (0.188 x 1.5") and the shield aperture was covered by a Newport 6057 UV filter for safety reasons. The UV filter completely absorbs the 253.7nm Hg line and attenuates the 312.6nm line. However, these lines lie below the lower limit of the tested spectroradiometer (350nm). The setup for the wavelength scale calibration is shown in Figure 3.7

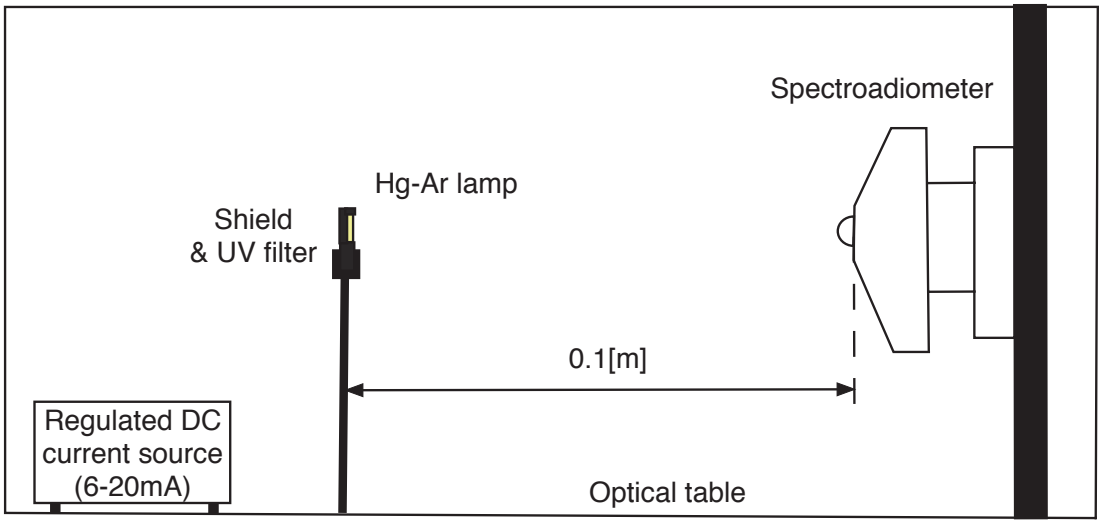

Figure 3.7: Radiometer wavelength scale calibration setup

The spectrum of the mercury-argon lamp was measured with an EKO MS-700 spectroradiometer and compared with spectral lines emitted by the lamp. Results were presented in Figure 3.8

Measured peaks almost perfectly match the spectral lines of a Hg(Ar) lamp. Therefore there was no need to calculate new polynomial coefficients.

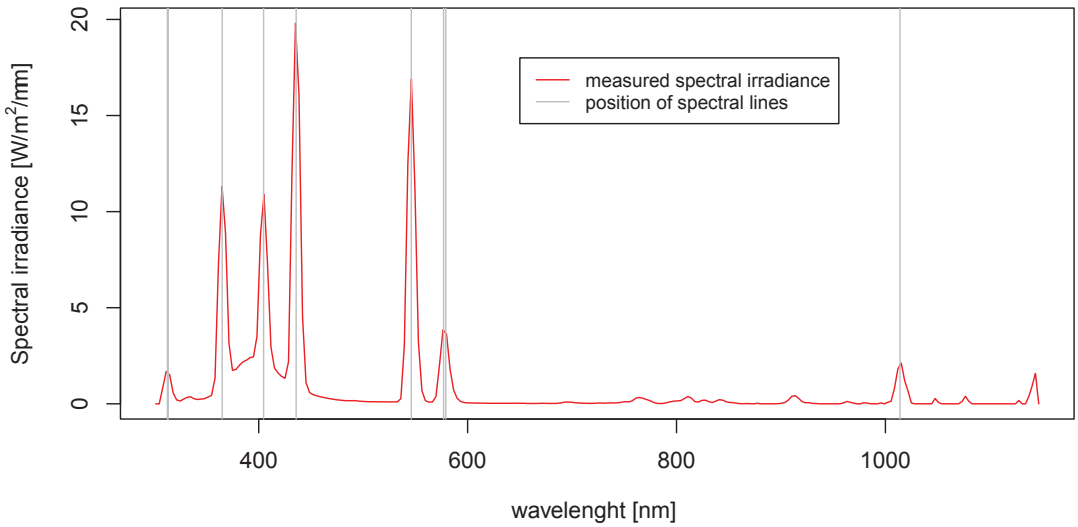

Figure 3.8: MS 700 spectroradiometer wavelength scale calibration

3.5.1.2 Sensitivity scale calibration

Accurate quantitative measurements of spectral irradiance are possible only if the radiometer's sensitivity scale is appropriately calibrated. As in many other metrological fields, calibration of a radiometer is followed by comparison with a spectral irradiance standard traceable to the SI units (most often a standard FEL lamp or less likely a hight temperature black body source). The calibration is then transferred to the radiometer under test. The uncertainty of the calibrated radiometer is at least equal to the combined uncertainties of: the used irradiance standard, the calibration transfer procedure and the radiometer specific uncertainty (temperature dependencies, temporal stability). In the results the radiometer obtains a set of new sensitivity coefficients for each channel.

The sensitivity of a radiometer is a function of a wavelength and incoming signal amplitude (if the sensor is not linear). Equation 3.8 expresses a generalised formula for sensitivity calibration.

$$s_{\lambda,r} = \frac{E_{e,\lambda,sis}}{v_{\lambda,r}} \tag{3.8}$$

where:

$s_{\lambda,r}$ - radiometer sensitivity

$E_{e,\lambda,sis}$ - spectral irradiance of a standard lamp

λ - wavelength

$v_{\lambda,r}$ - detector signal magnitude

Once the calibration is transferred from the spectral irradiance standard to the radiometer, the output spectral irradiance measurements can be calculated using equation 3.9

$$E_{e,\lambda,r} = s_{\lambda,r} \cdot v_{\lambda,r} \tag{3.9}$$

where:

$E_{e,\lambda,r}$ - spectral irradiance measured by the detector

Transfer of a calibration must be carried out with extreme care and attention to detail. While it seems like a trivial task, in reality many important factors may be overlooked. An appropriately made calibration transfer should not add more than 1% to the overall uncertainty of a calibrated device.

For this work, the sensitivity scale calibration was achieved with the use of a standard, spectrally calibrated, 1000W Oriel 63350 quartz tungsten-halogen FEL lamp. The calibration was performed in a darkroom with the lamp located at a distance of 0.5m from the surface of the detector. At the time of the measurements, the standard lamp held a valid calibration certificate traceable to the NIST radiation standards. The lamp was powered by a Newport 69935 radiometric power source, capable of providing stable (0.005%) current flow in a range of 0A to 10A. Here it was set to 8.2A. To limit the impact of a reflected light, the light source and detector were located inside a dark-room lined with black, matt fabric. In between of the light source and the detector an opaque baffle with embedded aperture was introduces. The size of the aperture was adjusted in such a way, that the whole lamp filament was visible from the perspective of the detector. Fifteen minutes settling time was allowed to enable the spectral irradiance to stabilise before measuring. In total five radiometers were tested (3xEKO MS700 and 2xKipp&Zonen CMP11). All radiometers were new, therefore they held valid calibration certificates issued by manufacturers. Radiometers

were installed in front of the lamp and measured consecutively. The EKO MS700 readout is digital. As such, no additional instrumentation was required to take the measurements. The CMP11 thermopile stack voltage was measured with a Campbell Scientific data logger set to 2.5mV input range. The sampling accuracy for this range is $0.33\mu V$, which relates to a $0.0385W/m^2$ quantisation error. The setup for the sensitivity scale calibration is shown in Figure 3.9.

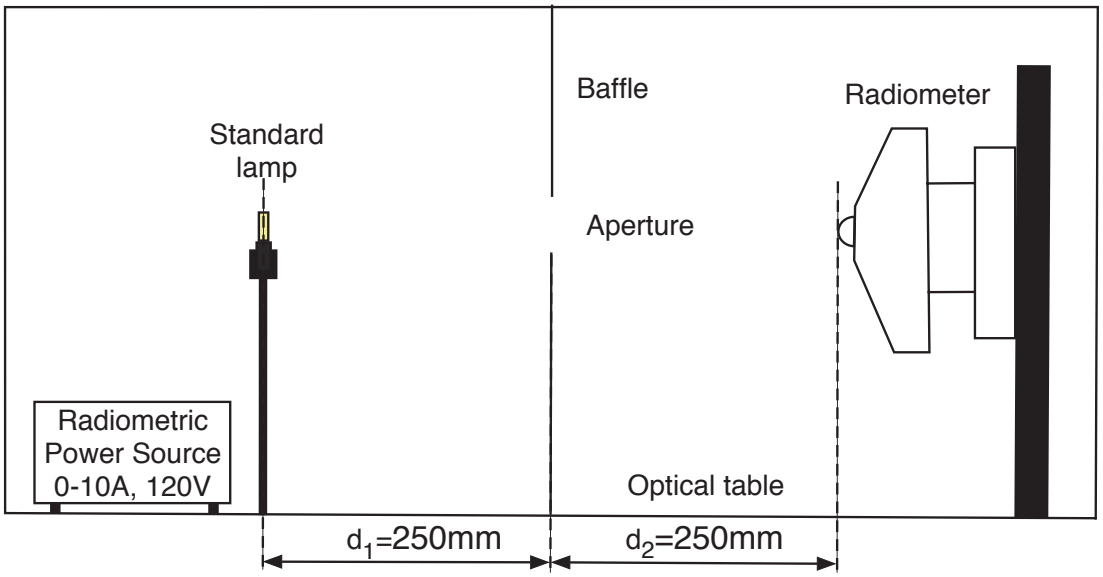

Figure 3.9: Radiometer sensitivity scale calibration setup

The irradiance measured by the Kipp&Zonen CMP11 pyranometers was compared with the integrated spectral irradiance of the standard lamp (as stated in its calibration certificate from manufacturer) what is shown in Table 3.5

Table 3.5: Measured vs. expected broadband irradiance

parameter	Range	Irradiance	Uncertainty	Relative error
symbol	λ_{min} - λ_{max}	E_e	u	δ
unit	$[nm]$	$[W/m^2]$	[%]	[%]
Oriel 63350	310-2800	272.61	3.7	0.53
$CMP11_{no_1}$	310-2800	267.59	<2	1.32
$CMP11_{no_2}$	310-2800	273.34	<2	0.80

The measured values stayed within error margins in relation to expectation

calculated from the standard lamp calibration certificate, giving confidence in the supplied sensitivity calibration of the thermopile pyranometers. At the same time, the measurements have validated the correctness of the experimental rig setup. Based upon manufacturer calibration certificate, the Kipp&Zonen CMP11 secondary standard pyranometers are calibrated against a primary standard pyranometer under a stable artificial light source (reference metal-halide lamp). The irradiance during calibration is equal to $500W/m^2$. Kipp&Zonen's primary standard radiometers are calibrated annually by the World Radiation Centre in Davos. This allows one to establish an uncertainty chain traceable to SI units. Referencing calibration to the World Radiation Reference Group reinforces the level of trust in manufacturer calibrations. Moreover, the manufacturers documentation clearly states methods used during calibration process. Such a state of affairs is a result of the existence of normative acts [67, 78–80], which impose set of requirements on pyranometers. Users, even if often not fully aware of underlying details, receive instruments from manufacturer which are compliant with ISO standards.

Whilst pyranometers have been present in everyday meteorological practice for almost a century [81], the history of outdoor spectroradiometers is considerably shorter. As it was already mentioned there is no international standard describing the calibration of the spectroradiometers, thus manufacturers can only follow their own "best practice" approach to achieve device calibration. In the next step of sensitivity scale calibration for this thesis, the EKO MS700 spectroradiometer was investigated.

The MS700 spectral range is much narrower than the band of the standard lamp therefore comparison of integral broadband irradiance was neither possible nor adequate. For this reason, the spectral irradiance measured by the spectroradiometer was directly compared with the spectral output of the standard lamp. Results of this comparison are shown in Figure 3.10.

Significant differences were observed. For most of the wavelength range the difference was around 17% with a mean value of 16.1% and standard deviation of 3.1% . Sensitivity calibration of a spectroradiometers is a challenging task and the combined uncertainty of a device of up to 10% is to be expected. However 17% can be considered an excessive deviation. Further analysis of the sensitivity shows that the main part of the differences is caused by systematic error (con-

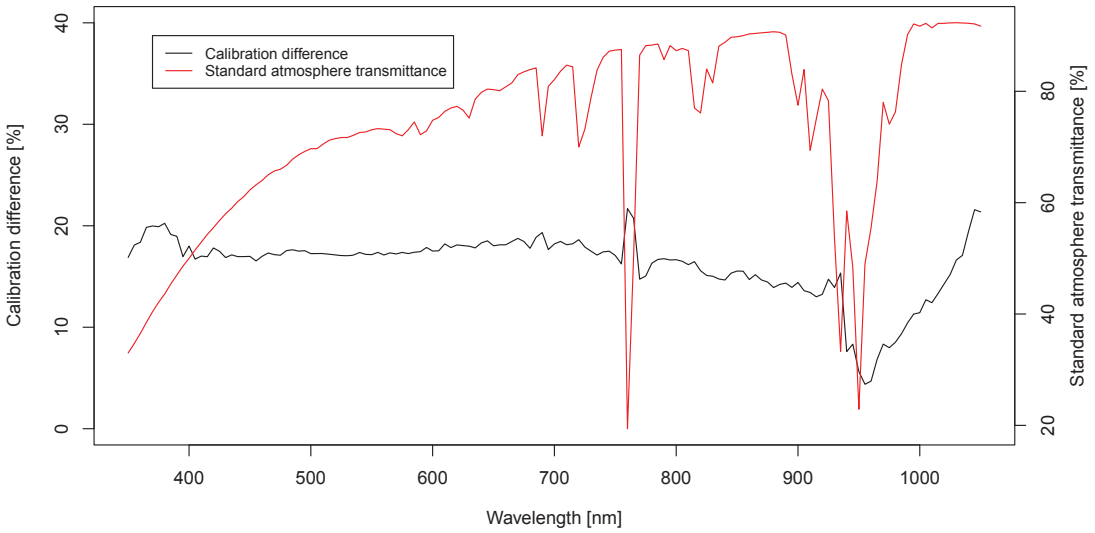

Figure 3.10: Difference between spectral irradiance of a standard lamp and spectral irradiance measured by EKO MS700 spectroradiometer

stant offset). Some additional differences are visible below 400nm, around 760nm and above 930nm. Below 400nm, the level of irradiance reaching the radiometer is very low (regardless of its origin: natural sunlight or halogen lamp). Also the radiometer sensitivity, defined in this case by the quantum efficiency of silicon is low (10%-30%). As a result, the lowered signal to noise ratio causes an increase in the uncertainty of measurements in this region. The 760nm peak in the calibration difference coincides with an O_2 atmospheric oxygen absorption band. The reduction in differences above 930nm coincides with an atmospheric water vapour absorption band. Comparison of the manufacturer and in-house calibration leads to the conclusion that the manufacturer calibrated the MS700 spectroradiometer under natural solar irradiance. It has been shown that errors between manufacturer and in-house calibrations coincide with regions of low level of input irradiance, however low signal to noise level may not be the exclusive reason behind the significant differences observed. Another effect that can contribute is sensor nonlinearity, which is addressed further in this thesis (see section 3.5.1.3). Measurements taken within strong atmospheric absorption band regions should not be used in the spectroradiometer calibration process. This aspect should not be omitted in case of artificial light sources, in situations

where an integrating sphere is a part of setup. In such cases the effective length of the path the light traverses before it reaches the sensor becomes substantial. Therefore air humidity starts to play a significant role as an absorber.

As a final result of this part of the investigation, new calibration correction coefficients for the spectroradiometers' sensitivity scales were calculated based on a standard lamp calibration as reference.

To verify that the spectroradiometer sensitivity scale was as poorly calibrated as the measurements here suggested, that MS-700 spectroradiometer was sent back to the manufacturer for recalibration. At that time, the manufacturer stated that new calibration facilities had been established at their site. According to documents received after recalibration, the new manufacturer calibration facility used an OL-FEL halogen standard lamp as an irradiance source. After receiving the instrument back, the new sensitivity calibration correction coefficients provided by the manufacturer were compared with those calculated from the CREST measurements and are shown in Figure 3.11 .

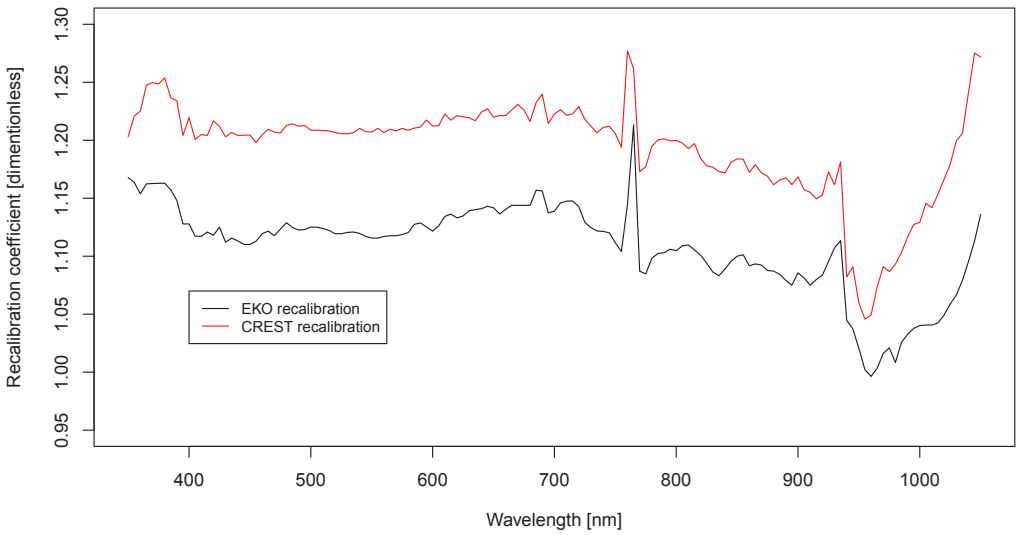

Figure 3.11: Spectrometer sensitivity calibration correction coefficients after recalibration: in-house vs. instrument manufacturer

The manufacturer recalibration improved the sensitivity calibration of the spectroradiometer in reference to the CREST calibration. However, there is still

a significant difference in between the rescaled initial spectral irradiance measured with the spectroradiometer and the reference spectral irradiance defined by CREST's calibration, in the range of 7% within the 400nm-900nm band (see Figure 3.12).

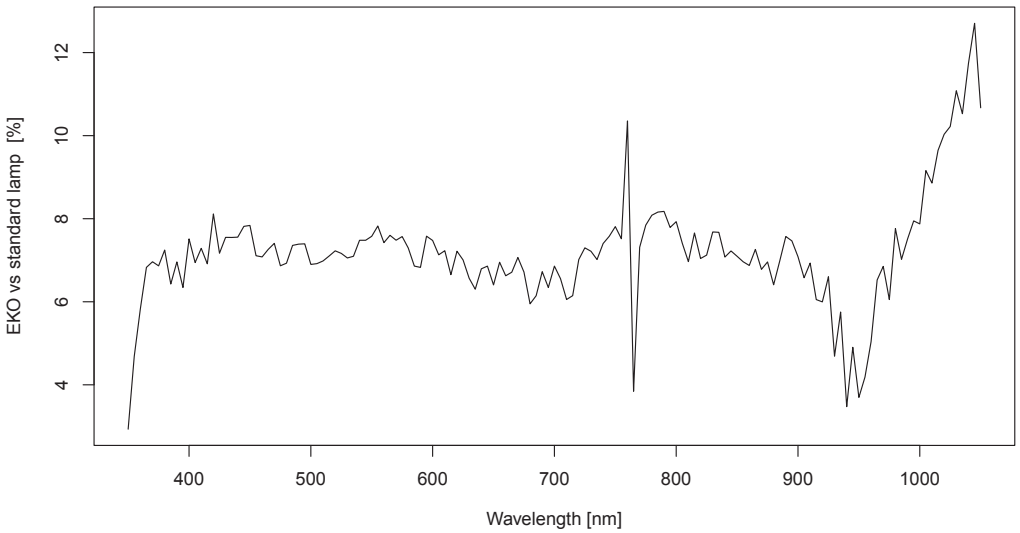

Figure 3.12: Difference between the initial measurements of a standard lamp spectral radiation scaled by calibration correction coefficients and expected spectral radiation

Almost constant difference between spectroradiometer sensitivity recalibration coefficients measured at CREST and those supplied by the manufacturer can be explained by the fact that in both cases the spectral characteristics of the standard lamps used were similar, but that the radiation intensity differed.

To validate the manufacturer recalibration, the MS-700 spectroradiometer was retested at CREST (using exactly the same experimental setup as for the initial standard lamp spectral radiation measurements). The results were compared with the corrected initial spectral radiation measurements of the standard lamp. The results of the comparison are shown in Figure 3.13.

The standard lamp spectral radiation measurements taken after manufacturer recalibration agreed with the expectation (from the standard lamp calibration certificate) to a greater extent than the initial standard lamp measurements scaled by the calibration correction coefficients. Figure 3.15 shows the percentage difference

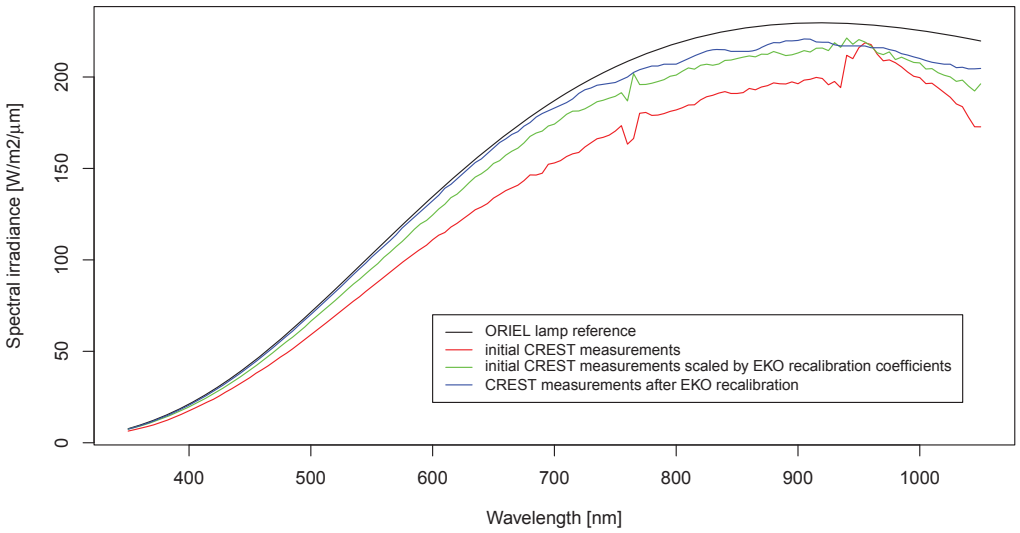

Figure 3.13: Standard lamp spectral radiation: lamp calibration certificate vs. CREST initial measurements scaled by calibration correction coefficients vs. CREST post recalibration measurements

between the measured standard lamp spectral radiation after manufacturer recalibration of the spectroradiometer and the expected spectral radiation (standard lamp certificate). Differences between the initially measured spectral irradiance scaled by sensitivity calibration correction coefficients and the spectral irradiance measured by spectroradiometer with internally modified sensitivity calibration are shown in Figure 3.14 .

As can be seen in Figure 3.14, the initial spectral irradiance measurements scaled by the manufacturer supplied calibration correction coefficients agreed with the remeasured spectral irradiance to within 6%. This value lies within estimated uncertainty margin for EKO MS700 spectral irradiance measurements.

After recalibration, the differences between the standard lamp spectral radiation measurements and expectations lie within acceptable margins. The difference between the measured and expected spectral radiation ranged from 1.5% to 4% for the wavelengths range of 350nm to 800nm and 4% to 8% for the wavelengths range of 800nm to 1050nm. Given than the spectroradiometer calibration did not change in the short time between manufacturer and CREST calibrations, all the differences in between results should be considered as caused by reproducibility of

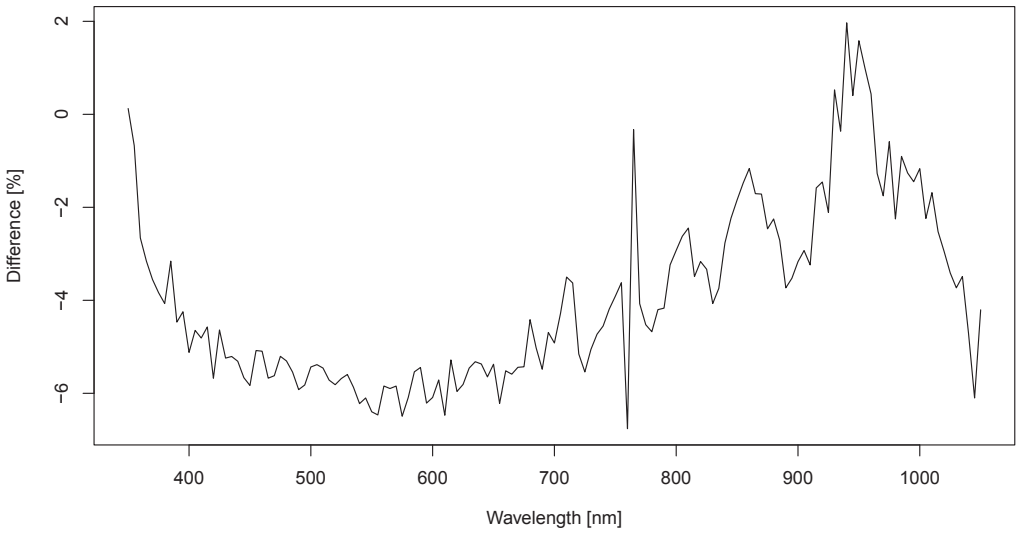

Figure 3.14: Differences between initially measured spectral radiation scaled by manufacturer calibration correction coefficient and spectral radiation measured by spectroradiometer after manufacturer recalibration

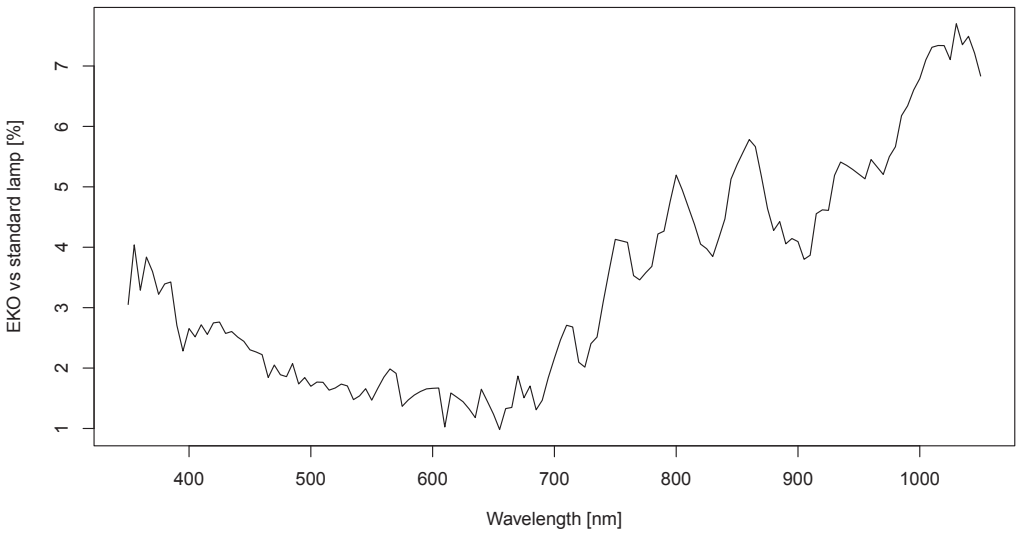

Figure 3.15: Difference between measurements of a standard lamp spectral radiation after manufacturer recalibration and expected spectral radiation of Oriel 69935 standard lamp

an experimental setup (mainly standard lamp calibration and lamp alignment). For this reason, a detailed investigation into the characterisation of a standard calibration lamp was undertaken (see chapter 4).

3.5.1.3 Linearity

The linearity of the irradiance sensor cannot be assumed apriori and must be experimentally verified. For that reason an appropriate experimental setup was created and is presented in Figure 3.16.

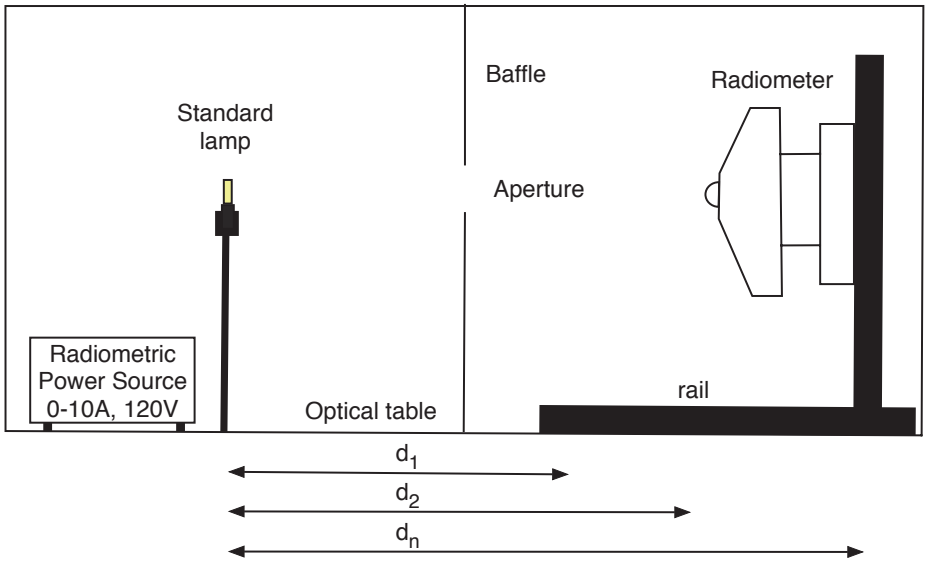

Figure 3.16: Experimental setup for radiometer linearity test

There are a number of methods allowing for detector linearity measurements. The method used for this experiment is based on the inverse square law (see equation 3.10).

$$E_{e,\lambda,d_2} \approx E_{e,\lambda,d_1} \cdot \frac{1}{(d_2 - d_1)^2} \tag{3.10}$$

where:

$E_{e,\lambda,d}$ - total irradiance at the distance d_2

d - distance from the light source

Given that the irradiance is a known function of a distance, various irradiance levels can be easily achieved by changing the distance between the light source and the radiometer. This is true under the assumption that the distance between the sensor and the light source is much greater than the size of the lamp filament and therefore the lamp approximates the point source. This method limits the required modification of the experimental setup to minimum and allows a more consistent measurement setup. The lamp voltage should not to be modified (this would have an impact on the spectral characteristic of emitted light), no additional optical elements (e.g. neutral density filters) are placed between the lamp and the radiometer. The single parameter being modified is the distance. The radiometer was installed on a rail sitting on top of an optical table. This allowed for simple and precise adjustment of the distance between radiometer and light source.

The main factor which influences the uncertainty of linearity measurements in this method is the radiometer positioning. In the presented setup the uncertainty of distance adjustment was on a level of ±1mm. The impact on irradiance is shown in Figure 3.17. It can be seen that for a distance adjustment uncertainty $\Delta d = 1mm$ the uncertainty in irradiance varies from 0.4% to 0.2%.

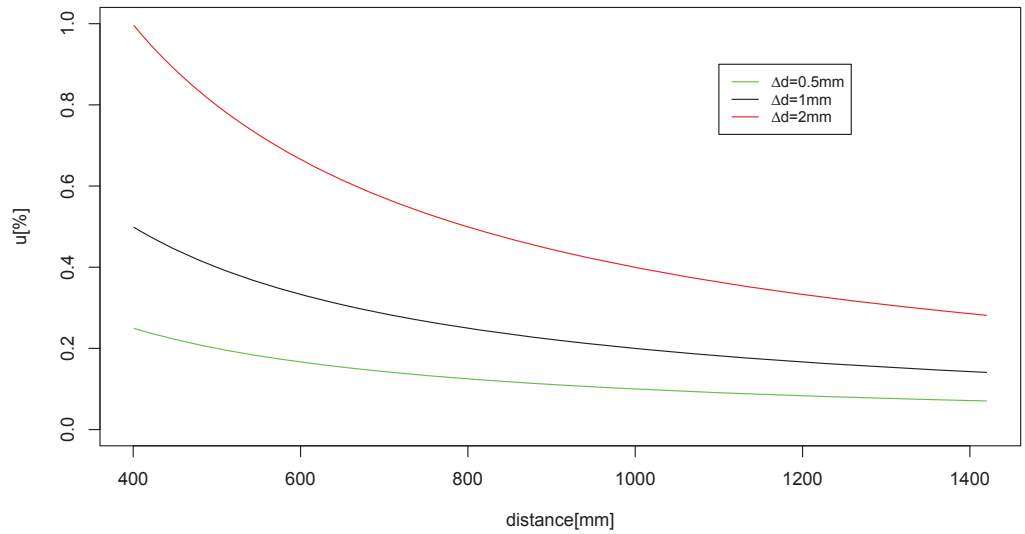

Figure 3.17: Uncertainty of reference irradiance introduced by the precision of distance adjustment

Figure 3.18 presents the nonlinearity of an EKO MS700 as a function of distance and wavelength. The presented results are based on a set of repeated measurements collected for ten different distances. For each distance, ten measurements were taken and averaged to limit the impact of random noise. Averaging also allows reduction of the impact of temporal fluctuations in lamp irradiance.

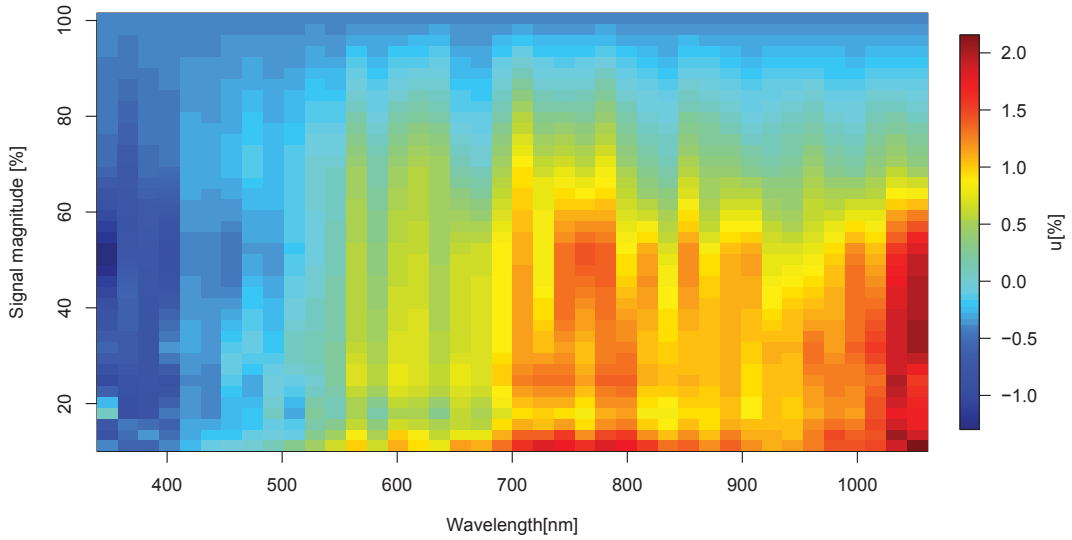

Figure 3.18: Non-linearity of the EKO MS700 as a function of the wavelength. 100% signal magnitude relates to the irradiance emitted from the FEL lamp at a distance of 500mm.

Analysis shows that the spectroradiometer nonlinearity stayed below 1.5% for signal magnitudes between 100% and 20%[1] and wavelength range 350nm to 1000nm. Nonlinearity varied in a range of 1.5% to 2.5% for signal magnitude below 20% and wavelengths above 1000nm. Increase in levels of nonlinearity was observed mainly for low signal magnitudes, where it is expected that noise levels will have a greater impact on uncertainty of the measurements. Detailed analysis of random noise influences is presented further in the following section.

[1] 100% represents an irradiance magnitude at the distance of 0.5m from the lamp

3.5.1.4 Random noise

Random noise in irradiance measurement cannot be removed by any correction. The only way to limit its impact is to average multiple measurements. It is not always possible to do this however and for that reason it is required to know what is the impact of random noise on a single measurement. To evaluate the magnitude of random noise, the spectral irradiance of a standard lamp was measured by spectroradiometer for 30 minutes in 10-second intervals. During all of that time, the metrological conditions were not varied.

The relative standard deviation of a measurement was calculated according to the formula 3.11

$$\%RSD = \frac{\sigma}{\hat{y}} \tag{3.11}$$

where:

$\%RSD$ - relative standard deviation

σ - unbiased standard deviation

$\hat{y}$ - mean value

Signal to noise ratio (SNR) can be then expressed as a reciprocal of %RSD as shown in equation 3.12

$$SNR = \frac{1}{\%RSD} = \frac{\hat{y}}{\sqrt{\frac{1}{N-1}\sum_{i=1}^{N}(y_i - \hat{y})^2}} \tag{3.12}$$

Results of the measurements are presented in Figure 3.19

For most of the wavelength range (up to 950nm) the %RSD stayed below 0.2%. A significant increase was observed between 950nm and 1050nm, where its value reached 0.5%. An even higher level of %RSD was observed in the range 350nm-400nm. Here, the %RSD reached 0.8%. The increase of %RSD is directly corelated with low signal to noise ratio. This happens because the detector quantum efficiency in the NIR and UV ranges reduces rapidly. Simultaneously,

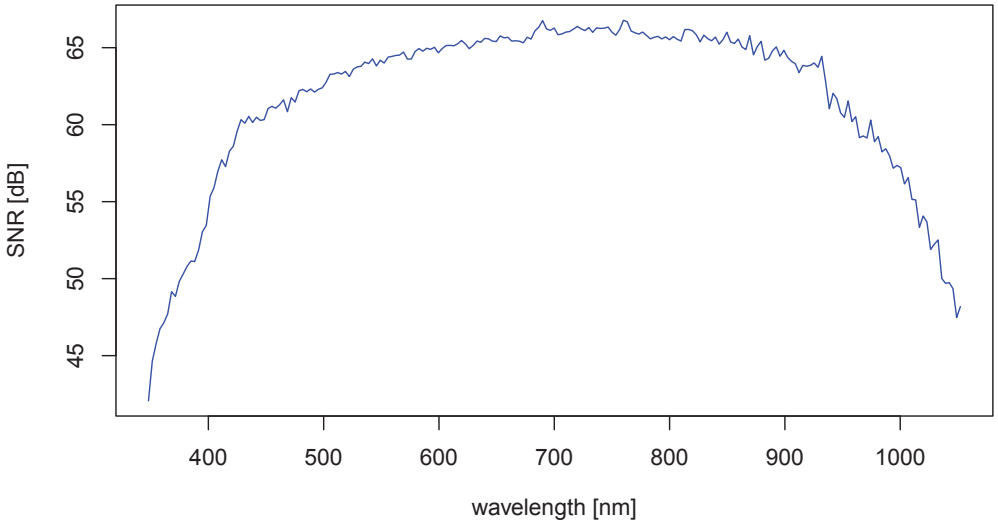

Figure 3.19: MS700 signal to noise ratio as a function of the wavelength

the level of irradiance emitted by the standard lamps is very low for UV, which explains the greater level of random noise in this region.

3.5.1.5 Angular response

Radiation impinges on photovoltaic modules from the whole hemispherical view factor. Whilst diffuse irradiance does not possess directional properties, this is not the case for direct irradiance. For direct radiation, the angle of incident varies significantly over the course of the day. To measure correct values of solar radiation it is required that radiometer response follows a cosine dependency.

The spectroradiometer was installed at a distance of 500mm from the standard lamp. The used rig allowed for rotation of a spectroradiometer around its axis, in such a way that the axis of rotation was through the centre of integrating sphere (see Figure3.20). Angular measurements were taken with 5° resolutions. The precision of angular adjustment was estimated at a level of 0.25°. For each angle, a set of ten repeated measurements was made.

Angular measurements were first averaged and normalised to the radiometer response at 0°. Differences between the normalised measurements and the cosine function (representing ideal cosine detector) for each angle were calculated. Re-

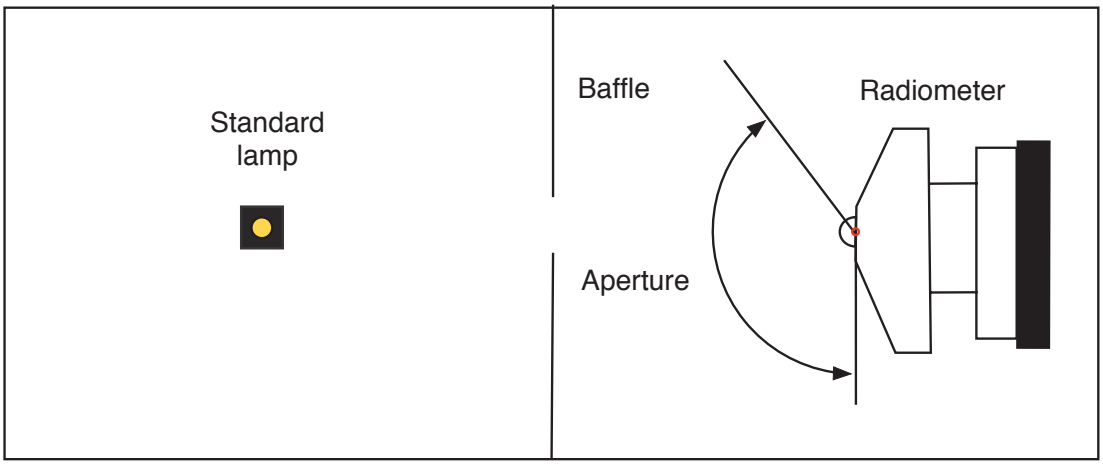

Figure 3.20: Angular response experimental setup

sults are presented as a function of the angle of incidence and the wavelength. Results of measurements are shown in Figure 3.21.

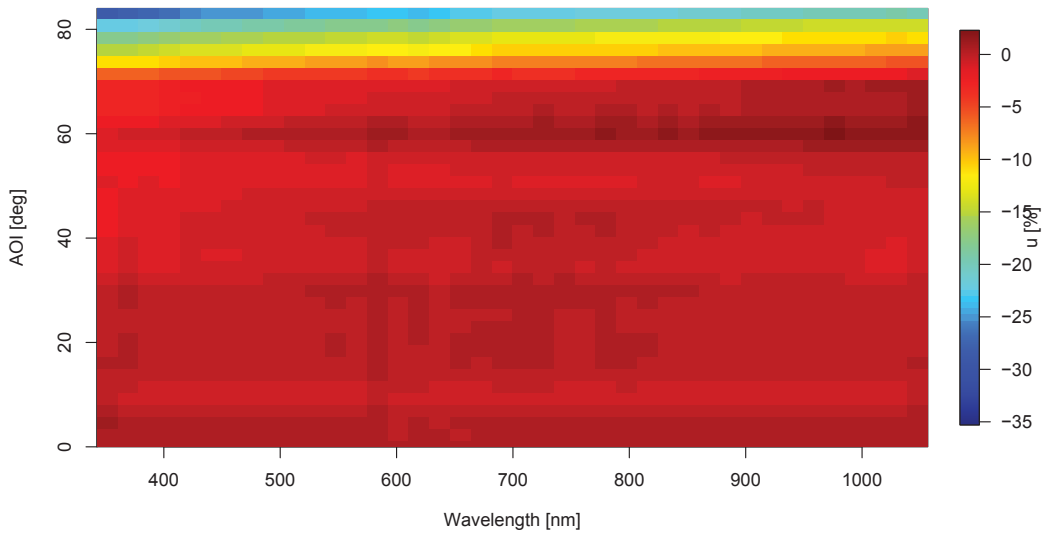

Figure 3.21: Deviation for ideal cosine response introduced by MS 700 spectrometer as a function of wavelength

Results of measurements recorded during this experiment show that the spectroradiometer sensitivity is fairly stable across the wavelength domain and for a wide range of angles of incidence. For incident angles between 0° and 40° spec-

troradiometer deviated less than -0.7% from the ideal cosine detector response. For incidence angles above 40°, the differences in responsiveness of the spectroradiometer for spectral radiation at 350nm and 700nm equaled 2%. This trend increases with the angle of incidence and reaches 10% at 85°. The measurement taken at 60° deviate slightly from the overall trend (an increase in sensor response has been detected). Above 70° a rapid drop off of responsiveness is observed reaching -20% for the near infrared range and -35% for the ultraviolet.

3.5.1.6 Temperature dependencies

The structure of a spectroradiometer always includes a set of optical elements aligned together in a specific configuration. Thermal expansion of materials can lead to the situation where the output signal is biased by the sensor temperature. More than that, the level of noise of the detector increases with temperature. The investigated spectroradiometer is equipped by the manufacturer with a thermal stabilisation system (a stack of Peltier elements). According to the data-sheet, the temperature of the spectroradiometer should not vary more than $\pm 5^0C$ from 25^0C. An appropriate experimental setup was created to investigate if temperature variations within this range can affect the uncertainty of measurement. The Peltier elements were controlled manually in such a way that the spectroradiometer temperature varied from 20^0C to 30^0C. At the same time, the spectroradiometer was used to measure irradiance emitted by a standard lamp. Investigation of results has not shown any significant temperature dependency over the stated range. The observed differences instead have the character and magnitude of a random noise. Figure 3.22 shows the relative standard deviation (%RSD) calculated from the group of spectral irradiance measurements taken under varying sensor temperature.

3.5.1.7 Reproducibility

The reproducibility of a calibration setup is mainly affected by the uncertainty of the geometrical alignment. To investigate how well an experimental setup can be recreated, a standard lamp and spectroradiometer were dismounted and the rig misaligned. Then the whole setup was recreated and readjusted. The mean from

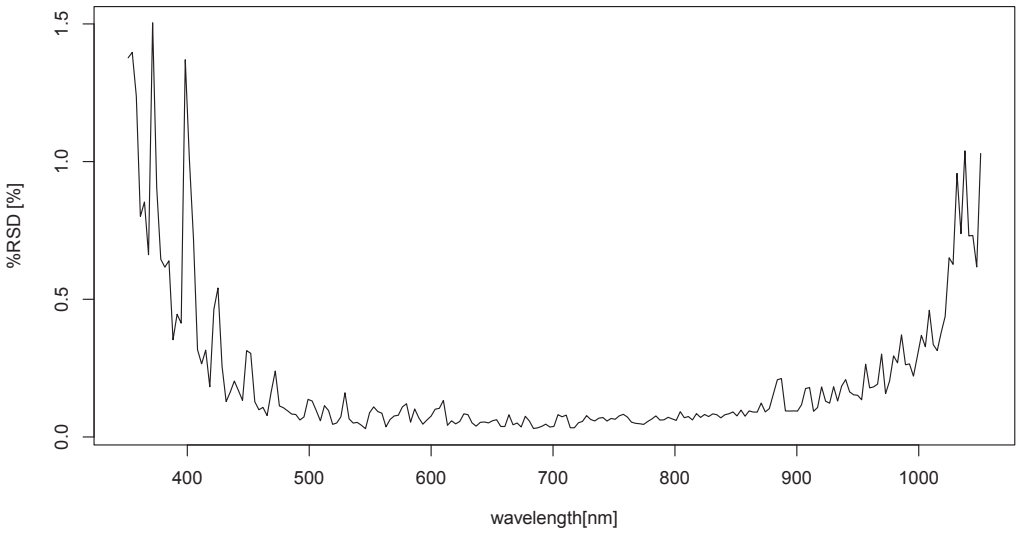

Figure 3.22: Impact of detector temperature variations on the results of measurements for temperature ranging from $20°C$ to $30°C$

ten consecutive measurements was recorded after each reconfiguration to minimise the impact of random errors. Reconfiguration was repeated for seven times. The mean standard error between measurements recorded after each reconfiguration then represents uncertainty caused by experimental setup reproducibility (see Figure 3.23).

As can be seen in Figure 3.23, the experimental setup can be recreated with uncertainty within $\pm 0.3\%$ and averaging at $\pm 0.05\%$ within the 350nm-1050nm ranges. This result is compatible with the reproducibility of a calibration setup reported by other researchers [76].

3.5.2 Outdoor calibration

In the previous section, indoor calibration procedures of radiometers and the related uncertainties were presented. Whilst indoor calibration can be followed without temporal and metrological condition constrains, it requires complex instrumentation, high levels of personnel expertise and high financial investment (upfront costs, maintenance costs). Accuracy limits for outdoor calibration of

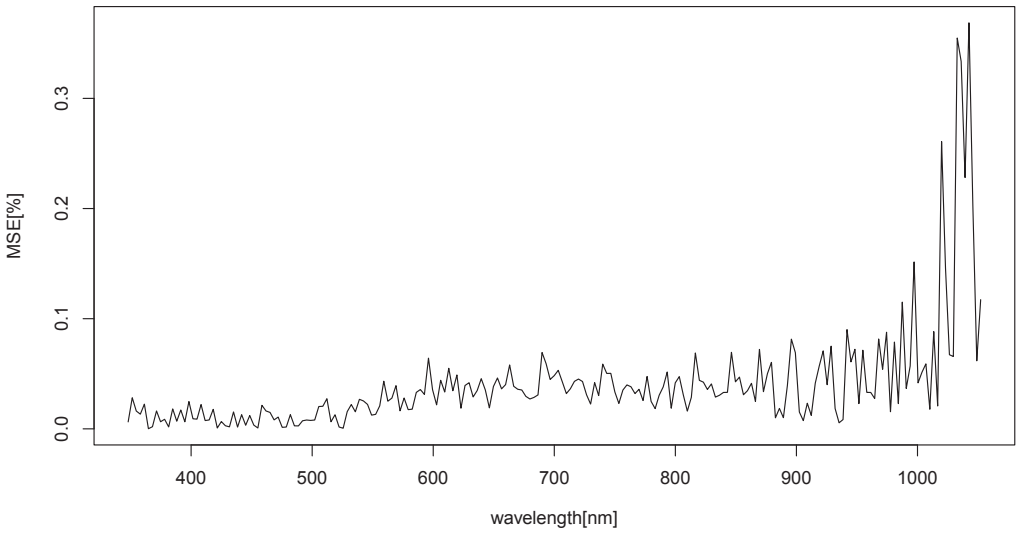

Figure 3.23: Reproducibility of the experimental setup

a radiometer (referring to WRC[1] Davos) were discussed in [82]. Accordingly, a state of the art outdoor calibration can achieve a 0.3% traceable uncertainty. Such a low level of uncertainty is achievable only by a reference group (WSG [2]), which includes a set of fully characterised absolute cavity radiometers. The calibration procedure is conducted in high mountain areas to minimise the impact of atmospheric variations. Such an extreme calibration approach is not within the scope of this thesis, however it proves that under specific circumstances very accurate calibration of radiometer can be achieved with the sun as a light source. Commercially available primary standard lamps offer at best 2% uncertainty. More frequently used secondary standard lamps can deviate from calibration by 10%, even though manufacturer certificates state much lower uncertainty figures [76]. The uncertainty of manufacturers' "uncertainty estimates" makes outdoor calibration even more attractive. The main interest of the author is in the calibration methods applicable to the users of photovoltaic systems. Use of sunlight for a radiometer calibration is the cheapest and the most applicable method of radiometer maintenance over the whole lifetime of a PV installation.

Outdoor conditions even if not perfect can be utilised for reasonable radiome-

[1]WRC - World Radiation Center
[2]WSG - World Standard Group

ter calibration if only the state of the atmosphere can be assumed as stable and if the sun disc can be seen by the radiometer. If the atmosphere composition is assumed as stable, measuring direct solar irradiance under various (but known) air masses allows for calculation of atmospheric transmission. In accordance to the Lambert-Beer law 2.5, the irradiance transmitted through the atmosphere maintains a logarithmic dependency on air mass. The result of a simple mathematical modification of the Lambert-Beer law is shown in equation 3.13

$$ln(E_{e,\lambda,T}) = ln(E_{e,\lambda,0}) - \acute{\tau}_{\lambda}(\theta) \tag{3.13}$$

where:

$E_{e,\lambda,0}$ - solar irradiance at the edge of the atmosphere

$E_{e,\lambda,T}$ - transmitted solar irradiance

$\acute{\tau}_{\lambda}$ - atmospheric optical depth

Atmospheric optical depth ($\acute{\tau}_{\lambda}$) is a function of the following atmospheric constituents: w - water vapour, a- aerosols, r- Rayleigh scatterers, g - trace gases, NO_2 - nitrogen dioxide, O_3 - ozone. Atmospheric optical depth is expressed by equation 3.14.

$$\begin{aligned}\acute{\tau}_{\lambda}(\theta) = AM_w(\theta)\tau_{\lambda,w)} + AM_a(\theta)\tau_a\lambda, a + AM_r(\theta)\tau_{\lambda,r} + \\ AM_g(\theta)\tau_{\lambda,g} + AM_{NO_2}(\theta)\tau_{\lambda,NO_2} + AM_{O_3}(\theta)\tau_{\lambda,O_3}\end{aligned} \tag{3.14}$$

where:

$AM_w(\theta)$,$AM_a(\theta)$,$AM_r(\theta)$,$AM_g(\theta)$,$AM_{NO_2}(\theta)$,$AM_{O_3}(\theta)$ - relative air masses for various atmospheric constituencies

$\tau_{\lambda,w}$,$\tau_{\lambda,a}$,$\tau_{\lambda,r}$,$\tau_{\lambda,g}$,τ_{λ,NO_2},τ_{λ,O_3} - spectral transmission of various atmospheric constituencies

The definition of relative air masses for various atmospheric constituencies would require detailed knowledge of the constituent gas profiles through the atmosphere.

By assuming a uniform distribution of constituents, the atmospheric optical depth can be expressed as shown in equation 3.15

$$\acute{\tau}_\lambda = AM(\theta)\left(\tau_{\lambda,w} + \tau_{\lambda,a} + \tau_{\lambda,r} + \tau_{\lambda,g} + \tau_{\lambda,NO_2} + \tau_{\lambda,O_3}\right) \tag{3.15}$$

where:

$\acute{\tau}$ - atmospheric optical depth

By linear regression, the irradiance under $AM = 0$ can be calculated and then compared with the standard extraterrestrial solar spectral radiation. By comparing measurements with standard values of extraterrestrial solar spectral radiation the calibration coefficients can be calculated.

It has been reported [83] that further modification of equation 3.13 can lead to better linear regression results. Major errors in the Langley calibration method come from fluctuation in the atmospheric extinction coefficient. The errors in measured irradiance increase with the air mass. A standard linear regression method thus favours high air mass points (higher weighting). A modification proposed by [83] is shown in Figure 3.16

$$\frac{ln(E_{e,\lambda,T})}{AM} = \frac{ln(E_{e,\lambda,0})}{AM} - \frac{\acute{\tau}_\lambda}{AM} \tag{3.16}$$

The extraterrestrial irradiance spectrum defined by Wehrli [50] was used. The Earth to sun distance correction was applied from equation 2.38.

The radiometer was mounted in the horizontal plane throughout the whole time of the measurement. For that reason, the measured irradiance was corrected for the cosine response of the radiometer (as shown in Figure 3.21). Data for zenith angle greater than 85° ($AM > 10$) were excluded from the analysis due to the limited responsiveness of the detector. Air mass was calculated based on the Kasten formula [84] .

Measurement of direct solar irradiance requires use of a radiometer with a field of view limited to around 8°. It can be done by collimation tube (e.g. pyrheliometer). Moreover, precise adjustment of radiometer orientation is required to make sure that the solar disk is visible to the detector. As the earth continuously changes its position in relation to the sun, use of a precision solar tracker is a

great advantage. Such a setup would be too complex and prohibitively expensive for applications in most photovoltaic monitoring systems. The method can be simplified by using a shade-unshade procedure. Direct solar irradiance can be expressed as the difference between total hemispherical solar irradiance measured by a wide viewing angle radiometer (e.g. pyranometer) and total hemispherical solar irradiance measured by the same radiometer while the solar disk is covered by a shading ball. The shade-unshade method thus uses only one radiometer to measure direct, diffuse and global solar radiation components. The shade-unshade method was selected for this experiment. Figure 3.24 presents the experimental setup used for the outdoor calibration.

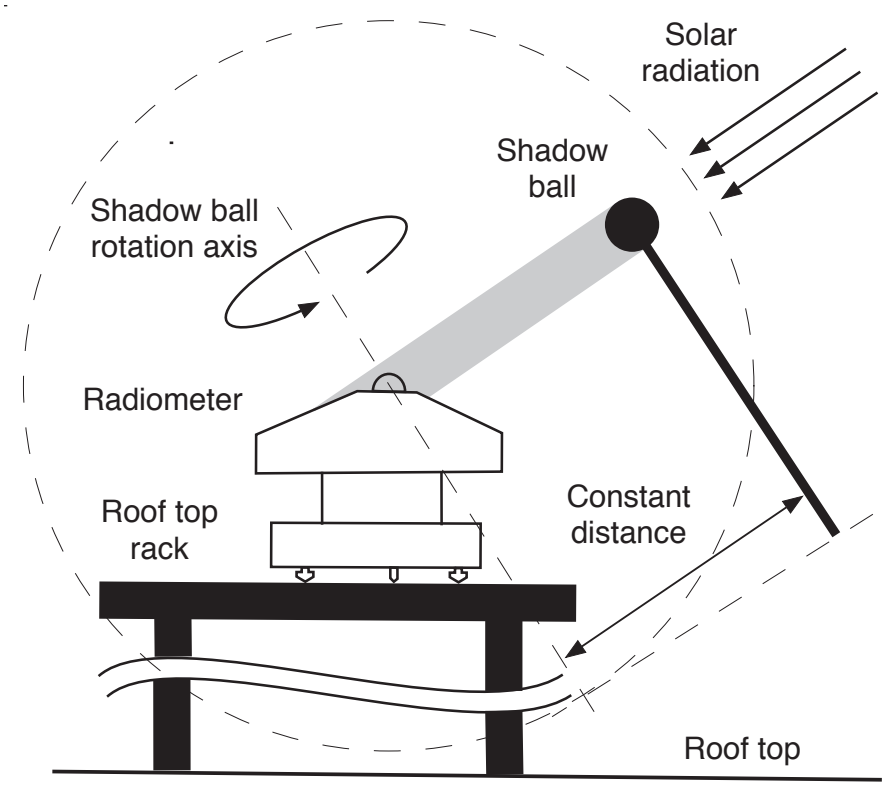

Figure 3.24: Outdoor radiometer calibration setup

The radiometer was installed on top of the roof to allow for an unobstructed field of view over a wide range of solar zenith angles. A shadow ball was selected instead of shadow band, which occludes a significant part of the sky. This decreases the magnitude of diffuse irradiance and would require an appropriate

correction coefficient to be applied. The shadow ball was installed in such a way that it remained at a constant distance from the radiometer integrating sphere. Its position was adjusted over the course of a day. Spectral irradiance for shaded and unshaded conditions were continuously measured. Measurements lasted from sunrise till sunset. Relative humidity decreased from around 60 to 50% during the day of the measurement and reached 80-90% during the preceding night. Night temperature ranged around $17°C$ reaching $28°C$ during the day. Data from the 19th of July 2013 (representing clear day) was used to create the presented results.

The Earth's atmosphere contains a range of a different particles and molecules. Absorption of radiation by these atmospheric constituencies often has a localised character. Other effects like scattering can overlay with molecular absorptions. For this reason, not every wavelength can be used for calibration purposes. Bands with strong molecular absorption must be avoided. After analysis of standard AM1.5 spectrum and literature [85] the following wavelengths were selected as the best candidates for spectroradiometer calibration: 354nm, 380nm, 453nm, 499nm, 519nm, 604nm, 675nm, 778nm, 865nm, 941nm, 1019nm. At the specified wavelengths solar irradiance is affected only by Rayleigh (dry air molecules) and Mie (aerosols) scattering. At the wavelengths 519nm and 604nm solar irradiance is additionally affected by ozone(O_3) and at 941nm by water vapour (H_2O) absorption. Solar irradiance at wavelength 1019nm is affected by aerosols only.

Figure 3.25 presents Langley plots of different channels of the radiometer. Linear regression functions were fitted for data from the Langley plots (the linear regression methodology described by Draper and Smith [86] was used). The intercept represents irradiance at the edge of the atmosphere (AM0). The slope represents the optical thickness of the atmosphere.

It can be observed that the plots presented in Figure 3.25 are not exactly linear. These nonlinearities could be caused by variation in atmospheric composition (mainly aerosols optical depth). Another reason behind such a state could be nonuniform distribution of specific atmospheric constituencies across the atmosphere. Measurements were taken with the radiometer fixed in the horizontal plane, across a wide range of air masses and signal magnitudes,therefore angular response and nonlinearity of the sensor may also have had an impact on results. It was noticed that the Langley plot variations from linear approximation have a

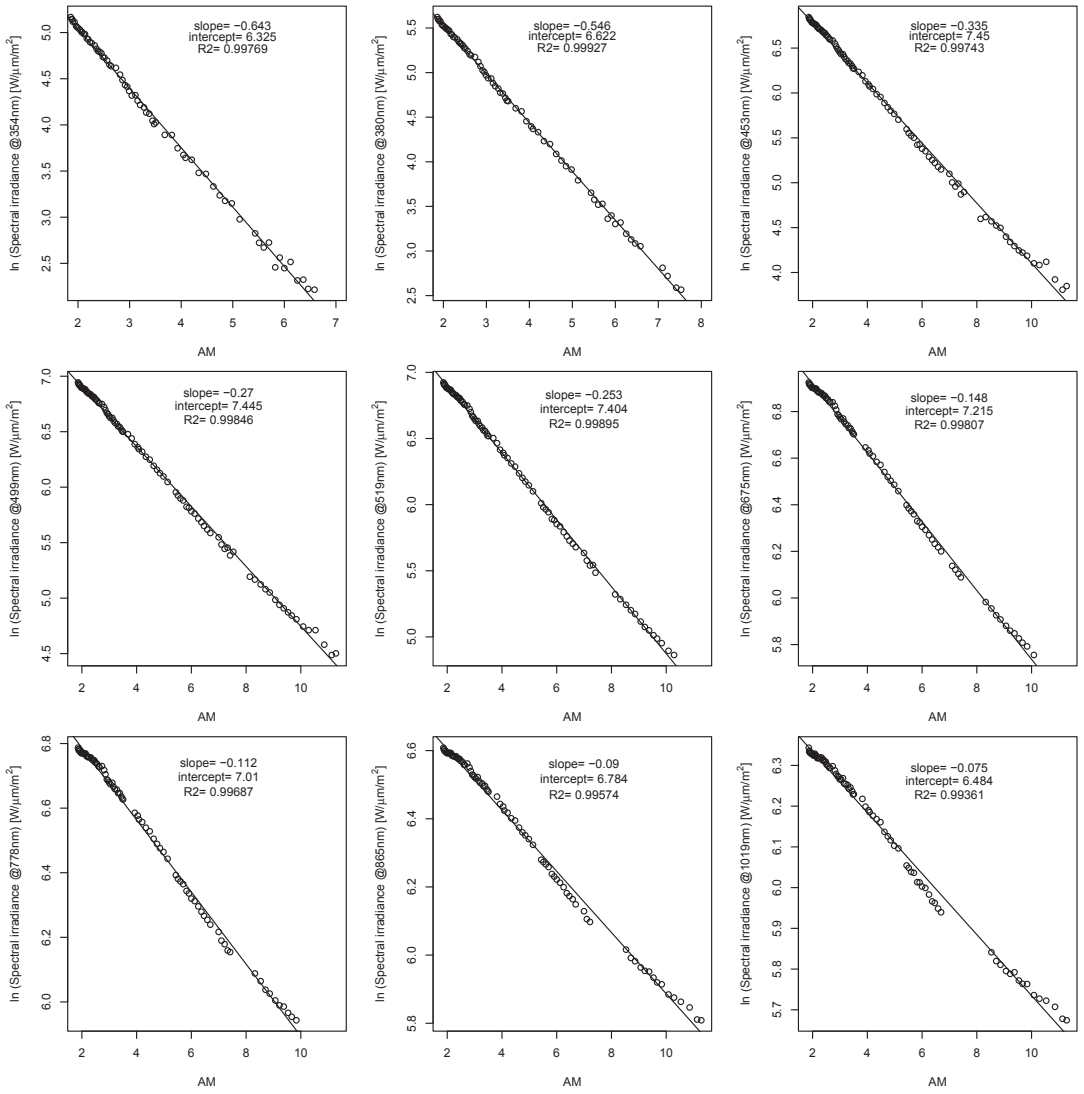

Figure 3.25: Langley plots for nine selected channels of tested spectroradiometer

systematic character across specific intervals (approximately : AM=2-3, AM=3-5, AM=5-8, AM=8-11). All measurements were taken with the spectroradiometer kept at a stable temperature of $25°C$. The only parameter which was varied was spectroradiometer exposure time. For this reason, the impact of exposure time switching was investigated. Figure 3.26 presents the linear fitting function residuals with overlaid exposure time values.

Figure 3.26 clearly shows, that residual values (especially for longer wave-

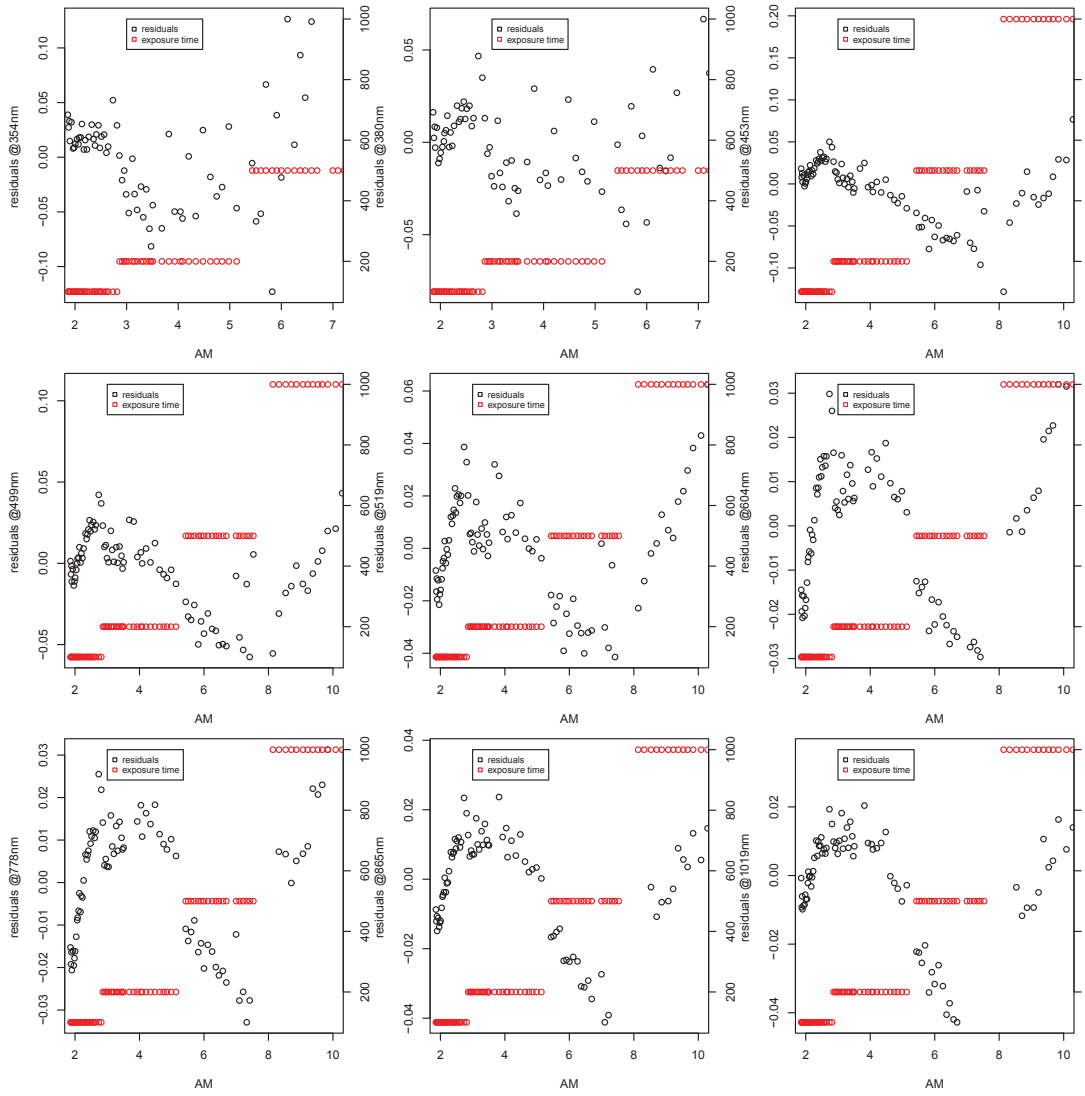

Figure 3.26: Linear fit residuals and exposure time plots for nine selected channels of tested spectroradiometer

lengths) are related to exposure time of a spectroradiometer. Observations made during indoor calibration (linearity test) have shown that nonlinearity was varying in sudden steps at around 90%, 60%, and 20% of a signal magnitude. This observation can now be explained by the impact of exposure time. Further improvements in spectroradiometer calibration could be achieved by recalibration of exposure time control. It should be noted that exposure time seems to stay con-

sistent from one measurement to another, offsetting the exposure time can solve the non-linearity problem. Correction of the exposure times would require modification of the spectroradiometer firmware, what was not possible for the device under test. Numerical correction of the results was applied instead. To calculate correction coefficients, at first a linear expression was fitted to the measurements taken for all exposure times. Then residuals between the linear fit and the actual measurements were calculated. Residuals were grouped based on exposure time. Average residual values for each of the exposure times was then calculated. This average residual value was then added to the measurement results. The resulting corrected Langley plots are shown in Figure 3.27. Linear fit residuals after application of corrections are shown in Figure 3.28.

Accuracy of calibration of a spectroradiometer sensitivity scale does not have any adverse impact on calculation of the atmospheric optical depth as long as the radiometer responds linearly to the incoming signal. It can be seen in Figure 3.27 that the applied corrections significantly improve the linearity of the spectroradiometer. This issue should be addressed by the manufacturers calibration procedure, as it has a significant impact on uncertainty of calibration and measurement results during device operational time.

Figure 3.29 presents overlay of measures and extrapolated spectral solar irradiance for the selected channels.

Based on corrected Langley plots optical depth and then transmittance of the atmosphere for the beam irradiance were calculated. Next resultant values were compared with results of SMARTS[1] simulation.

The SMARTS [87] model was used to model atmospheric transmittance on the day of the measurement for comparison with the Langley plots results. Parameters for the SMARTS model (extraterrestrial spectrum: Wehrli 85 , pressure: 1013hPa, aerosols model: Maritime, O_3 concentration: $0.28 Atm/cm$, turbidity: 0.1, gaseous pollution: light, precipitable water: $2.5 cm$) were set to represent the environmental conditions during the time of the measurements. Figure 3.30 shows the comparison between measured (Langley plots) and modelled (SMARTS) atmospheric transmittance.

Most of the atmosphere transmittance measurements agreed well with the

[1]SMARTS - The Simple Model of the Atmospheric Radiative Transfer of Sunshine

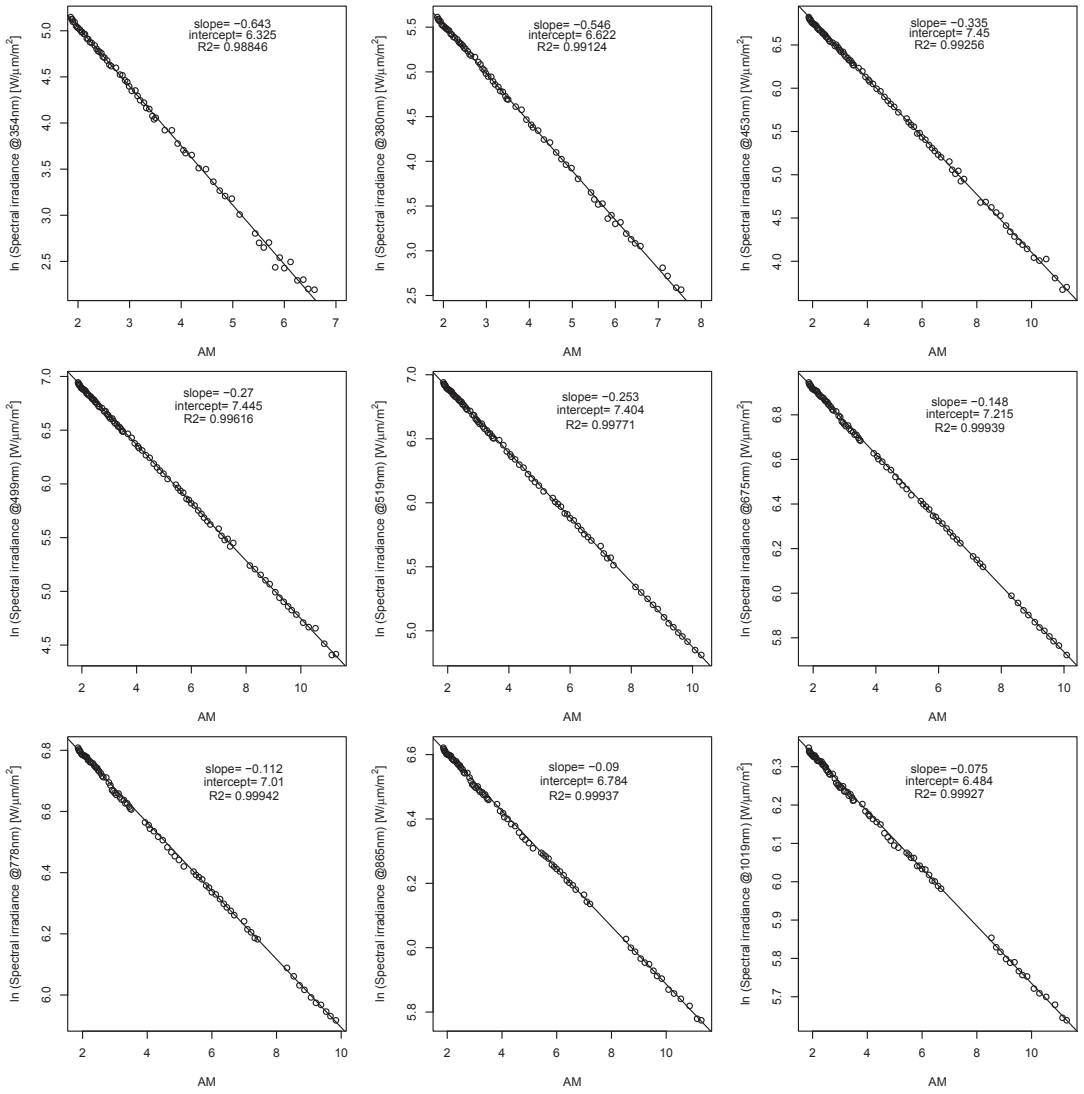

Figure 3.27: Corrected Langley plots for nine selected channels of tested spectroradiometer.

results generated by the SMARTS model. Only in the ultraviolet region were significant differences observed. The observed differences are quite likely caused by the level of gaseous pollution. The impact of ozone was ruled out, as the transmittance would then be also affected in the Chappuis band (at around 600nm). The sensitivity scale calibration started from validating the SMARTS modelled spectrum against the measurements from a CMP11 broadband radiometer. The inte-

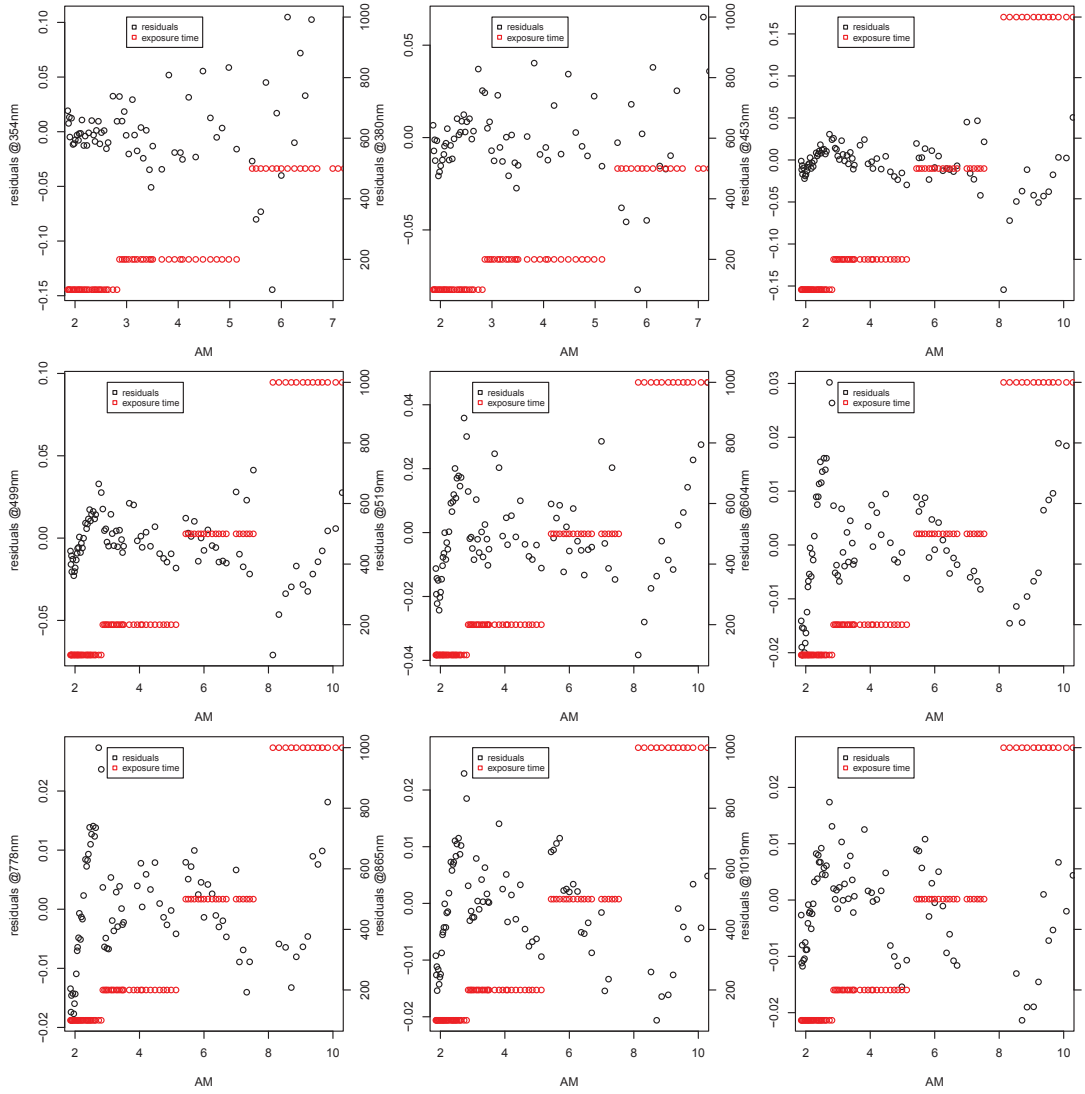

Figure 3.28: Linear fit residuals and exposure time plots for nine selected channels of tested spectroradiometer after application of corrections

gral spectral, horizontal, global irradiance calculated from the adjusted SMARTS was equal to $825.0 W/m^2$. For comparison, a broadband pyranometer CMP11 measured a global irradiance of $827.3 W/m^2$ at the same time. The two results differed by 0.28%, an order of magnitude below the acceptable value. A summary of the calculated horizontal, global broadband irradiances for different bandwidths is shown in Table 3.6.

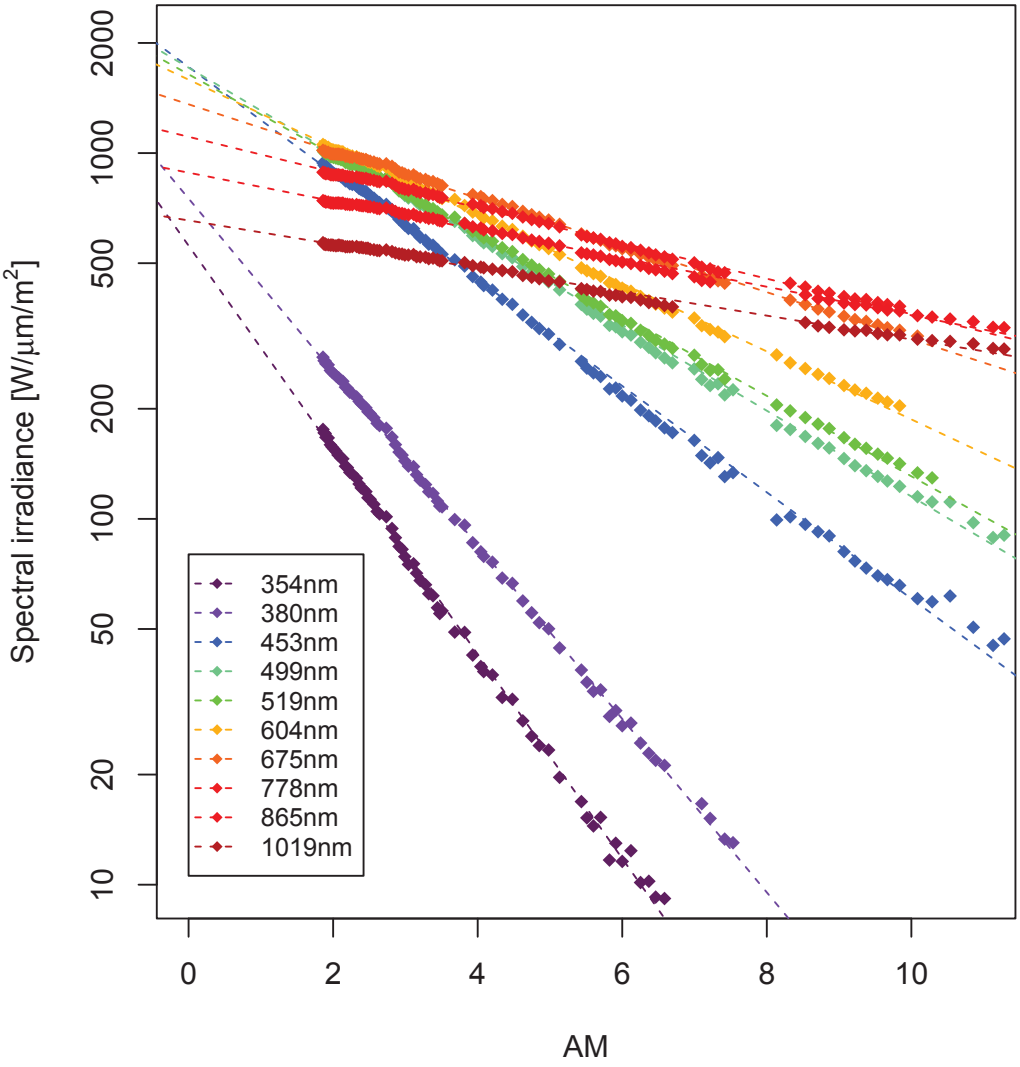

Figure 3.29: Measures and extrapolated spectral solar irradiance for the selected channels

The expected irradiance that the spectroradiometer would measure at the edge of the atmosphere ($m = 0$) was calculated from the intercept of the linear fit of the Langley plots. The Wehrli [50] extraterrestrial solar spectrum was used as a reference. To reflect the limited spectral resolution of the spectroradiometer (FWHM[1]=10nm), the reference extraterrestrial spectrum was convoluted with

[1]FWHM - full width at half maximum, defined as an expression of the extent of a function,

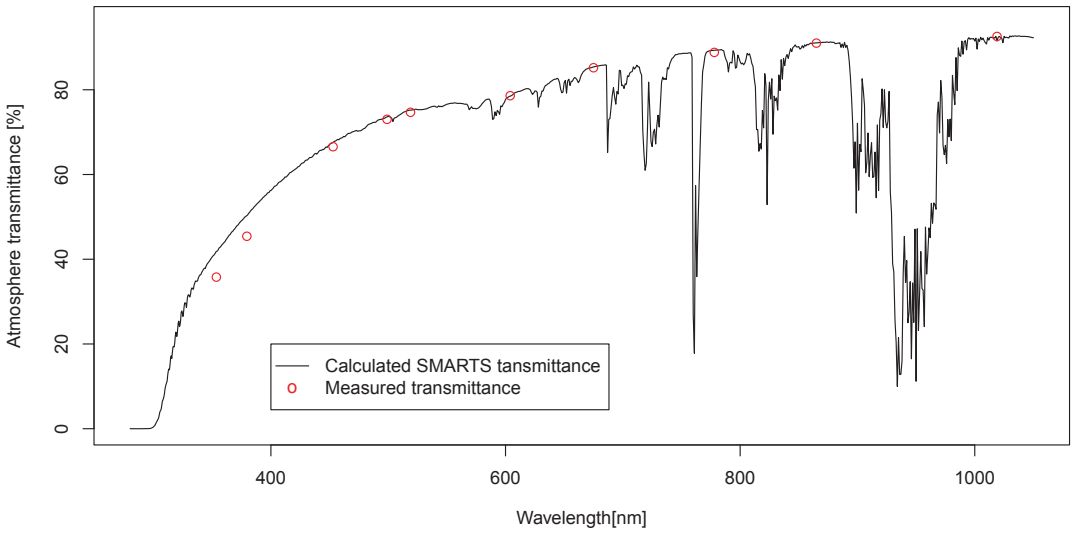

Figure 3.30: Comparison between modelled and measured transmittance of the atmosphere for beam radiation

Table 3.6: Comparison between modelled and measured broadband irradiance

Bandwidth $[nm]$	SMARTS(model) $[W/\mu m/m^2]$	CMP11(measured) $[W/\mu m/m^2]$	EKO MS700(measured) $[W/\mu m/m^2]$
199-4000	831.0	x	x
285-2800	824.0	827.3	x
310-1150	691.6	688.6	600.0

a rectangular window of the length of 10nm, resulting in the moving average value of the reference extraterrestrial spectrum. Original and filtered Wehrli extraterrestrial spectra are shown in Figure 3.31.

It is of great importance to reflect band-integrating properties of the radiometer in preparation of the reference spectrum, as otherwise extraterrestrial reference irradiance (especially for the wavelengths below 600nm) will not be representative for what the spectroradiometer realistically measures. A comparison between the differences of Wehrli high resolution (0.5nm) and filtered (10nm) reference extraterrestrial irradiance for the selected channels is shown in Figure

given by the difference between the two extreme values of the independent variable at which the dependent variable is equal to half of its maximum value

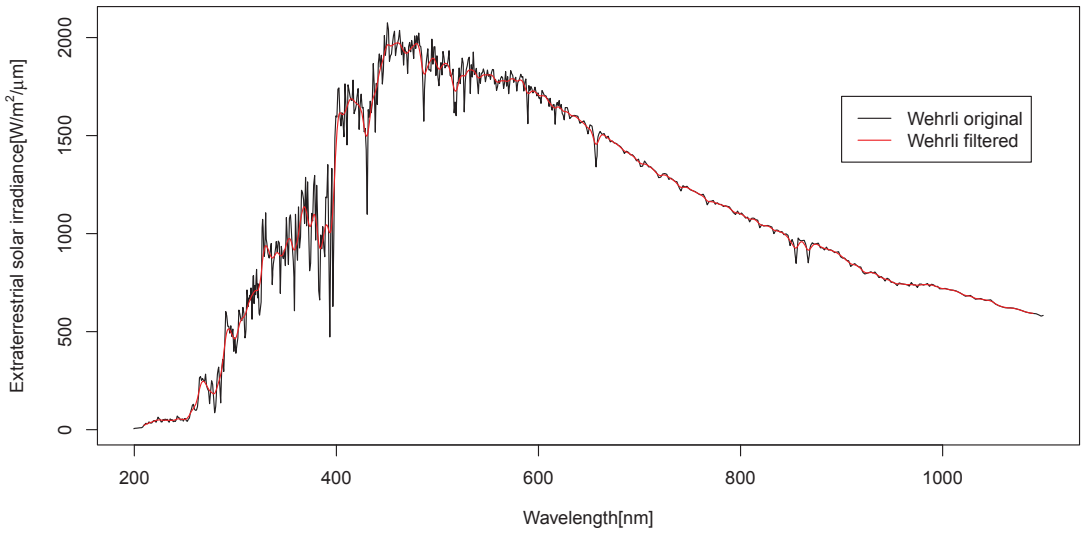

Figure 3.31: Wehrli extraterrestrial spectra: original and filtered.

3.32

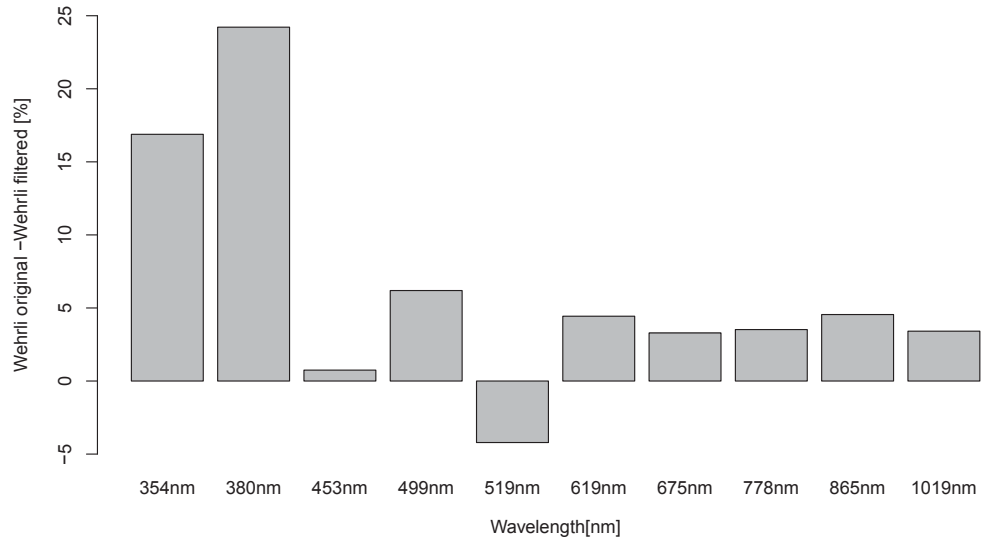

Figure 3.32: Wehrli extraterrestrial spectra: difference between the original and filtered spectral irradiance for the selected channels

Figure 3.33 presents the ratio between extraterrestrial irradiance extrapolated from measurements and the reference extraterrestrial irradiance (Wehrli85) . This

ratio represents the radiometer calibration correction coefficient.

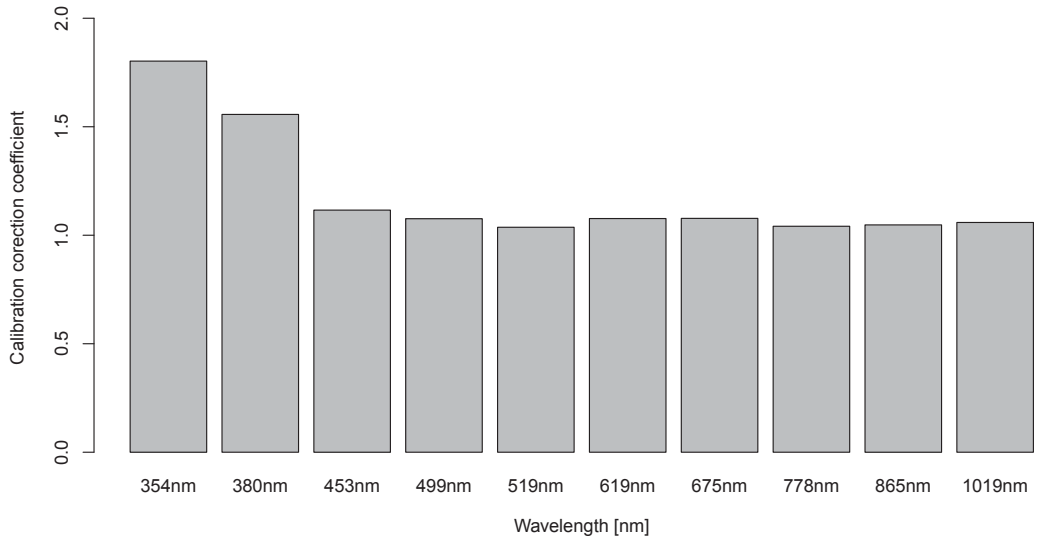

Figure 3.33: Radiometer calibration correction coefficient calculated from Langley method

Figure 3.34 presents the relative error between extrapolated (from measurements) and standard (Wehrli) extraterrestrial irradiance.

As shown in Figure 3.34, the Langley method revealed a similar trend to the one observed during indoor calibration. The spectroradiometer under test systematically understated the real value of irradiance. The magnitude of these differences is consequently lower across the whole wavelength range for the Langley calibration in comparison to the indoor standard lamp calibration.

In a final step use of SMARTS modelled spectrum for spectroradiometer calibration was considered. The spectral irradiance measured under clear sky conditions was compared with the one calculated by SMARTS. The results of this comparison are shown in Figure 3.35. The SMARTS spectrum was filtered in a similar way, as the reference extraterrestrial Wehrli spectrum to reflect the spectral resolution of the spectroradiometer.

As previously observed, the measured spectral irradiance was significantly below expectations.

In Figure 3.36 calibration results achieved from indoor and outdoor campaigns are compared. As shown, the sensitivity calibration coefficients calculated

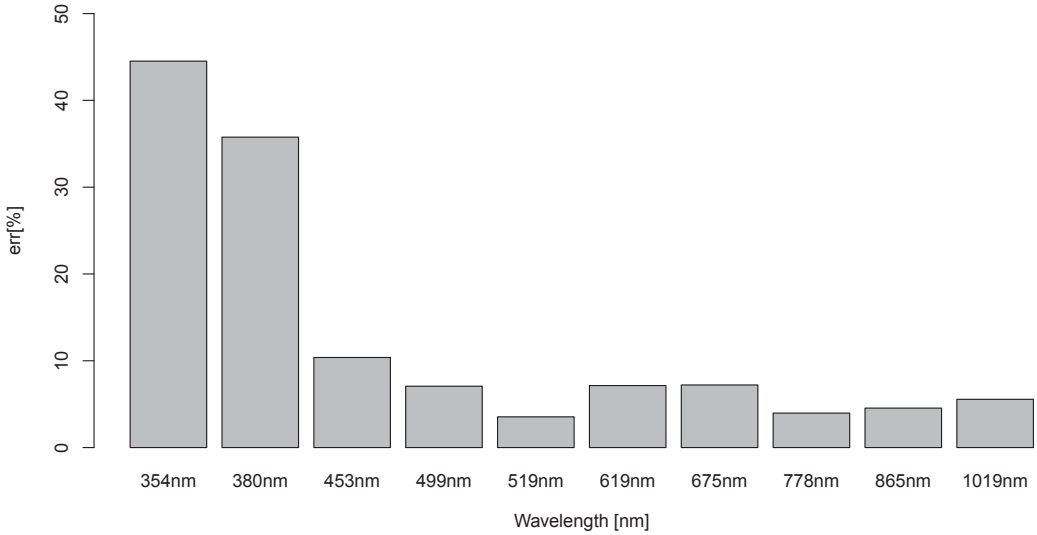

Figure 3.34: Relative difference between the radiometer sensitivity calibration stated by the manufacturer and calculated from Langley plots

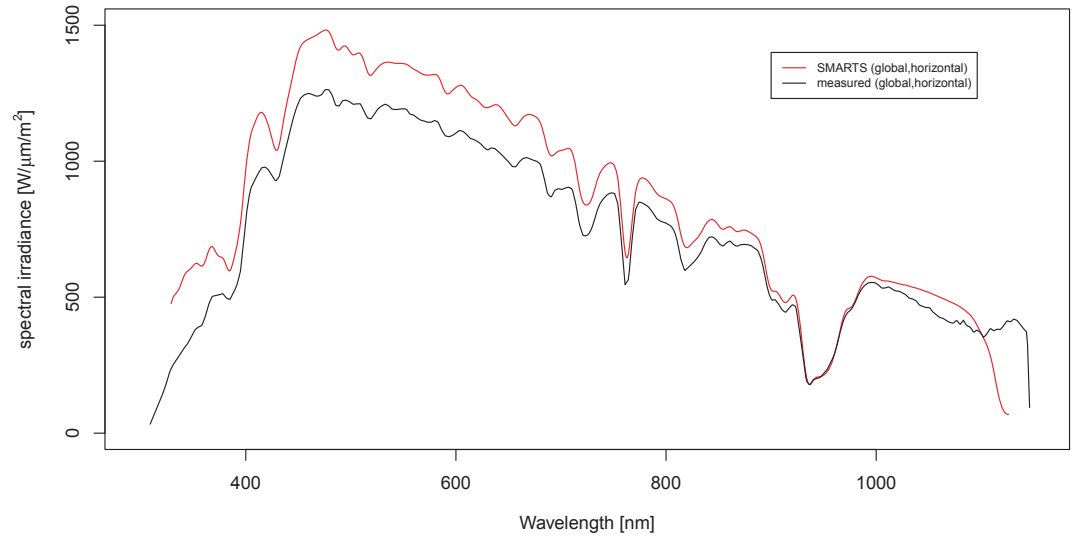

Figure 3.35: Spectral irradiance measured by spectroradiometer vs. modelled from SMARTS

from the adjusted SMARTS model are in good agreement with the sensitivity calibration coefficients calculated based on standard lamp measurements. The Langley plots method has created lower sensitivity calibration coefficients, than

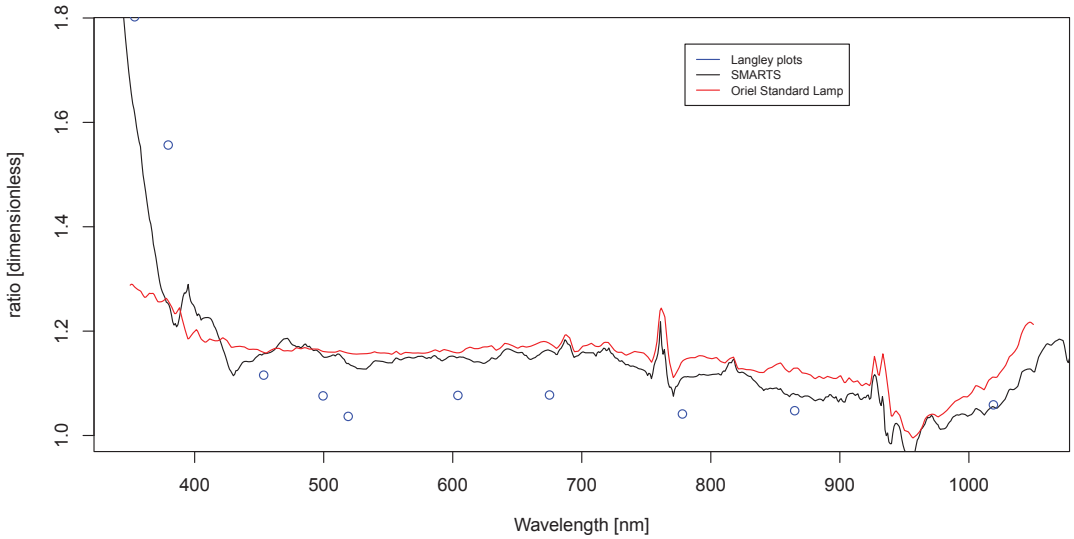

Figure 3.36: Comparison between Oriel standard lamp,Langley and SMARTS calibration methods for spectroradiometer EKO MS700_07

the adjusted SMARTS and standard lamp methods.

3.6 Conclusions

The outdoor calibration campaign has shown that spectroradiometer calibration can be achieved even without highly specialised equipment, under clear sky conditions. The method combining Langley plots with SMARTS modelling and a broadband irradiance crosscheck has been proven to agree with standard lamp calibration.

The Langley method performed worse than expected, giving sensitivity calibration results significantly lower than standard lamp and adjusted SMARTS methods (especially between $600nm$ and $800nm$). The main reason for this is linked to spectroradiometer nonlinearities caused by sensor exposure times. Each of the exposure times has a specific sensitivity coefficient, therefore only measurements taken with the same exposure time can be compared. The standard lamp emitted an irradiance of around $220W/m^2$ in the plane of the spectroradiometer. The exposure time during standard lamp calibration was always equal to $500ms$. Under outdoor conditions, a 500ms exposure time is only achieved for air mass ranging between 5-8. Therefore only this region should be used for Langley calibration for comparison. Use of such a narrow range of air masses increases the uncertitting of a Langley plot, however. What is more important, the standard lamp calibration procedure is a one-point measurement and it assumes linearity of the radiometer. If the standard lamp calibration is taken in a measurement region affected by radiometer nonlinearities (e.g. AM=5-8, 865nm), the whole calibration can be affected. For 865nm, residuals between linear fit and measured irradiance were in the range of -3% to -5% of the measured signal. This explains why the Langley calibration delivered lower values of the calibration correction coefficients. Incidentally the SMARTS calibration delivered similar results to the standard lamp calibration, as the nonlinearities seems to have the same character for short exposure times ($50ms$ and $100ms$ as the one observed for $500ms$ (e.g. $AM = 2, \lambda = 865nm$). In regions where nonlinearities of the radiometer were less noticeable ($300nm - 400nm$) agreement between Langley and SMARTS calibration was much better.

The proposed nonlinearity correction linearised the spectroradiometer sensitivity throughout the different exposure times, but additional, indoor and outdoor

calibration of the spectroradiometer should be repeated after linearity corrections are applied to establish correct sensitivity calibration. This issue should be further investigated. Another source of errors in the Langley plot method, specific to the spectroradiometer under test, is its sensitivity to the wavelength domain calibration of the radiometer. Wavelength domain calibration of the investigated spectroradiometer is limited due to its low resolution (256 channels, FWHM=10nm).

Comparison with an adjusted SMARTS model under clear sky conditions has given calibration results very close to standard lamp, with the majority of differences lying down in regions of UV and strong atmospheric absorption bands. As previously mentioned, the SMARTS based calibration was affected by nonlinearities of the sensor in a similar way to the standard lamp calibration, resulting in higher calibration correction coefficients.

Standard lamp calibration problematic in UV regions, where the levels of detector sensitivity and the radiant power emitted by the halogen lamp are very low. It should be noted that the standard FEL lamp had a history of 35h use (out of 50h stated lifetime) at the time of spectroradiometer calibration, therefore calibration of the UV range could have been affected to a certain extent.

Chapter 4

Experimental evaluation of FEL lamps

4.1 Introduction

The standard of spectral irradiance as realised with the use of a FEL 1000W halogen lamp, has been found a major source of uncertainty in a spectroradiometer calibration. The calibration uncertainty of a FEL lamp based spectral irradiance standard in optimum conditions goes down to 1.5%, with the typical expected value ranging between 3% and 5%. FEL lamps utilised to implement standards of spectral irradiance by the NIST[1] and various commercial retailers are not proprietary products. FEL lamps are manufactured by a number of companies, with the leading ones being Osram, GE, Philips, Ushio, Eiko. Regardless of the manufacturer, technical specifications of FEL lamps are mostly the same (colour temperature of 3200K, CC-8 tungsten filament type, operating voltage of 120V, rated power of 1000W, output flux of 27500lm). Some differences can be found between shapes of glass envelope and tungsten filament, however these differences should not have a major impact on the distribution of spectral irradiance emitted by the lamp. Lamps manufactured by various companies should not present any significant difference in their output characteristics, given that they are operated under the same conditions. However, a comparison of spectral

[1]NIST - National Institute of Standards and Technology

irradiance characteristics of standard FEL lamps exposes significant differences between manufacturers. Figure 4.1 presents the characteristics of spectral irradiance standards offered by Gooch&Housego and Newport (Oriel) in relation to typical reference spectral irradiance standard. The presented ratios highlight the relative calibration differences of third-party spectral irradiance standards in reference to the NIST's typical FEL spectral irradiance standard lamp.

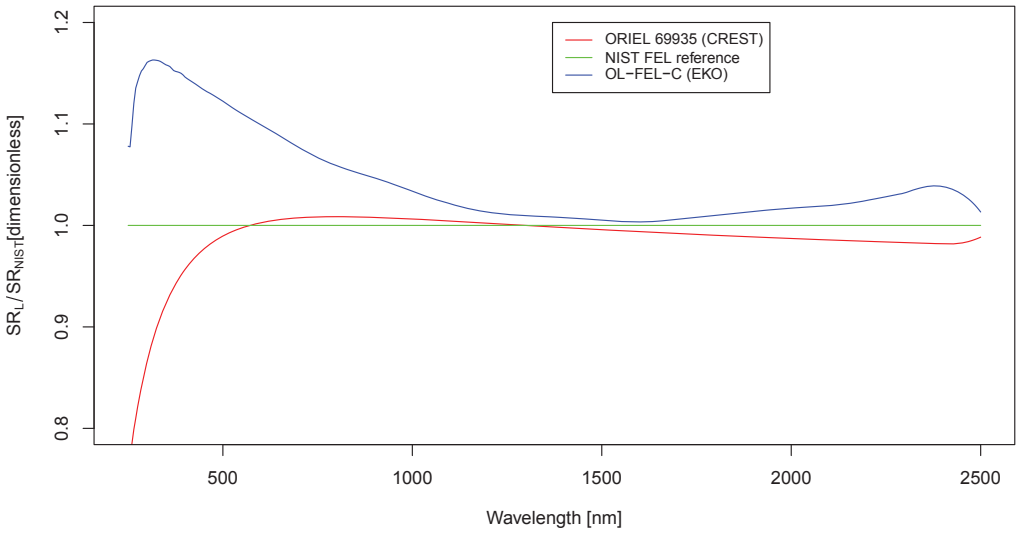

Figure 4.1: Ratio between spectral irradiance of investigated standard lamp (SR_L) and spectral irradiance of NIST reference lamp (SR_{NIST})

The observed disagreement between lamps characteristics cannot be explained only by the minor structural differences between bulbs. The results suggest that the reason for such significant differences must lie in operating conditions (mainly filament temperature) or invalid lamp calibration (pre conditioning, calibration transfer, used reference spectral irradiance standard). According to the manufacturer's data, the peak in spectral irradiance characteristics of the Gooch&Housego OL-FEL-C (EKO) spectral irradiance standard is shifted towards shorter wavelengths in reference to Oriel 69935 (CREST) and NIST (typical). Gooch&Housego OL-FEL-C (EKO) spectral irradiance standard emits 3.5% more radiant power than the typical NIST reference spectral irradiance standard within the wavelength range 300nm-2500nm. The Oriel 69935 spectral irradiance standard used by CREST differed only by 0.1% in terms of total emitted radi-

ant power in comparison with the NIST FEL typical standard lamp. It has to be noted that the stated absolute difference in total radiant power is not evenly distributed across the wavelength domain. In the case of the Oriel spectral irradiance standard, lower output in UV is balanced out by higher output in the NIR part of the spectrum. Moreover, a large difference in UV radiation only has a small contribution to the total radiant power, as the halogen lamp emits little UV light. The Oriel standard of spectral irradiance uses an Osram-Sylvania 1000W FEL halogen lamp, the same one as used by NIST. Therefore characteristics of these two lamps differ less due to a very similar filament and envelope construction, unlike the OL-FEL-C spectral irradiance standard, which uses a GE FEL lamp.

It seems that, regardless of bulb make, spectral irradiance standard lamps are at first calibrated in regard to the total irradiance, and then in regard to the spectral irradiance distribution. The relatively small difference in total irradiance emitted by Oriel (CREST) and Gooch&Housego OL-FEL-C (EKO) spectral irradiance standards translate disproportionally into much higher differences in spectral irradiance. This parameter is of special interest for the photovoltaic industry. The possibility of the coexistence of two standard lamps, which hold valid, traceable calibration certificates, but at the same time differ significantly one from another, can be confusing to the end user. Such a situation allows for an additional level of freedom during the lamp calibration process. It is a great importance to clarify, whether spectral characteristics of FEL lamps differ because of specific lamp construction and materials or if the observed variations are caused explicitly by operational conditions.

4.2 Experimental evaluation

4.2.1 Introduction

A better understanding of the physical properties of FEL lamps is essential for minimising the uncertainty of spectral irradiance standard. As was presented in Figure 4.1, the spectral irradiance characteristics of standard lamps differ significantly from one another. The questions to be answered are: how much does the spectral irradiance characteristic and total radiant flux of FEL lamps vary between different lamp manufacturers; how much do the variations in lamp construction influence spectral irradiance characteristics, and; how this information can be utilised to validate the calibration of the standard lamp.

Spectral characteristic of a standard FEL lamp is defined by the following factors[1]:

- filament temperature
- filament area
- tungsten emissivity
- quartz glass envelope transmission
- other effects (light recycling processes, internal reflections)

[1]Halogen gas filling the envelope has been reported not to have a noticeable influence on the spectral characteristics of the lamp [88]

4.2.2 Methods

4.2.2.1 Physical model of the FEL lamp

According to NIST, calibration of the FEL lamp based standard of spectral irradiance is done by a direct comparison of a lamp under test with a working standard at a specified set of wavelengths not affected by atmospheric absorption bands. The spectral characteristic of the tested lamp is then defined by the formula 4.1 [89] fitted to measured points.

$$E_{e,\lambda,FEL} = \lambda^{-5} exp\left(c_0 + \frac{c_1}{\lambda}\right) \cdot \left(C_0 + C_1\lambda + C_2\lambda^2 + C_3\lambda^3 + C_4\lambda^4 + C_5\lambda^5\right) \quad (4.1)$$

where:

c_1 - first radiation constant $c_1 = 2\pi hc^2$

c_2- second radiation constant $c_2 = hc/k$

C_1, C_2, C_3, C_4, C_5 - polynomial coefficients

This standard formula expresses the spectral irradiance of FEL lamps as a product of an approximated Planck's law and high order polynomials. The first part of the formula expresses the spectral radiation of a black body at the temperature equal to the true lamp temperature. The polynomial part accounts for characteristic scaling and all other lamp-specific factors (residues). Formula 4.1 gives a simple mathematical solution for fitting spectral irradiance characteristics of the lamp. Regardless of its simplicity, it does not represent the physical properties of a lamp. A more accurate description, which takes into account the physical properties of the FEL lamp, is given by formula 4.2.

$$E_{\lambda,FEL}(T) = E_{\lambda,B}(T) \cdot \epsilon_{\lambda,W}(T) \cdot C_{\lambda,\epsilon} \cdot T_{\lambda,env} \cdot R_{\lambda,env} \cdot C_{\lambda,r} \quad (4.2)$$

where:

$E_{\lambda,B}$ - spectral irradiance of a black body

$\epsilon_{\lambda,W}$- tungsten spectral emissivity

$C_{\lambda,\epsilon}$ - emissivity correction due to light recycling

$T_{\lambda,env}$ - transmittance of a quartz envelope

$R_{\lambda,env}$ - reflection from the envelope

$C_{\lambda,r}$ - high order polynomial for a residual correction

4.2.2.2 Measurements of true filament temperature

The emissivity of a tungsten filament is a function of a temperature and a wavelength. For this reason, the filament temperature cannot be determined correctly from the spectral characteristics of the lamp, based on a black body model, if the filaments' emissivity is unknown. The temperature of a body can be easily calculated from two narrow-band measurements of spectral irradiance as long as the body's emissivity at these wavelengths is known (see equation 4.3).

$$T(\lambda_1, \lambda_2) = \frac{\epsilon_1}{\epsilon_2} \cdot \frac{c_2 \cdot (\frac{1}{\lambda_2} - \frac{1}{\lambda_2})}{lnR - 5 \cdot ln(\frac{\lambda_1}{\lambda_2})} \tag{4.3}$$

where:

R - ratio of the spectral irradiance observed at λ_1 and λ_2

ϵ_1, ϵ_1- tungsten spectral emissivity at λ_1 and λ_2

Equation 4.3 creates the theoretical basis for constructing a pyrometer[1]. It is based on a Wien's approximation of a Planck's law and is valid only for Wien's region ($c_2/T\lambda >> 1$). An application of equation 4.3 is limited to the short wavelengths only (commonly used criterion is $c_2/T \approx 5\lambda_{max}$).

As the emissivity of the filament radiator is unknown, a spectral pyrometry technique was used to calculate a true filament temperature. A simple transformation of Wien's approximation of Planck's law results in equation 4.4.

$$ln(\lambda^5 E_{e,\lambda}) = -\frac{c_2}{\lambda T} + ln(\epsilon c_1) \tag{4.4}$$

[1]pyrometer - a radiometric device capable of taking contactless temperature measurements based on radiation emitted by the investigated body. In opposition to a pyranometer, which measures broadband total hemispherical radiation, a pyrometer collects radiation only from a narrow viewing angle and within a single (less frequently multiple) spectral band

Wien's approximation of Planck's law becomes linear if the following coordinates system is used $x = \frac{c_2}{\lambda}$ and $y = ln(\lambda^5 E_{e,\lambda})$. Wien's equation in such a coordinate system has a slope coefficient $a = \frac{1}{T}$ and the intercept $b = ln(\epsilon c_1)$. Linearisation of Wien's equation allows for a simple method of calculating the true temperature of the emitter, when the emitter emissivity stays unknown, if only the sufficient number of points spread across the spectrum is taken into account.

As the equation 4.4 is based on Wien's approximation of Planck's law, it has to be ensured that any measurements used for analysis lie within Wien's region. The maximal filament temperature is expected not to exceed 3400K, therefore the longest wavelength that fulfils Wien's criterion is $\lambda_{max} = 846nm$. Measurements below 400nm were rejected because of a low signal to noise ratio (SNR). Low SNR is caused by the low level of radiation emitted by the halogen source and the limited sensitivity of the spectroradiometer detector in the UV region.

4.2.2.3 Long-term stability

Five 1000W FEL halogen lamps manufactured by: Osram-Sylvania, General Electric, Platinum, Ushio and Donar were used to perform long-term stability test. This includes lamps which have proven to be selected most frequently for the implementation of a standard of spectral irradiance. Additionally, two low quality lamps were included for comparison. Halogen lamps change their characteristics during the initial period of use. Moreover some lamps may present instability in radiant flux even after the initial burn-in. For these two reasons it is required to anneal lamps before calibration can take place. At first the lamps were visually inspected for any visible defects. After visual inspection, the lamps were cleaned with isopropyl alcohol to remove any dust residues from the surface of the quartz envelope to avoid the possibility of glass staining. Next, each lamp was annealed for a total period of 96h. This interval allowed lamps to go through the initial burn-in of 46h, and then through the manufacturers stated lamp lifetime of 50h. Lamps were annealed under controlled power of 925W, which represents 92.5% of their nominal power. Operating lamps below their rated power during the annealing process does not affect a halogen cycle. The efficiency of a halogen cycle

decreases when the delivered power falls below 80% of its nominal value. Given that the halogen cycle is not affected, operating the lamp below rated power extends the lifetime of the lamp.

A reference cell and the EKO MS700 spectroradiometer were used continuously throughout the time of the test to measure emitted radiation at the distance of 500mm from the lamp. This allowed investigation of radiation variations during the process. The experimental setup used for these measurements is shown in Figure 4.2 and 4.3.

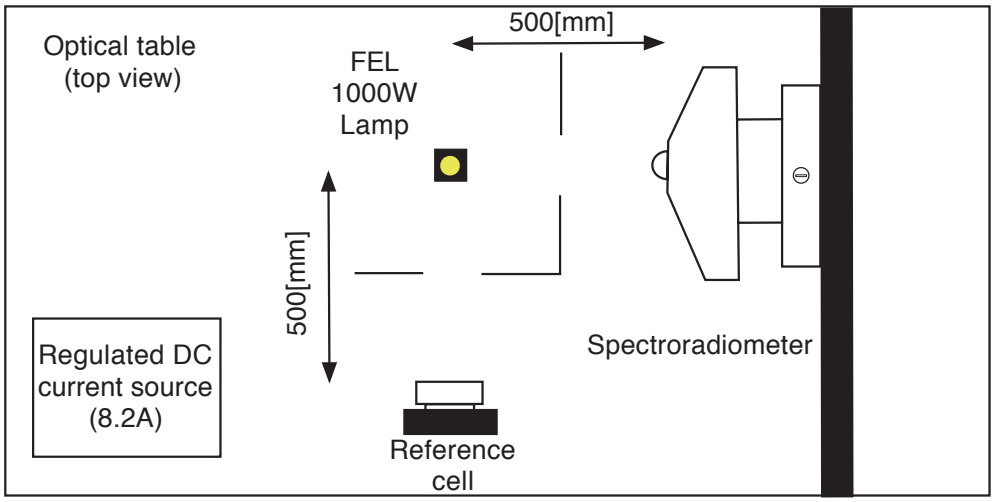

Figure 4.2: Experimental setup for FEL lamps annealing

During the test, the following parameters were monitored: spectral irradiance; lamp current and voltage; short circuit of a reference cell, and; reference cell temperature. After the test, all lamps were checked to see if they developed any coloration of the envelope. Inspection was carried out with the use of photographic techniques. This way subtle envelope coloration, barely visible to the human eye could have been revealed. Each lamp was photographed with uniform, daylight-balanced backlight. Images were further analysed via image processing software to enhance visibility of any coloration occurring in the visible spectrum. Figure 4.4 illustrates the experimental setup used for acquisition of lamp photographs.

Annealed lamps without coloration were compared against the calibrated reference lamp (Oriel), which held a valid calibration certificate. Magnitude of the

Figure 4.3: Experimental setup for FEL lamps annealing - photography of the lamp mounted in testing post

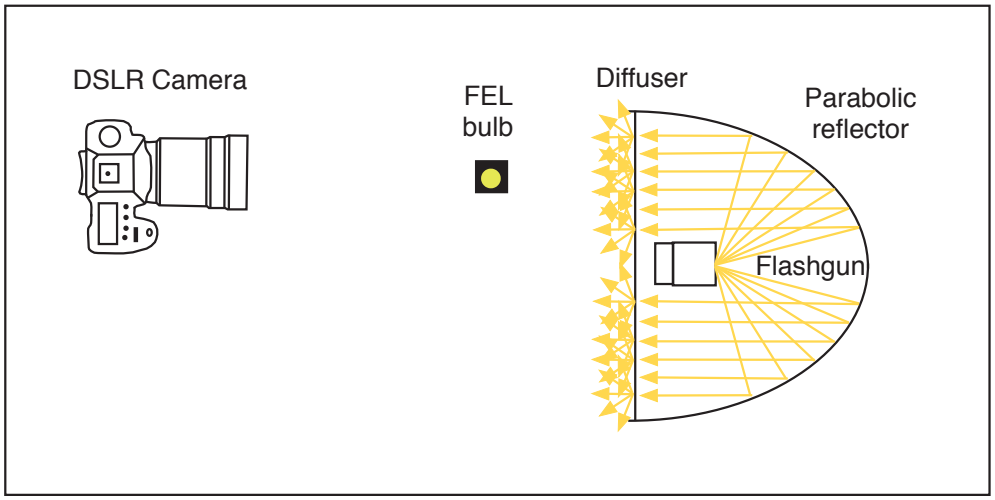

Figure 4.4: Experimental setup for acquisition of lamp photographs for coloration inspection

spectral irradiance differences was expressed as a ratio between the spectral irradiance of the lamp under test and the spectral irradiance of a reference standard lamp.

4.2.2.4 Impact of filament physical properties on emitted spectral irradiance

Figure 4.5 presents a dependency graph between delivered electrical power, lamp filament physical properties and emitted spectral irradiance.

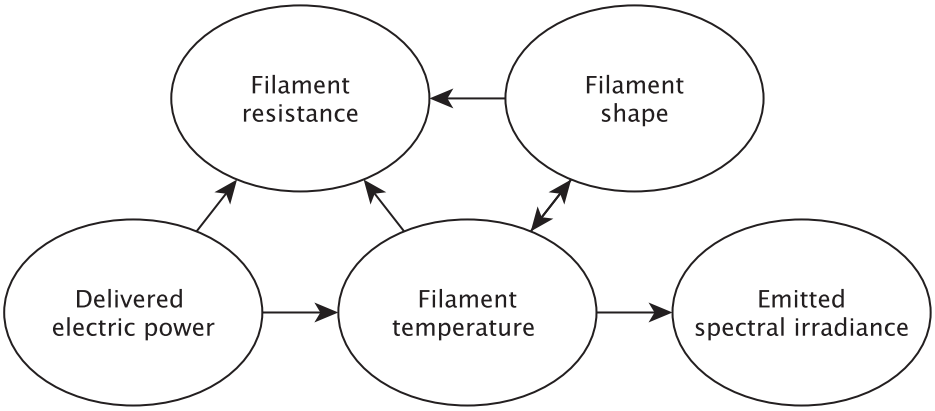

Figure 4.5: Dependencies between filament parameters

Delivered electric power has the greatest impact on the temperature of the filament, therefore also on intensity and spectral characteristics of the irradiance emitted by the lamp. This parameter can be controlled precisely and even used to advantage in the metrological setup. The emissive properties of the lamp heavily depend on filament physical properties (geometrical shape, resistance, used material emissivity). Figure 4.6 shows a comparison between FEL lamps manufactured by different companies.

It can be seen in Figure 4.6 that the quartz envelopes are very similar across all manufacturers. The most significant variation is in the shape of the filament. The shape of the filament and its active area impacts the radiant flux and spectral characteristic of the lamp. Depending on lamp construction it is not always obvious which part of the filament takes part in optical radiation emission. Even if the active area of two different filaments is the same, each of them may emit different quantities of radiant flux depending on filament geometry. Filament geometry may also promote the light recycling processes. Photographic techniques were utilised for comparison of filament shapes and active filament areas during

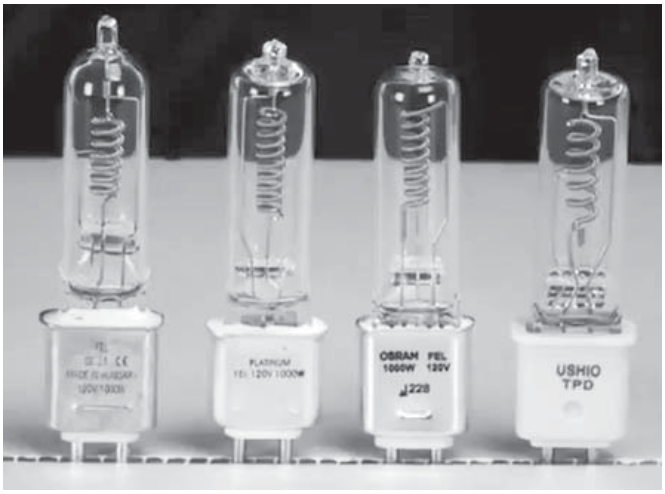

Figure 4.6: Comparison between different brands of FEL lamps (starting from left GE, Platinum, Osram, Ushio)

lamp operation. To acquire active filament photographs, a DSLR[1] camera was used. The camera was equipped with a 200mm macro lens resulting in magnification of x0.254. A neutral density filter was used to reduce the radiant power to 0.392% of its initial value to obtain properly exposed filament photographs. Figure 4.7 presents the experimental setup used for the acquisition of photographs of an active filament area.

To investigate dependencies between delivered electric power, filament temperature and lamp resistance, spectral characteristics of the lamps were measured under varying current rates. Halogen lamp degradation increases significantly when it is working above its rated conditions. This is because of an increased evaporation ratio of the filament and consecutive inefficiency in the halogen cycle. For this reason the power delivered to the lamp was set not to exceed 1025W (102.5% over the rated value of 1000W). Operating the lamp over the rated conditions did not cause lamp degradation as the measurements were carried out only for a short period of time (not exceeding 3h per lamp). Measurements were followed under the same experimental setup as the one shown in Figure 4.2 despite the fact that delivered power varied in the range of 200W-1025W.

[1]DSLR - Digital single-lens reflex camera

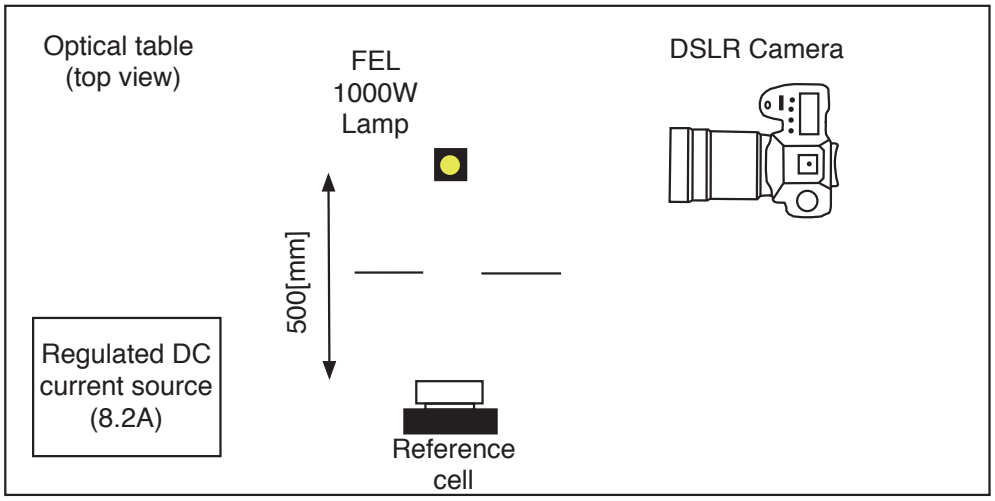

Figure 4.7: Experimental setup for the acquisition of active filament photographs

4.2.3 Results

4.2.3.1 Long-term stability

The burn-in process allows lamps to go through initial degradation. After this process lamps operated under stable conditions should present stable radiant flux output. The operational position of the lamp impacts filament degradation as the convective circulation of the halogen gas inside the lamp's envelope is being affected. Tested lamps were operated in the vertical position, which provides the best convection, what slows down degradation.

Figure 4.8 presents temporal variations of radiant flux of Ushio, Osram-Sylvania and GE FEL lamps during the long-term stability test.

In Figure 4.8 it can be observed that each lamp presented instability of radiant flux during the annealing process. Two types of instabilities can be distinguished: one induced by lamp structural changes (long-term degradation, recrystallisation) and the other induced by power source instability (short term steps).

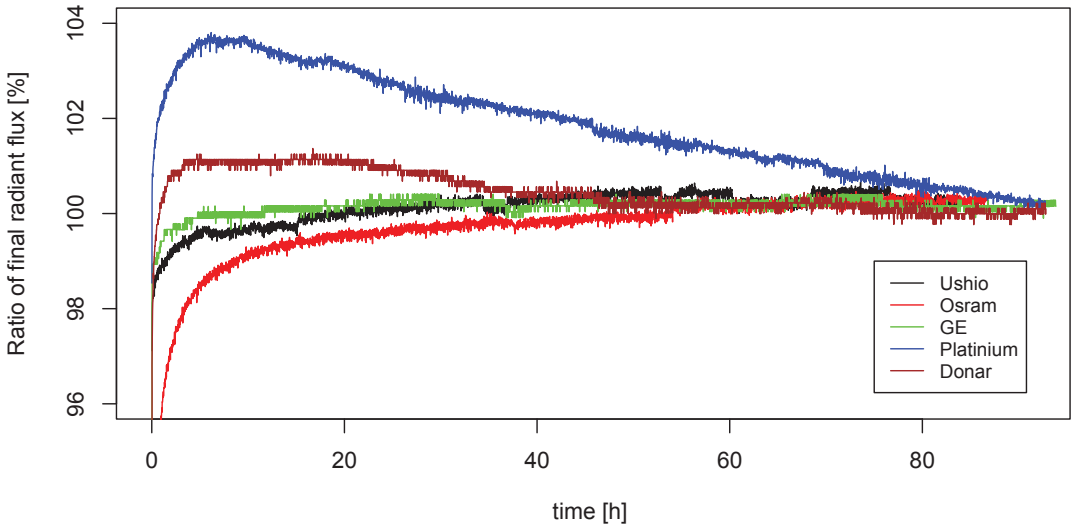

Figure 4.8: Variations of radiant flux during the long-term stability test

Radiant flux of Ushio, Osram-Sylvania and GE lamps varied the most during the initial 15h of the long-term stability test. For the remaining time, radiant flux of these lamps increased by less than 1%. The Donar lamp stabilised temporarily just after 5h, and then between 20h and 40h its radiant flux decreased by 1%. This change could have been caused by recrystallisation of the filament. After 40h of annealing the Donar lamp presented stable output. The Platinum lamp presented continuous decrease of radiant power during the time of the test. Final output flux was reduced by 3.8% in comparison to its initial value. The cause of the observed decrease of radiant flux was coloration of an envelope.

Some observed variations of radiant flux relate to instantaneous variations of the voltage supplied to the lamps. These variations do not reflect actual changes in the resistance of the lamp and are linked to limited accuracy of the used digital radiometric power supply. According to the manufacturer's data-sheet, the metering accuracy is limited to $\pm 0.05\%$, digital voltmeter resolution equals to 0.1VDC, digital current meter resolution equals to 0.01A and output voltage ripple equals to 0.05%. After taking into consideration all of these parameters, instantaneous variation of radiant flux can be explained. Improvements in the accuracy of the power source would have a positive impact on the overall uncertainty of radio-

metric measurements. To eliminate the instability of a radiometric digital power source, radiant flux was corrected based on measured voltage variations. Corrections were applied in such a way that lamp radiant power was increased or decreased by ±0.05% to ±0.1% proportionally to measured voltage. An example of radiant flux correction is presented in Figure 4.9. Corrected radiant flux for tested lamps is shown in Figure 4.10.

During the final 30h of the long-term stability test Ushio, Osram-Sylvania, GE and Donar lamps presented level of stability better than 0.017%/h. Variations of radiant flux followed different paths depending on the lamp. Lamps were annealed under the constant power regime. This means that the actual temperature of the lamp filaments could have varied across the tested lamps set. Different temperatures of lamp filaments during the long-term stability test may explain various paths of lamp output power. It was observed that some of the tested bulbs were stabilising faster than others. To investigate this issue further, long-term stability testing should be repeated under various filament temperature regimes. This way an optimal filament temperature profile for bulb ageing could be found.

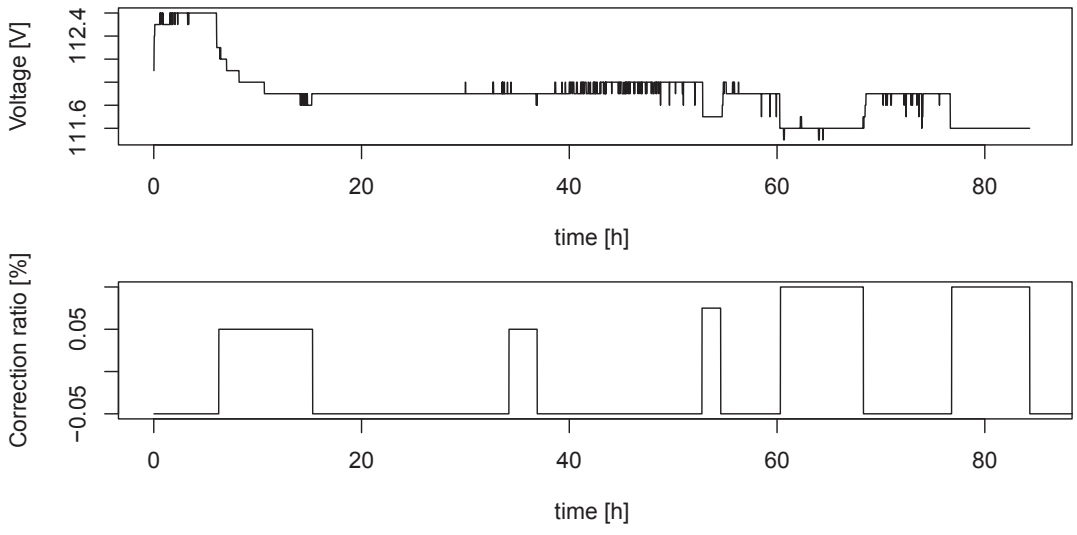

Figure 4.9: Sample correction applied to Ushio radiant flux to compensate for radiometric power source instability

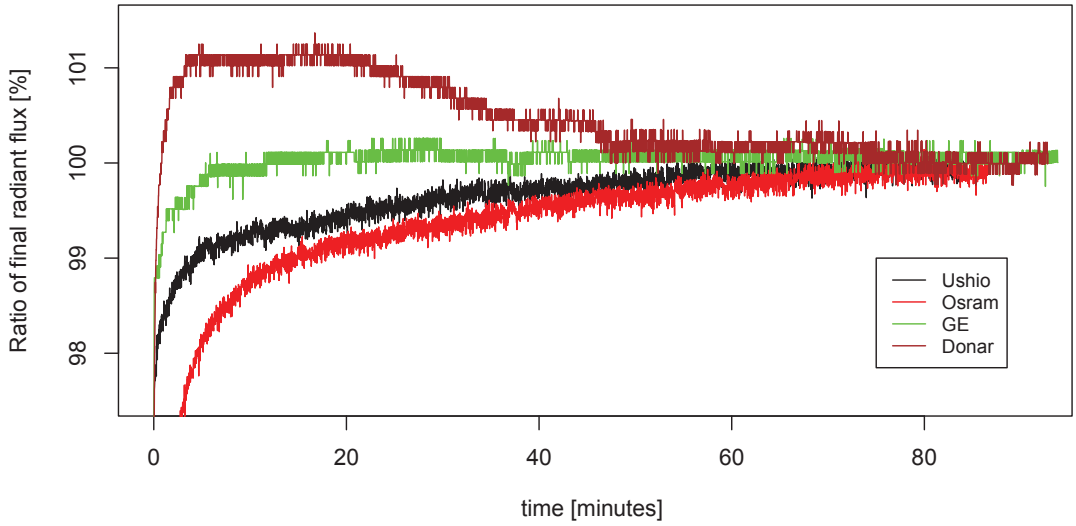

Figure 4.10: Variations of radiant flux during lamp annealing after voltage correction

For all of the observed cases filament texture remained unchanged after 96h of annealing. Significant differences were observed only at the top of the filament support structures. Detailed visual inspection revealed that the surface texture of the filament supports has, in case of Platinum, Donar and GE lamps, changed from shiny (metallic) to matt and grainy. Contrary to this, the surface texture of the filament support of Ushio and Osram-Sylvania lamps remained unaltered. Figure 4.11 and 4.12 show comparisons between the surface texture of a filament and filament support after 96h of annealing for Ushio and GE lamps respectively.

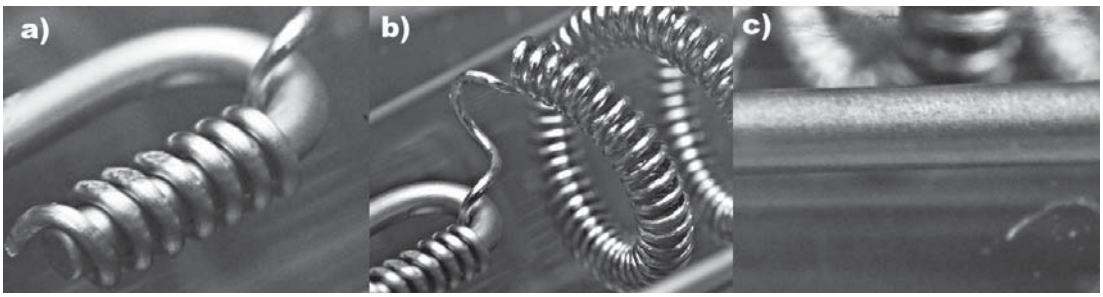

Figure 4.11: Enlargements of filament degradation of Ushio lamp after 96h of annealing: a) and c) filament support b) filament

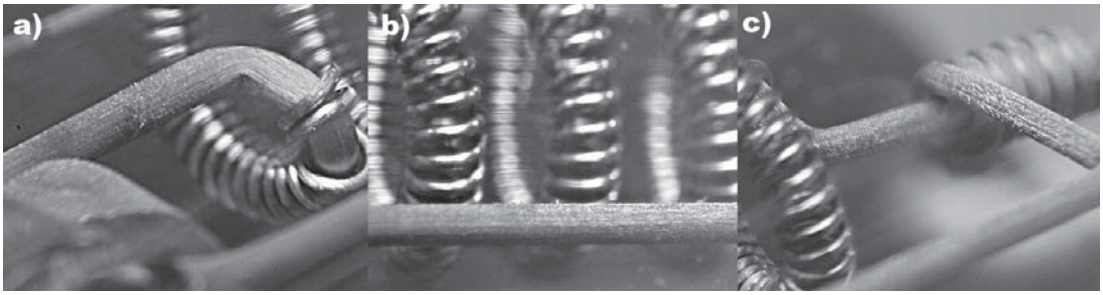

Figure 4.12: Enlargements of filament degradation of GE lamp after 96h of annealing: a) and c) filament support b) filament

The annealing process should not leave significant coloration of the lamp envelope. Photographic inspection has shown that each of the tested lamps developed coloration of a bottom part of the glass envelope. One out of five tested lamps developed significant coloration of the glass envelope near the filament region. Figure 4.13 presents these results.

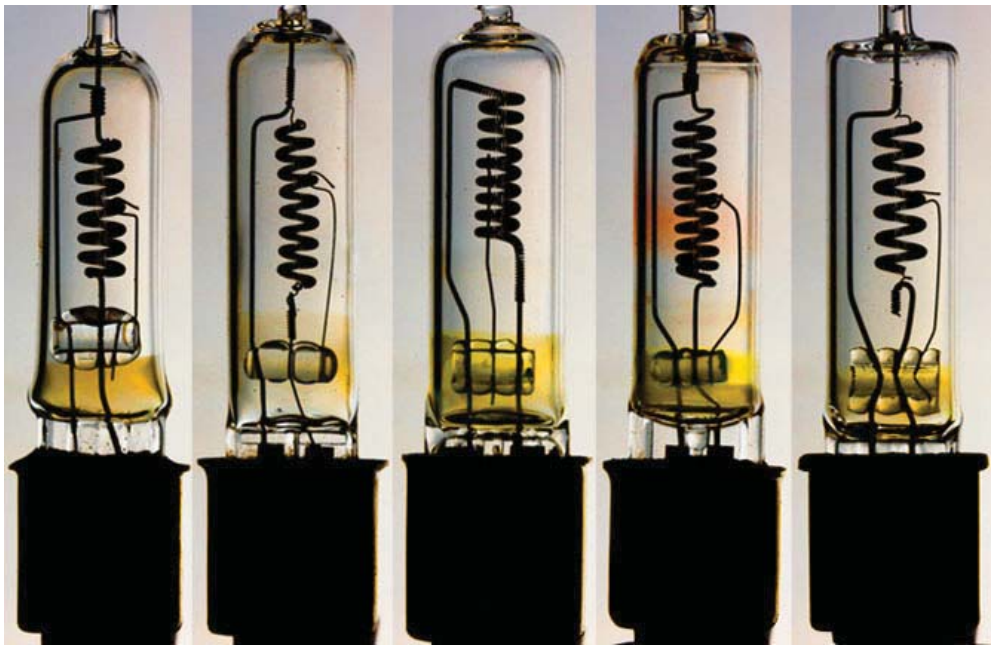

Figure 4.13: Coloration of different FEL lamps after 96h of annealing. Starting from left to right: General Electric, Donar, Osram-Sylvania, Platinum, Ushio

This measurement was repeated for another sample of the Platinum lamp.

The second sample developed the same significant coloration. Both Platinum lamps failed to stabilise at acceptable power levels after annealing. Platinum lamps were thus rejected from further investigation.

4.2.3.2 True filament temperature measurements

Given that the shape of the filament remains unchanged, the character of emitted irradiance stays constant in relation to true filament temperature. Tungsten emissivity varies across the wavelength's domain and with temperature. Therefore, the true temperature of the filament differs from the colour temperature of the emitted light. Knowing the tungsten emissivity, the true temperature and the geometry of the filament allows prediction of the spectral irradiance emitted by a filament. A spectral pyrometry technique was used to measure the filament's true temperature. Accuracy of the implemented algorithm was validated against the modelled spectral characteristics of a black body ($\epsilon_\lambda(T) = 1$), grey body ($\epsilon_\lambda(T) = 0.385$) and tungsten body ($\epsilon_\lambda(T) \neq const$) for temperature of 3100K. Figure 4.14 presents modelled spectral radiation characteristics of black, grey and tungsten bodies at 3100K.

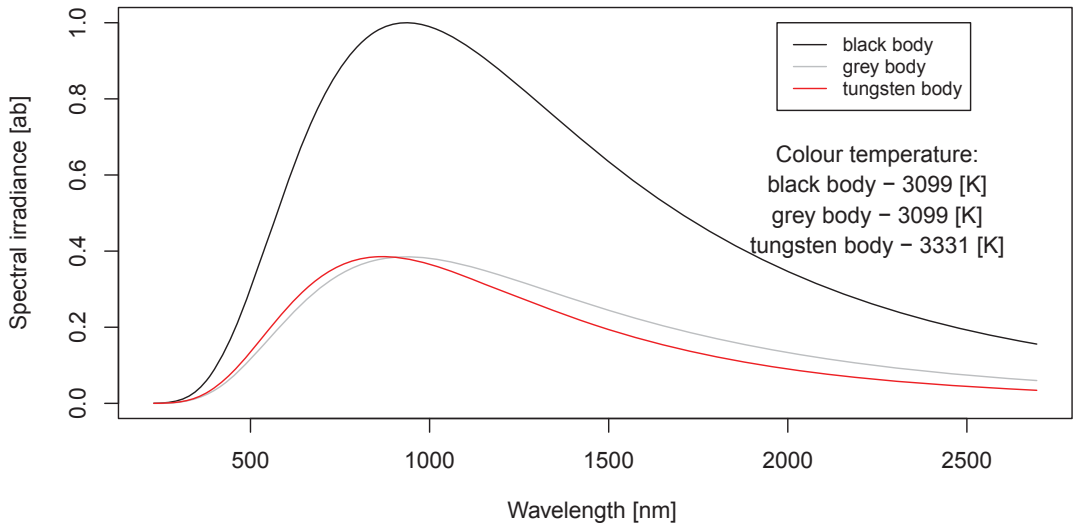

Figure 4.14: Modelled spectral radiation characteristics of black, grey and tungsten bodies

It is shown in Figure 4.14 that the colour temperature of the light emitted by a tungsten body is around 7.5% higher than its true temperature (3100K).

The true temperature of a tungsten body calculated from its spectral irradiance, with use of the spectral pyrometry method, agreed with the expected value within the margin of 1.2%. Figure 4.15 presents black, grey and tungsten body characteristic in linear coordinate system.

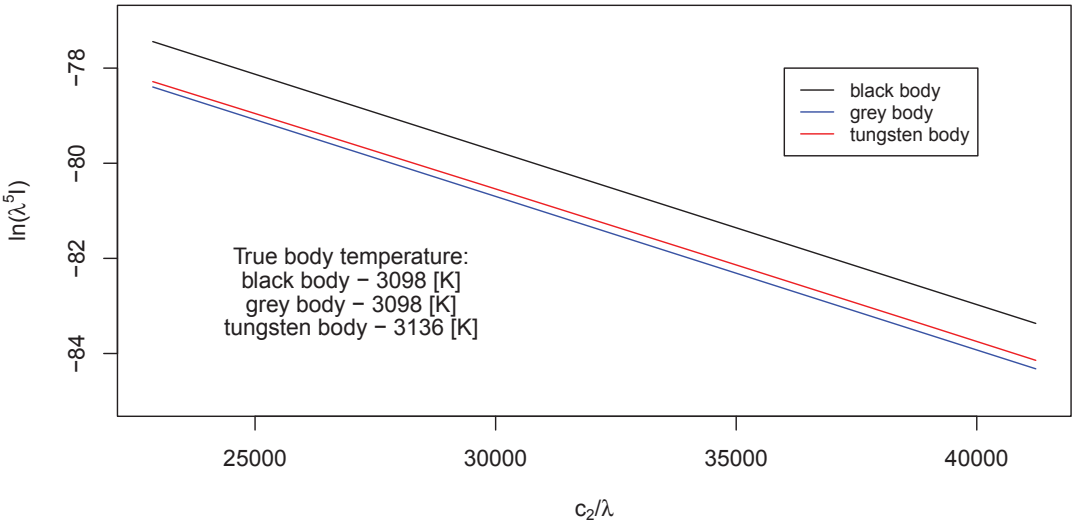

Figure 4.15: Temperature calculations based on spectral pyrometry method

The tungsten body's true temperature calculations were validated against black body calculations for a range of 2000K to 3400K. The resulting difference between calculated and model tungsten true body temperatures are shown in Figure 4.16. True body temperature calculations are based on spectral pyrometry method for a range of 2000K to 3400K. Colour temperature calculations are based on best fit of the black body model to the observed results.

As is shown in Figure 4.16 the difference between the expected and calculated true tungsten body temperature increases slightly ($\approx 0.43\%/1000K$) with the increase of the body temperature. The lamp's colour temperature varies in a range of 2760K-3300K. These measurements are in close accordance with data published by Stock[90].

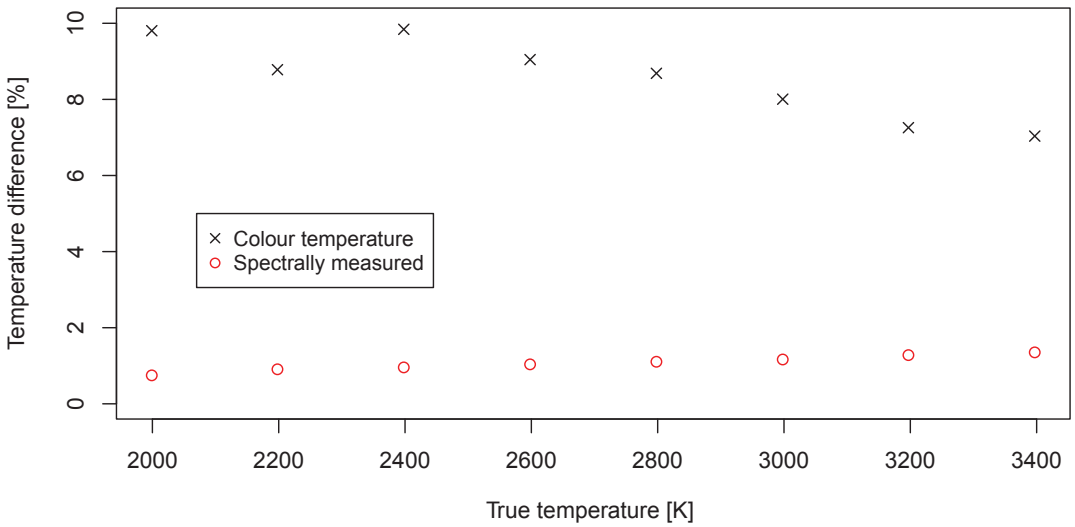

Figure 4.16: Differences between true body temperature, colour body temperature and spectrally measured body temperature

Tungsten resistivity is a function of temperature. Given that the filament's true temperature is constant, resistivity of filaments should be the same regardless of manufacturer. Any differences in filament resistance should therefore be caused only by the filament geometry and the resistance of power leads. Under operational conditions, resistance of the leads is much lower than the resistance of the filament. Leads remain at much lower temperatures, they are significantly shorter and thicker than the filament wire. Moreover the observed shape of the leads was very similar across the whole range of investigated lamps. Therefore the impact of leads on the observed lamp resistance is minor. Figure 4.17 presents variations of the filament resistance as a function of the measured true filament temperature and the filament shape.

As shown in Figure 4.17, resistance of the filament across the investigated temperature range agreed well with modelled resistivity of tungsten scaled by a proportionality factor. A proportionality factor ranging from 0.45 to 1.35 reflects variations of the resistance between different lamp makes. The resistance of the observed filaments varied by less than 10%. Only the resistance of the filament of the Platinum lamp differed significantly from the rest.

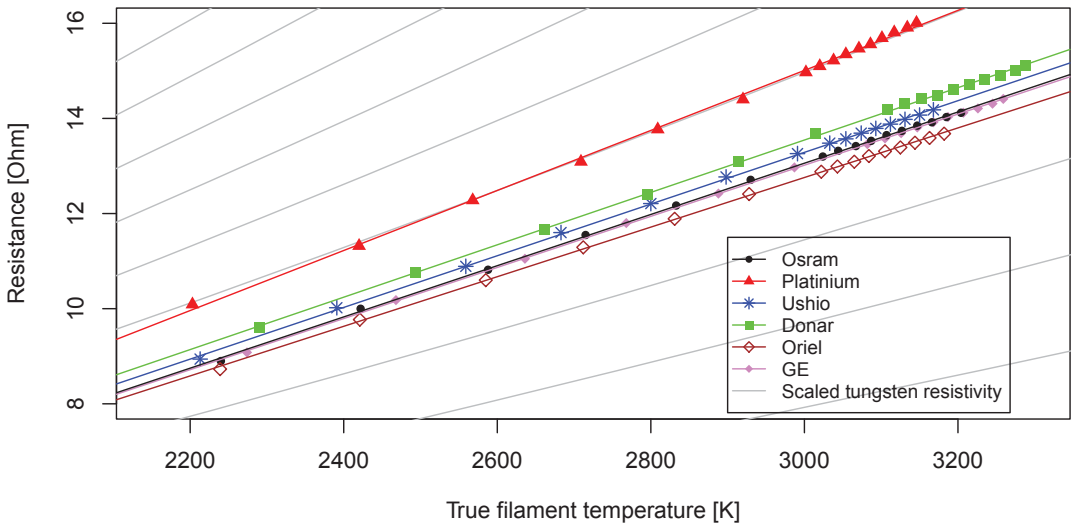

Figure 4.17: Resistance of the filament as a function of filament temperature. Set of curves showing tungsten resistivity curve scaled by multiplicative factor was shown as a reference. A proportionality factor ranging from 0.45 to 1.35 reflects variations of the resistance between different lamp makes

Accordingly to the Stefan-Boltzmann law, the density of a power emitted by a black body is proportional to the fourth power of the black body temperature. The relationship between electric power delivered to the lamp and fourth power of the filament's true temperature was investigated. The results are shown in Figure 4.18.

As is shown in Figure 4.18, the fourth power of the filament's temperature is linear to the delivered electric power. Using this relation is a simple way of controlling filament temperature. This can be achieved only if delivered electric power, filament temperature and typical characteristics of a standard lamp are known. If in addition the active area of the filament is known, an absolute radiant power emitted by the filament can be calculated. It is worth noting that Osram and Oriel spectral irradiance standard characteristics are almost identical. This is due to the fact that Oriel uses Osram lamps to build their standard lamps. This relation can also be clearly seen when normalised spectral characteristics of the lamps are compared (see 4.19).

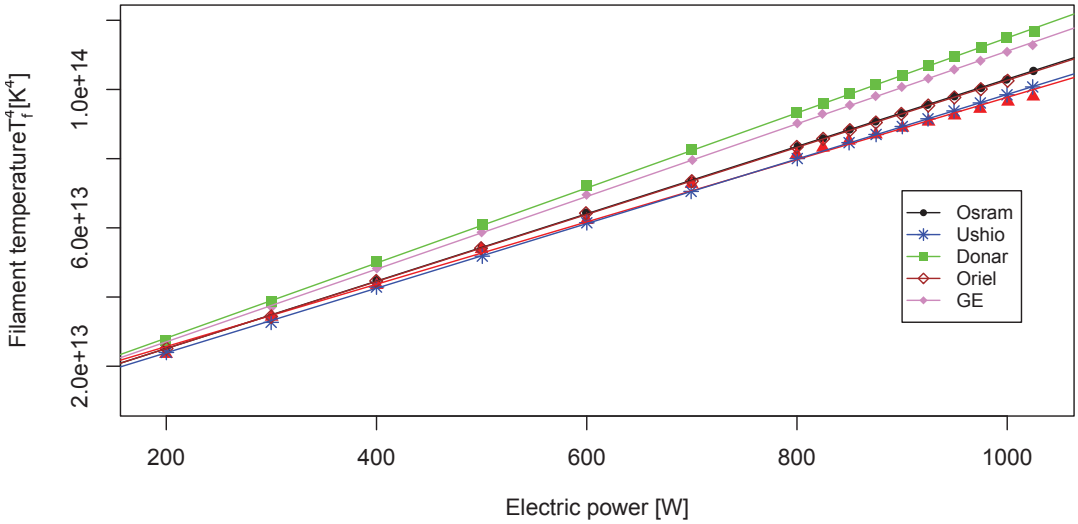

Figure 4.18: Filament temperature as a function of supplied electric power

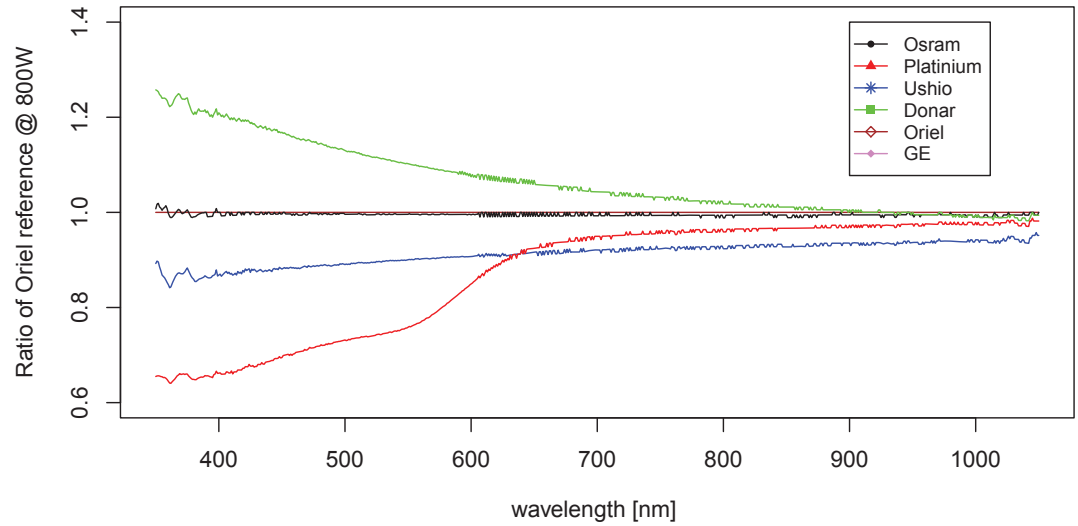

Figure 4.19: Normalised spectral characteristic of investigated lamps at a supplied electric power of 800W

Figure 4.19 confirms the variations in lamp temperatures observed in Figure 4.18. Lamps whose filaments reached higher working temperatures (Donar, GE) presented increased radiation in the range of shorter wavelengths. Accordingly lamps that were working at lower temperatures (Ushio, Platinum) present slight

decreases in radiation within a range of short wavelengths. Characteristics of Osram and Oriel spectral irradiance standards differ the least across the inspected 350nm-1050nm ranges. In addition, the Platinum lamp has a lower than average emission between 350nm-650nm due to envelope coloration.

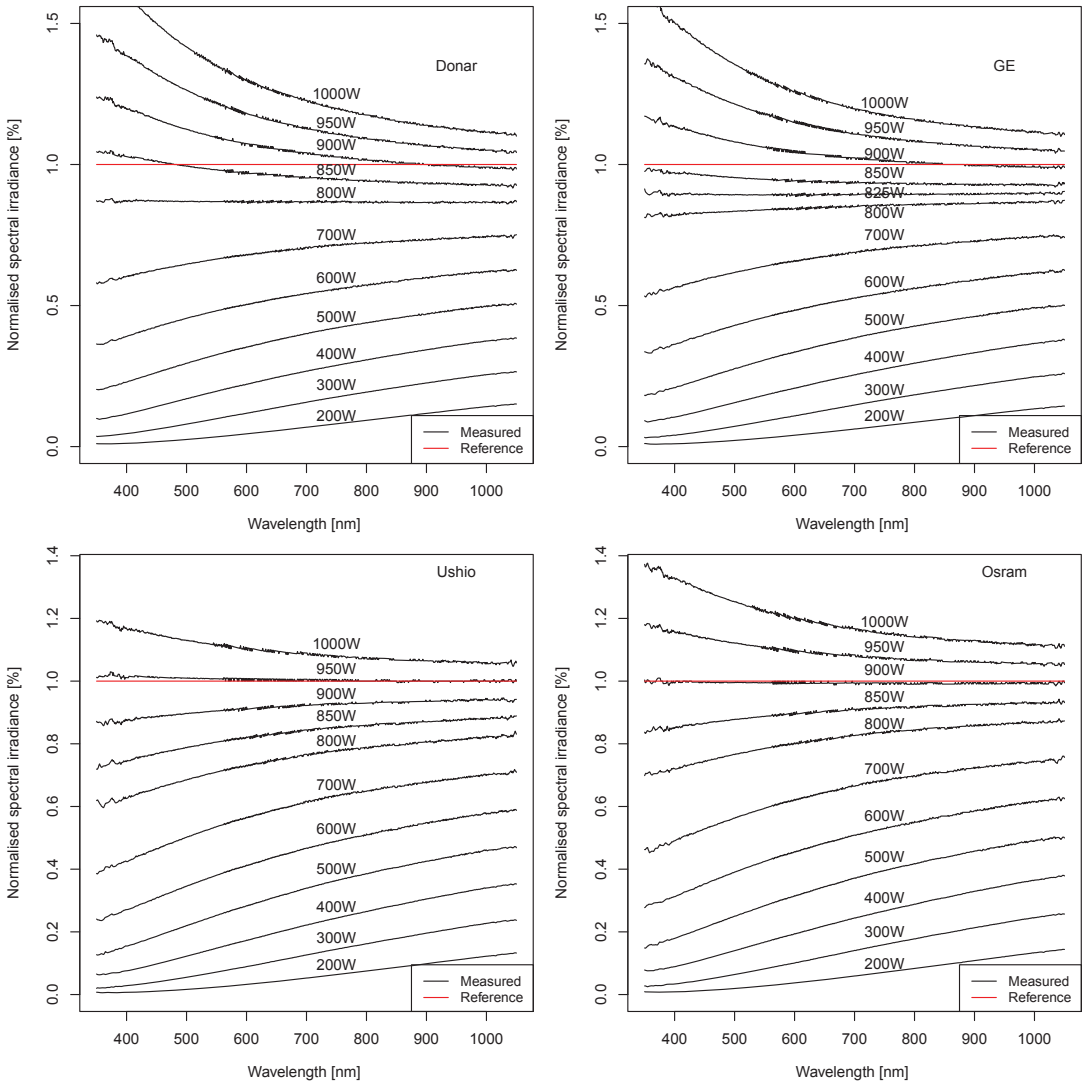

Figure 4.20: Normalised spectral characteristic of investigated lamps under supplied electric power ranging from 200W to 1000W

Figures 4.19 and 4.20 prove that variations in the spectral characteristics of different lamps working at comparable temperatures do not differ significantly and can be closely matched by an appropriate adjustment of power supplied to the lamp. Table 4.1 presents electric power, voltage, current and resistance of the lamps at the spectral equilibrium.

Table 4.1: Electrical parameters of investigated lamps in spectral equilibrium

Manufacturer	Power [W]	U [V]	I [A]	Resistance [Ohm]
Oriel	900	109.7	8.20	13.34
Osram	≈900	≈110.8	≈8.12	≈13.65
Ushio	≈940	≈113.7	≈8.27	≈13.75
GE	≈810	≈105.1	≈7.71	≈13.63
Donar	≈795	≈105.9	≈7.51	≈14.10

Reaching spectral equilibrium required diametrically different electric power to be delivered to the lamps. Given that, at the spectral equilibrium temperatures of lamps equalise, the density of radiated power should be the same across the lamp types. In Figure 4.20 it is clearly visible that Donar and GE lamps, when balanced against the spectrum, emit much less radiant power than the reference Oriel spectral irradiance standard. In contrast, once spectrally matched, Ushio and Osram lamps presented very similar magnitude of the absolute spectral radiant power when compared to the Oriel reference lamp. Variation of the absolute radiant power between investigated lamps can only be explained by differences in filament shape and the effective active area of filaments.

4.2.3.3 Impact of the filament shape

As was discussed in section 4.2.2.1, the radiant flux emitted from the lamp is a function of lamp design and the operational parameters it is working at. The initial hypothesis in this chapter is that there is no significant variation in filament shape between various manufacturers. This turned out not to be the case. To reveal differences in filament shapes and their active areas, each lamp was photographed from eight angles while powered up. Figure 4.21 presents photographic comparisons of filament shapes seen from the direction normally used for calibration (side 5).

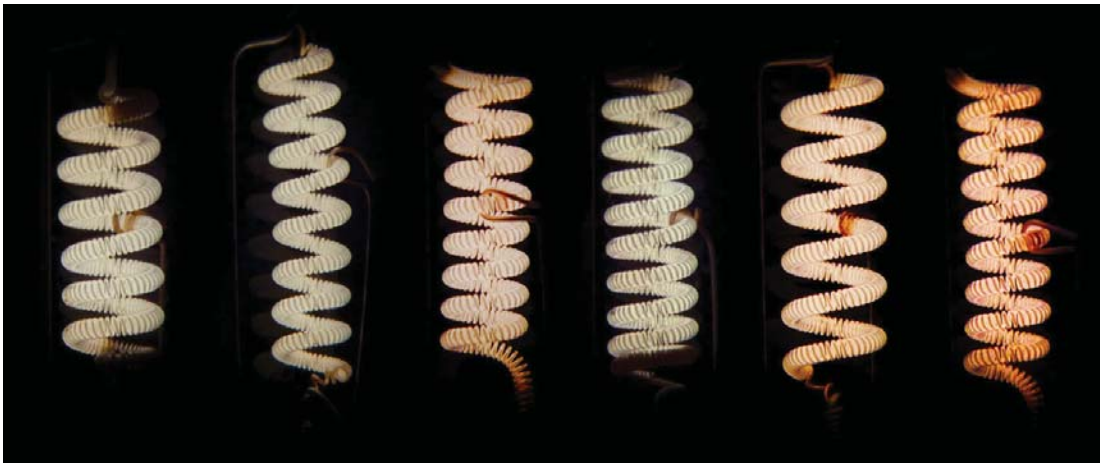

Figure 4.21: Comparison of filament shapes and observed colours under operation under current of 8.2A. From left to right: GE, Donar, Osram, Platinum, Ushio, Oriel (reference calibrated Osram lamp)

As can be observed in Figure 4.21, filaments differ in term of count of coils and coil diameter. Regardless of that, all manufactures use the same CC8 filament type code. It should be noticed that there is a difference in filament colour. This again proves variations between filament temperatures. Additionally the colour of the Platinum lamp filament has been affected by pink coloration of an envelope. Osram and Oriel filaments presented very close relations in term of filament shape.

Measurements of the apparent active area of filaments were based on analysis of photographs. First an appropriate magnification scale was applied. Next, based on brightness criterion, pixels were classified for those that belong to the active filament area and for those that do not. However the calculated apparent active area of the filament dis not correspond with filament true area seen from the camera perspective. The apparent active area of the filament corresponds to the filament image. Figure 4.22 presents comparison between filament active areas.

As was shown in Figure 4.22 the active area of the filament varies significantly from one lamp to another as well as in relation to the direction of observation. These variations are related to the manufacturer specific construction of the filament and the filament support. Osram and Oriel spectral irradiance standards

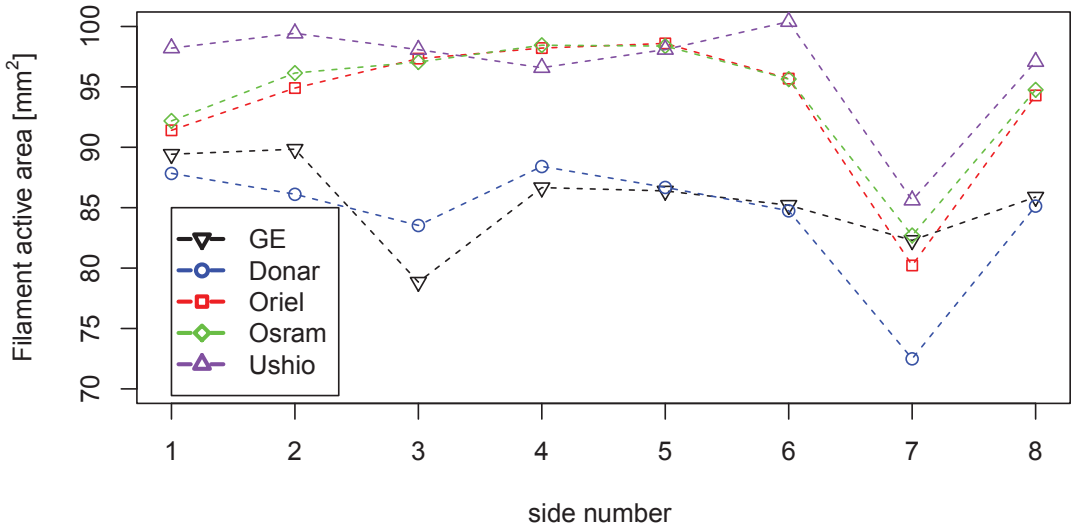

Figure 4.22: Comparison of apparent active filament area for five FEL lamps. Measurements taken from eight sides spread evenly around the lamp filament

present small differences in active filament shape, especially for sides 3 to 6. Small variations in active filament area, observed for lamps made by the same manufacturer, indicate that the radiant flux of these lamps is going to vary marginally.

In the previous section, it was shown that the absolute electric power required to reach spectral equilibrium of emitted irradiances differed significantly. At spectral equilibrium (same filaments temperatures), the radiation density for various filaments equalises. Therefore the total radiant power emitted by the filament only depends on the filament apparent active area. Variations of filament areas shown in Figure 4.22 correlate strongly with the absolute radiant power emitted by filaments. Apparent active filament areas were used to correct the total radiant power output of tested lamps. Figure 4.23 shows the normalised spectral characteristics of tested lamps after the application of apparent active filament area corrections.

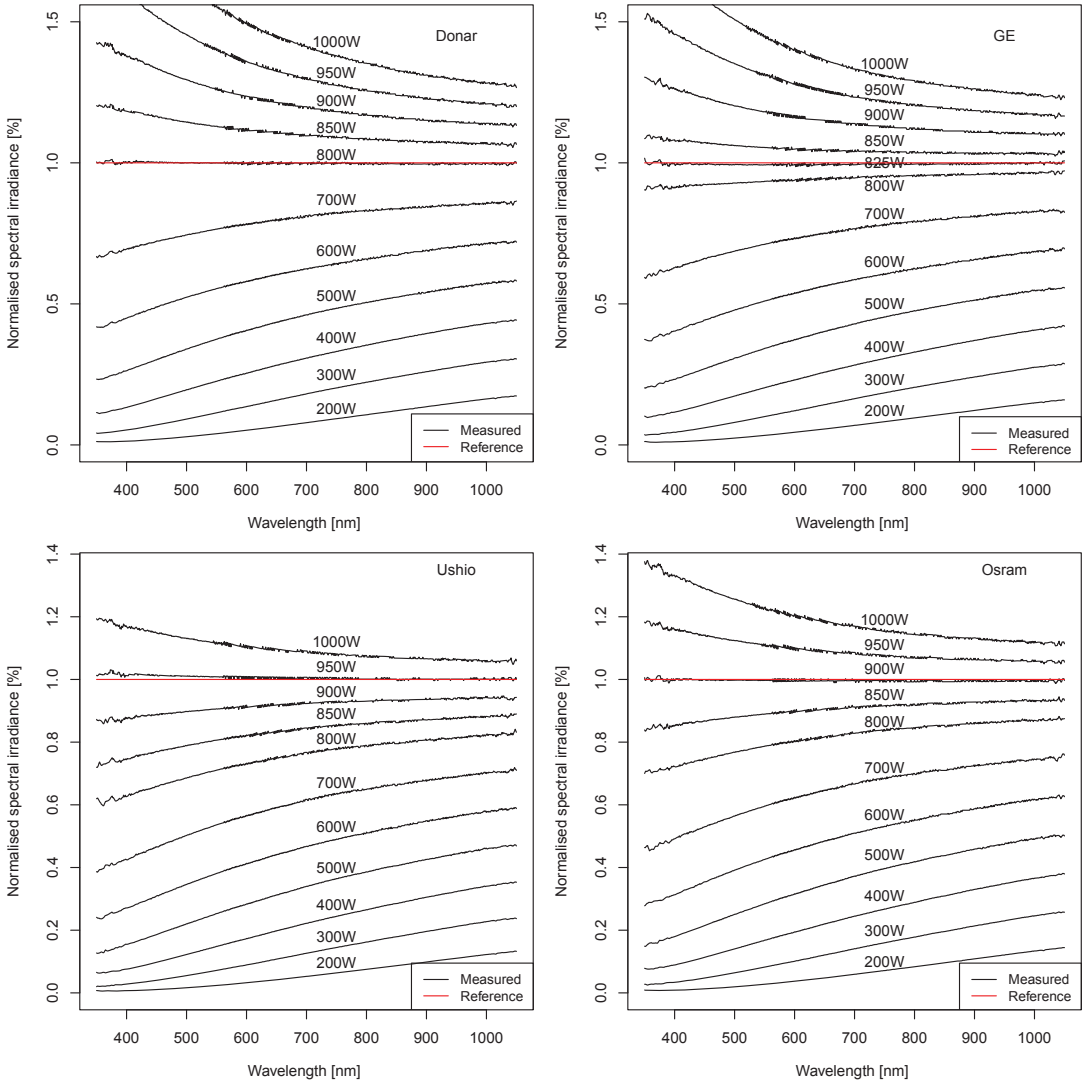

Figure 4.23: Normalised spectral characteristic of investigated lamps under supplied electric power ranging from 200W to 1000W after application of filament area correction coefficients.

4.2.4 Simplified FEL lamp calibration validation method

The results presented in the previous sections of this chapter referred to a typical NIST lamp. It was shown that the filament apparent active area and filament temperature are two parameters directly related to quality and quantity of emitted radiant power. To accurately measure the temperature of the filament, via the spectral pyrometry method, a calibrated spectroradiometer is required. To overcome this requirement, the author suggests the use of two narrowband measurements as a calibration validation tool. A schematic of this concept is shown in Figure 4.24.

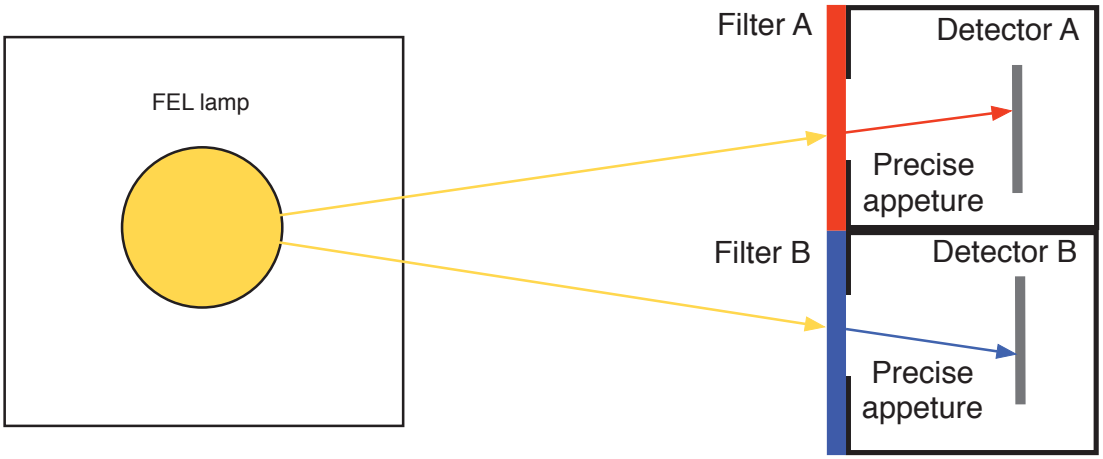

Figure 4.24: Two-point calibration validation of the reference FEL lamp with use of two narrowband detectors

.

The calibration validation method presented in Figure 4.24 utilises two filtered detectors. Interference filters are characterised by maxima located at 450nm and 800nm and the full width half maximum of 10nm. To standardise the proposed technique the detectors should have the same sensitivity at both used wavelengths. Such detectors are easily available. The ratio between irradiance at 450nm and 800nm stays in functional relation to the filament temperature as shown in Figure 4.25

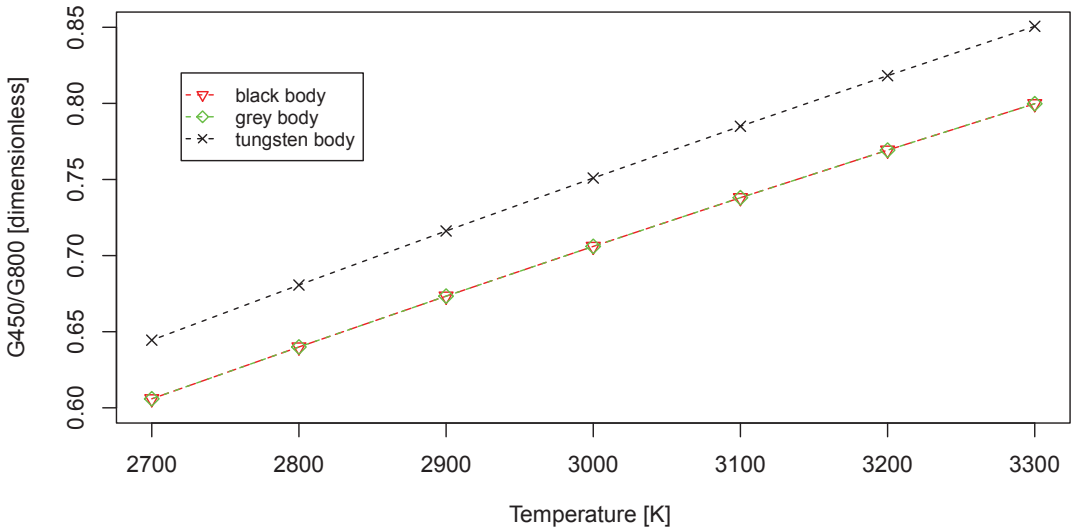

Figure 4.25: Dependency between a true filament temperature and the ratio of narrowband irradiance at 450nm and 800nm

.

With this very simple technique the temperature of the filament can be repetitively set to its required value and actively stabilised at this point. In the proposed solution, feedback from the detectors is used to actively stabilise filament temperature by controlling the power source. The intensity of emitted radiation depends on temperature, therefore overall stability of the radiant output of the lamp is improved. Because of the fact that the control signal is a ratio of two narrowband irradiances, the position of the detectors in relation to the monitored lamp does not impact on the accuracy of the measurement. The combination of the proposed filament temperature control method with typical characteristics of a FEL lamp at the known temperature gives a simple, reliable and cost effective way of providing a spectral irradiance calibration.

4.3 Conclusions

The physical model of the most commonly used working standard of spectral irradiance (FEL lamp) has not been defined so far. Moreover the FEL lamp based standard of spectral irradiance does not implement any control measures to validate the stability of standard operation. This situation increases the level of uncertainty in the spectral irradiance measurements.

Significant differences ranging from -20% to 15% between the stated absolute spectral irradiances of calibrated FEL lamps were observed for different manufacturers. These observed differences do not imply poor quality of lamp calibration (compared lamps were working under different electrical conditions). It needs to be stressed, however, that the existence of a situation in which spectral irradiance emitted by two standard FEL lamps significantly differs should not be acceptable.

Electric current values ranging from 7.9A to 8.2A were found as the most common operating conditions for the standard lamps produced by different manufacturers. This can be explained by the fact that the lamp structure differs from one manufacturer to another. Nevertheless, the previously discussed difference between calibrations stated on the certificates of the various lamps suggests that they must have been operated under various filament temperatures. This suggests that the utilisation of a stabilised current source does not seem to be the best possible way of controlling operational conditions for the spectral standard lamp. This method may lead to significant errors in laboratory practice and may promote excessive bulb degradation during its stated lifetime. Variations of the lamp structure may remain unnoticed while having an impact on the spectral characteristics of the emitted radiation.

It has been confirmed that the initial ageing of the lamp has a significant impact on the lamp's output. Moreover, the character of the output variations depends on the temperature the lamp is aged at. During the first 5h of ageing the output of all lamps gradually increased. After this time Osram and Ushio lamps reached 98.5% and 99% of their final (observed after 96h) output and were continuously increasing their output during the remaining time of the test. GE lamp stabilised the quickest, reaching 99.9% of its final output after only 5h of ageing. Donar lamps reached 101% of their final output after 5h of ageing. During

the final 30h of a long-term stability test Ushio, Osram-Sylvania, GE and Donar lamps presented levels of stability better than 0.017%/h.

Filament true temperature measurements based on spectral pyrometry principal yielded good accuracy. The true temperature of a tungsten body calculated from its spectral irradiance, with use of the spectral pyrometry method, agreed with the expected value within the margin of 1.2%.

The undertaken experiment confirms that the spectral characteristics of the lamps do not differ significantly between various manufacturers as long as an excessive degradation of the lamp is not observed. The operating temperature of the filament should be used as a parameter, which defines operational conditions of the standard lamp, instead of the current. This would allow for better unification of the spectral irradiance standard lamp characteristics between different manufacturers.

Spectral emissivity of filaments has been found closely comparable across different lamp makes. Therefore if the filaments are kept in the same temperature, the spectrum as well as density of the emitted radiation matches up closely. The apparent area of a filament can then be used as a factor which defines absolute magnitude of radiant power emitted from the lamp. Variation of the filament active area observed between different lamp makes ranged from -2% to -13% from the Oriel reference lamp. Significant active filament area variations of up to 20% were observed depending on the orientation of the filament.

This research shows that the spectral characteristic of a FEL lamp can be predicted from the lamp's basic physical properties, with an uncertainty not exceeding 5% from the traceable spectral irradiance standard lamp. This approach can therefore be used to characterise FEL bulb in the case where traceability is not required, traceable standard of spectral irradiance is not available or as an additional validation measure of the lamp calibration. Simple narrowband measurements were proposed as a technique for controlling and stabilising filament temperature.

Chapter 5

Variability of measured spectral irradiance

5.1 Introduction

This chapter presents the results of investigations undertaken in the field of spectral solar irradiance variability. Differences between spectral irradiances observed during the time of the experiment undertaken , modelled by SMARTS and defined in AM1.5 standard are discussed. The results presented are based on measurements of spectral irradiance taken over the period of four years. The availability of similar observations is very limited. There are no other sources of similar measurements available for the landmass of the UK that are known to the author. A differentiation in materials and manufacturing technologies of commercially available photovoltaic devices raises questions about the significance of spectral effects on the cumulative and instantaneous energy production of photovoltaic systems. The UK has a maritime climate, which is characterised by frequent cloud cover and high humidity. It is of great importance to recognise to what extent the accuracy of photovoltaic system monitoring can be affected by not considering ongoing spectral effects in the atmosphere, especially under cloudy sky conditions. The presence of spectral effects has been widely discussed [91–94] but no comprehensive long-term measurements were taken to resolve this debate. A metrological campaign and subsequent investigation provide a statistical anal-

ysis of spectral irradiance in this maritime climate and discusses its impact in terms of photovoltaic systems applications.

This chapter focuses on the statistical representation of the magnitude and character of spectral irradiance variations in a maritime climate. Firstly, the experimental setup designed and implemented to gather spectral irradiance data is presented. Secondly, data quality assessment methods are presented. In the results section, long-term spectral irradiance averages measured in two incident planes, are discussed and compared with the standard AM1.5 spectrum and SMARTS modelled yearly averaged irradiance. Comparison between broadband irradiance calculated from spectral measurements and potential electric current for the measured photon flux is discussed. Finally, variations of the spectral irradiance are investigated in the context of variability of specific atmospheric conditions: clearness index and air mass index.

5.2 Methods

5.2.1 Irradiance measurements

For the purpose of this work a dedicated meteorological station with state-of-the-art irradiance measurement devices was designed and implemented. The station is equipped with spectroradiometers and pyranometers capable of measuring a hemispherical solar irradiance. Two visible-near infrared (VIS-NIR) EKO MS-700 grating spectroradiometers, two Kipp&Zonen CMP11 broadband pyranometers and two Kipp&Zonen CV2 pyranometer ventilation units were deployed. Radiometers were installed in two different planes on the top of the roof of the School of Electronic, Electrical and Systems Engineering, Loughborough University. The first spectroradiometer was installed in a horizontal plane, the second one in an inclined plane (inclination angle of 45°). Both spectroradiometers were configured to measure hemispherical irradiance (viewing angle of 180°). Two CMP11 pyranometers were installed in the respective planes for a broadband irradiance reference. Data have been continuously logged since 20/10/2009. Figure 5.1 presents the setup for the reference irradiance measurements.

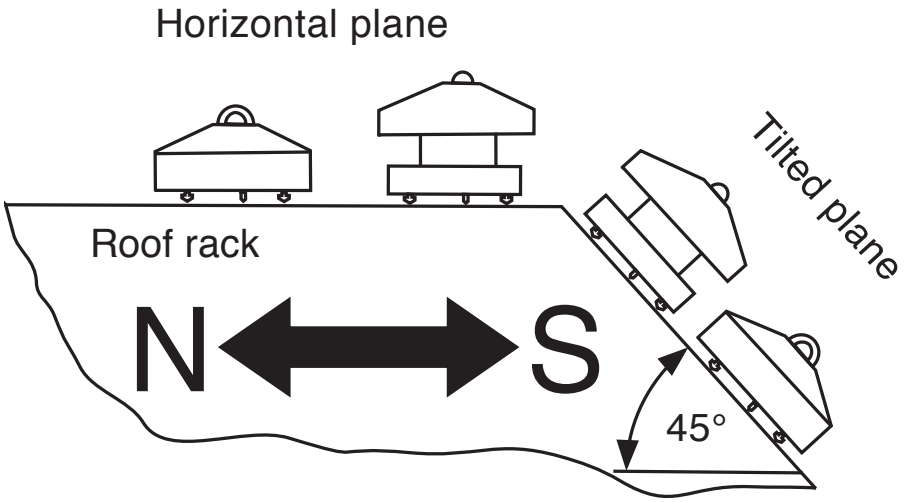

Figure 5.1: The irradiance measurements diagram

5.2.2 Data acquisition

Signals from the two CMP11 pyranometers are logged by a CR1000 data-logger. The data-logger settings were adjusted to minimise an impact of signal degrading factors. 50Hz AC electromagnetic interference was rejected by setting the subsampling interval to 25ms. The logger analog input amplifier offsets were minimised by the use of reverse measurement mode. A differential measurement mode was used to improve a noise rejection. These precautions are essential to achieve high quality measurements as the pyranometer output rarely exceeds a level of 10mV, therefore the generated signal is prone to the impact of environmental electromagnetic interference (EMI). The spectroradiometers contain an embedded analog signal-processing unit therefore no additional digitising data logger is needed to obtain measurement data. The EKO MS700 spectroradiometers communicate over RS232 interface and are connected to an RS232 TCP/IP gateway. Data were logged over the university network on a remote server at one-minute intervals. The data logging was controlled by a dedicated LabView application, written specifically for this research. Further details of the metrological setup can be found in Appendix B and Appendix C.

5.2.3 Data quality assessment

Data used in the following analysis were logged between 20/10/2009 and 31/12/2013. Before and during this period of time the author undertook additional metrological exercises to assess the quality of the collected data. The most important and the most problematic task was to establish correct calibration of the spectroradiometers. Calibration procedures were discuses in Chapter 3. The data collection was occasionally affected by the spectroradiometer downtime due to recalibration, modifications of the logging system, problems with a network communication and servicing of the logging computer. For this reason, data availability was first studied to ensure that collected datasets are statistically representative and are not biased by periods of limited data availability. Figure 5.2 shows the monthly averaged availability of spectral data during the whole period of observations.

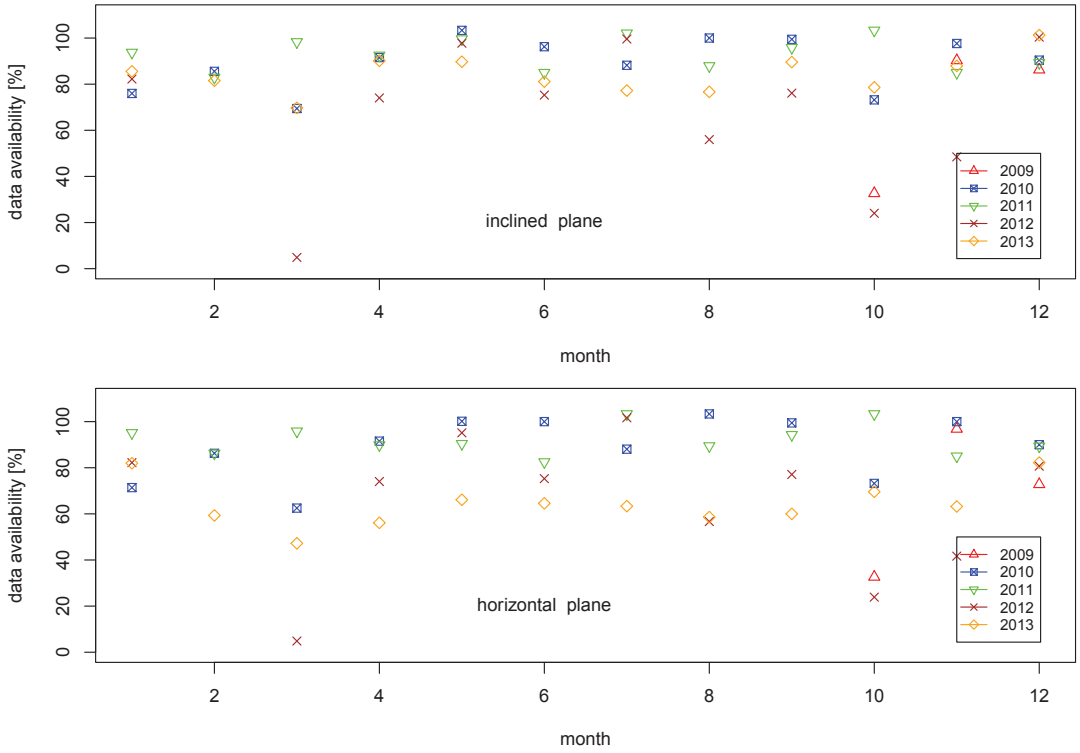

Figure 5.2: Spectral data availability by month

Separate availability values are marked for every month of observations. As it can be seen in Figure 5.2 for the most of the months average data availability was varying in the range of 80% to 100%. This range assures that calculations based on the dataset will not be biased by excessive data loss, and that the results derived from the undertaken analysis are statistically valid.

Monthly averaged data availability was mainly affected by continuous data losses due to system maintenance downtime (e.g. inclined plane observations during period of February and March 2012 were affected by exporting the spectroradiometer for recalibration, October 2012 by in-house recalibration). It has to be noted that even for these periods a fair amount of data for analysis was collected during other years. Over four years of observations, no calendar month was affected by data loss to the extent, which would invalidate statistical representativeness of observations.

Every hour, the data logging system should collect sixty spectral curves per spectroradiometer. It was observed that, while operational, the system was not always able to record every minute. The statistical significance of this is presented in Figure 5.3.

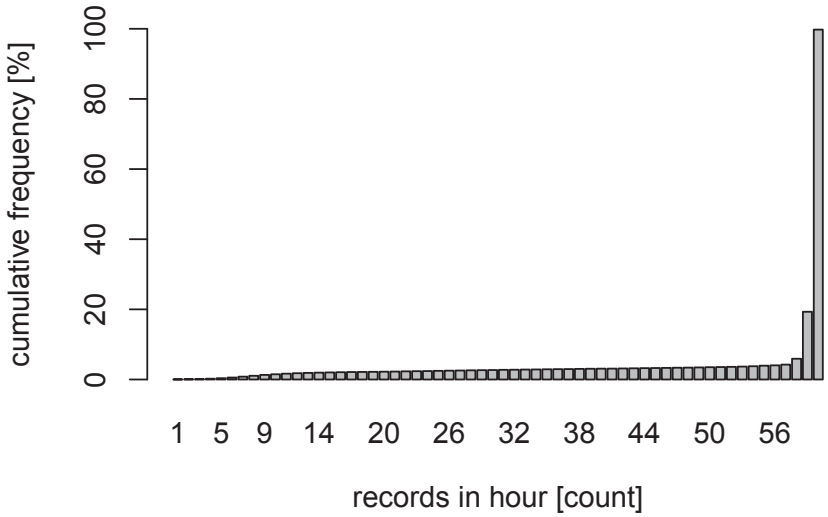

Figure 5.3: Cumulative frequency distribution of spectral data availability within each hour

Figure 5.3 shows the cumulative probability of the count of spectral curves

recorded per hour. It can be seen that for 94% of the time when the system was running, data availability was in the range of 97%. To use data in the most effective way, hours with availability greater than 50% were not deleted from the dataset. Instead, an hourly data availability weighting factor was assigned, varied from 0.5 for 50% of samples to 1 for 100% samples per hour. The hours of measurements where data availability was lower than 50% were rejected as not representative.

5.2.4 Equipment quality assessment

Spectroradiometer and pyranometer measurements were calibrated according to the methodology described in Chapter 3 to guarantee a high quality results.

At the beginning of the outdoor metrological campaign, all of the spectroradiometers were installed in the same horizontal plane and logged for a period of fourteen days. This allowed for an additional cross-comparison of results before and after application of calibration coefficients. At this stage, seven spectroradiometers in total were compared[1]. The relative deviation of spectral irradiance from the mean spectral irradiance measured was calculated for each spectroradiometer. The results are presented in Figure 5.4.

The results presented in figure 5.4 are based on irradiance measurements before application of corrective calibration coefficients.

After application of an initial indoor calibration correction to the results of this inter-comparison, the spectroradiometers differed by less than 1% over the full wavelength range. This proves high repeatability of an indoor calibration procedure applied to the spectroradiometers prior to the outdoor campaign. The differences in calibration between spectroradiometers before recalibration was up to 5%. Interestingly, the highest differences were observed in the range 700-950nm. In this region, the sensitivity of the silicon array detector used to build spectroradiometers is high and should not cause such problems. The author suspected that the reason for such significant differences lies in poor repeatability of the calibration process used by the manufacturer. The likelihood is that the

[1]The remaining five spectroradiometers were planned to be used in different locations around Europe and the USA. Due to premature cancelation of the project, data from these sites could not be obtained.

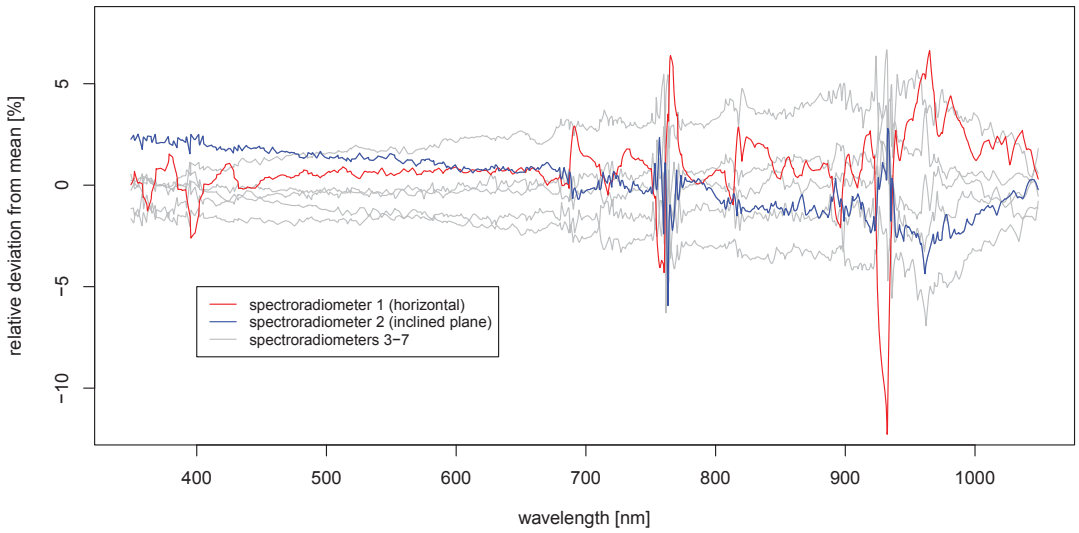

Figure 5.4: Relative averaged deviation of the spectroradiometers from the mean.

manufacturer used outdoor methods to achieve calibration as the most significant errors in calibration were observed in regions of water molecular absorption. These results once again demonstrate that the lack of standards applicable to spectroradiometer calibration brings a significant amount of uncertainty to the calibration of the equipment.

5.2.5 Data analysis

Similar observations have been carried in the past only in a very limited number of cases, especially in the UK. For this reason, the dataset recorded here is especially valuable for better understanding and assessment of spectral irradiance variations under realistic sky conditions. It can be argued that a period of four years of observations is not sufficiently long to draw definitive conclusions about long-term spectral irradiance variations. Nevertheless, the dataset recorded during this work is the longest continuous terrestrial measurement campaign to date and can be successfully used for a short and middle term analysis. Figure 5.5 presents a schematic layout of the data processing and analysis process used for the preparation of the results.

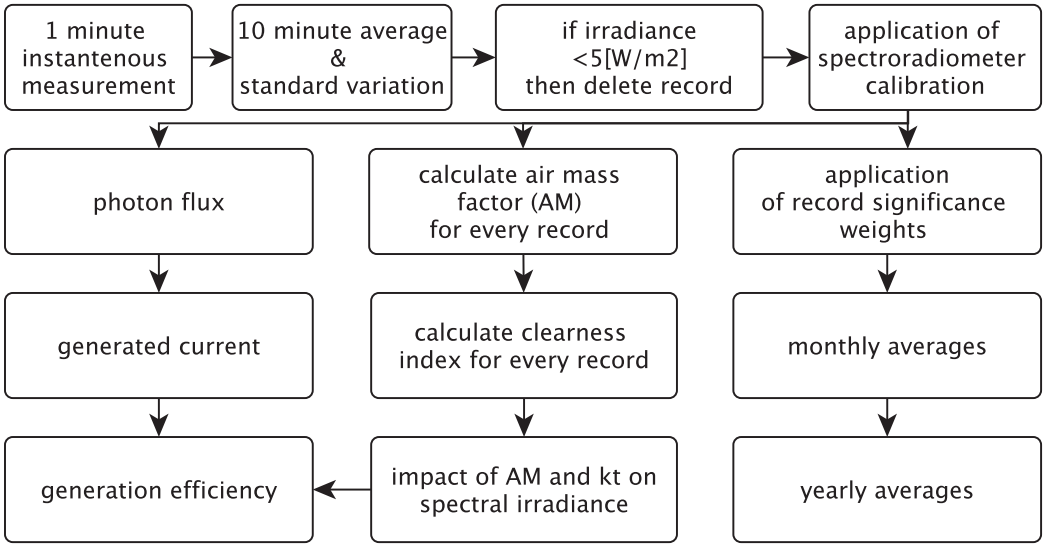

Figure 5.5: Data analysis diagram

Due to the large size of the dataset and the nature of the investigation, an optimised database for online analytical data processing (OLAP) was developed and implemented. Handling multi-gigabyte metrological datasets is not a trivial task, therefore it required a significant effort to undertake additional research in the field of data warehousing, database design and database performance tuning. Data were systematically imported into the database with use of purpose-written ETL (extract transform load) software. Dedicated SQL[1] queries were used to apply the calibrations and to validate, aggregate, and classify the data. Use of the database simplified the data processing, allowing investigation of relations between measured parameters to the great extent. Use of a database system proved itself useful as a research tool. Since it is not the main objective of this chapter, further details with regards to implementation of the database infrastructure are not discussed in further detail.

To characterise the impact of spectral variations of an incident irradiance on a specific photovoltaic device, a "spectral efficiency of generation" (η_G) is defined here. The value of η_G is calculated as the ratio of the number of carriers

[1]SQL - Structured Query Language

which would have been generated by a specific photovoltaic device under a given spectrum to the corresponding incident photon flux (see equation 5.1).

$$\eta_G = \frac{\int_{\lambda_1}^{\lambda_2} \phi_{e,\lambda} \cdot EQE_\lambda \mathrm{d}\lambda}{\int_{\lambda_1}^{\lambda_2} \phi_{e,\lambda} \mathrm{d}\lambda} \cdot 100\% \tag{5.1}$$

where:

$\phi_{e,\lambda}$ - spectral photon flux

EQE_λ- spectral external quantum efficiency of a photovoltaic device

The efficiency of generation under a given spectral irradiance can be calculated for a specific device technology in this way. The integral boundaries (λ_1, λ_2) should cover the range of non-zero spectral response of the device. Use of the whole broadband spectrum would lead to a situation where changes in spectral irradiance outside the spectral range of the device would impact generation efficiency, even when the actual generation processes in the device were unaltered. Figure 5.6 illustrates why such boundary selections should be made.

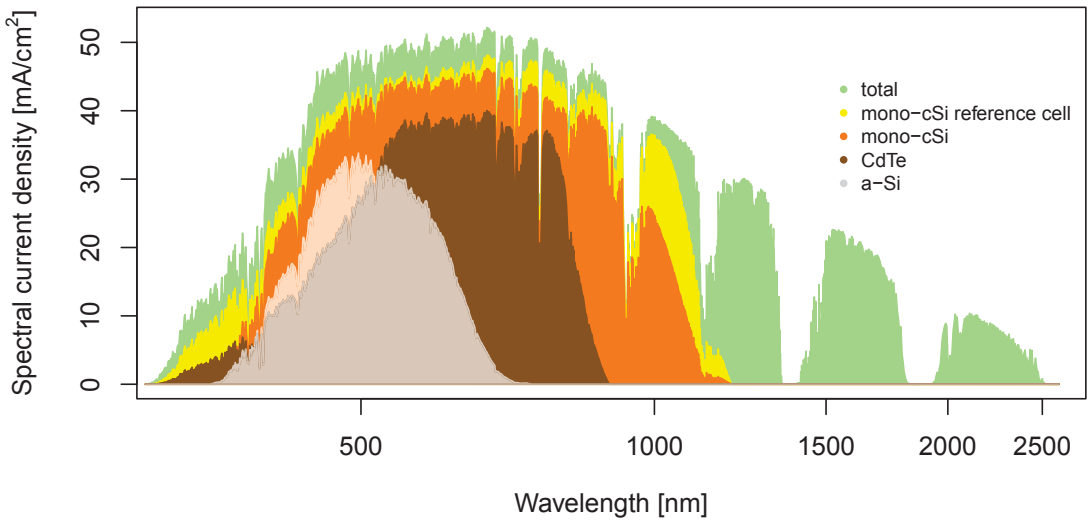

Figure 5.6: Potential of a broadband irradiance to generate electric current for various photovoltaic cell technologies for standard spectrum AM1.5. Spectral responses for presented modules according to ESTI (European Solar Test Installation)

A common method of expressing the impact of spectral variations of an incident irradiance on photovoltaic device is with the average photon energy (APE). In this work, application of APE has been intentionally avoided in favour of η_G.

5.2.6 Data classification

To investigate how specific atmospheric conditions affect spectral irradiance, recorded data were classified with three criteria:

- clearness index (k_t)
- standard deviation of irradiance (δE_e)
- air mass (AM)

The first criterion allows the selection of all data where clearness is within an expected value. This criterion on its own can lead to misinterpretation of results, as it can be fulfilled under different cloudiness scenarios. For example, rapidly passing clouds can create average value of clearness index similar to light but stable overcast conditions. While the solar disk remains unobstructed, the same clouds can increase the clearness index value above the clear sky case, by reflecting the direct irradiance towards the ground. For this reason, knowing the temporal variability of irradiance is necessary to prevent misinterpretation. The standard deviation of spectral irradiance cannot be used in isolation, as its value can be low under heavily overcast conditions as well as under clear sky conditions. Periods when the irradiance varies significantly should not be used for analysis, as the sky cloudiness condition is undefined. For this reason, data characterised by high variability were rejected. Table 5.1 presents the combination of criteria that must be fulfilled to indicate a specific state of the sky during a given hour of observation. Selected criteria and limits are based on the data observed during the measurement campaign and on modified classification methodology discussed in chapter 2.

The last classification criterion, the air mass factor, is more deterministic. It can be calculated from the time of day and year and from geographical coordinates of the location. Air mass scales the magnitude of spectral effects taking place in the atmosphere.

Table 5.1: Criteria for classification of the atmospheric conditions

		δE_e (10-minute)	
		<5%	>5%
k_T	<0.35	overcast at various AM	variable overcast
	>0.35	clear sky at various AM	(data rejected)

5.3 Results

5.3.1 Temporal spectral distribution of solar irradiance

To illustrate how the spectral irradiance characteristic varies over the year under clear sky conditions, the SMARTS model was used. To generate SMARTS data, dedicated software was developed (for more details please see Appendix D). A global spectral irradiance for the horizontal and inclined plane was generated in 10-minute intervals. The results of calculations were averaged on "per day of the year" basis. The results are shown in Figure 5.7. Similar simulations were repeated for direct and diffuse components of spectral irradiance. The results are shown in Figures 5.8 and 5.9.

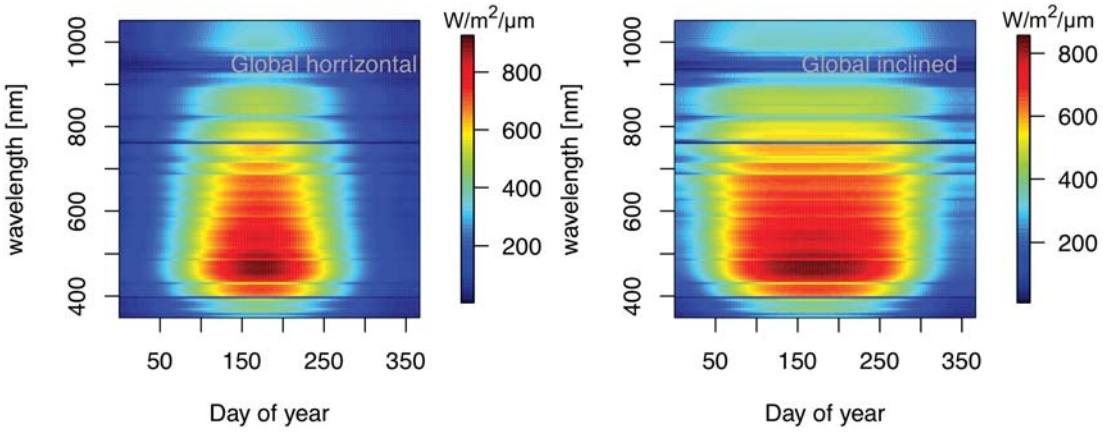

Figure 5.7: Spectral distribution of global irradiance for horizontal and inclined planes modelled with use of SMARTS

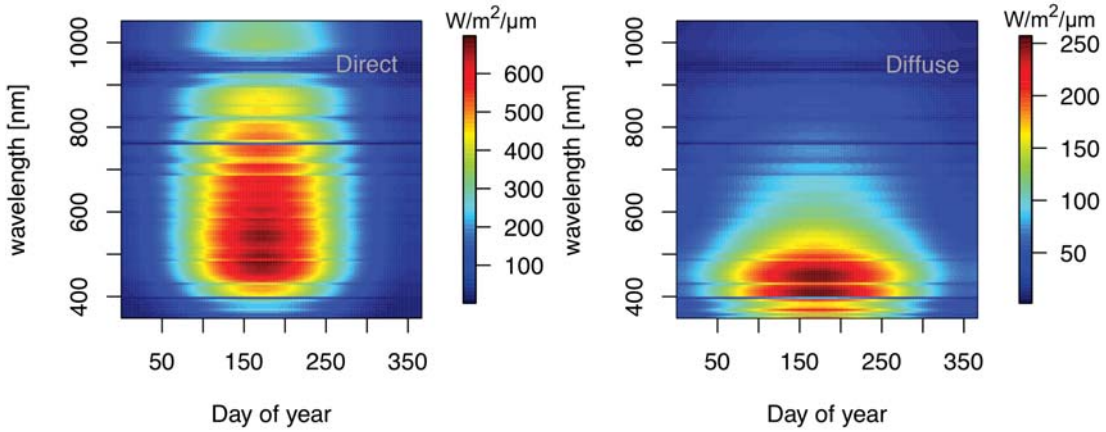

Figure 5.8: Spectral distribution of irradiance for horizontal plane modelled with use of SMARTS

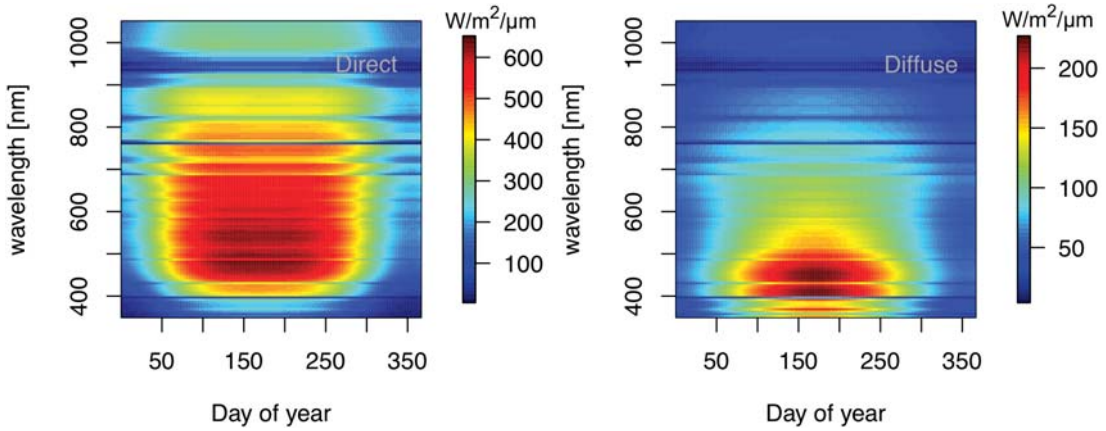

Figure 5.9: Spectral distribution of irradiance for 45° inclined plane modelled with use of SMARTS

The SMARTS simulations show how the spectral irradiance varies throughout the year in the horizontal and inclined planes under a clear sky scenario. In the natural environment clear sky conditions are not permanently observed. For this reason, data from four years of observations were averaged on a "per day of the year" basis. This way a yearly distribution of daily averaged spectral irradiance was created. Significant seasonal variations of solar daily irradiation and the impact of the clouds do not allow for clear observation of variations of spectral irradiance across a wide temporal perspective. This is especially trou-

blesome during autumn and winter months. For this reason daily averages were normalised. As previously, to remove year-to-year variations, solar spectral irradiance was at first averaged on the per day of the year basis. Then normalisation was applied, whereby the integral value of each of the spectral irradiance distributions was scaled to unity. Such normalisation allows for clearer visualisation of spectral irradiance variability across the year. Figures 5.10 and 5.11 show the solar spectral irradiance distribution variation over the average year.

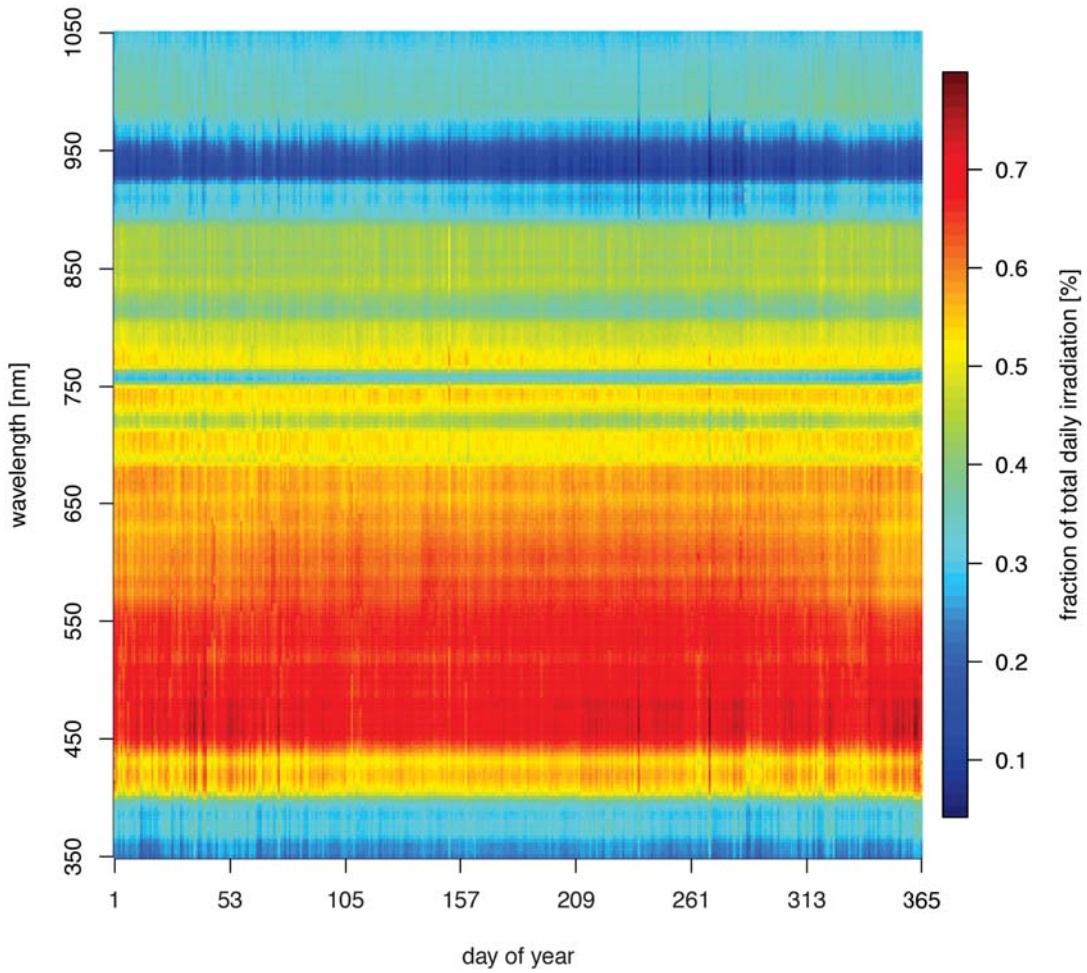

Figure 5.10: Yearly spectral distribution of normalised daily averaged irradiance across on horizontal plane.

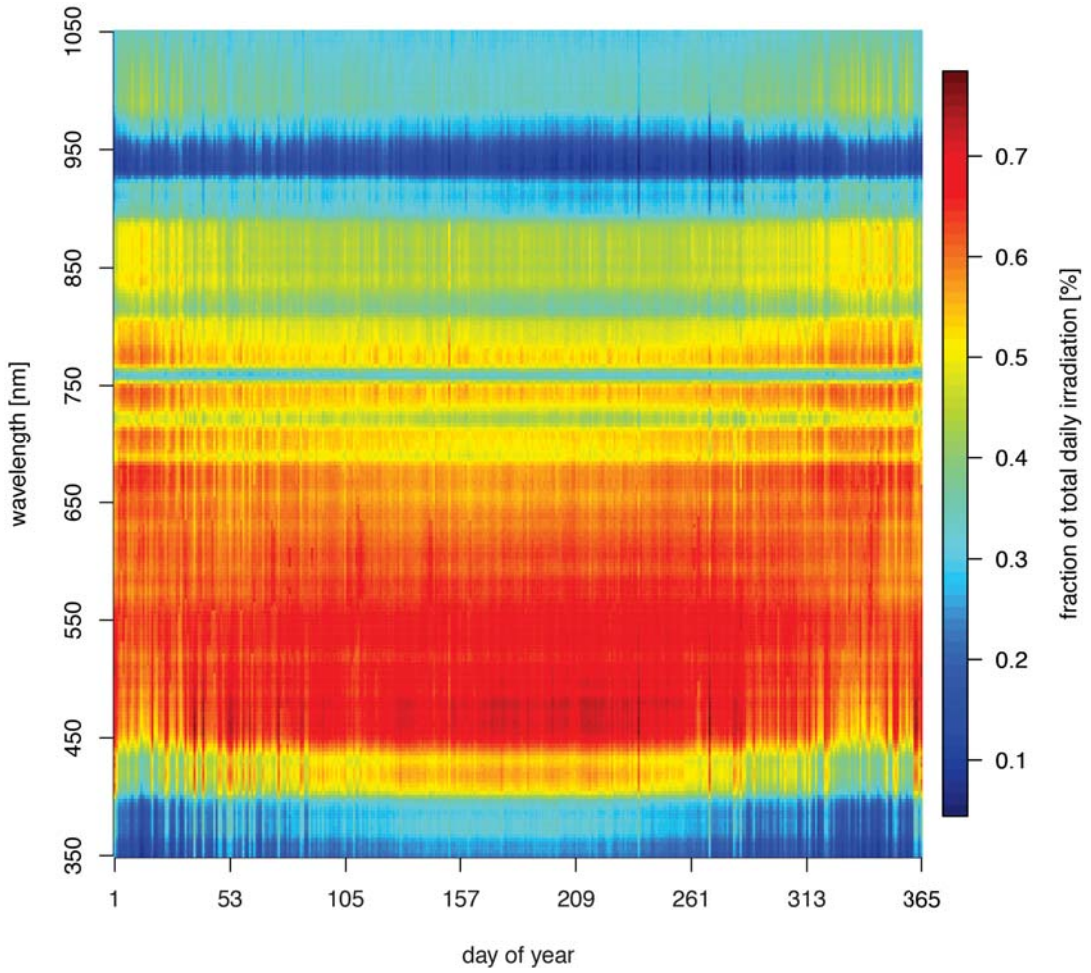

Figure 5.11: Yearly spectral distribution of normalised daily averaged irradiance across on inclined plane(45°).

In figure 5.11 it can be observed that the distribution of solar spectral irradiance on the inclined plane shifts towards longer wavelengths during autumn and winter months. The overall impact of these variations on the distribution of yearly spectral irradiation is reduced by the fact that the strong spectral variations coincide with times of relatively low absolute values of irradiance. From Figure 5.11 it can be seen that the distribution of spectral irradiance on the horizontal plane is almost stable across the year with some seasonal variations present in the range 550-650nm.

The inclined spectrum is affected the most in the winter and autumn months due to high air mass. A clear shift towards longer wavelengths in spectral distribution of irradiance can be observed. In the inclined plane the spectrum is dominated by the direct irradiance component, as a large part of the diffuse sky irradiance is excluded by the reduced view factor. This red shift is significantly reduced for horizontal spectral irradiance, which can be attributed to the counteracting impact of the diffuse irradiance. During the winter and autumn, the increasing value of air mass causes a shift in the direct spectral irradiance towards longer wavelengths, but the ratio between the diffuse and the direct irradiance increases. This happens due to the fact that the amount of direct irradiance is reduced by a steeper incident angle, while the diffuse fraction stays unaltered (the sky is still blue in the winter). As the diffuse irradiance spectrum is rich in short wavelengths, it cancels out air mass red shift. The cloud impact on spectral irradiance is studied further in this thesis.

5.3.2 Measured spectral irradiance vs. AM1.5 standard

The average spectral irradiance from all of the measurements collected during this campaign was calculated. The resulting long-term average allows for validation of the adequateness of the AM 1.5 spectrum, which is commonly used as a reference in photovoltaic performance standards. The standard AM1.5 spectrum is defined for a plane inclined at 37°. The measurements collected here were taken in a plane inclined at a 45° angle. To make the comparison valid, a synthetic spectrum was calculated for the horizontal and for the inclined (45°) planes by use of the SMARTS model. Besides the angle of incidence, all SMARTS parameters were set to the same values as defined for AM1.5 standard. The measured spectral irradiance was normalised against the calculated value of synthetic irradiance at 860nm. At this wavelength, the solar spectral irradiance is weakly affected by atmospheric constituents (region of atmospheric window). It should be noted here that the uncertainty of the absolute calibration of the spectroradiometer in the region of 860nm does not have any impact on the results of this inter-comparison. This is because all the channels of the spectroradiometer were calibrated with use of thermal light source, which has a continuous spectral char-

acteristic. Uncertainty of an absolute calibration is then dependant mainly on lamp calibration. Comparison between the observed, long-term, average spectral irradiance and the reference AM1.5 spectrum is presented in Figure 5.12.

It can be seen that the measured average horizontal spectral irradiance differs significantly from the modelled AM1.5 spectrum for wavelengths below 700nm. The observed differences increase towards shorter wavelengths. This relationship suggests a greater impact of Rayleigh scattering than the standard AM1.5 spectrum assumes (AM1.5 spectrum is defined for relatively low turbidity of 0.084 and no pollution). Only part of the scattered fraction of beam irradiance reaches the ground as diffuse irradiance, as it is lowered by the backscattered fraction. The inclined spectrum exhibits a similar characteristic to the horizontal spectrum, but the impact of the direct beam irradiance is more pronounced. Such significant differences between the standard AM1.5 spectrum and results of observations required an additional check to ensure that such values are realistic. For this reason, synthetic spectra were generated in 10-minute intervals and compared with the observations. There results are presented in the next section.

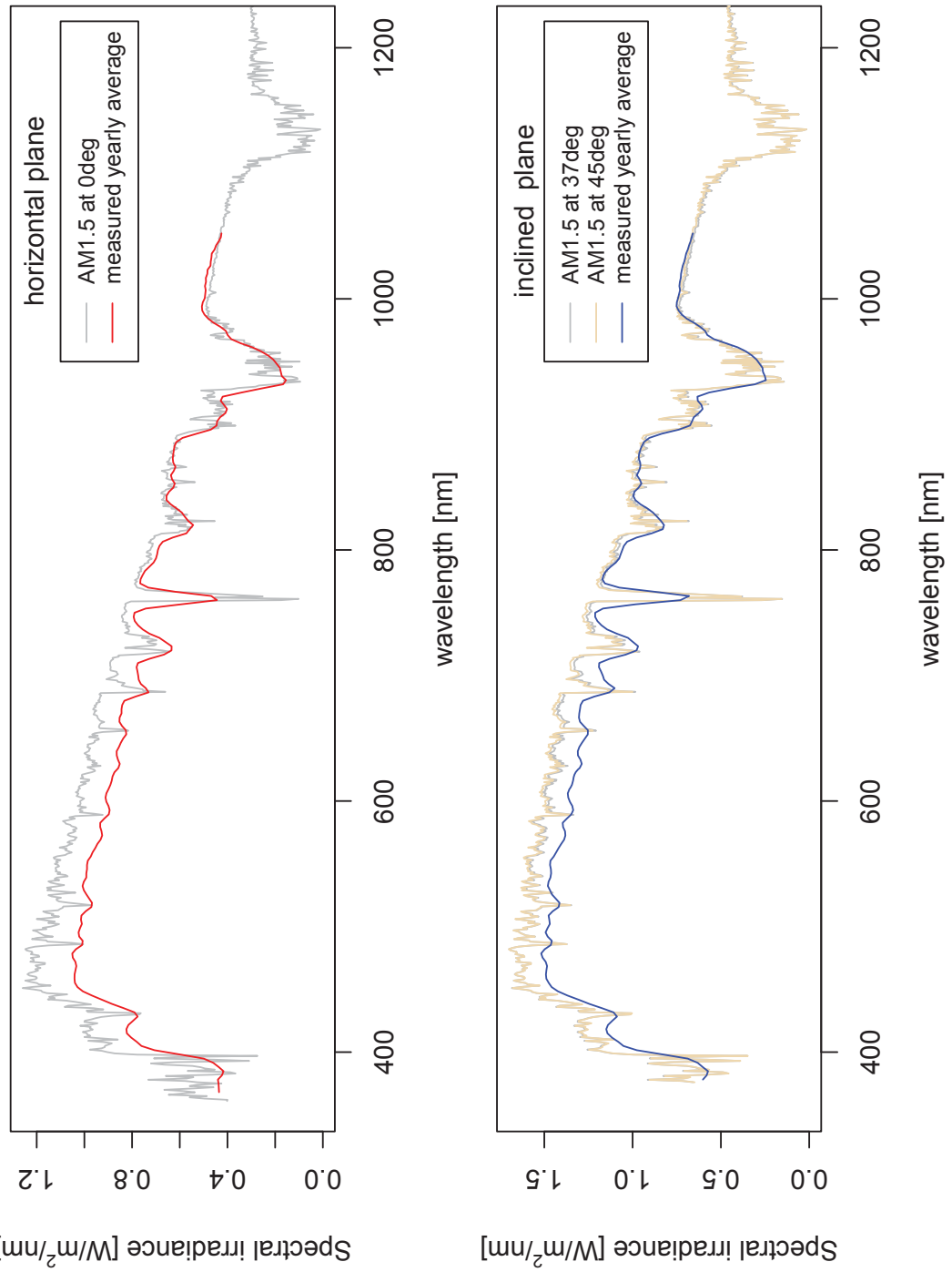

Figure 5.12: Yearly averaged spectral irradiance vs. AM1.5 reference spectrum. Spectra were normalised against AM1.5 spectrum at 860nm

5.3.3 Measured spectral irradiance vs. SMARTS

The observed differences between measured and equivalent standard AM1.5 spectrum are significant. To investigate the cause, measured average spectral irradiance and AM1.5 spectrum with yearly averaged spectral irradiance modelled by SMARTS were compared. The question is whether the average synthetic spectrum modelled for a year in 10-minute intervals gives results that are closer to the observed characteristics than the AM1.5 standard. The results are presented in 5.13.

In the horizontal plane, the averaged SMARTS spectrum closely matches the AM1.5 for wavelengths longer than 700nm. Below 700nm, the SMARTS yearly averaged spectrum presents a slight decrease in comparison to the AM1.5 standard, but it is smaller than the one observed from the measurements (differences between the SMARTS yearly averaged spectrum and average measured spectrum are smaller than observed for the AM1.5 standard spectrum). For the inclined plane, the yearly averaged SMARTS spectrum presents a more pronounced decrease in magnitude of spectral irradiance below 700nm in comparison to the AM1.5 standard. The measured averaged spectral irradiance and SMARTS model match more closely for wavelengths above 600nm. In the range 350-600nm, measured irradiance lies between the AM1.5 standard and yearly averaged SMARTS spectra. These results suggest that the underestimating of Rayleigh scattering by the AM1.5 standard spectrum postulated earlier is not the case. However, it should be noted here that the inclined radiation is also affected by clouds and backscattering. Clouds limit the impact of the direct irradiance and introduce more of a diffuse like spectrum. It can be concluded that SMARTS can produce results closer to the measurements than the AM1.5 standard, however the impact of the clouds remains not addressed. Tables 5.2 and 5.3 present summary of a correspondence between measured yearly average, simulated(SMARTS) yearly average and AM1.5 spectra for horizontal and 45° inclined planes.

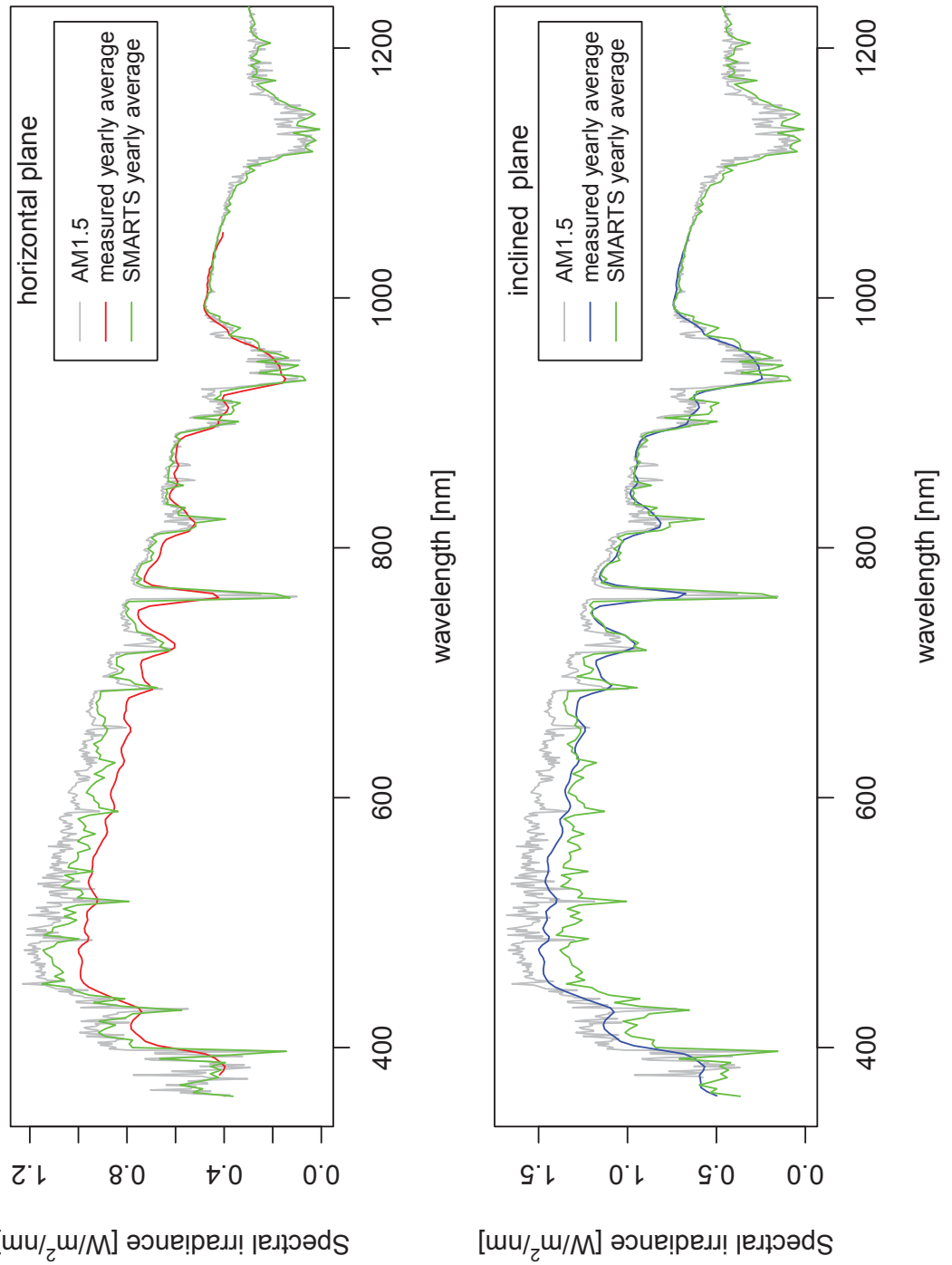

Figure 5.13: Yearly averaged spectral irradiance vs. yearly averaged SMARTS spectrum (AM1.5 conditions). Spectra were normalised against AM1.5 spectrum at 1000nm

Table 5.2: Correspondence between measured yearly average, SMARTS yearly average and AM1.5 spectra for horizontal plane

Band	Correspondence		
		SMARTS yearly average	AM1.5
350nm-700nm	SMARTS yearly average	X	medium
700nm-820nm		X	excellent
820nm-1200nm		X	excellent
350nm-700nm	Measured yearly average	medium	poor
700nm-820nm		good	good
820nm-1200nm		very good	very good

Table 5.3: Correspondence between measured yearly average, SMARTS yearly average and AM1.5 spectra for 45° incline plane

Band	Correspondence (45° incline plane)		
		SMARTS yearly average	AM1.5
350nm-610nm	SMARTS yearly average	X	poor
610nm-760nm		X	poor
760nm-1200nm		X	excellent
350nm-610nm	Measured yearly average	medium	poor
610nm-760nm		very good	poor
760nm-1200nm		excellent	excellent

5.3.4 Seasonal variability of spectral irradiance

For a better understanding of why the measured yearly averaged spectral irradiance differs from AM1.5 standard, spectral irradiance was averaged for each month of the year separately. Results are presented in Figure 5.14 and 5.15 for horizontal and inclined planes respectively.

Measurements presented in Figures 5.14 and 5.15 reveal significant differences between horizontal and inclined planes for the autumn and winter months. Spectra observed on the inclined plane are dominated by direct irradiance. Spectral irradiance in the horizontal plane varies seasonally the most between 550nm and

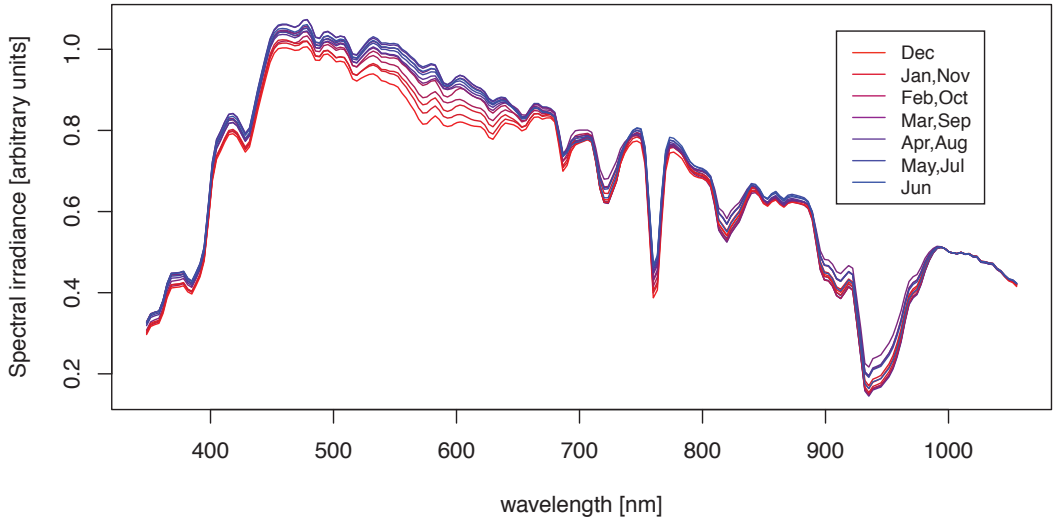

Figure 5.14: Monthly averaged spectral irradiance measured at the horizontal plane. Spectra were normalised against AM1.5 spectrum at 1000nm

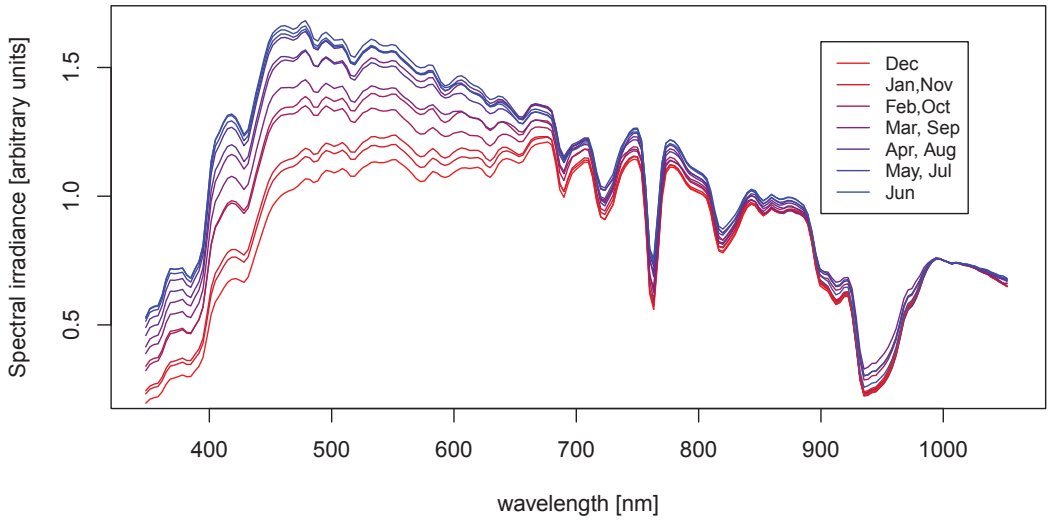

Figure 5.15: Monthly averaged spectral irradiance measured at the inclined plane. Spectra were normalised against AM1.5 spectrum at 1000nm

650nm. The observed differences are related to seasonal variations of the ratio between direct and diffuse irradiance. During the winter months the diffuse irradiance becomes more influential due to the lower amount of direct irradiance

reaching the observation plane. In addition, seasonal increase in ozone concentration impacts on the diffuse irradiance. Ozone undergoes photo-dissociation during summer months, which lowers its absorption. The results presented demonstrate that the plane of observation significantly changes the ratio between diffuse and direct components of the total irradiance. The diffuse irradiance and steeper angle of incidence of the direct irradiance compensate the seasonal red shift of the beam spectrum in the horizontal plane during the winter months. Whilst it was shown that the season of the year has a higher impact on spectral irradiance on the inclined plane, it must be stressed, that the monthly average spectral irradiance tends to vary significantly on a year-to-year basis. In Figure 5.14 it can be observed that the magnitude of the September average spectrum is slightly higher than that of August, for example. This may be caused by the fact that during the limited period of the campaign Septembers were on average less cloudy than Augusts. In accordance with the last statement, seasonal classification gives only a generic idea of how the spectral irradiance will vary over the year on different planes. To remove the impact of cloudiness from month to month variations, more detailed classification criteria, other than simple month of the year clustering, must be used.

5.3.5 Clearness index variations

Clearness index is one of the main criteria, which defines the state of the atmosphere in terms of the clearness and cloudiness. It has to be stressed that the use of a clearness index alone may lead to false classification of the sky condition. For example, the high air mass & low turbidity can produce the same clearness index as the low air mass & high turbidity. The same clearness index values can also be observed under the turbid sky with irradiance enhanced by the reflections from broken clouds and when the sky is clear & cloudless.

Variations in cloud coverage, turbidity and the air mass shift spectral irradiance distribution observed on the surface of the earth. For this reason, clearness index variations were investigated in more detail starting from statistical properties. The frequency distributions of the observed 10-minute averaged clearness index for every month of the year is presented in Figure 5.16. As it was mentioned

in section 5.2.6 the clearness index on its own is not capable of comprehensive classification of the sky cloud state and for this reason irradiance standard deviation has to be introduced. Figure 5.17 presents the 10-minutes frequency distributions of the observed irradiance standard deviations for every month of the year. As shown in Figure 5.16 clearness index during the most of the year has a bimodal distribution with the first maximum lying at around k_t=0.2 and the second at k_t=0.5-0.6. The first maximum represents overcast conditions. The second maximum represents clear sky conditions. Similar results have been reported by other researchers [95]. The second maximum shifts seasonally due to varying air mass. The region between the two maxima represents the period of transition between clear and overcast sky, optically thin clouds (hazy sky) as well as increase in the air mass. As shown in Figure 5.17, the scale of temporal variations in irradiance depends on the time of the year, but their character remains the same. These dependencies can also be seen in Figure 5.18, where the frequency distribution of observation count is shown against clearness index and the logarithm of the relative temporal standard deviation of irradiance. The logarithmic scale is used for better separation between groups. Three groups can be observed in these plots: The first group is defined for clearness index from 0 to 0.35 and δE_e from 3% to 30%. This group of measurements represents periods with continuous overcast sky. The second group is defined for clearness index 0.35 to 0.7 and δE_e from 20% to 60%. This group represents periods with heavily variable cloud cover. The third group is defined for clearness index 0.35 to 0.7 and δE_e from 0.3% and 5%. This group represents periods of time without cloud, with very low irradiance variation. Seasonal shift of the maximal clearness index is clearly visible within this group reaching 0.7 in June and 0.5 in December.

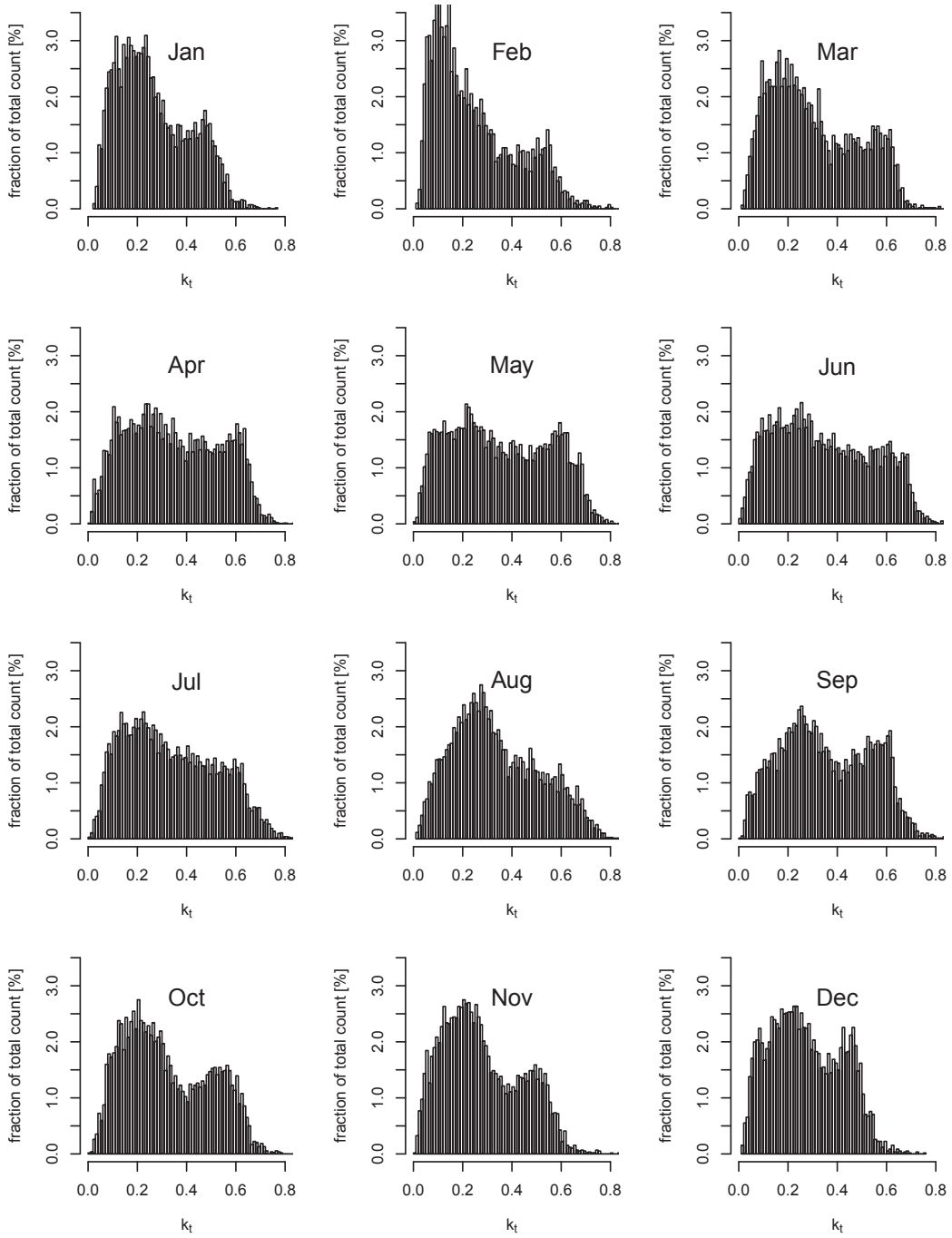

Figure 5.16: Frequency distribution of an hourly averaged clearness index values observed during the campaign.

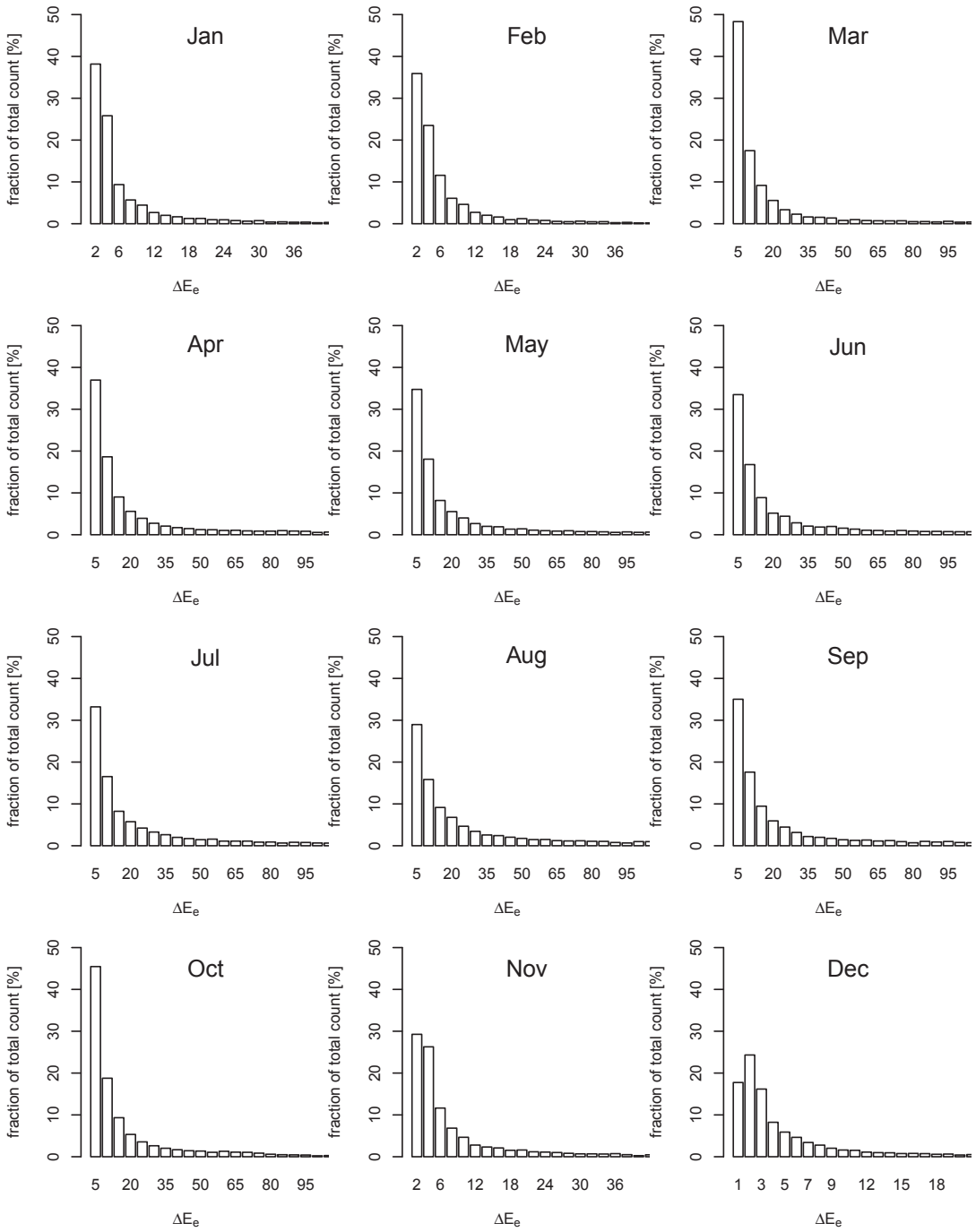

Figure 5.17: Frequency distribution of 10-minute standard deviation of irradiance values observed during the campaign.

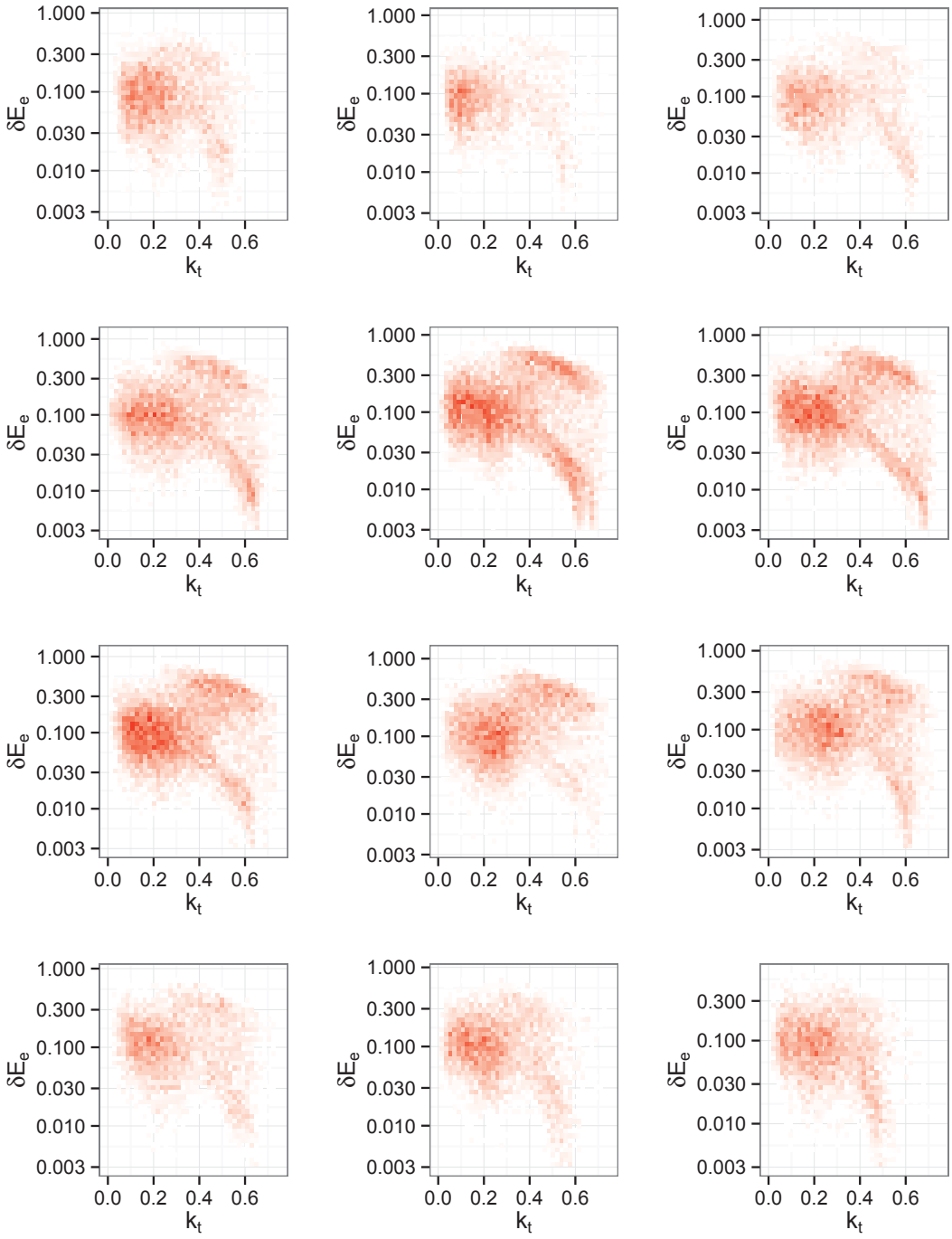

Figure 5.18: Monthly frequency distribution of 10-minute relative temporal standard deviation of irradiance values observed during the campaign vs. clearness index.

5.3.6 Broadband irradiance vs. photon flux

Based on 10-minute averaged spectral irradiance, the corresponding spectral photon flux and broadband radiant power were calculated. The ratio of these two values represents the difference between broadband irradiance measurements (widely used as a reference in photovoltaic industry) and the potential of this irradiance to generate photocurrent. It can be considered as the photocurrent generation efficiency of the incident radiation (η_J).

$$\eta_J = \frac{\int \phi_{e,\lambda} \cdot EQE_\lambda \mathrm{d}\lambda}{\int E_{e,\lambda} \mathrm{d}\lambda} \tag{5.2}$$

where:

$\phi_{e,\lambda}$ - spectral photon flux

EQE_λ- spectral external quantum efficiency of a photovoltaic device

$E_{e,\lambda}$- spectral irradiance

The distribution of the total available current as a function of irradiance current generation efficiency is shown in Figure 5.19. The full spectral range of the spectroradiometer (350nm to 1050nm) was used in the calculations.

As presented in Figure 5.19, a great part of the available solar irradiance on the horizontal plane is characterised by current generation efficiency varying from 0.52 to $0.55 A/W (\pm 3.3\%)$. This variation is greater for the inclined plane, where about 20% of the total irradiance is transmitted with current generation efficiency ranging from between 0.54 to $0.57 A/W (\pm 4.65\%)$. These results clearly show, that variations of spectral irradiance can have a significant impact on the accuracy of reference irradiance measurements, especially in case of spectrally sensitive photovoltaic device technologies.

In Figure 5.20, the distribution of the total available current in relation to clearness index (k_t) is shown.

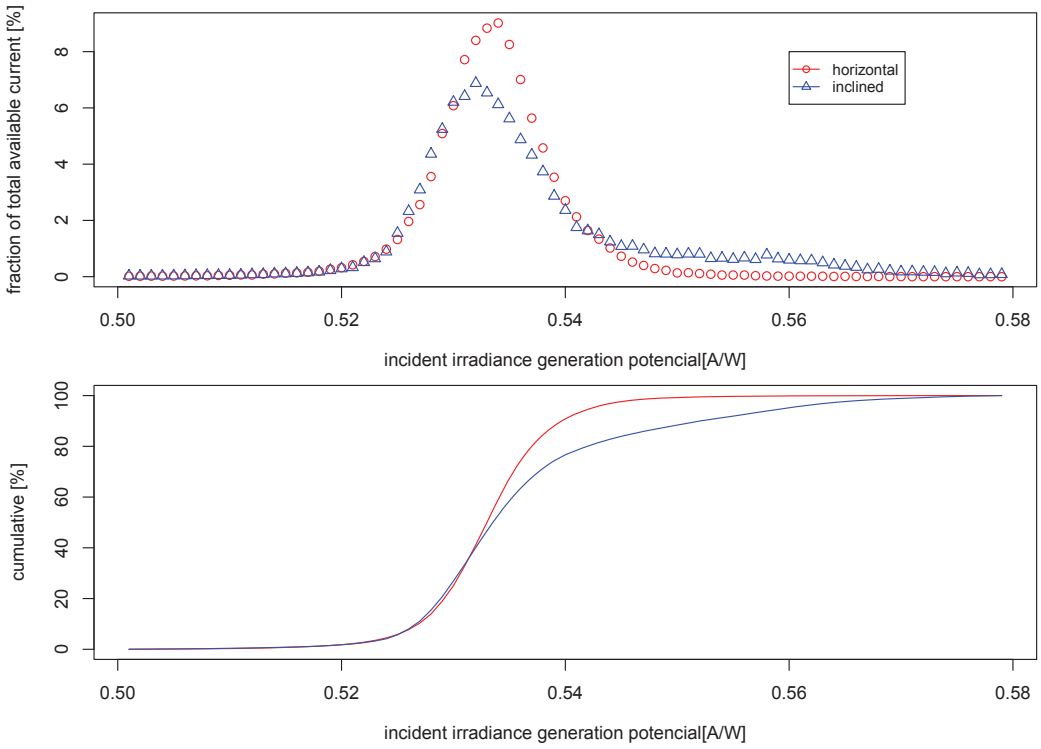

Figure 5.19: Distribution of the total available current vs. irradiance current generation efficiency

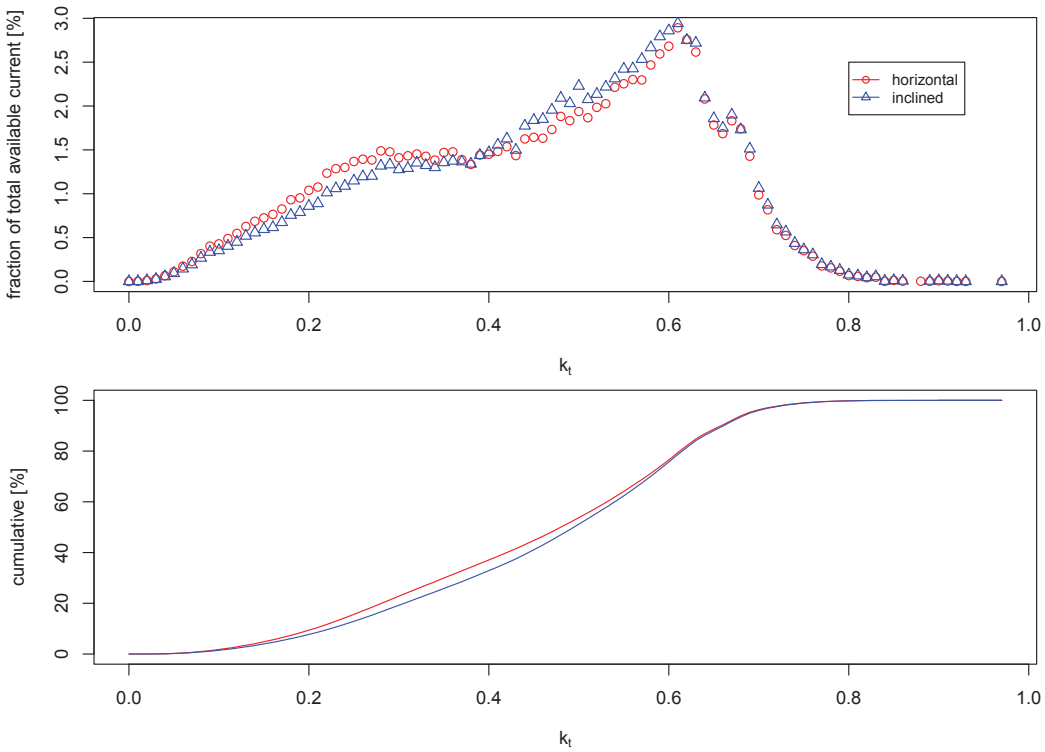

Figure 5.20: Distribution of total available current vs. clearness index.

Only a fraction (23.9%) of the total current generation occurs under high clearness indexes ($k_t \approx 0.6$). A significant part (76.1%) of the total current generation takes place under clearness index varying from 0.1 to 0.5. Such values of clearness index are achieved under cloudy sky conditions or high air mass. For this reason use of the clear sky model for spectral irradiance prediction may not be sufficient. Better understanding of the impact of clouds on spectral irradiance is required.

5.3.7 Impact of spectral variations on efficiency of photovoltaic devices

Efficiency of a photovoltaic device can be defined only for a specific spectral distribution of the solar irradiance. The photovoltaic industry adopted the standard AM 1.5 spectrum for this reason. In the real world, the distribution of spectral irradiance differs from the standardised values. This leads to the situation where field efficiency of the photovoltaic device may differ from the one defined under standard test conditions. These efficiency variations are therefore caused by variations of spectral composition of the incident irradiance, not the variations of the spectral response of the photovoltaic device itself. Knowledge about the character of photovoltaic device efficiency variations caused by the spectral composition of the incident irradiance allows for improvement in the methodology used for photovoltaic device efficiency rating. In this section variations of generation efficiency (η_G) for three photovoltaic device technologies (multi-cSi, a-Si, CdTe) are presented. Figures 5.21 to 5.26 show variations of device generation efficiency under natural spectral irradiance. As the plane of observation has an impact on the spectral irradiance, two plane orientations were considered (horizontal and inclined at 45°). Figures are presented for each month of the year to separate other seasonal effects.

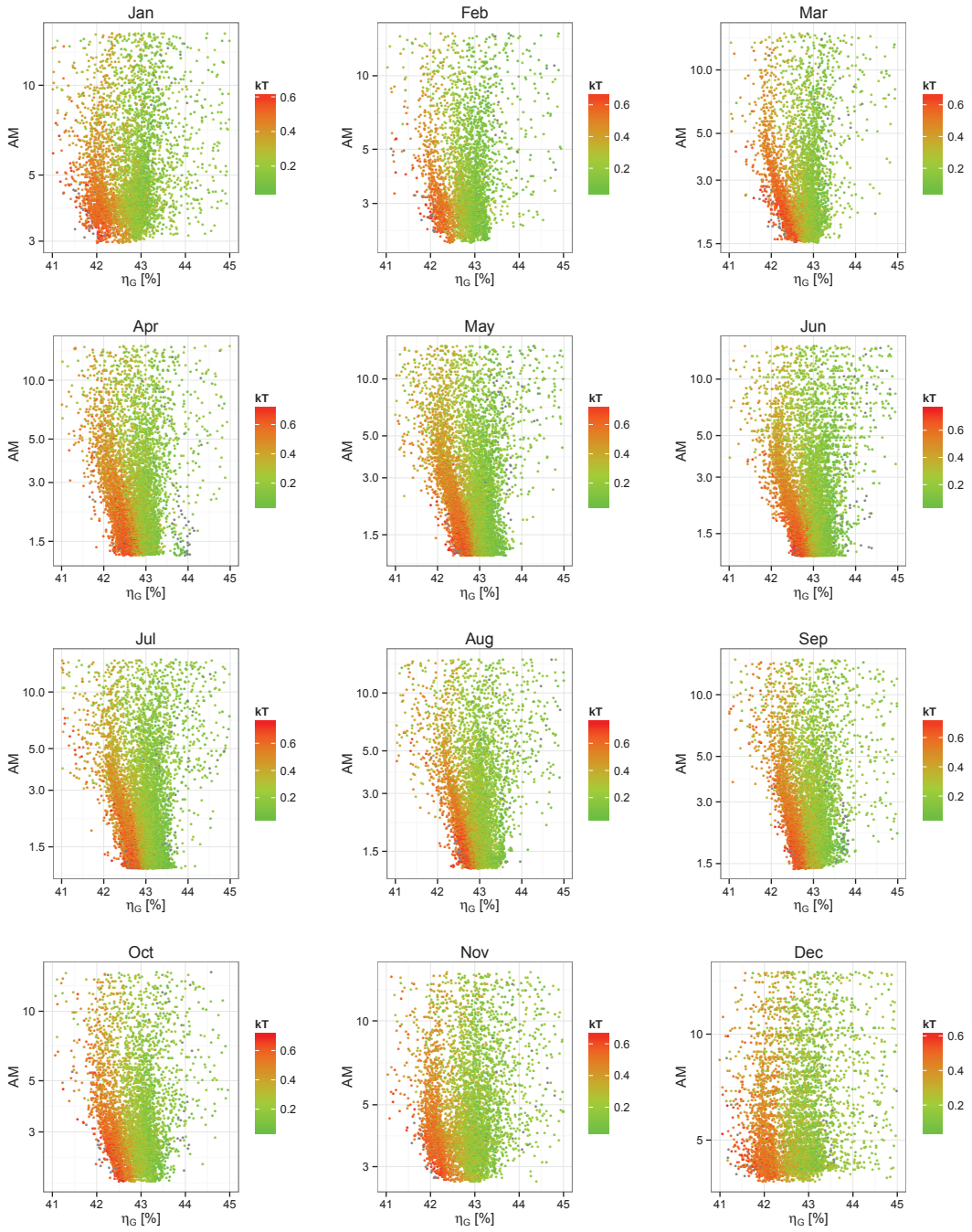

Figure 5.21: Variations of generation efficiency (η_G) under natural spectra observed for an a-Si device for the horizontal plane

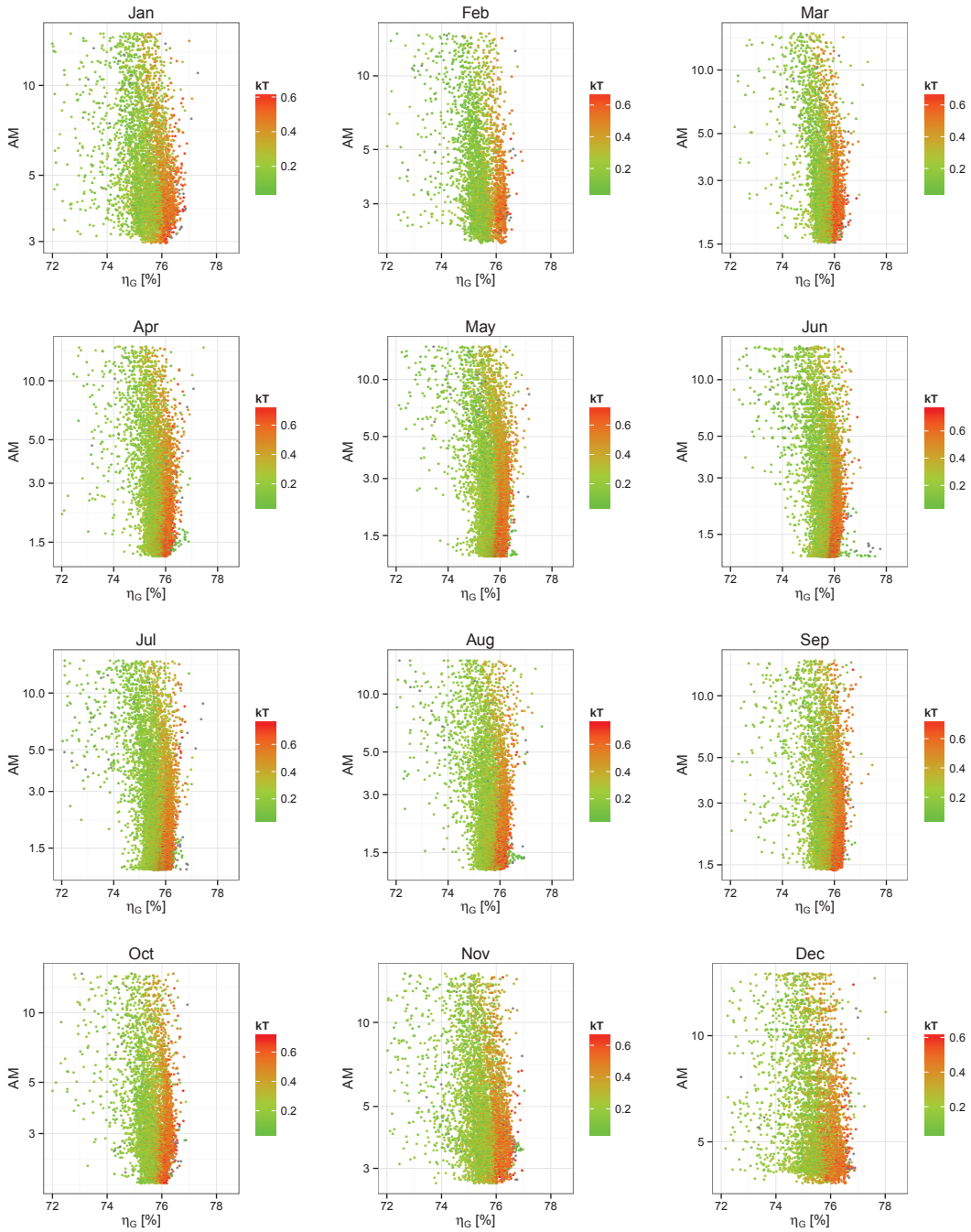

Figure 5.22: Variations of the photovoltaic device generation efficiency (η_G) under natural spectra observed for a multi-cSi device for the horizontal plane

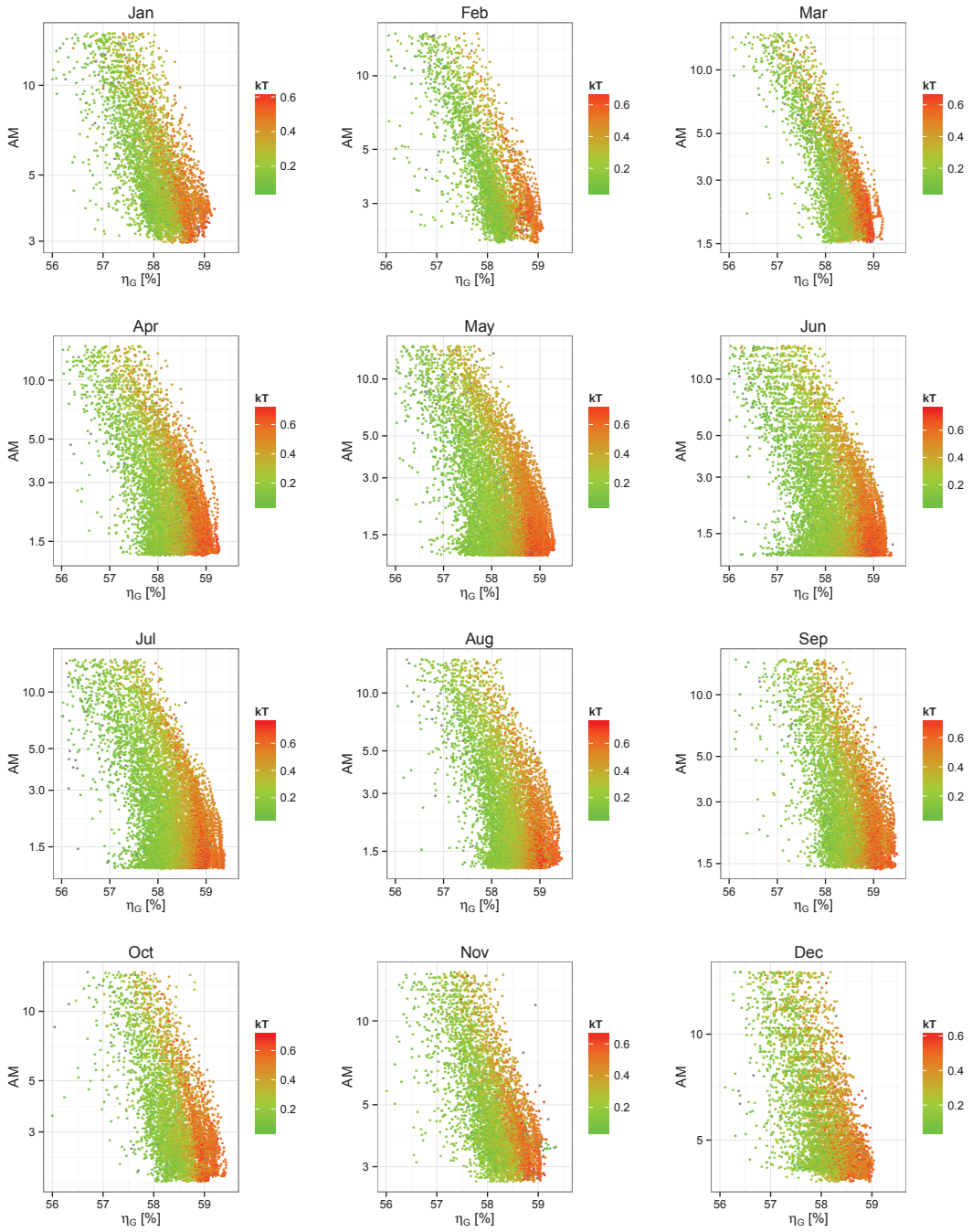

Figure 5.23: Variations of the photovoltaic device generation efficiency (η_G) under natural spectra observed for a CdTe device for the horizontal plane

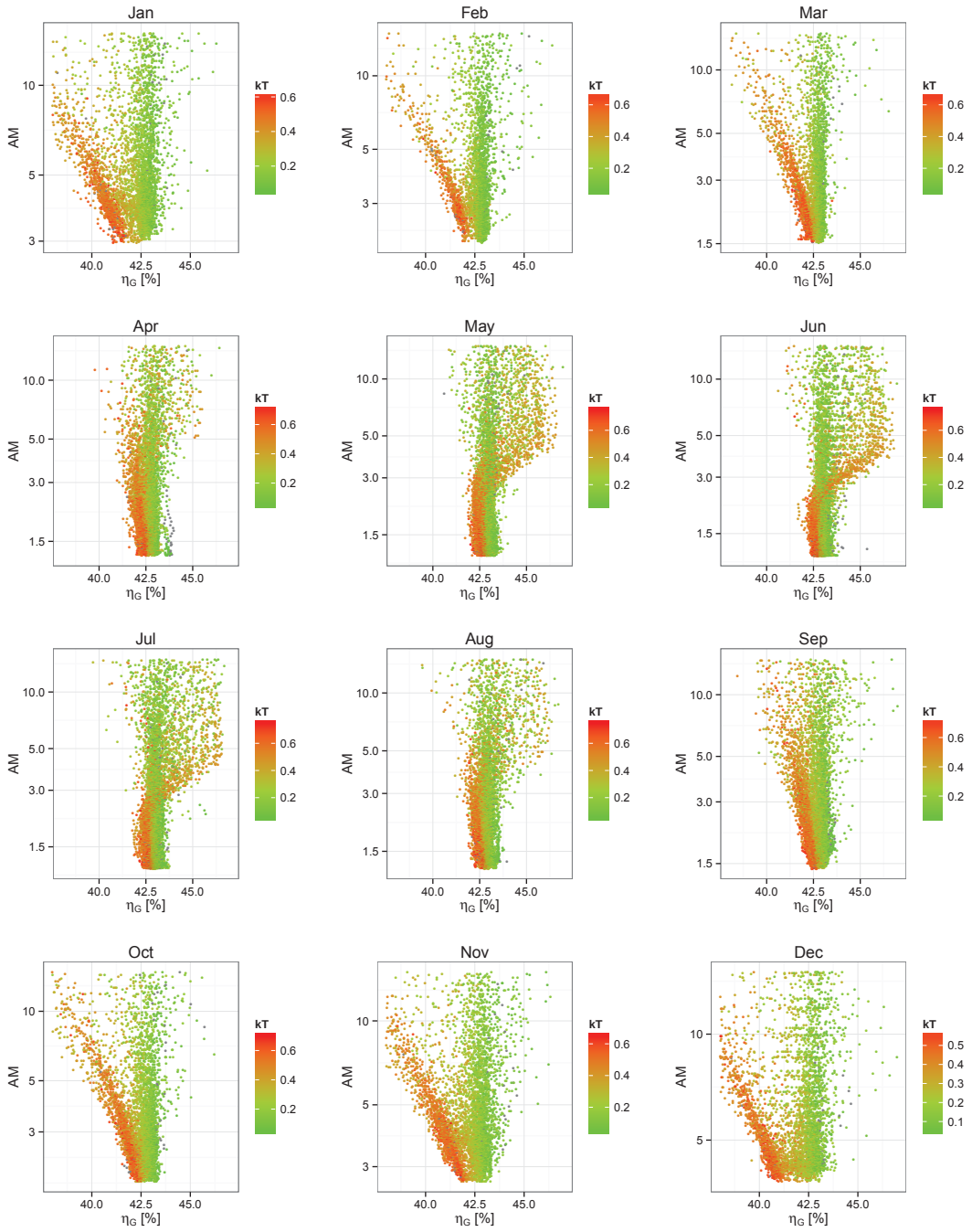

Figure 5.24: Variations of the photovoltaic device generation efficiency (η_G) under natural spectra observed for a-Si device for an inclined plane

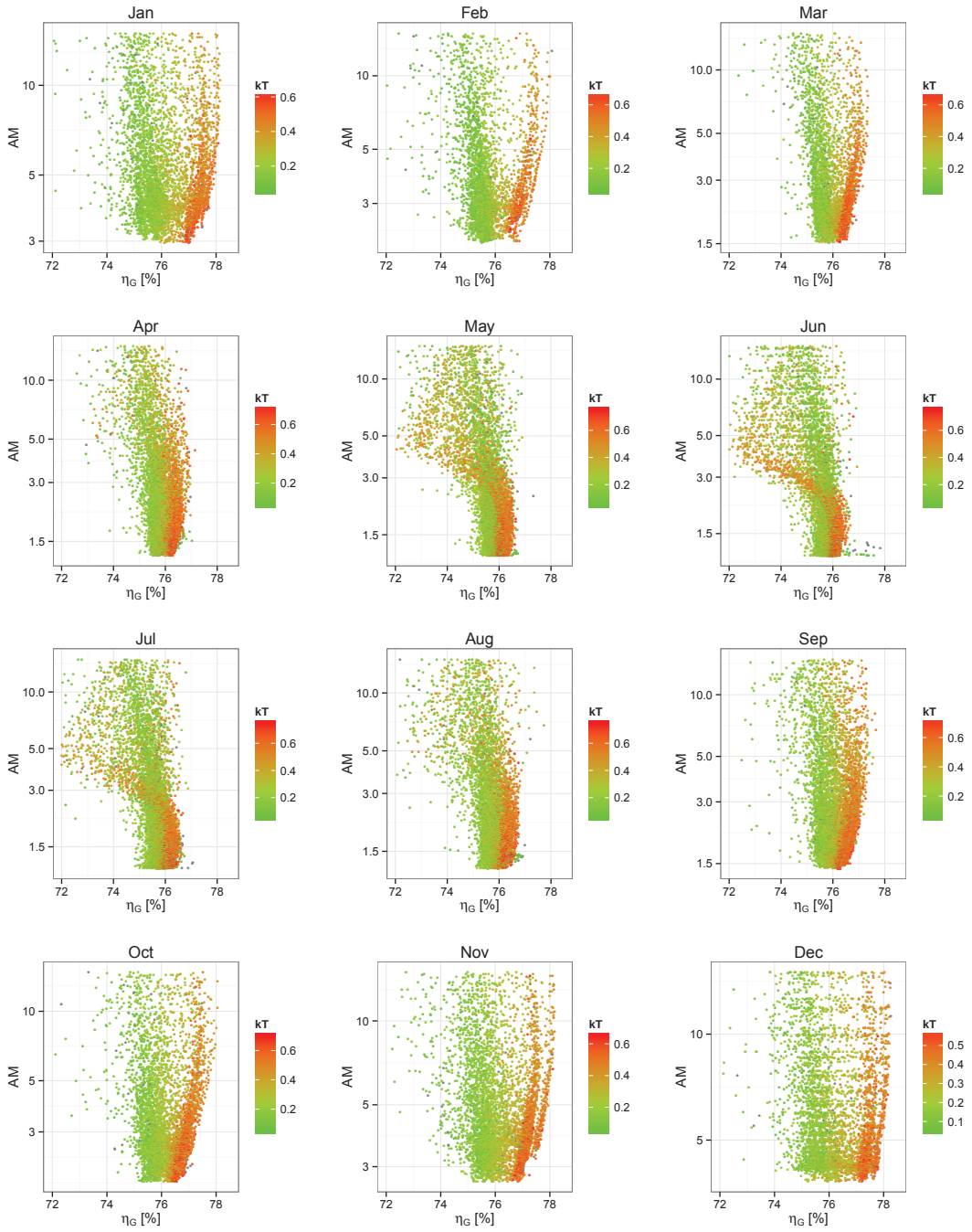

Figure 5.25: Variations of the photovoltaic device generation efficiency (η_G) under natural spectra observed for a multi-cSi device for an inclined plane

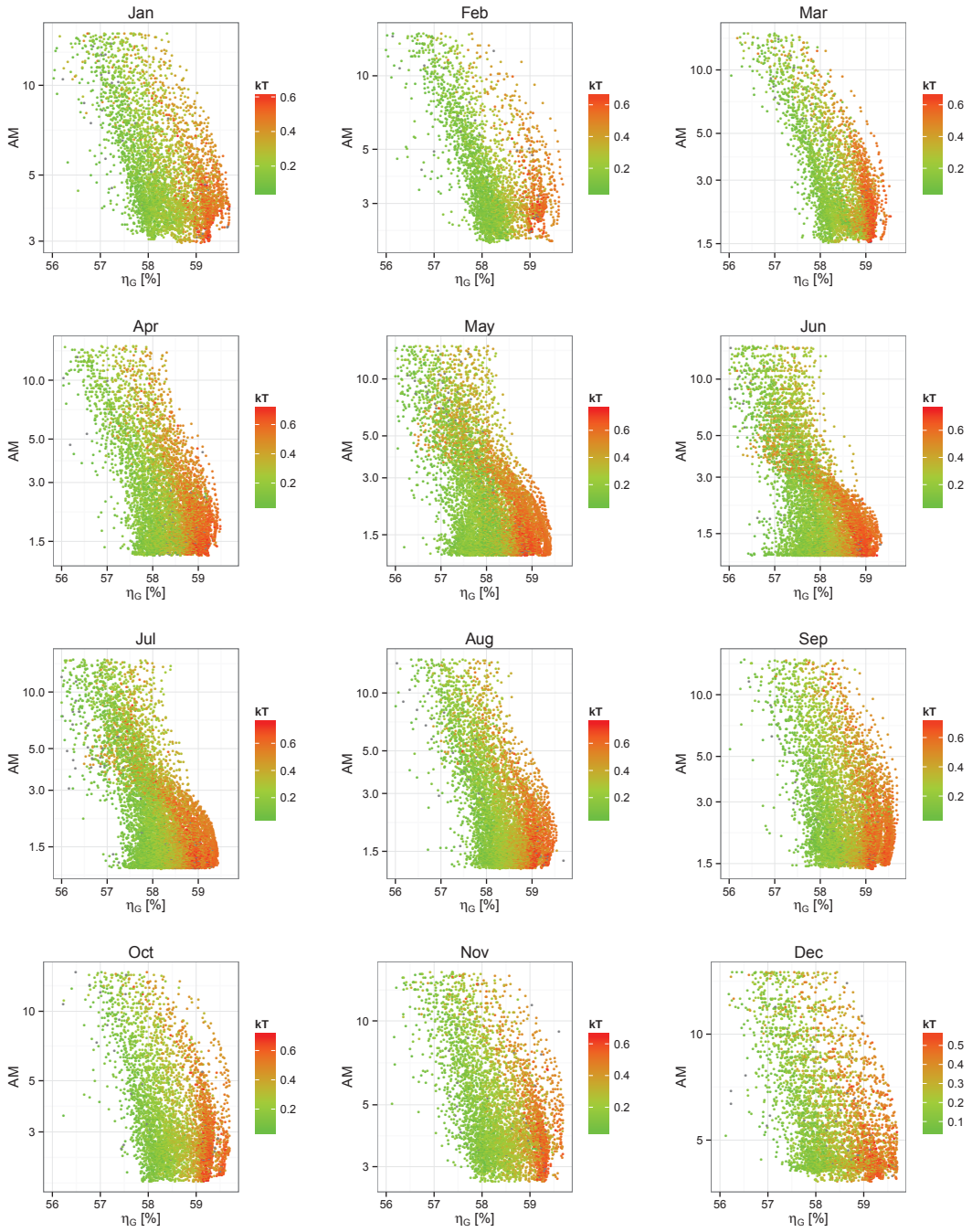

Figure 5.26: Variations of the photovoltaic device generation efficiency (η_G) under natural spectra observed for a CdTe device for an inclined plane

For the horizontal plane, the observed efficiency variations stayed within 1.5% - 2%. It can also be clearly seen that the efficiency variations of the photovoltaic devices depends on the cloudiness index. In the case of a-Si, observed performance for high clearness index values was around 0.5%-1% lower when compared to low clearness. In contrast, the multi-cSi device performed on average by 0.5% better under the high clearness than under the low clearness. The CdTe device demonstrated similar dependency to the multi-cSi device, however the efficiency spread was wider reaching 1% difference between high and low clearness indexes. The CdTe device also showed a greater dependency of the efficiency on increasing air mass, while the multi-cSi devices efficiency was almost independent from air mass value. In the case of the inclined plane, spectral effects impact device efficiency to a greater extent than for the horizontal plane. Differences between high and low clearness are larger. In addition, during the summer months, under high clearness, a significant change in device generation efficiency can be observed for air mass greater than 3. This is attributed to the fact that the direct solar irradiance stops reaching the inclined plane for the air mass above 3 (specific to the measurement setup here, because the sun rises and sets behind the module plane during these months). Therefore diffuse irradiance becomes dominant and dictate performance of the photovoltaic device. The a-Si device performance increases under these conditions, while multi-cSi and CdTe devices present decrease of efficiency. Up to 5% of a difference in photovoltaic device efficiency between high and low clearness conditions can be observed for the a-Si device and 3% for multi-cSi and CdTe devices. Maximal differences are observed under high air mass. It was shown here, that the field efficiency of the photovoltaic device could differ from the standard value because of the spectral composition of the incident irradiance. Observed trends in generation efficiency heavily depends on the plane of observation, time of the year and the spectral response of a specific photovoltaic cell technology. Further analysis of the reasons causing these differences is presented in further sections of this chapter.

5.3.8 Clear sky spectrum

Figure 5.27 shows a simplified representation of irradiance paths under clear sky conditions and ongoing scattering effects in the atmosphere.

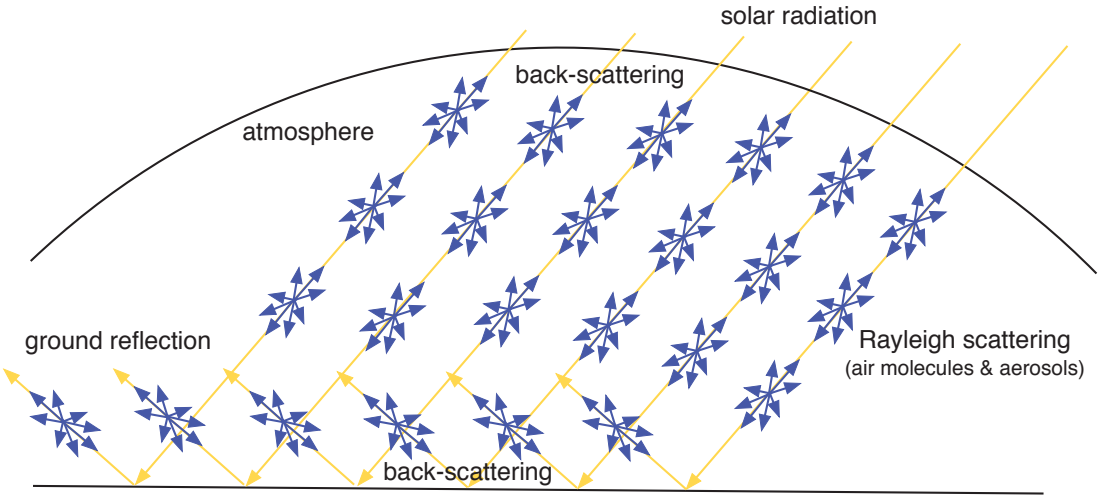

Figure 5.27: Schematic representation of irradiance paths under clear sky and ongoing scattering effects in the atmosphere

During a clear day, solar irradiance reaching the surface of the earth is incident in the form of direct irradiance from the solar disc and as diffuse irradiance from the rest of the sky. Most atmospheric constituents are fairly stable in time and space. Effects caused by these constituents are therefore mainly scaled by the air mass factor, whose value varies significantly over the course of the day and year. One of the dry air constituents that is characterised as highly variable and location dependent is the type and concentration of aerosols. Aerosols cause an increase of scattering processes in the atmosphere and that impacts the ratio between diffuse and direct irradiance and ultimately can limit the amount of irradiance reaching the ground. To analyse variations of spectral irradiance caused by the atmosphere under clear sky condition, a set of relevant observations was selected from the measured dataset. Observations were classified according to methodology presented in section 5.2.6

Figure 5.28 presents the impact of the atmosphere on the horizontal spectral irradiance under the clear sky conditions.

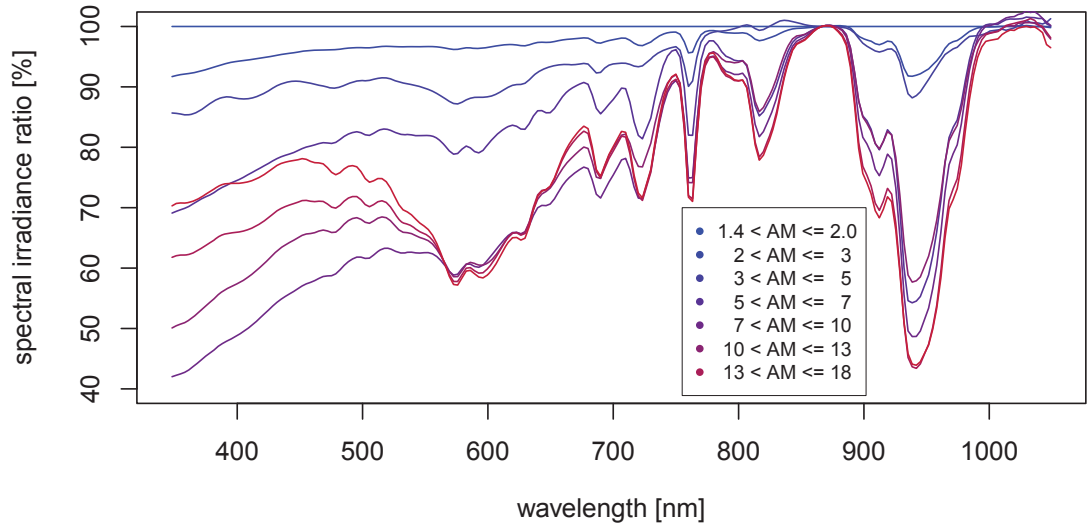

Figure 5.28: The impact of the atmosphere on the horizontal spectral irradiance under the clear sky conditions as a function of variable air mass. Presented parameter has been calculated as a ratio between the spectral irradiance measured under various air mass and the spectral irradiance measured under the air mass ranging 1.4 to 2.0. Measurements were normalised at 865nm.

As shown in Figure 5.28, an increasing air mass shifts the spectral irradiance towards longer wavelengths. More blue part of the spectrum is attenuated. For higher air masses the clear division between direct and diffuse fractions becomes more visible.

5.3.9 Cloudy sky spectrum

Figure 5.29 shows the representation of irradiance paths under cloudy sky conditions and ongoing scattering effects in the atmosphere.

Due to their white colour that can be observed with the naked eye, clouds are often recognised as being spectrally neutral. This is partially true, only for a case where the visible part of the spectrum is considered. Clouds spectral albedo starts to slowly decrease from 600nm and at 1200nm it reaches $\approx$ 75% of its initial value [96–98]. It is well known that cloud cover shifts daylight temperature towards higher temperature (shorter wavelengths). This fact seems to contradict with the impact of clouds spectral albedo. Especially that the blue

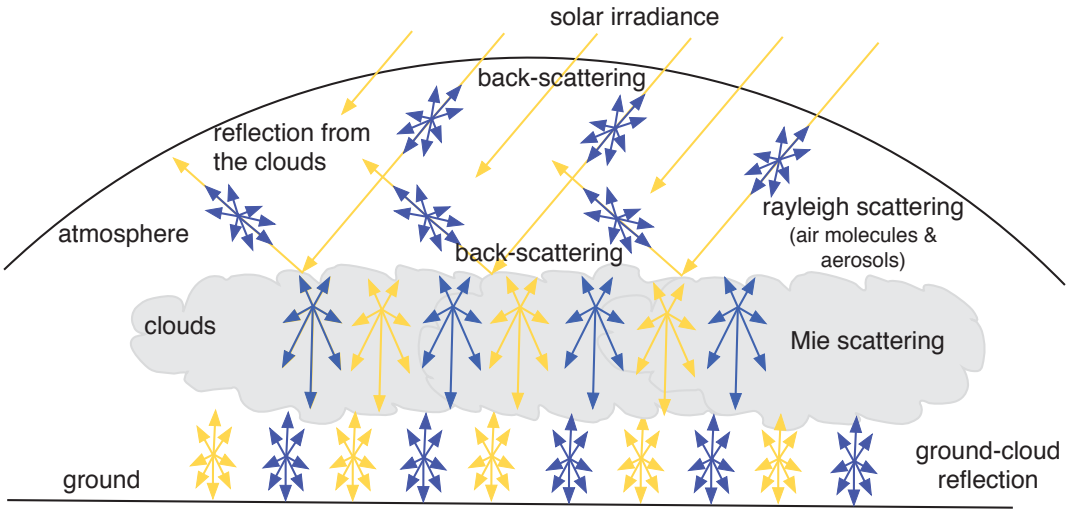

Figure 5.29: Schematic representation of irradiance paths during cloudy day and ongoing scattering effects in the atmosphere.

shift is observable in the VIS domain where the spectral albedo of the clouds stays relatively constant. Therefore there must exist another mechanism causing an enrichment of the spectral irradiance in its blue part during cloudy days.

As already mentioned an extraterrestrial irradiance is being back-scattered in the direction of space. The magnitude of scattered irradiance is symmetric for a forward and backward directions of irradiance propagation. Under a clear sky conditions approximately 10% of total horizontal terrestrial irradiance comes as a diffuse fraction and 90% as a direct. Irradiance reflected from the top of the clouds undergoes the scattering, similarly to the down-welling irradiance. The backscattered fraction of the irradiance, initially reflected from the cloud, reaches the top of the cloud again. Back-scattered irradiance has the spectral characteristic of diffuse irradiance, therefore it is rich in short wavelengths, according to the Rayleigh theory. Figure 5.30 presents the described situation.

The ratio between diffuse and direct irradiance is significantly altered under the presence of the clouds and will vary depending on the reflectance of the cloud. The ratio between direct and diffuse irradiance will be lowered by the spectral albedo characteristic of the clouds as well as by the zonal albedo (if only different to snow).

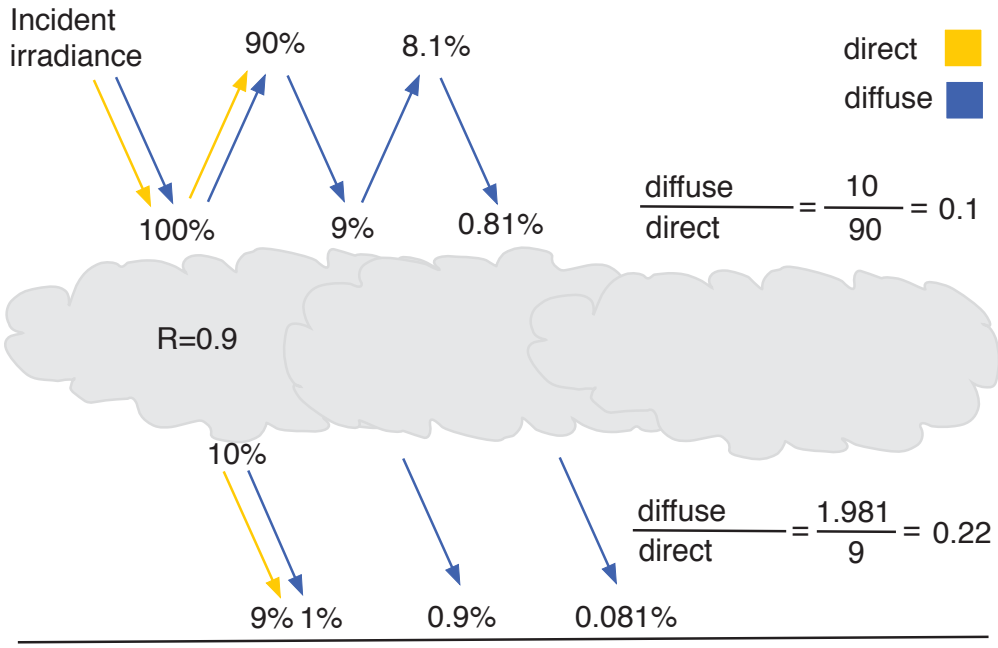

Figure 5.30: Irradiance backscattering at cloudy conditions

To investigate the impact of clouds further, the measured horizontal spectral irradiance was used. To isolate the impact of clouds from the impact of the other atmospheric constituencies, data were filtered out to include only measurements taken under the air mass lower than 1.4. Then seven clearness index ranges were defined (from k_t=0-0.1 to k_t=0.6-0.7), where the last one represents the clear sky condition (baseline for a relative spectral transmittance). Average spectral irradiance was calculated for each of the clearness ranges. Then ratios between average spectral irradiances and the baseline (k_t=0.6-0.7) were calculated. Resultant ratios describe the impact of the cloudy sky on spectral irradiance as a function of the cloudiness index. To simplify the comparison, the ratios were normalised at 865nm (non-absorbing band). The data used were limited to include the period between the 15th of June and the 15th of July of each of the year of observations. Figure 5.31 presents the results achieved.

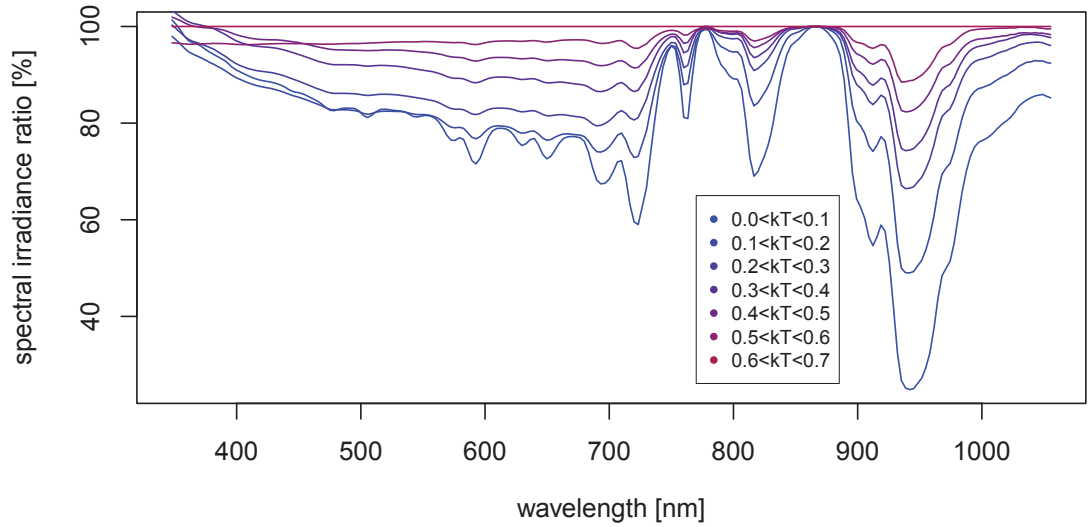

Figure 5.31: The impact of the atmosphere on the horizontal spectral irradiance under the cloudy sky conditions as a function of a clearness index

The impact of the clouds on the spectral irradiance received by the surface of the earth is far from neutral. The visible spectrum in blue range seems to be transmitted more effectively than the red spectrum. Such an observation does not imply that the spectral transmittance of the cloud is actually spectrally dependant. It was impossible to the author to measure the spectrum above and below the cloud at the same time. Therefore it cannot be confirmed that the presence of the clouds can impact the amount of diffuse irradiance available above the clouds. However the observations undertaken prove the blue shift under the cloudy sky. The infrared part of the spectrum is affected as well by expanding water absorption bands. This situation even further impacts the current generation efficiency of the incident irradiance.

5.3.10 Partially cloudy sky spectrum and its variations

Figure 5.32 presents possible irradiance paths under partially cloudy skies.

During a partially overcast day, irradiance reaching the surface of the earth can be modified by the largest number of effects. Moreover, cloud coverage can vary dramatically within a short period of time and between close locations. If

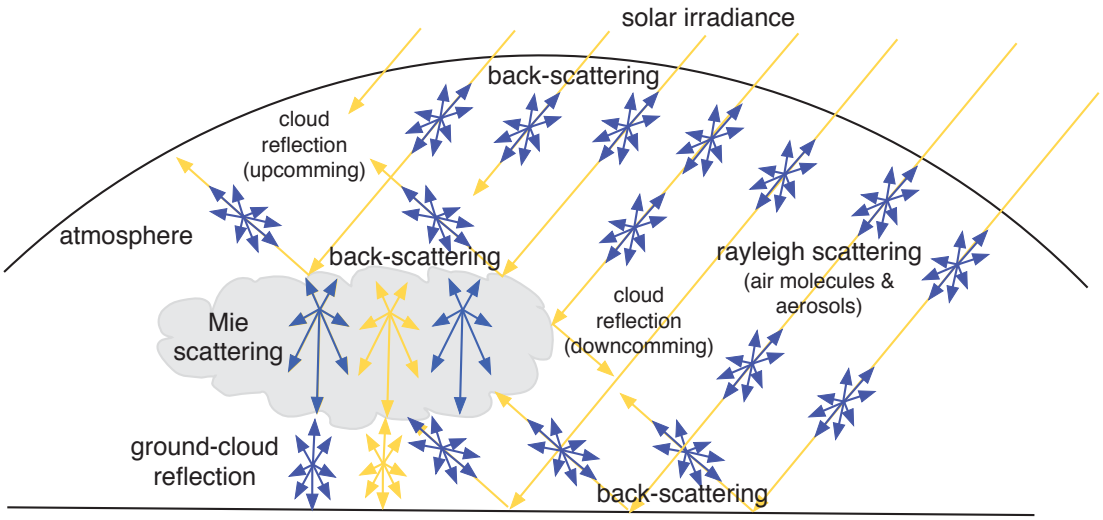

Figure 5.32: Schematic representation of irradiance paths during partially cloudy day and ongoing scattering effects in the atmosphere

the clouds do not cover the solar disc, direct irradiance reaches the surface in the same quantity as for clear day conditions. Part of both the direct and diffuse irradiance can be reflected upwards (back to space), but also downwards again. Irradiance reflected from the top surface of the clouds undergoes scattering. Its backscatter fraction contributes to down-welling irradiance as was explained in the previous section. Diffuse and direct irradiance that traverses through the cloud is selectively attenuated due to water vapour molecular absorption (mainly in the infrared). Cloud particles cause Mie scattering, therefore besides absorption bands, the spectrum of the transmitted irradiance does not change. Direct irradiance transmitted through the cloud changes its character from collimated to diffuse. Diffuse irradiance transmitted through the cloud loses its initial polarisation. It is expected that the greatest shift of the spectrum towards short wavelengths is to be observed in the case of a single cloud covering the solar disk, with the rest of the diffuse irradiance reaching the surface. With increasing cloud cover, as long as the solar disk is still visible, it is expected that spectrum will be shifted towards longer wavelengths.

5.4 Conclusions

Most of the time spectral irradiance is considered as a secondary effect. However differences between average measured spectral irradiance and reference AM1.5 spectrum, as well as temporal variations of spectral irradiance show that the importance of the spectrum seems to be underestimated. The analysis undertaken provided reliable long-term spectral irradiance data. It was shown that the AM1.5 spectral characteristic of solar irradiance (used as a standard for module characterisation) differs significantly from the observed, long-term average value. Sources of observed differences were defined and investigated. Variations in spectral irradiance affect the generation efficiency of common photovoltaic devices. The observed differences are larger for narrowband photovoltaic devices. The proposed generation efficiency of a photovoltaic device (η_G) presents seasonal dependencies in a way that can be related directly to energy yield. This is a consequence of seasonal variations of the air mass and the cloudiness. On top of these seasonal trends, instantaneous variations of η_G were also observed. These variations are attributed to the variations of the atmosphere composition, mainly due to aerosols. Spectral irradiance variations were discussed in a context of various types of the sky condition (clear sky, partially cloudy sky, full overcast). Figure 5.33 summarises the resulting shifts in the spectrum depending on sky condition.

Figure 5.33: Spectral shift vs. sky conditions

As shown in Figure 5.33 the greatest shift to the blue occurs when the direct component of irradiance is being suppressed and the diffuse irradiance is present (i.e singular cloud covering the sun disc, during the sunrise and sunset, sun out of the field of view of a detector/module). Introduction of an additional overcast to the previous scenario will reduce the blue shift as only the fraction of diffuse

irradiance will then reach the surface of the earth. This shift will be the strongest under fully overcast sky. Under clear sky condition direct irradiance is dominant over the diffuse, therefore overall spectrum will shift towards red part. If an additional overcast is introduced, shift to the red is strengthened. The red shift can be further increased by reflection of the direct irradiance from the clouds.

The presented findings lead towards redefinition of a spectral irradiance standard, that could allow for improvements in the field of photovoltaic system yield calculations in the future. Separate spectral characteristics should be defined for the clear and the cloudy skies. The appropriate use of existing spectral models (e.g. SMARTS) can provide location and the plane of observation specific reference spectra. For places where the plane of array is installed at an angle, the definition of separate spectra for specific months should also be considered important. Such a set of reference spectral irradiances could be easily implemented in a PV energy yield prediction tools and photovoltaic monitoring systems. Further work towards standardisation of a realistic spectral irradiance is required.

Chapter 6

Impact of spectral mismatch on accuracy of reference irradiance measurements

6.1 Introduction

Solar radiation is the most significant factor, which determines the energy output of photovoltaic devices. In photovoltaic systems, various detectors (e.g. thermopile pyranometer, mono-cSi reference cells, multi-cSi reference cells) are used to provide the system operator with information about the available solar irradiance resource (reference irradiance). Depending on the detector used, reference measurements may differ from the photovoltaic device output. There are a number of reasons for the differences observed (e.g. angular response, reflection losses, response time, long term stability, temperature dependency, linearity, different orientation of the plane of array and the plane of a reference detector, geographical dislocation). In this chapter the author concentrates on another factor - the spectral response mismatch. The spectral response mismatch in conjunction with wavelength-dependent atmospheric attenuation processes can lead to a situation where an excessive systematic error is introduced to the results

of the measurements. It should be noted, that the other factors used have a non-negligible impact on the accuracy of the reference irradiance measurements and cannot be ignored in a case of a general investigation. In this work the author limits his interest to the impact of the spectral mismatch. Effects caused by variations in solar spectral irradiance on the accuracy of the reference irradiance measurements were not extensively investigated in the past. Analysis of the impact of atmospheric phenomenon affecting the spectral solar irradiance is preceded by a short theoretical introduction to the underlying physical processes and used modelling tools. The work presented in this chapter extends the level of understanding of the impact of the variability of the solar spectral irradiance and the spectral response mismatch on the accuracy of the reference irradiance measurements.

6.2 Methods

Photovoltaic devices are sensitive to the photon flux not the radiant power of the incident irradiance. Use of thermal detectors (pyranometer) as a reference detector for photovoltaic devices causes a systematic error and it reduces the accuracy of the result of the measurement. A semiconductor detector, characterised by the spectral sensitivity, which significantly differs from the spectral sensitivity of the monitored photovoltaic device is also not optimal and impacts on the accuracy. It is important to clarify to what extent the spectral mismatch between the reference detector and the photovoltaic device can affect the accuracy of the reference measurements.

6.2.1 Detector response mismatch under the clear sky conditions

The simplest way of expressing the impact of the spectral mismatch between the reference detector and the photovoltaic device is to calculate the ration of their outputs (S_d, S_s) across the range of possible spectral conditions.

$$M_{specific} = \frac{S_d}{S_s} \tag{6.1}$$

where:

$M_{specific}$ - reference irradiance detector mismatch for the specific irradiance

S_d - output signal from the photovoltaic device

S_s - output signal from the reference detector

The response from the photovoltaic device can be calculated from the equation 6.2. Note that the photovoltaic device response is equal to the short circuit current generated by the device (I_{SC}).

$$S_d = \int E_{e,\lambda} \cdot SR_{\lambda,device} \mathrm{d}\lambda \tag{6.2}$$

where:

SR_{device} - spectral response of the device

Responses from the reference irradiance detectors are calculated in the same way (see equation 6.3)

$$S_s = \int E_{e,\lambda} \cdot SR_{\lambda,detector} \mathrm{d}\lambda \tag{6.3}$$

where:

$SR_{\lambda,detector}$ - spectral response of the detector

In total, six types of photovoltaic devices and two types of reference detectors were investigated: multi-cSi, a-Si, CIS, CdTe, HIT, mono-cSi, thermopile pyranometer and mono-cSi reference cell. Figure 6.1 presents the spectral responses of the photovoltaic devices and reference detectors used by the author for the purpose of this investigation.

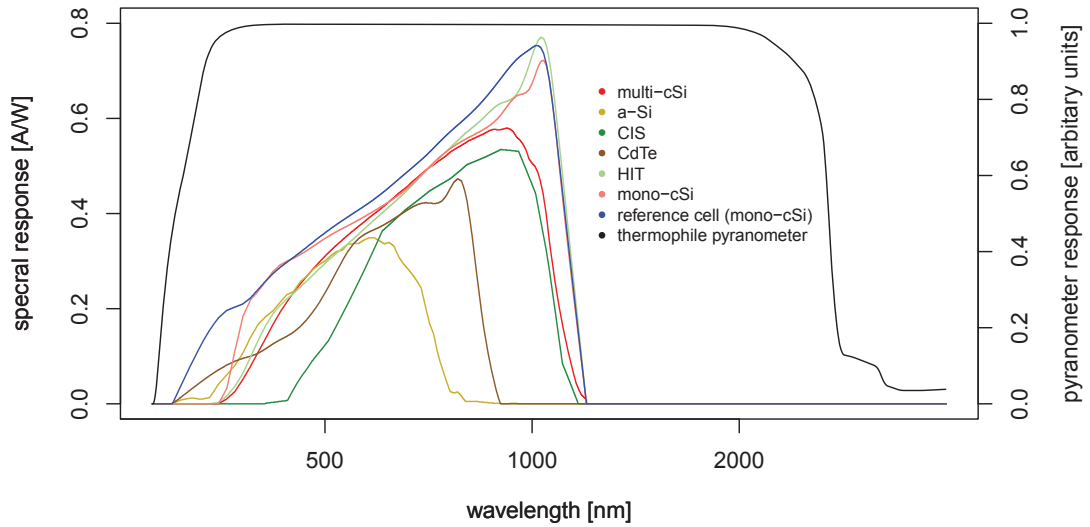

Figure 6.1: Spectral response of the devices used for the calculations

The detector response mismatch under specific irradiance($M_{specific}$) was normalised against its value at the standard AM1.5 conditions. This way the detector response mismatch can be easily compared in-between the reference detectors types.

$$M_{norm} = \frac{M_{specific}}{M_{AM1.5}} \tag{6.4}$$

where:

M_{norm} - normalised detector response mismatch

$M_{AM1.5}$ - detector response mismatch for standard AM1.5 spectrum

6.2.2 Detector response mismatch under the variable atmospheric conditions

Spectral irradiance can be easily calculated for the standard atmospheric conditions. Correction coefficients can be applied to any combination of reference detector and monitored photovoltaic device. However, the atmospheric composition is not constant, it undergoes continuous variations in time and space.

To investigate the impact of the atmospheric parameter variation on the accuracy of reference irradiance measurements, the author established ranges within which specific atmospheric parameters are expected to vary. The atmospheric parameters were altered throughout these ranges and the relevant spectral irradiance was calculated. The resulting spectral irradiance was then used to calculate the specific detector response mismatch ($M_{specific}$).

Next, an absolute difference between the specific detector response mismatch ($M_{specific}$) and the detector response mismatch under the standard atmospheric conditions ($M_{AM1.5}$) was calculated. The final result is presented as a relative difference of these two detector response mismatches. Calculations were done for two types of the reference detectors (the broadband and the mono-cSi). Equation 6.5 presents mathematical representation of the calculations.

$$\delta M = \frac{M_{specific} - M_{AM1.5}}{M_{AM1.5}} \tag{6.5}$$

where:

δM - relative mismatch difference

The relative mismatch difference (δM) represents a percentage by which detector response differs from its value under standard conditions. This difference does not express an overall impact of the solar spectral irradiance variations on detector response mismatch. The reason behind it is that the solar spectral irradiance at the standard atmospheric conditions can be accurately predicted with use of SMARTS[1] or other spectral irradiance model. Therefore, only the impact of deviation of the atmospheric conditions from their standard values should be considered.

The presented approach allows for an assessment of the impact of the variations of the specific atmospheric constituents from their standard values. This gives a clear indication of which atmospheric parameters variations have the highest impact on detector response mismatch.

[1]SMARTS - Simple Model of the Atmospheric Radiative Transfer of Sunshine

6.2.3 Standard AM1.5 spectrum

Over the years photovoltaic industry adopted the AM1.5 spectral irradiance[71] as the reference for characterisation of spectrally sensitive devices. This standard defines the direct and the global spectral irradiance under a set of specific conditions:

- inclined plane at 37° tilt towards equator
- air mass equal to 1.5 (48°15′33″ zenith angle[1])
- Ångström turbidity at 500nm equal to 0.084
- total column precipitable water equal to 1.42cm
- total column ozone equal to 0.34cm
- 1976 U.S standard atmosphere
- surface albedo of a light soil

The standardised AM1.5 spectrum gives only an approximation of the expected solar spectral irradiance, so it is not capable of representing seasonal and site-specific spectral irradiance variations (e.g. caused by variable air mass, aerosols concentration, precipitable water, impact of the clouds, zonal spectral albedo).

6.2.4 Spectral irradiance modelling

More detailed characterisation of the terrestrial spectral irradiance can be calculated from the available models of the atmospheric radiative transfer. These models can be classified in groups:

- restrictive code narrow band models (e.g. MODTRAN[2] [99])
- transmittance parametrisation models (e.g. SMARTS [87])

[1] value of the zenith angle calculated according to Kasten formula. At this range a simple formula ($\frac{1}{cos(\theta)}$) yields very close results of 48°11′23″

[2] MODTRAN -MODerate resolution atmospheric TRANsmission model

In comparison with the constant AM1.5 standard, the transmittance parametrisation models offer improved accuracy at the low computational cost. The SMARTS model has been used by the research community internationally and had become an unofficial standard for the spectral irradiance modelling in engineering applications, including photovoltaics. Use of SMARTS requires set of user specified input parameters to define the state of the atmosphere. The SMARTS model is a useful tool for investigating the effects of variation of different atmospheric constituents under clear sky conditions.

A substantial part of the work undertaken in this chapter uses the SMARTS spectral irradiance model. A dedicated batch-processing tool has been developed to run large numbers of simulations. Description of the software is given in the Appendix D. The SMARTS model takes as an input a set of atmospheric parameters, out of which some are deterministic and other not. The deterministic parameters of the SMARTS model include:

- geographic location
- time and date
- orientation of the receiving surface (tilt & azimuth)
- extraterrestrial spectrum
- atmosphere model
- carbon dioxide
- sun to earth distance variations

The non-deterministic parameters of the SMARTS model include:

- turbidity
- precipitable water
- ozone concentration
- aerosols type

- air pollutions
- zonal albedo (seasonally variable)

As shown above, the SMARTS parametrisation allows for simulation of the influence of most atmospheric parameters of interest in this study. Because of the SMARTS model's limitations, the impact of the clouds will not be discussed in this chapter. The impact of the clouds on spectral irradiance has been to a certain extent studied in chapter5.2.1 and was proven to be an important factor.

6.3 Results

6.3.1 Radiant power vs. photon flux

Initially the spectral irradiance is modelled without taking into account any variations in the atmospheric parameters. The nondeterministic atmospheric parameters were set to the mean values defined in reference AM1.5 spectrum. The presented results show the ratio of radiant power and photon flux received by the Earth's surface as a function of the air mass and the inclination angle of the receiving plane. Assuming a theoretical ideal device with 100% external quantum efficiency, all incident photons would have created a carrier. Therefore photon flux can be directly translated to photocurrent. The ratio of photocurrent and radiant power gives the total potential of the broadband irradiance to generate photocurrent (η_J).

As shown in Figure 6.2, both diffuse and direct irradiances are shifted towards longer wavelengths with increasing air mass. This occurs in both planes of observation. The observed results follow expectations. With increasing air mass, the direct irradiance is affected more heavily by the atmosphere. The spectral composition of purely diffuse skies is not expected to vary significantly with air mass. However the circumsolar fraction of diffuse irradiance causes an analogous shift in diffuse irradiance spectrum as direct irradiance. As expected, the potential of global irradiance to generate photocurrent differs significantly depending on the plane of array. This initially seems to contradict with the results of the observations presented for direct and diffuse fractions. To understand this further, the

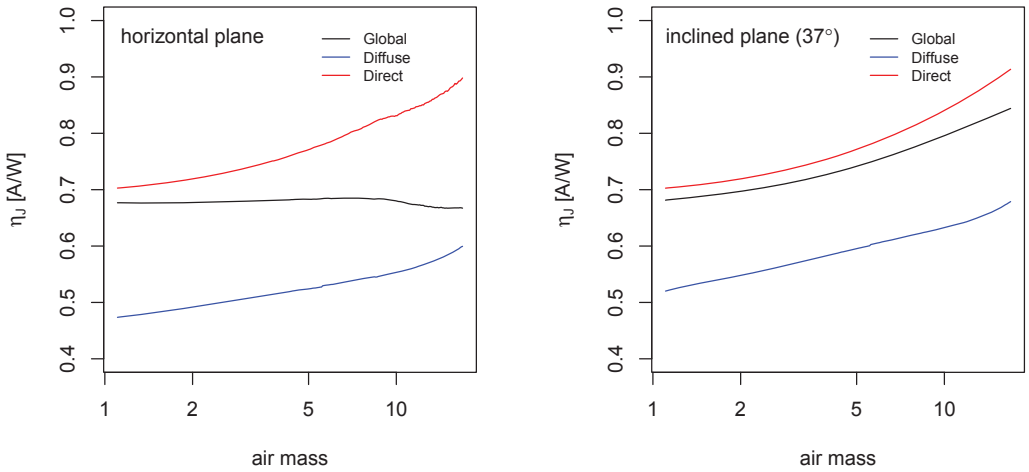

Figure 6.2: Total potential of broadband radiant power to generate photocurrent as a function of the air mass for two orientations of receiving plane: horizontal and south facing 37°-incline. Global, direct, and diffuse irradiances were presented separately. A 100% efficient device was assumed.

ratios of diffuse to direct irradiance need to be taken into account as presented in Figure 6.3.

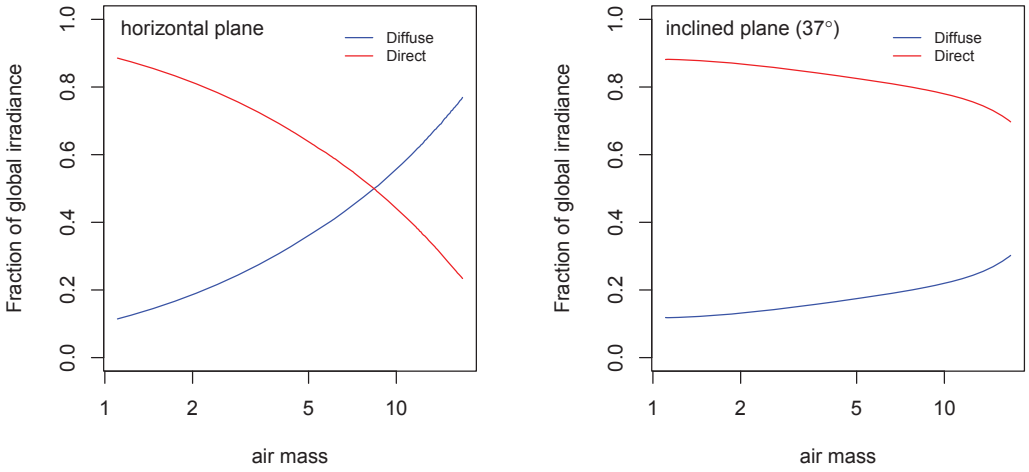

Figure 6.3: Share of direct and diffuse in a global irradiance for two planes of observation: horizontal and south facing 37°-incline.

As show in Figure 6.3 the ratios of diffuse to direct irradiance are very dif-

ferent for the horizontal and the inclined plane. With increasing air mass, the contribution of diffuse irradiance increases much faster in horizontal plane, than in the inclined plane. For the horizontal plane, the increasing diffuse irradiance compensates for the "red shift" demonstrated in Figure 6.2. This effect is less pronounced in the case of the inclined plane. Therefore, an increase in current generation potential of the radiant power is observed.

The results presented lead to the conclusion, that spectral variations in irradiance are not only dependent on the atmospheric composition and air mass, but also on the orientation of the receiving plane. Photovoltaic modules mounted horizontal will experience different spectral irradiance than modules installed in an inclined plane. Another fact worth noting is that the module reflectance for direct and diffuse irradiance differ, as direct irradiance is reflected more efficiently with an increasing angle of incident. This leads to the conclusion, that under a high air mass (high AOI), the fraction of direct irradiance reaching the cells will be decreased further by reflection. This effect will have a limiting impact on spectral differences. The utilisation of broadband radiometers (thermopile pyranometers) at the inclined plane will result in a greater discrepancy between measured radiant power and available photon flux than in a case of the horizontal plane.

6.3.2 Spectral sensitivity mismatch between the photovoltaic device and the reference broadband radiometer

Results presented up to now used total photon count available across the whole solar irradiance spectrum. Such an approach sets the scene and presents the impact of the spectral distribution of solar irradiance on the photon flux and radiant power. To discuss the impact of the spectral solar irradiance composition on the accuracy of a reference irradiance measurements for photovoltaic applications, simulated solar spectral irradiance was combined with the spectral responses of commonly used photovoltaic cells and broadband radiometer. It is assumed, that the composition of the atmosphere does not change, and the simulated spectral irradiance vary solely due to the impact of the air mass and orientation of

the receiving plane. Variations of the atmosphere's composition are considered separately in section 6.3.4

A ratio between broadband reference irradiance and photocurrent generated by various photovoltaic devices ($M_{specific}$) was calculated. To simplify the comparison between the different technologies value of $M_{specific}$ was normalised by $M_{AM1.5}$. Values defined as such can be treated as a technology specific corrective coefficient of the broadband radiometer. Figure 6.4 presents corrective coefficients for a reference broadband radiometer for different module cell technologies.

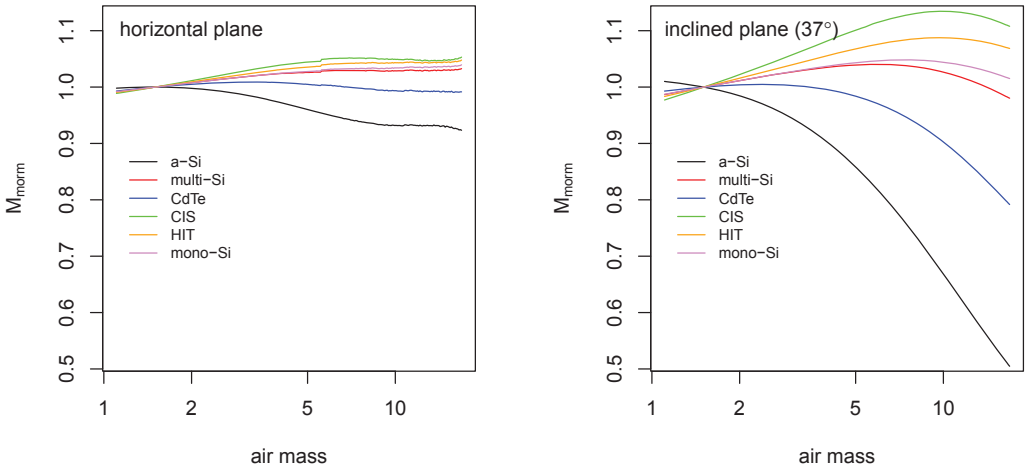

Figure 6.4: Broadband radiometer correction coefficients for a variety of cell technologies.

Figure 6.5 presents corrective coefficient for multi-crystalline silicon solar cell in dependence of air mass for horizontal and inclined plane where direct and the diffuse irradiance fractions were overlaid.

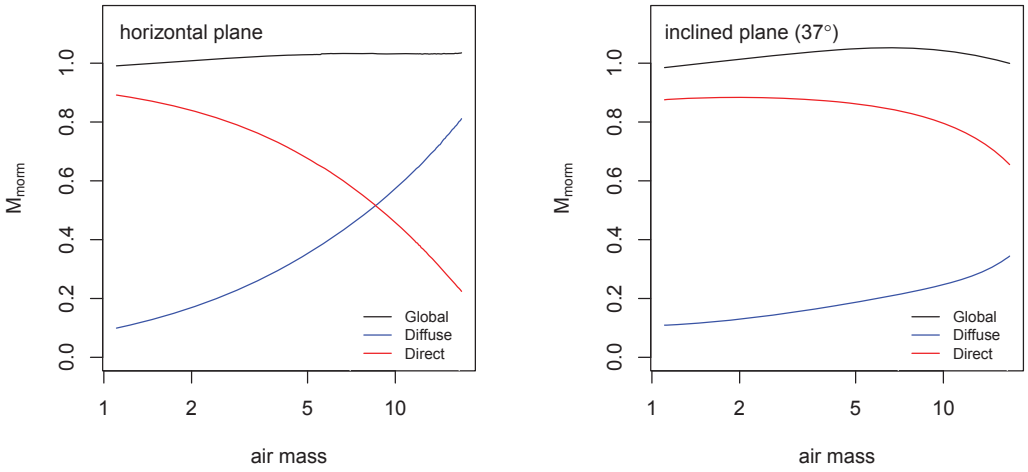

Figure 6.5: Broadband radiometer correction coefficients for multi-cSi cell.

In the figures presented it can be observed, that regardless of photovoltaic device technology, the ratios between generated short circuit current and measured broadband irradiance vary less significantly for a horizontal plane than for an inclined plane. Variations are heavily dependent on cell specific spectral response. The coefficients presented can be used as a simple way of correcting the broadband irradiance measurements for the spectral irradiance effects. Moreover it was shown that the level of utilisation of the diffuse irradiance has the greatest impact on the difference between generated short circuit current and the observed radiant power. As presented in chapter 5, the global spectral irradiance under cloudy skies is dominated by the diffuse fraction. Spectral correction coefficient of a broadband irradiance can be defined for every combination of the air mass and direct to diffuse irradiance ratio. This opens up the possibility of achieving a correction method of broadband radiometer measurements applicable for all sky conditions and relevant to any cell technology.

6.3.3 Spectral sensitivity mismatch between the photovoltaic device and the reference cell

Using a reference cell instead of broadband radiometers seems to be beneficial from the perspective of minimising spectral mismatch. However it should be noticed that the relative differences in the spectral response of a mono-crystalline silicon reference cell and the broadband radiometer are in many occasions smaller than the differences between mono-crystalline silicon reference cell and photovoltaic devices of a different technology. For an example, the response from a broadband detector is closer to the response of the CdTe based device than the response from a mono-crystalline reference cell. Figure 6.6 presents corrective coefficients for mono-crystalline silicon reference cell for different photovoltaic device technologies.

Figure 6.6 demonstrates that using a mono-crystalline silicon solar cell reduces spectral mismatch between the reference detector and the photovoltaic device only for a limited number of photovoltaic device technologies. Further corrections are still required to minimise the effect of spectral mismatch.

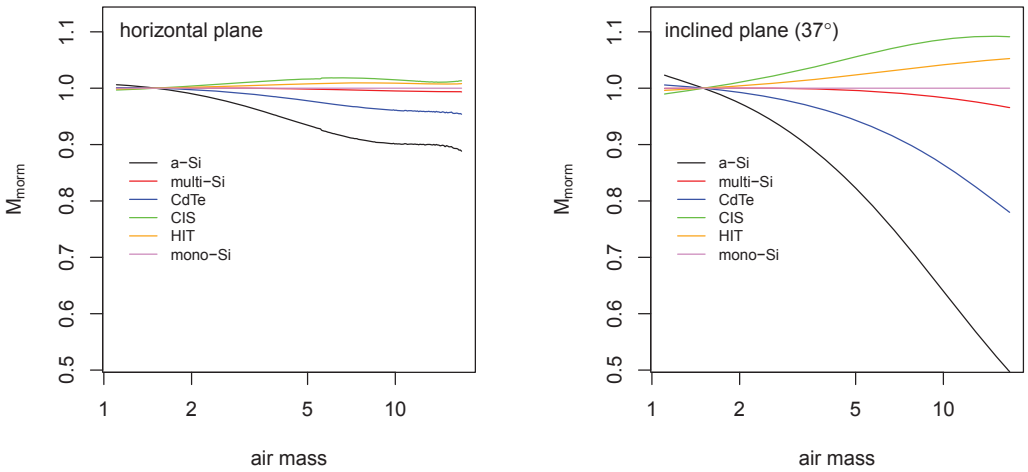

Figure 6.6: Reference cell generation potential correction coefficient for a variety of cell technologies.

6.3.4 Impact of atmospheric parameters variations on the accuracy of the reference measurements

In previous sections it was shown that the spectral mismatch between a reference irradiance detector and a specific photovoltaic cell have a significant impact on accuracy of the reference measurements. Up to this point, the spectral composition of the atmosphere was assumed to be constant with time. The only parameters varied were the air mass and the incident plane. These assumptions are far from being realistic. Some of the atmospheric constituents vary seasonally and others on a daily basis. Impact of variations of the atmosphere's composition on the accuracy of the reference measurements for specific cell technologies was investigated to reveal the most influential atmospheric constituents. Attention was focused on six atmospheric properties:

- aerosol loading
- aerosol types
- precipitable water
- ozone concentration

- atmospheric pollutants
- zonal spectral albedo

Spectral effects caused by these constituents are scaled by air mass. Moreover, the inclination angle of the receiving plane affects the ratio between diffuse and direct solar spectral irradiance. Thus, the analysis takes into account the air mass and inclination angle as additional variables. Analysis of the impact of each constituent is preceded by a short description of phenomena caused by the different constituents. Furthermore, the expected ranges of variation are discussed in details.

6.3.4.1 Aerosols

A quantitative and qualitative description of aerosol content is given by the aerosol optical depth. The aerosol's optical depth is a wavelength-dependent function of concentration and shape of aerosol particles[100–102]. The smaller the particles, the stronger the spectral effects become. A simple equation representing the aerosol optical depth (6.6) was proposed by Ångström [103].

$$\tau_a = \frac{\beta}{\lambda^{\alpha}} \tag{6.6}$$

Parameter λ in the equation 6.6 denotes the wavelength. Parameters α and β denote wavelength-independent, unitless Ångström turbidity coefficients. Parameter β relates to aerosols load and is defines as an aerosols optical thickness at $\lambda = 1\mu m$. Parameter α relates to the average particle size. The Ångström approach assumes unimodal distribution of particles shape, which is debatable in the natural environment. Aerosol optical depth observations are based on a set of direct normal irradiance measurements taken at the wavelengths affected by specific scattering effects (e.g. AERONET[1] [104] : 340nm, 380nm, 440nm, 500nm, 675nm, 865nm). Observations of the direct irradiance at two different wavelengths allows the calculation of the Ångström exponent (see equation 6.7).

$$\alpha = \frac{ln\tau_1 - ln\tau_2}{ln\lambda_1 - ln\lambda_2} \tag{6.7}$$

[1] AERONET - Aerosol Robotic Network

Aerosol optical depth is retrieved from two kinds of measurements. The first one uses ground-based sun photometers and compares direct solar irradiances measured for selection of narrow bands (e.g. AERONET). The second method is based on satellite measurements of spectral irradiance reflected from the surface of the earth, oceans or clouds (e.g. MODIS[1] Terre/Aqua). Satellite measurements are considerably less accurate in terms of absolute measurement uncertainty, but they provide much higher spatial resolution. In the natural environment, the monthly averaged aerosol optical depth vary mainly in a range of 0.1 to 0.3, with extremes reaching 0.7-1.5 in regions affected by large forest fires or sandstorms (where τ_{500}=1.5 means that under air mass AM=1.2 83.5% of a direct irradiance at 500nm region is being scattered by aerosols). Figure 6.7 shows the aerosol optical depth retrieved from spectral measurements recorded by MODIS Terra satellite in September 2012.

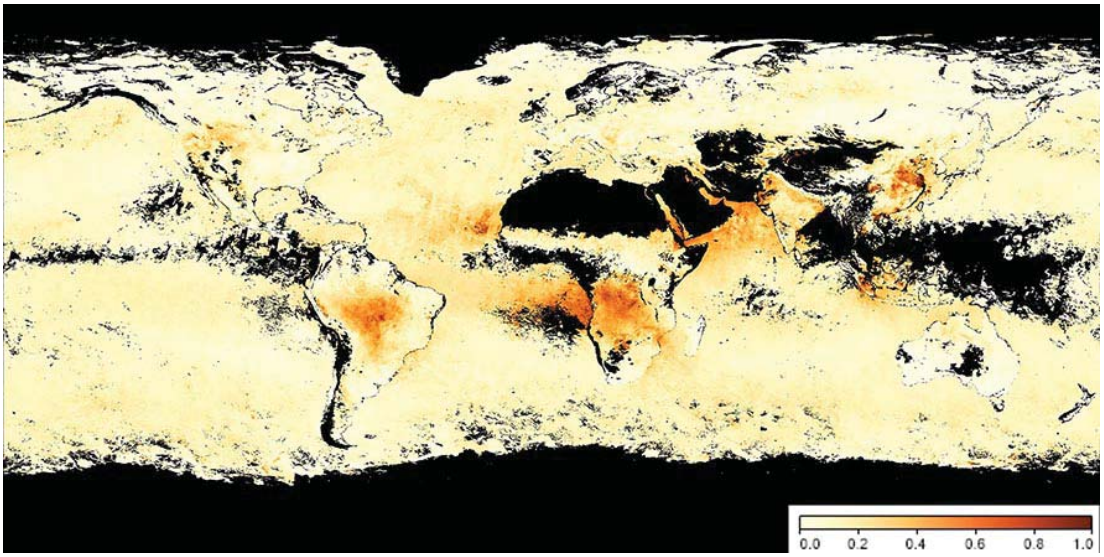

Figure 6.7: Global aerosols distribution for September 2012 registered by MODIS Terra meteorological satellite (black colour represents regions, where data is unavailable

As it can be observed in Figure 6.7 the aerosol's optical depth over Europe is on the lower end of the observable range. Figure 6.8 shows aerosol optical

[1]MODIS - Moderate Resolution Imaging Spectroradiometer

depth retrieved form MODIS Terra satellite spectral irradiance measurements taken between April and September 2012.

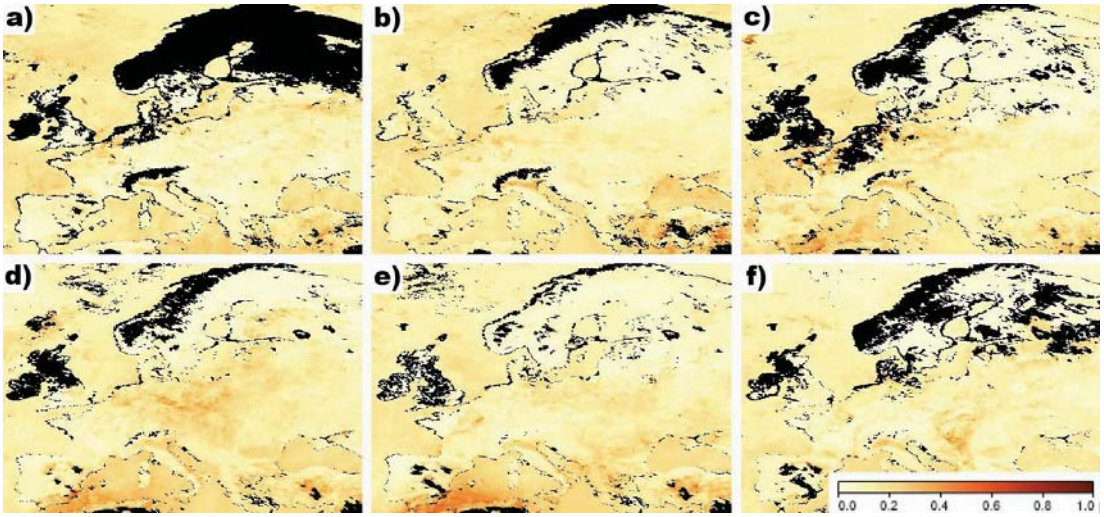

Figure 6.8: Aerosols distribution measured by MODIS over Europe : a) April, b) May, c) June, d) July, e) August, f) September

Whilst the aerosol optical depth does not vary dramatically across Europe (if not affected by localised pollution centres or incidental events), other places on Earth can be heavily affected by seasonal forest fires, sandstorms, particulate matter (PM) pollution to a much greater extent. Figure 6.9 shows aerosol optical depth retrieved from spectral measurements taken by MODIS Terra satellite in September 2012 over different parts of the world.

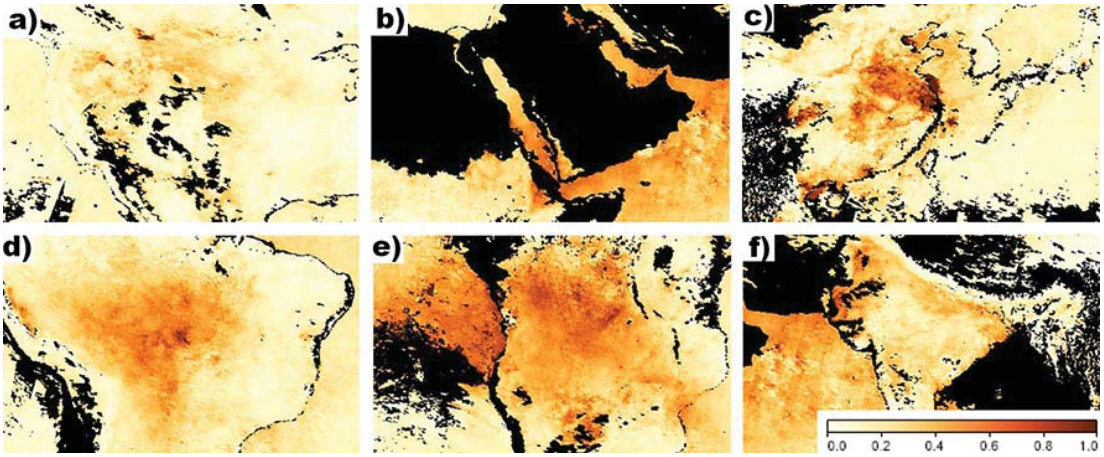

Figure 6.9: Aerosols distribution registered by MODIS over different parts of the world, accordingly: a)North America, b) Middle East c) East Asia, d) South America, e) South Africa, f) India

A more accurate but less spatially dense set of aerosol's optical depth measurements is being created by a network of terrestrial sun-photometers (AERONET). Figure 6.10 illustrates variations of the aerosol optical depth registered at the selected geographic locations by the AERONET.

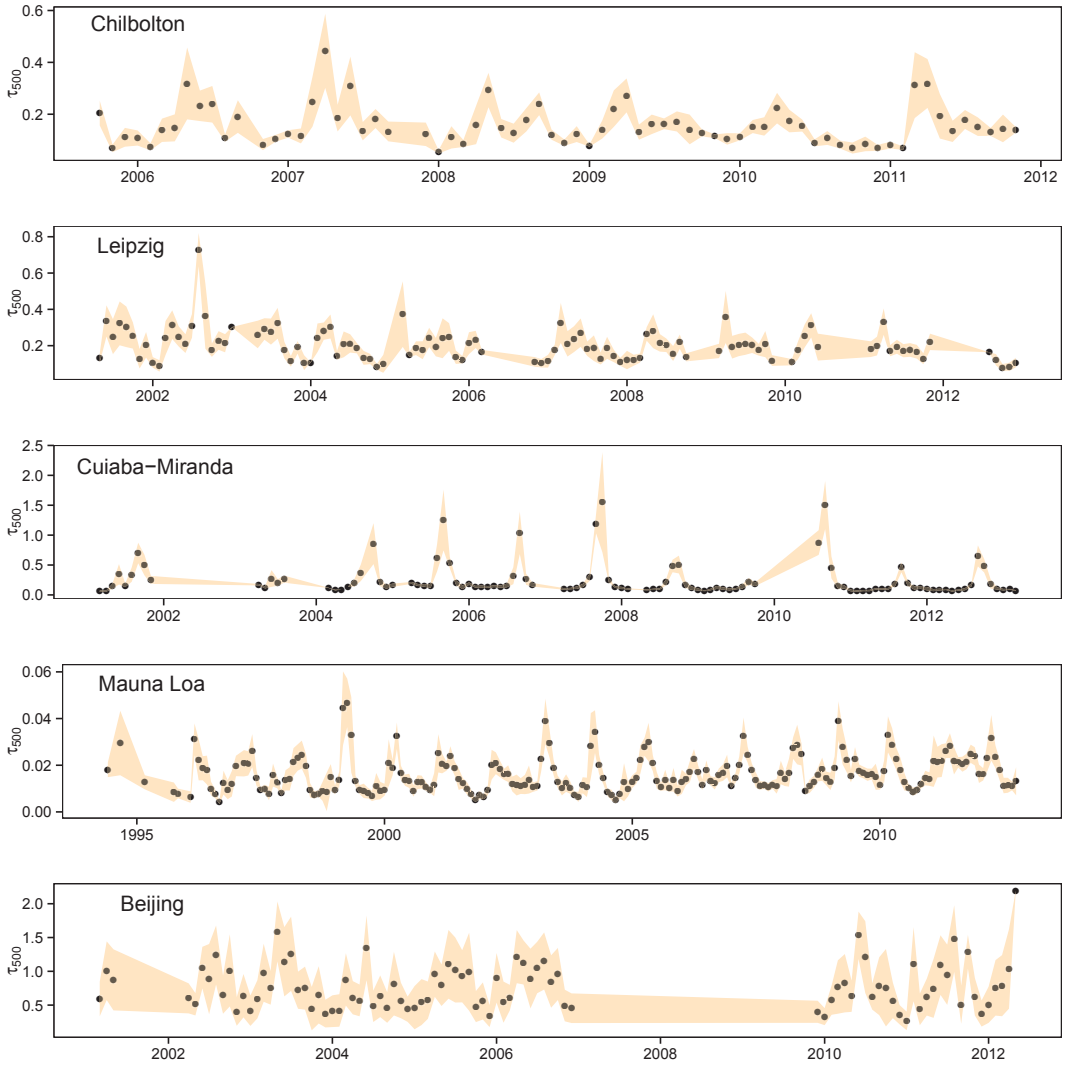

Figure 6.10: Aerosol optical depth (tau_a) measured for 500nm in different geographic locations including: Chilbolton (UK), Leipzig (Germany), Cuiaba-Miranda (Brazil), Mauna Loa (USA), Beijing (China) measured by the AERONET network

As shown in Figure 6.10 aerosol optical thickness can significantly vary between locations, but also in the temporal domain. As an example, Cuiaba-Miranda shows moderate aerosol optical thickness for the most of the time, with an incidental increase caused by seasonal forest fires. Variations in types of aerosols and concentrations have a significant impact on spectral irradiance reaching the surface of the earth in the visible range. Therefore aerosols are considered a relevant factor impacting energy generation of photovoltaic modules. To investigate the impact of aerosols variations on the specific solar cell technologies spectral irradiance was simulated with SMARTS. Simulations were repeated for a range of aerosol concentrations typically observed in natural environment and across the most probable air mass values. Remaining SMARTS model parameters (precipitable water, ozone concentration, atmospheric pressure, aerosols model, pollutions) were set as defined in a standard.

Simulated spectral irradiance was combined with the typical spectral response of a given cell technology resulting in expected photocurrent density (output signal S_D). The relative difference (δM) between specific detector response mismatch under the modified atmospheric conditions ($M_{specific}$) and the standard detector response mismatch value ($M_{AM1.5}$) at the standard atmospheric conditions was calculated.

This demonstrates by how much the detector response mismatch varies from its value standard value $M_{AM1.5}$[1] distribution of spectral irradiance. Figures 6.11 to 6.22 present relative differences between detector response mismatch under specific turbidity in relation to detector response mismatch under standard atmosphere turbidity (0.084). Calculations were performed for a set of most common photovoltaic cells and in relation to broadband pyrometer and mono-cSi reference cell. Where possible results were presented in the same scale for a broadband and mono-cSi reference detectors to simplify a comparison.

[1]The adjusted standard spectrum represents spectral irradiance simulated with use of SMARTS model, where parameters were set to standard values, but the adjustments were made for the specific plane of array and the air mass

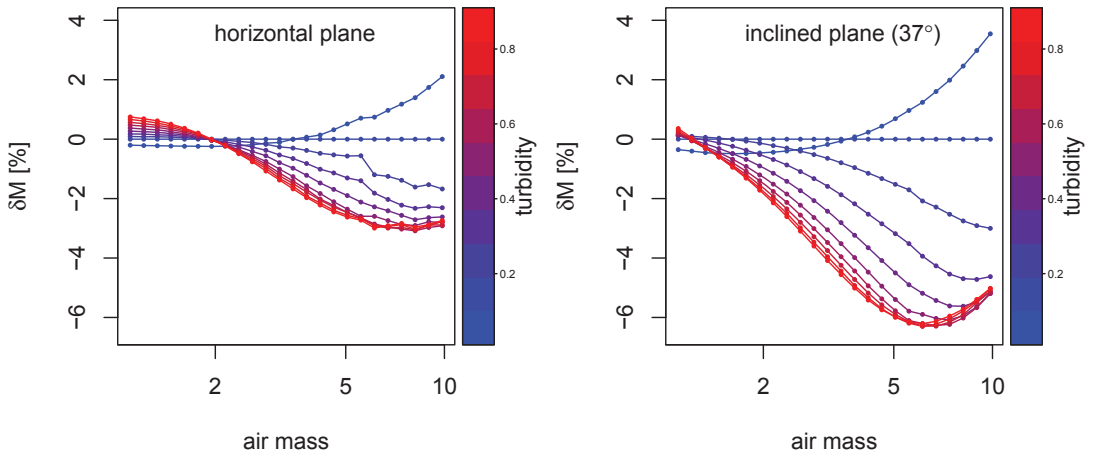

Figure 6.11: Impact of aerosols concentration on the relative difference between $M_{specific}$ and $M_{AM1.5}$ for a multi-cSi cell and a broadband reference detector

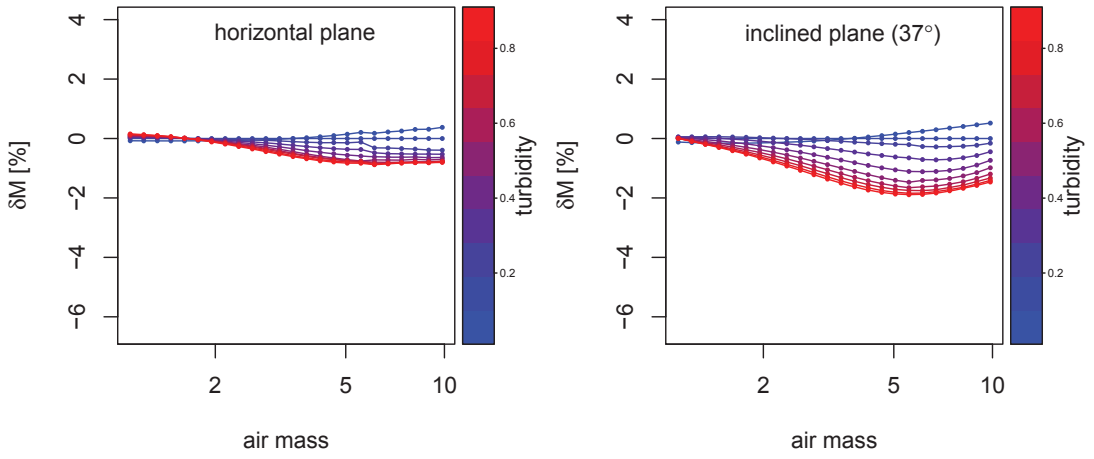

Figure 6.12: Impact of aerosols concentration on the relative difference between $M_{specific}$ and $M_{AM1.5}$ for a multi-c-Si cell and a mono-cSi reference detector

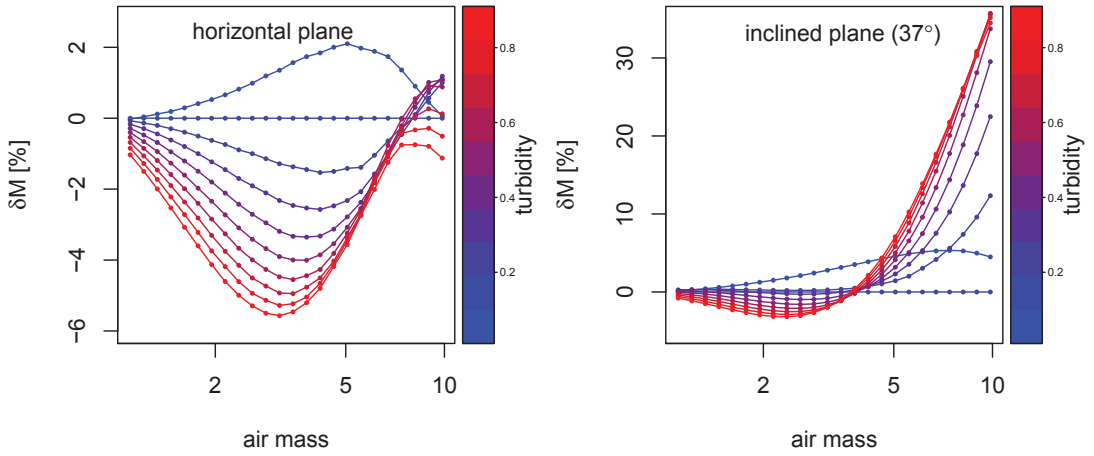

Figure 6.13: Impact of aerosols concentration on the relative difference between $M_{specific}$ and $M_{AM1.5}$ for an a-Si cell and a broadband reference detector

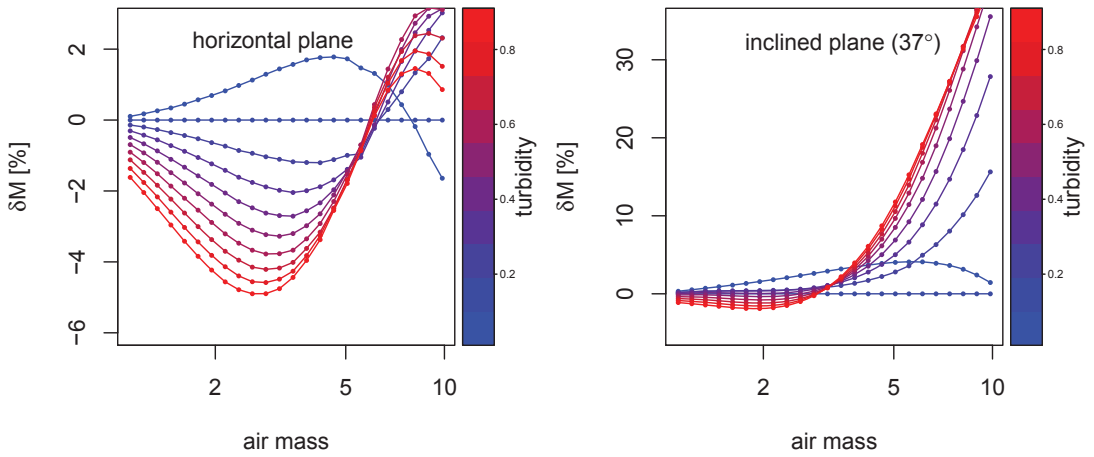

Figure 6.14: Impact of aerosols concentration on the relative difference between $M_{specific}$ and $M_{AM1.5}$ for an a-Si cell and a mono-cSi reference detector

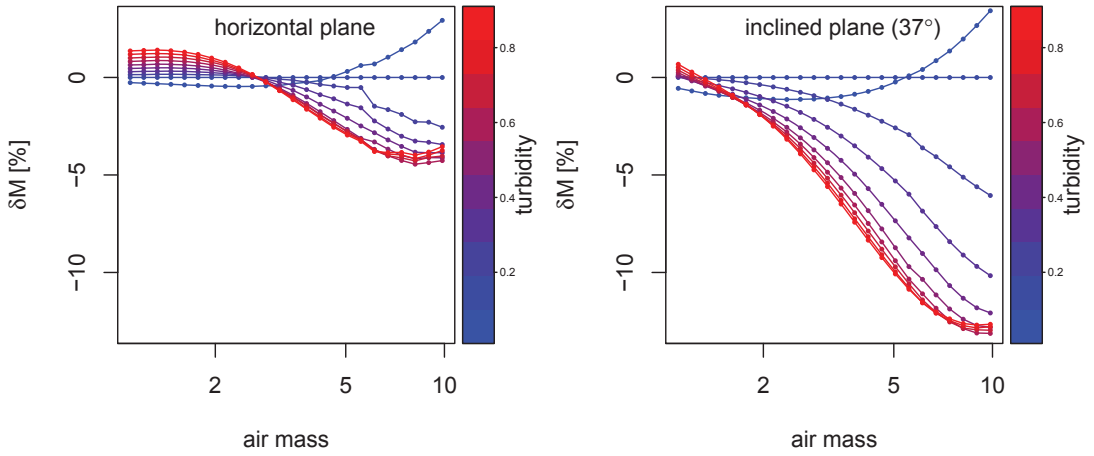

Figure 6.15: Impact of aerosols concentration on the relative difference between $M_{specific}$ and $M_{AM1.5}$ for a CIS cell and a broadband reference detector

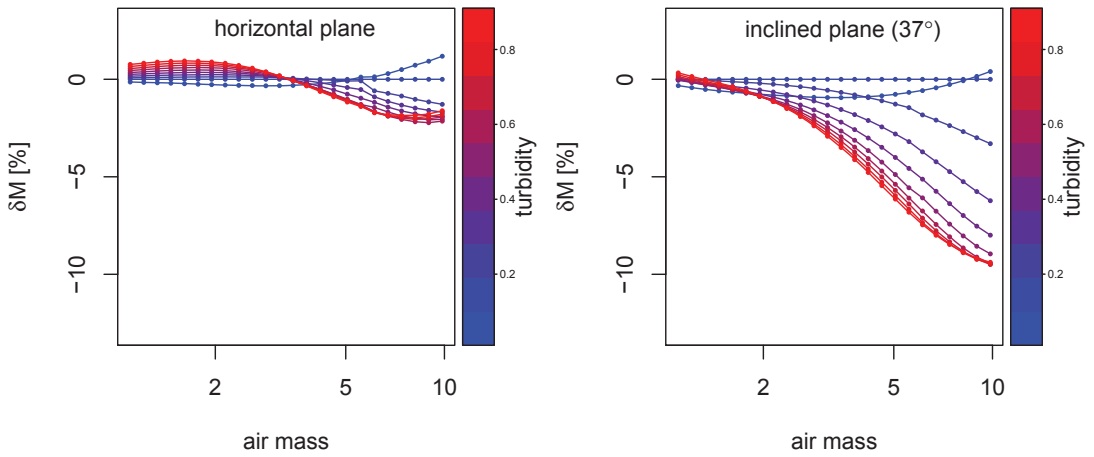

Figure 6.16: Impact of aerosols concentration on the relative difference between $M_{specific}$ and $M_{AM1.5}$ for a CIS cell and a mono-cSi reference detector

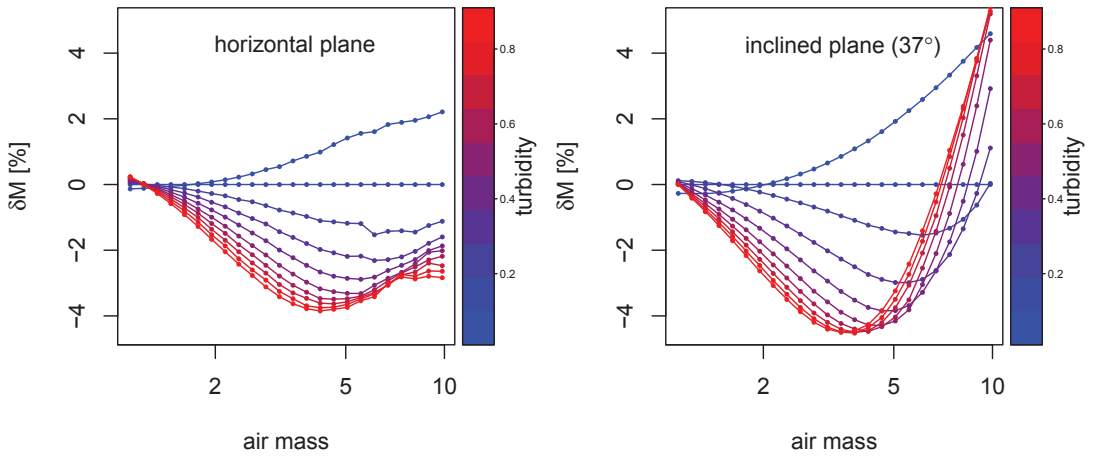

Figure 6.17: Impact of aerosols concentration on the relative difference between $M_{specific}$ and $M_{AM1.5}$ for a CdTe cell and a broadband reference detector

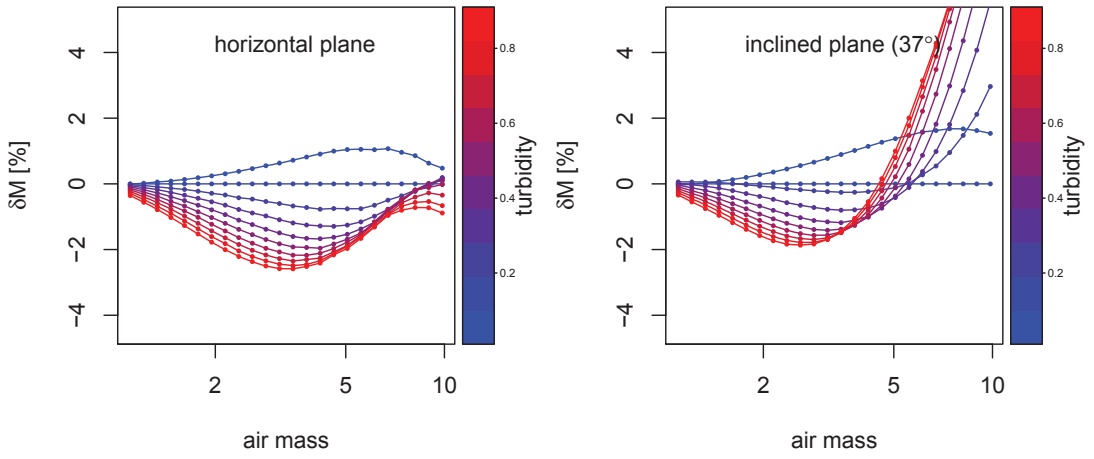

Figure 6.18: Impact of aerosols concentration on the relative difference between $M_{specific}$ and $M_{AM1.5}$ for a CdTe cell and a mono-cSi reference detector

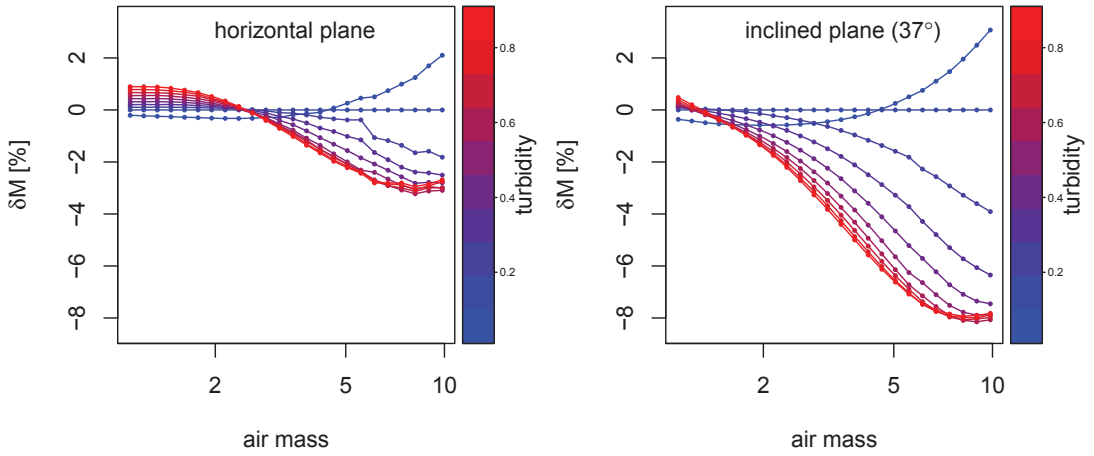

Figure 6.19: Impact of aerosols concentration on the relative difference between $M_{specific}$ and $M_{AM1.5}$ for a HIT cell and a broadband reference detector

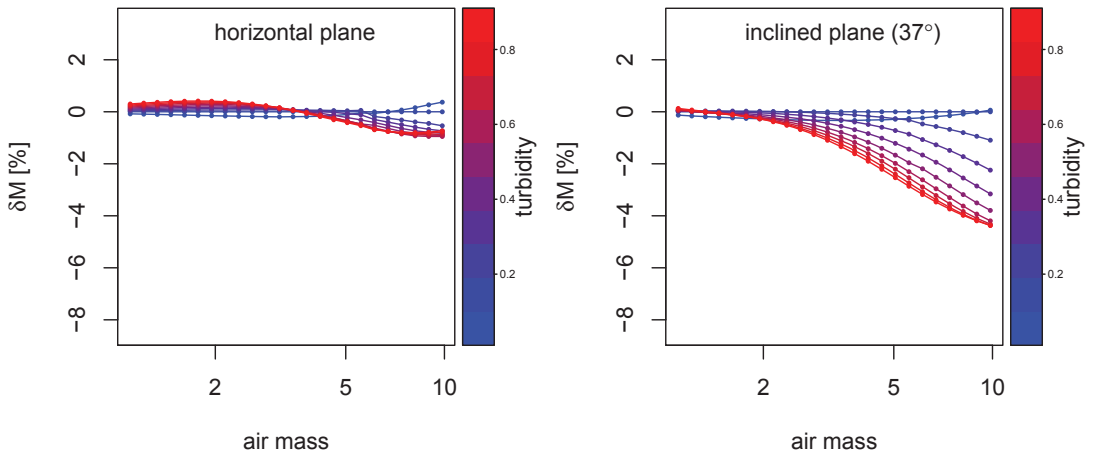

Figure 6.20: Impact of aerosols concentration on the relative difference between $M_{specific}$ and $M_{AM1.5}$ for a HIT cell and a mono-cSi reference detector

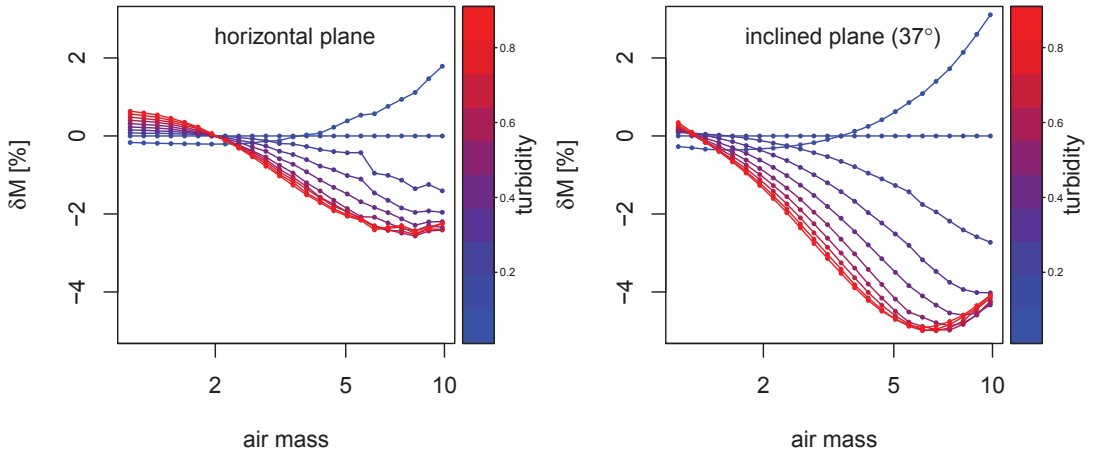

Figure 6.21: Impact of aerosols concentration on the relative difference between $M_{specific}$ and $M_{AM1.5}$ for a mono-cSi cell and a broadband reference detector

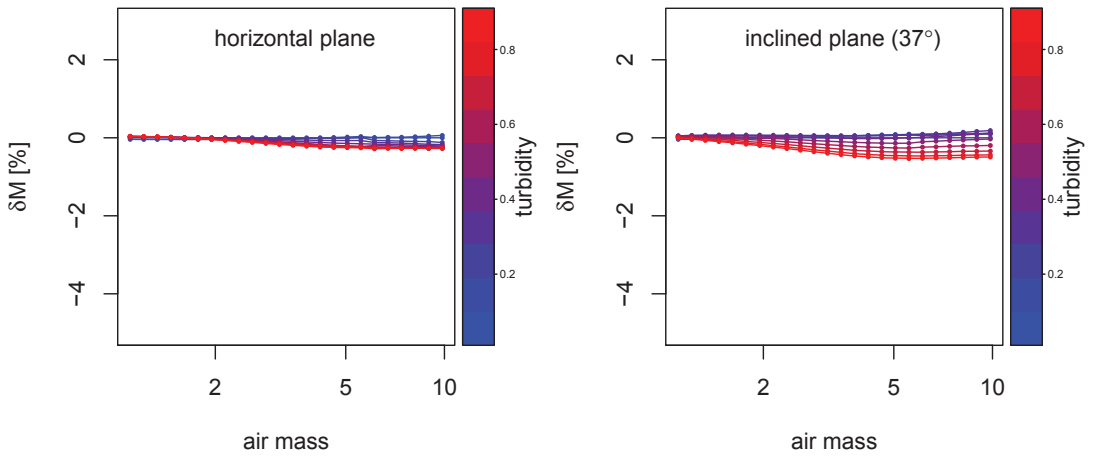

Figure 6.22: Impact of aerosols concentration on the relative difference between $M_{specific}$ and $M_{AM1.5}$ for a mono-cSi cell and a mono-cSi reference detector

Aerosols impacted on detector response mismatch in all presented cases. The magnitude and character of observed changes are photovoltaic device technology specific. The differences between horizontal and inclined planes can be observed. These differences become more significant for narrowband technologies (e.g. a-Si) and under high air mass. The dependence on the air mass is not monotonic. This is attributed to the variation of the diffuse and the direct components ratio. In some cases (excluding CIS, HIT, mono- and multi-crystalline cells in horizontal planes), the relative differences in detector mismatch was equal or greater than 3% for the air mass less than 3. This indicates a non-negligible effect of turbidity on spectral irradiance. Aerosol variations should not be ignored in the case of photovoltaic applications. In general, a lower difference in generation efficiency was observed for a mono-cSi reference cell than for a broadband detector. For air masses below 4 all cells performed closer to the mono-cSi reference cell than to the broadband reference detector. The greatest improvement was achieved for mono-cSi and multi-cSi cells. For air masses above 4 the response of a-Si and CdTe was closer to the broadband reference detector, however it should be noted that the relative difference was very high for both reference detectors at this point.

Besides the aerosol concentration (turbidity), the type of aerosols also impact differently on the spectrum. Figures 6.23 to 6.34 present relative differences in detector response mismatch under specific aerosols type in relation to the current generation efficiency of incident solar radiation under standard atmosphere (rural aerosol loading). Calculations were performed for a set of common photovoltaic cells and in relation to broadband pyrometer and mono-cSi reference cell.

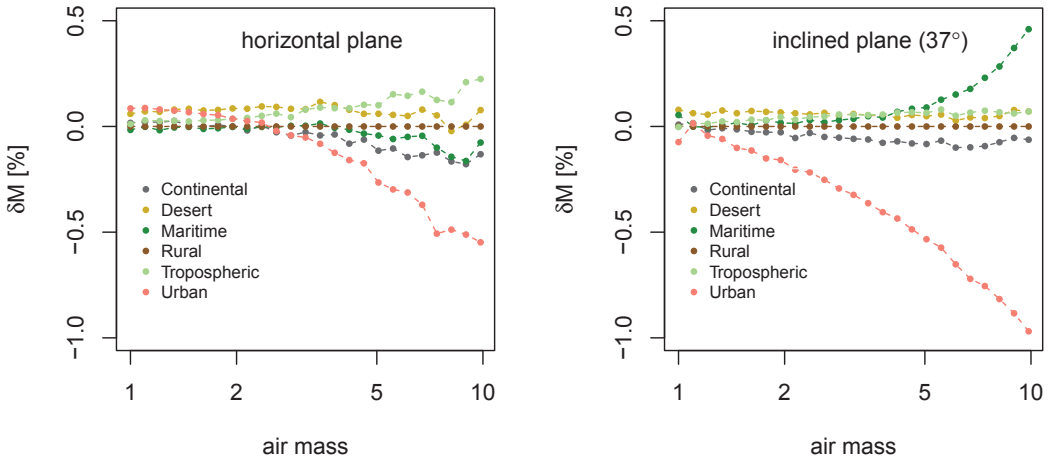

Figure 6.23: Impact of aerosols type on the relative difference between $M_{specific}$ and $M_{AM1.5}$ for a multi-cSi cell and a broadband reference detector

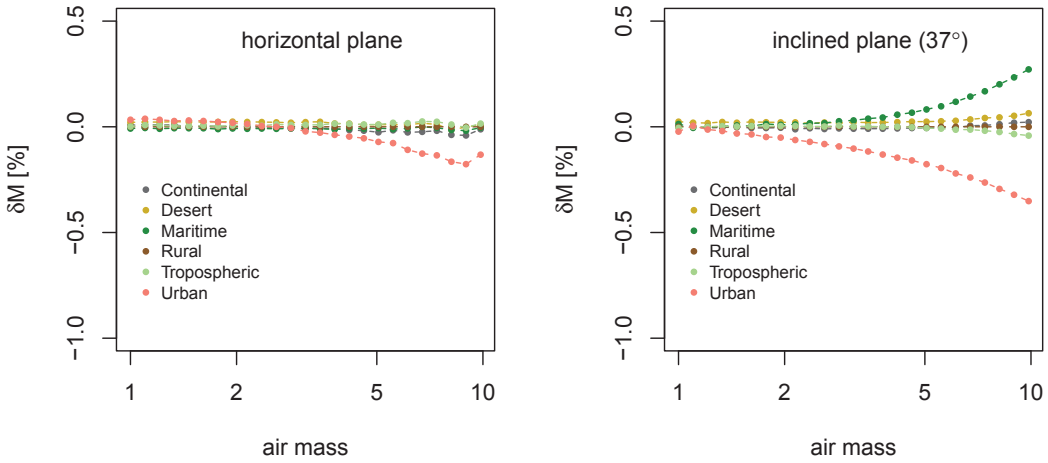

Figure 6.24: Impact of aerosols type on the relative difference between $M_{specific}$ and $M_{AM1.5}$ for a multi-cSi cell and a mono-cSi reference detector

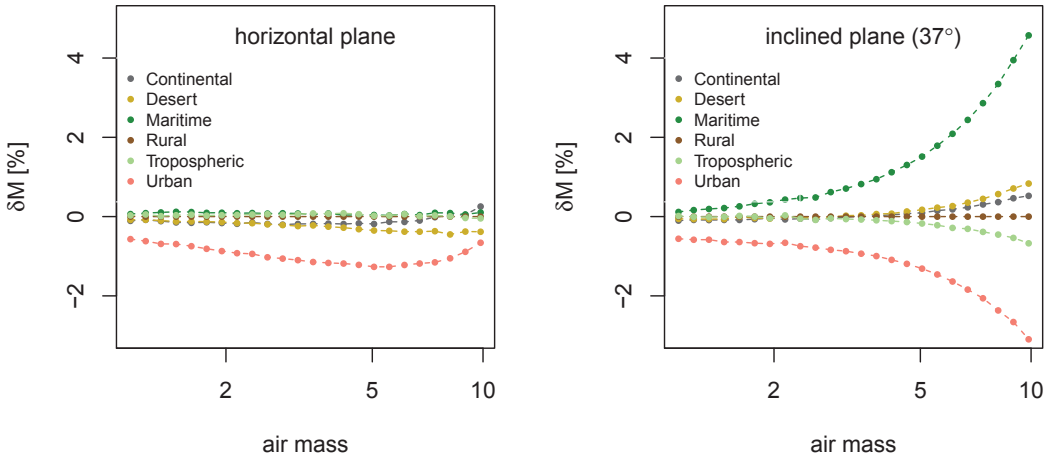

Figure 6.25: Impact of aerosols type on the relative difference between $M_{specific}$ and $M_{AM1.5}$ for an a-Si cell and a broadband reference detector

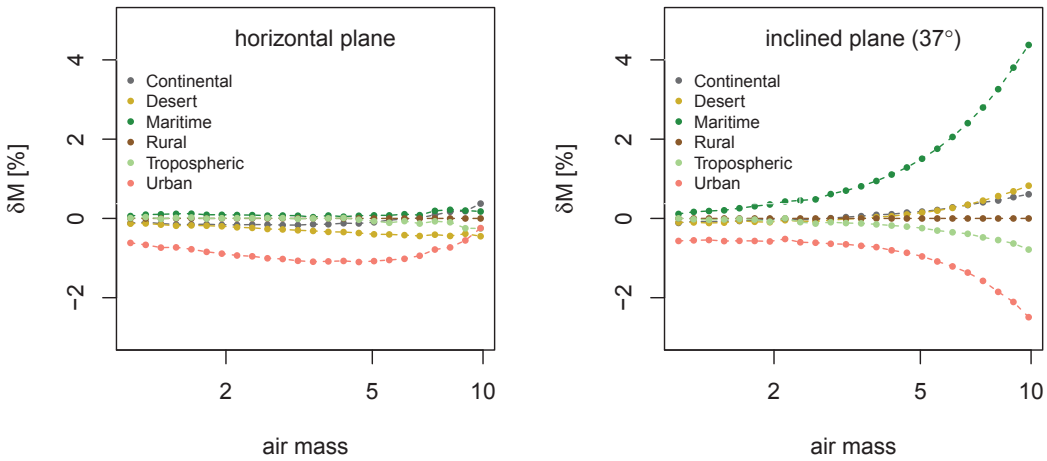

Figure 6.26: Impact of aerosols type on the relative difference between $M_{specific}$ and $M_{AM1.5}$ for an a-Si cell and a mono-cSi reference detector

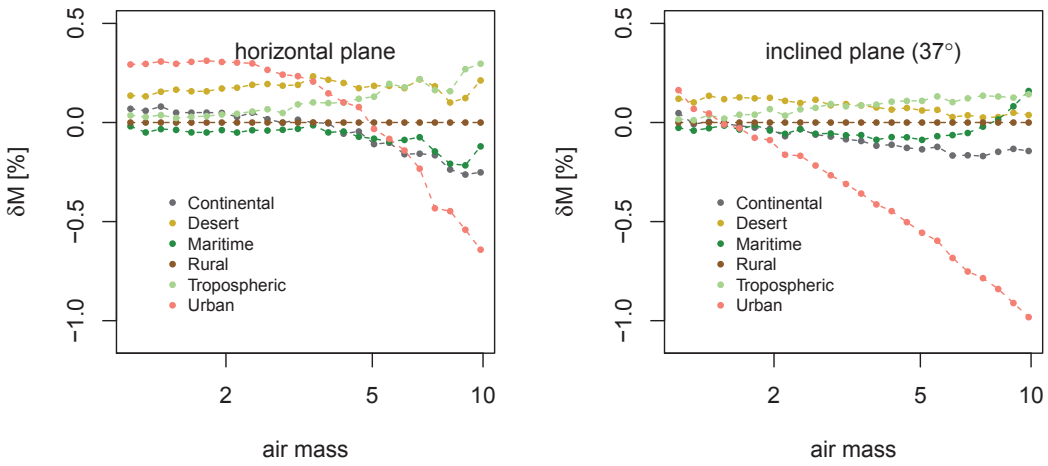

Figure 6.27: Impact of aerosols type on the relative difference between $M_{specific}$ and $M_{AM1.5}$ for a CIS cell and a broadband reference detector

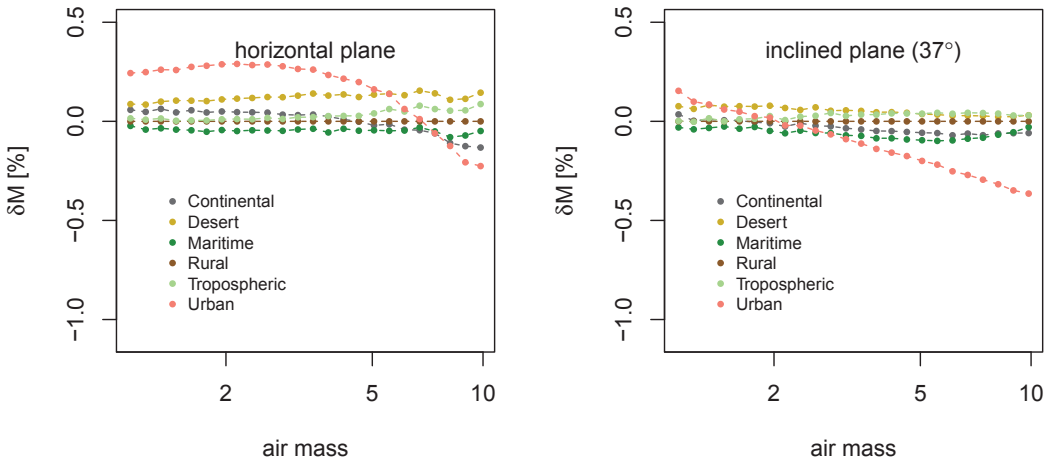

Figure 6.28: Impact of aerosols type on the relative difference between $M_{specific}$ and $M_{AM1.5}$ for a CIS cell and a mono-cSi reference detector

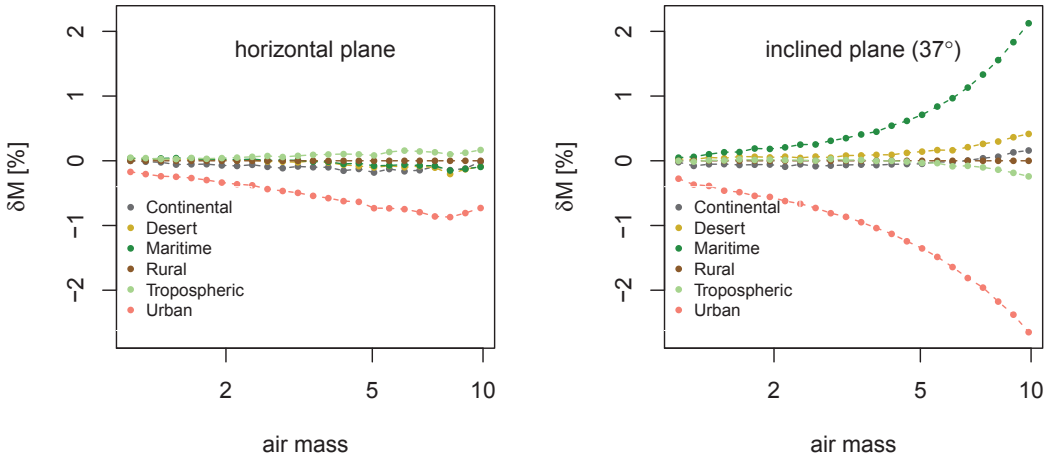

Figure 6.29: Impact of aerosols type on the relative difference between $M_{specific}$ and $M_{AM1.5}$ for a CdTe cell and a broadband reference detector

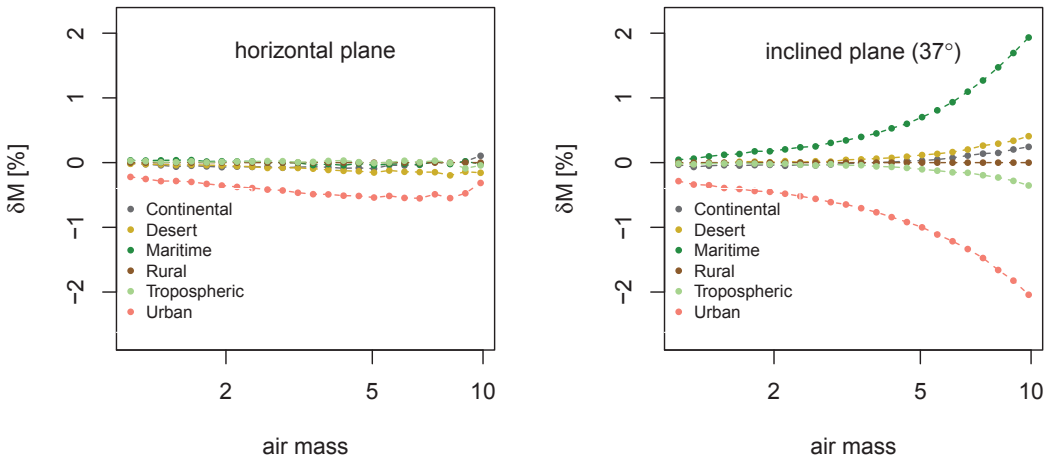

Figure 6.30: Impact of aerosols type on the relative difference between $M_{specific}$ and $M_{AM1.5}$ for a CdTe cell and a mono-cSi reference detector

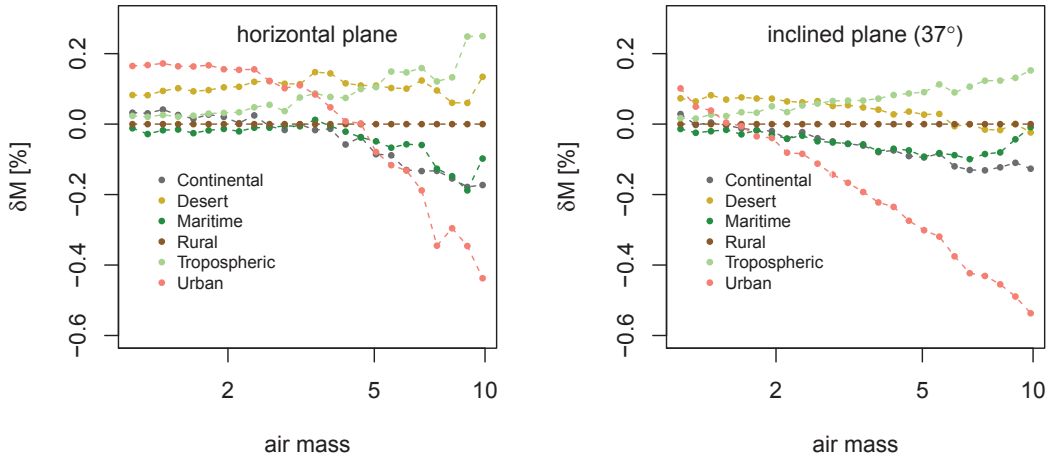

Figure 6.31: Impact of aerosols type on the relative difference between $M_{specific}$ and $M_{AM1.5}$ for a HIT cell and a broadband reference detector

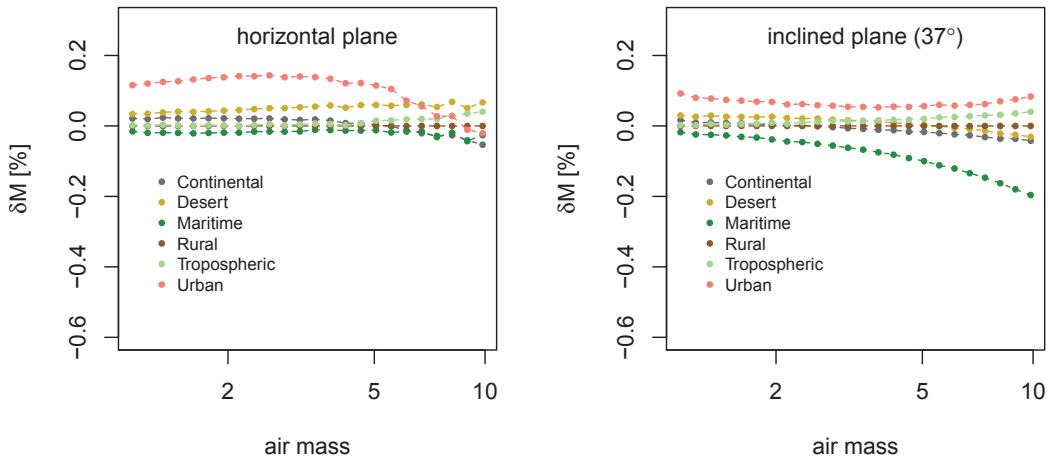

Figure 6.32: Impact of aerosols type on the relative difference between $M_{specific}$ and $M_{AM1.5}$ for a HIT cell and a mono-cSi reference detector

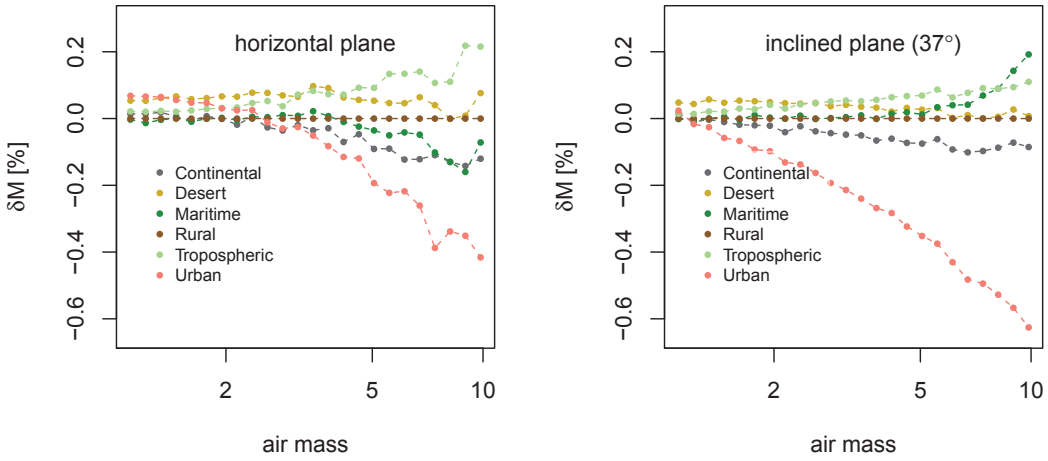

Figure 6.33: Impact of aerosols type on the relative difference between $M_{specific}$ and $M_{AM1.5}$ for a mono-cSi cell and a broadband reference detector

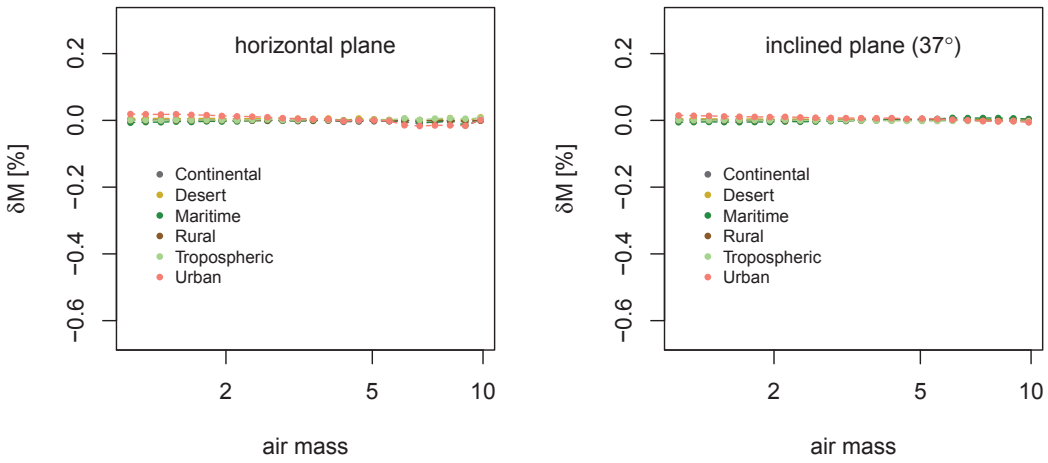

Figure 6.34: Impact of aerosols type on the relative difference between $M_{specific}$ and $M_{AM1.5}$ for a mono-cSi cell and a mono-cSi reference detector

Different aerosol types seem not to have such a strong effect as turbidity (aerosols loading). In most cases the impact of the aerosols type caused less than a 0.5% of difference in detector mismatch in comparison to rural aerosols type used in standard spectrum. Amorphous silicon and CdTe were affected the most with extremes reaching from 4% to -2% for a-Si and 2% to -3% for CdTe. It should be noted, that these extremes occurred for urban and maritime aerosol types. This analysis has shown that the impact of aerosol types can be treated as a secondary factor in most cases. Utilisation of a mono-cSi detector instead of broadband detector for reference measurements can even further decrease the strength of an impact of aerosol type. These improvements were not observed in case of a-Si and CdTe cells.

6.3.4.2 Precipitable Water

Precipitable water has a limited impact on spectral irradiance in the visible range. Weak absorption bands are in the spectral regions of $560nm - 610nm$, $680nm - 750nm$. The main absorption bands are in the infrared and microwave region. Yearly averaged precipitable water varies from $0.6g/cm^2$ in the polar climate to $4.4g/cm^2$ for the tropical climate [105]. Short-term anomalies from long term observations do not exceed 200%. Column precipitable water (CPW) is an integral of absolute air humidity over the thickness of the atmosphere. In other words it can be defined as a water column (expressed in g or cm) that would have been created if the entire water vapour from the atmosphere over a given area (m^2,cm^2) would have precipitated. When calculating the radiative transfer, the total precipitable water (TPW) is frequently used, which takes into account effective thickness of the atmosphere (similarly to the air mass).

Figure 6.35 presents the water vapour transmittance of the direct radiation for precipitable water equal to $w = 1g/cm^2$ (black line). The area around the line represents variations for w ranging from $0.1cm$ to $12cm$. This range generously covers the values of total precipitable water in the atmosphere observed.

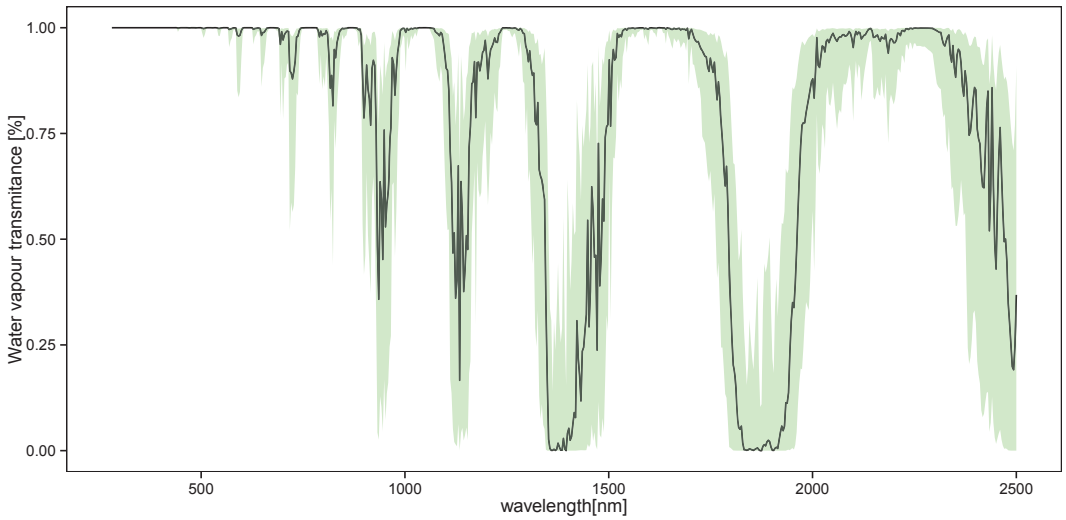

Figure 6.35: Water vapour transmittance for precipitable water vapour ranging from $0.1g/cm^2$ to $12g/cm^2$

Figure 6.36 presents H_2O absorption of a different bands for precipitable water ranging from w=0.1 to w=12.

It is shown in Figure 6.36 that some water absorption bands are within the spectral working range of photovoltaic cells, therefore they will have an impact on generation efficiency. The impact of precipitable water on photovoltaic cells was investigated similarly to the impact of aerosols. Spectral irradiance was calculated for precipitable water vapour varying in the range of 1 to $12g/cm$. The spectral irradiance was then combined with the external quantum efficiency of the specific photovoltaic devices. Relative differences between the specific and standard detector response mismatch was calculated.

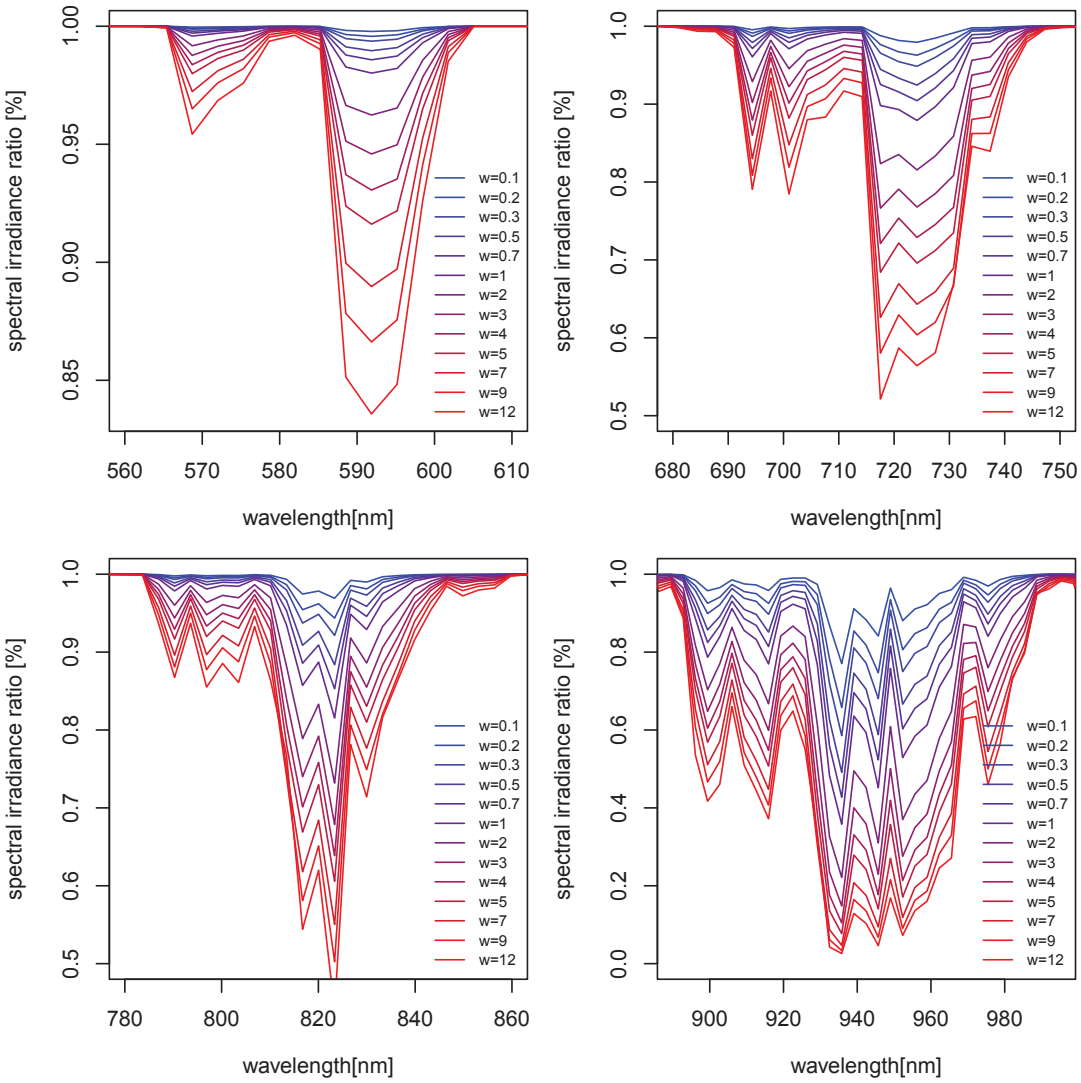

Figure 6.36: Band absorption caused by precipitable water (w) ranging from 0.1 to 12

The impact of precipitable water variations on the difference in specific cell and reference irradiance detector responses was presented in Figures 6.37 to 6.48. Calculations were performed for a set of most common photovoltaic cells and in relation to broadband pyrometer and mono-cSi reference cell.

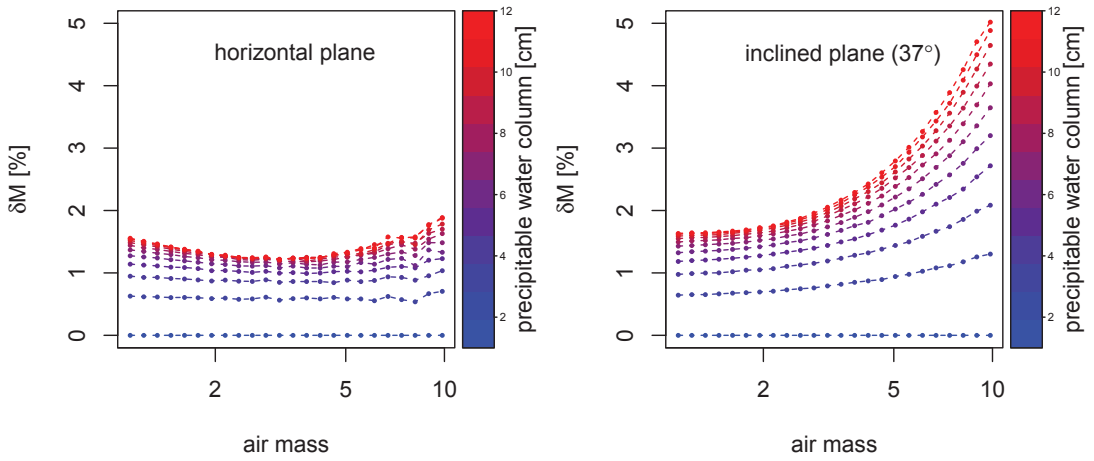

Figure 6.37: Impact of the precipitable water variations on the relative difference between $M_{specific}$ and $M_{AM1.5}$ for a multi-cSi cell and a broadband reference detector

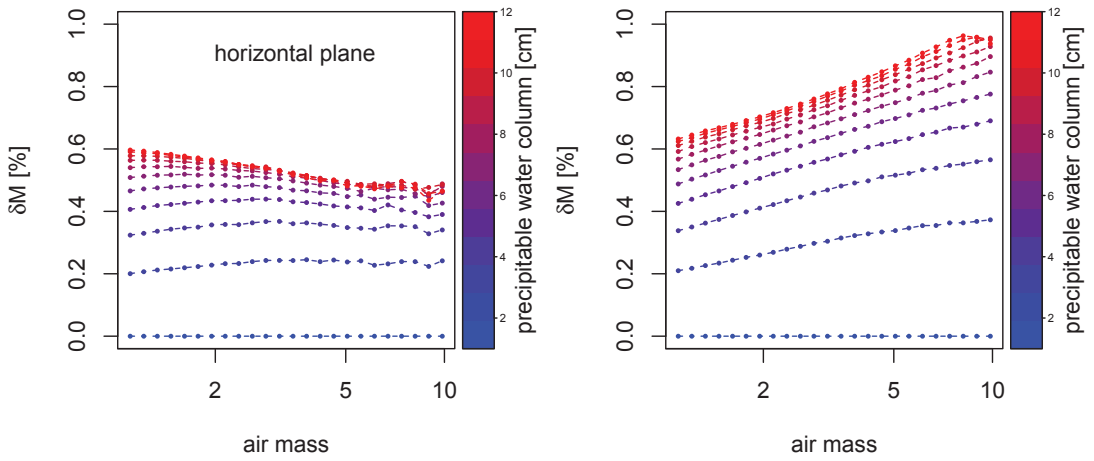

Figure 6.38: Impact of the precipitable water variations on the relative difference between $M_{specific}$ and $M_{AM1.5}$ for a multi-cSi cell and a mono-cSi reference detector

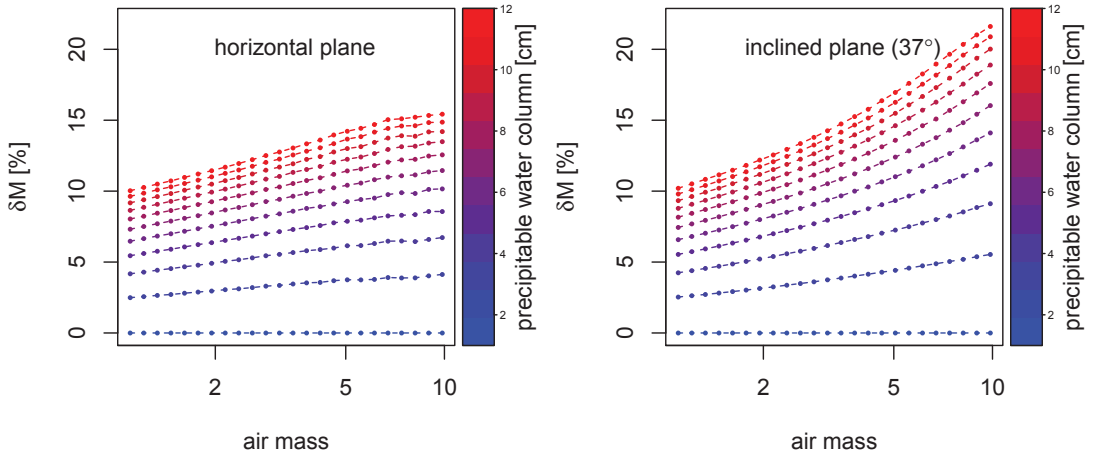

Figure 6.39: Impact of the precipitable water variations on the relative difference between $M_{specific}$ and $M_{AM1.5}$ for an a-Si cell and a broadband reference detector

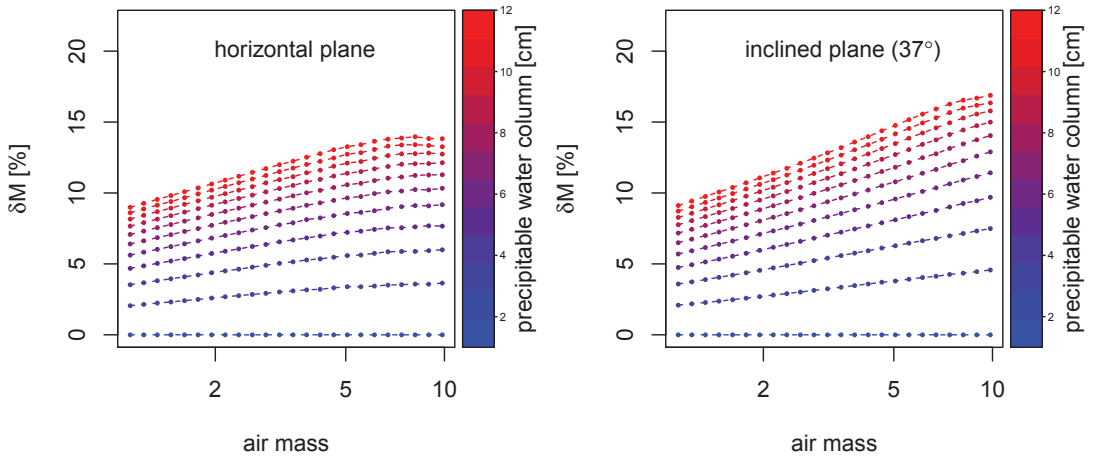

Figure 6.40: Impact of the precipitable water variations on the relative difference between $M_{specific}$ and $M_{AM1.5}$ for an a-Si cell and a mono-cSi reference detector

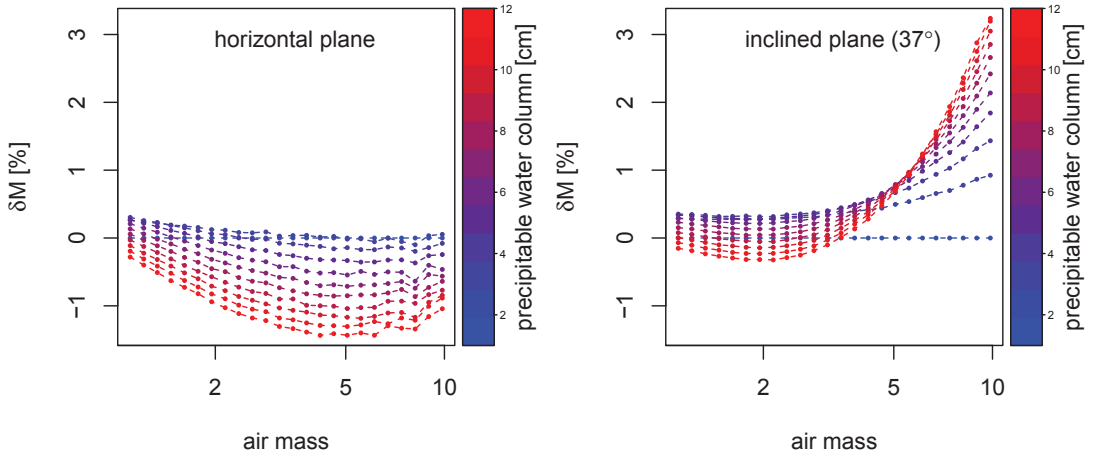

Figure 6.41: Impact of the precipitable water variations on the relative difference between $M_{specific}$ and $M_{AM1.5}$ for a CIS cell and a broadband reference detector

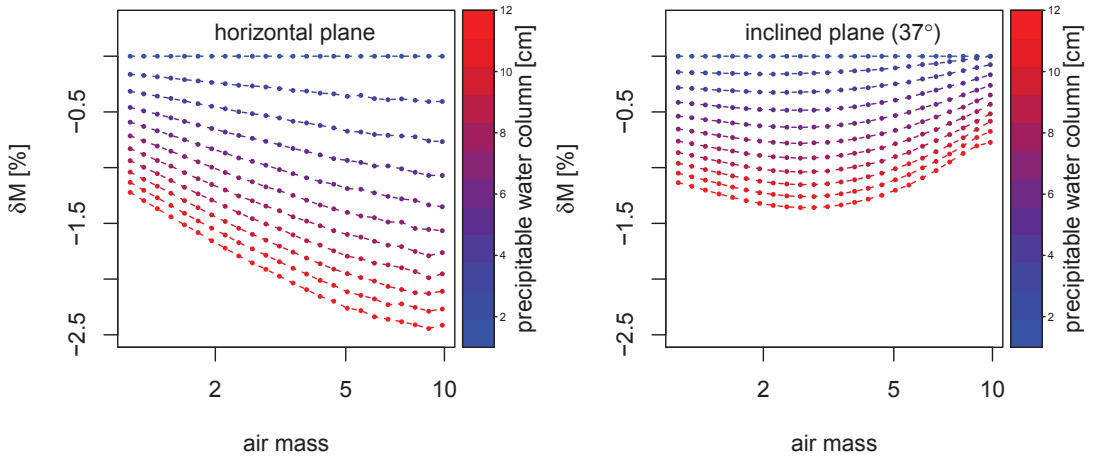

Figure 6.42: Impact of the precipitable water variations on the relative difference between $M_{specific}$ and $M_{AM1.5}$ for a CIS cell and a mono-cSi reference detector

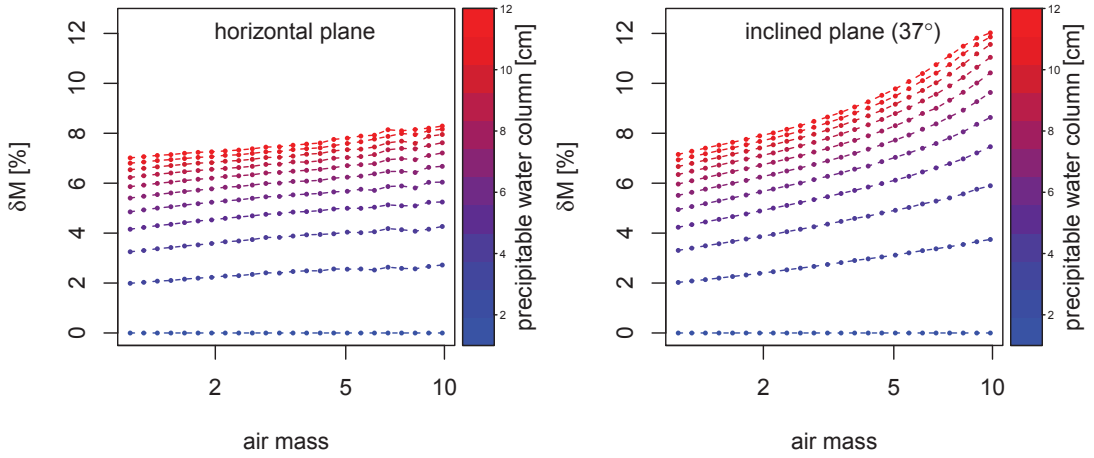

Figure 6.43: Impact of the precipitable water variations on the relative difference between $M_{specific}$ and $M_{AM1.5}$ for a CdTe cell and a broadband reference detector

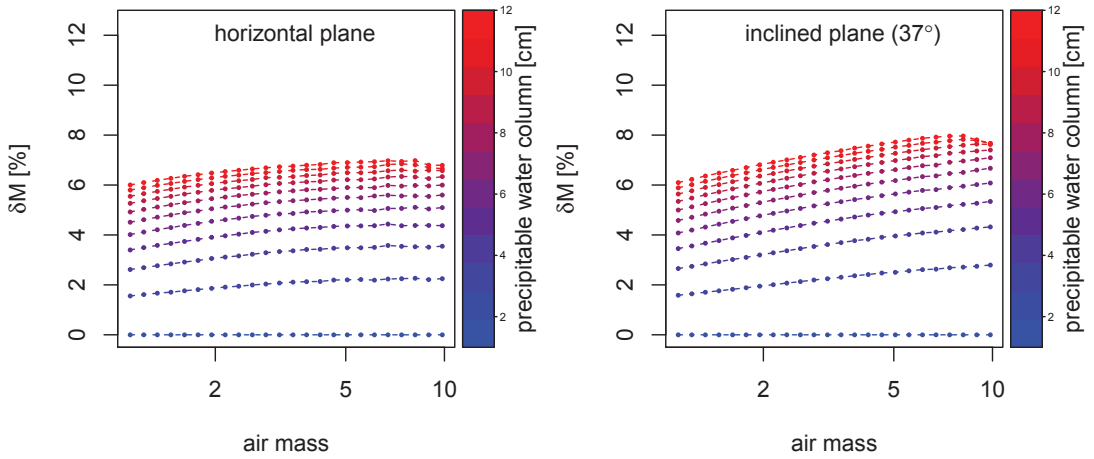

Figure 6.44: Impact of the precipitable water variations on the relative difference between $M_{specific}$ and $M_{AM1.5}$ for a CdTe cell and a mono-cSi reference detector

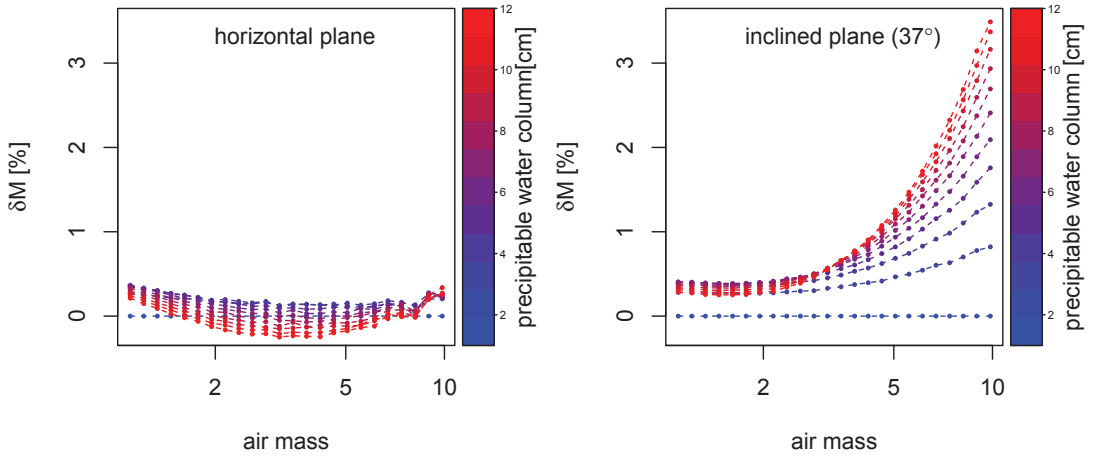

Figure 6.45: Impact of the precipitable water variations on the relative difference between $M_{specific}$ and $M_{AM1.5}$ for a HIT cell and a broadband reference detector

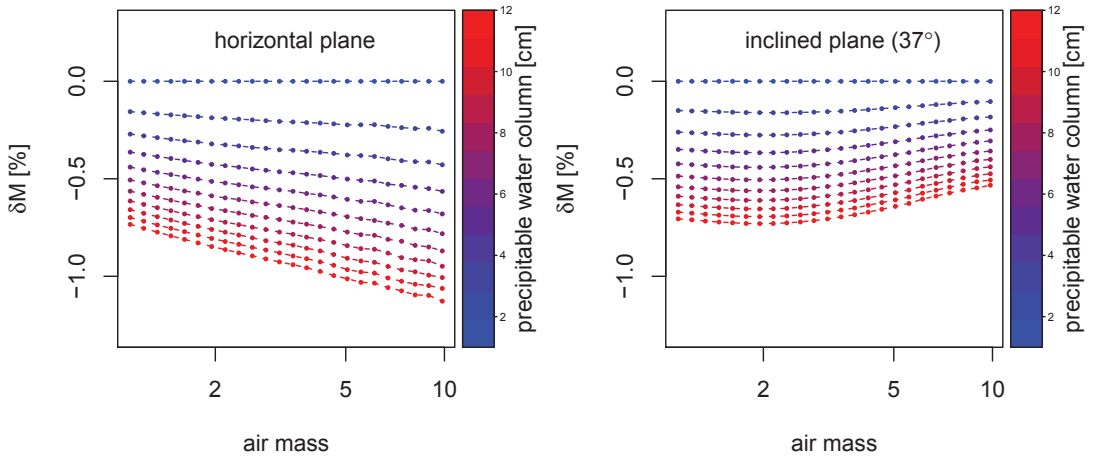

Figure 6.46: Impact of the precipitable water variations on the relative difference between $M_{specific}$ and $M_{AM1.5}$ for a HIT cell and a mono-cSi reference detector

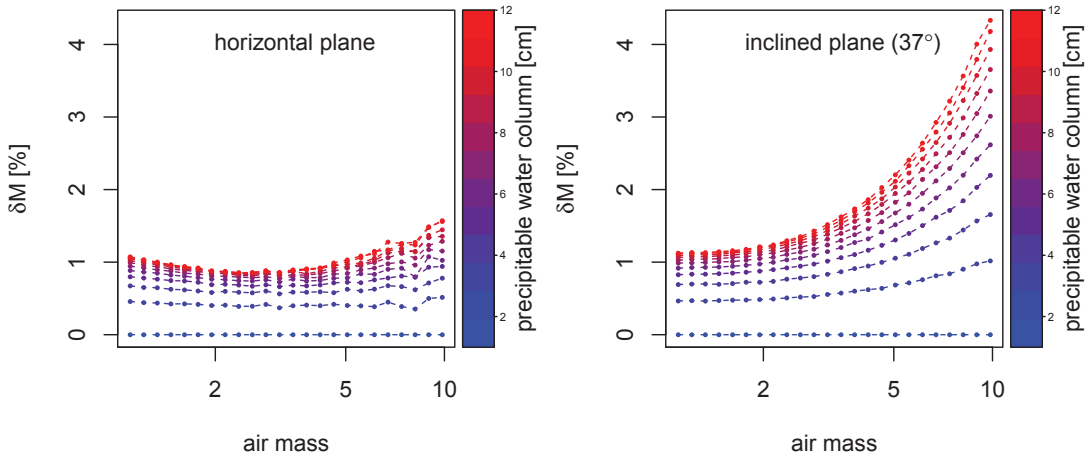

Figure 6.47: Impact of the precipitable water variations on the relative difference between $M_{specific}$ and $M_{AM1.5}$ for a mono-cSi cell and a broadband reference detector

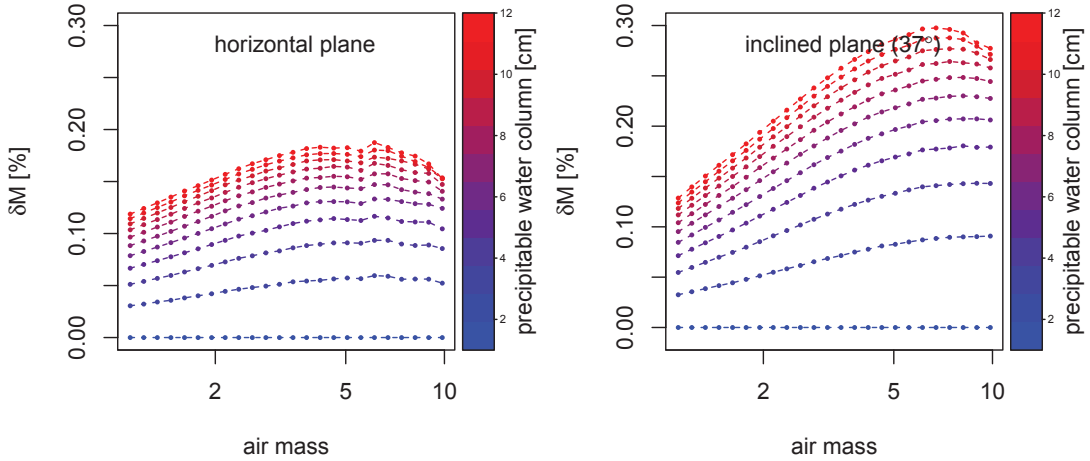

Figure 6.48: Impact of the precipitable water variations on the relative difference between $M_{specific}$ and $M_{AM1.5}$ for a mono-cSi cell and a mono-cSi reference detector

The impact of precipitable water on the observed values of the relative difference in detector response mismatch is the most significant for amorphous silicon reaching a worst case of a 20%. These results seem to contradict the expectation, that no impact of water vapour would be observed in this case. Only a marginal part of water absorption bands overlay with spectral sensitivity characteristic of amorphous silicon. However δM relates to broadband or mono-cSi reference detector responses, as these are the most commonly available types of reference irradiance detectors, with measurement available from meteorological stations. The fact that these parameters relate to a broader irradiance range than the a-Si covers, allows for an explanation of the observed results. Whilst the water vapour affects amorphous silicon only marginally, it heavily affects the infrared fraction of the spectrum. Therefore, measurements taken by a broadband radiometer are affected by water vapour, while the amorphous silicon solar cell's current generation remains unchanged, thus a-Si is affected in a positive fashion. CdTe was the second-most affected technology by water vapour. While extreme values of precipitable water reaching $12 g/cm$ are not likely to be frequently observed in the natural environment, a significant impact of precipitable water is still expected in case of a-Si or CdTe cells. The example of precipitable water shows, how non-direct spectral effects can influence the uncertainty of reference irradiance measurements.

6.3.4.3 Ozone

Short term and long term variations of ozone concentration are present in the natural environment. The main two reasons that cause variations of ozone concentration are : ozone transport and photo-dissociation. The majority of atmospheric ozone is located in the lower part of the stratosphere (below 30km). In the northern hemisphere the lowest ozone concentration is observed in late autumn and the highest in early spring. This happens because ozone-rich air is transported towards the poles in the winter time. Due to low sun altitude and short day length, ozone in a the lower part of the stratosphere does not undergo photo-dissociation as it is effectively shielded from ultraviolet radiation by high stratosphere ozone. This situation changes in the spring when high stratosphere ozone shielding does not work as efficiently, due to effect of angle of incidence changes and increasing day length. In effect, the concentration of ozone starts to drop. For the purpose of this work, ozone concentration was varied from 200DU to 500DU. [1] With a standard value of 340DU. Figures 6.49 to 6.60 present an impact of variations of the ozone concentration on the current generation potential of incident irradiance for a variety of photovoltaic cells.

As shown in Figures 6.49 to 6.60 for most photovoltaic cells ozone concentration has rather small impact (less than 0.5% across wide range of air mass). The only exceptions are a-Si and CdTe cells, where the impact of ozone reached extremes of 4% and 2% respectively. In all cases the current generation efficiency was lower for higher ozone concentrations. Also no significant differences were observed between horizontal and inclined planes. The greatest impact of ozone concentration variation observed in the case of a-Si and CdTe is attributed to the absorption in the Chappuis band (around 600nm). While this absorption affects all the cells investigated, its scale varies with the cell bandwidth. Use of a mono-cSi reference cell in comparison to broadband detector does not bring significant improvement to the accuracy of reference irradiance measurements. Ozone impact should not be ignored in case of a-Si and CdTe cells.

[1] DU - Dobson unit; equivalent to the $10\mu m$ ozone column

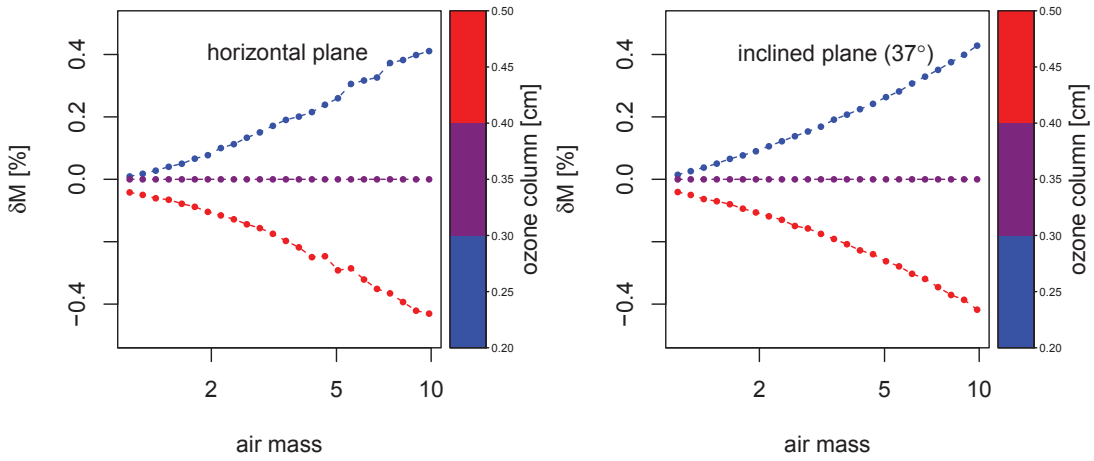

Figure 6.49: Impact of the ozone variations on the relative difference between $M_{specific}$ and $M_{AM1.5}$ for a multi-cSi cell and a broadband reference detector

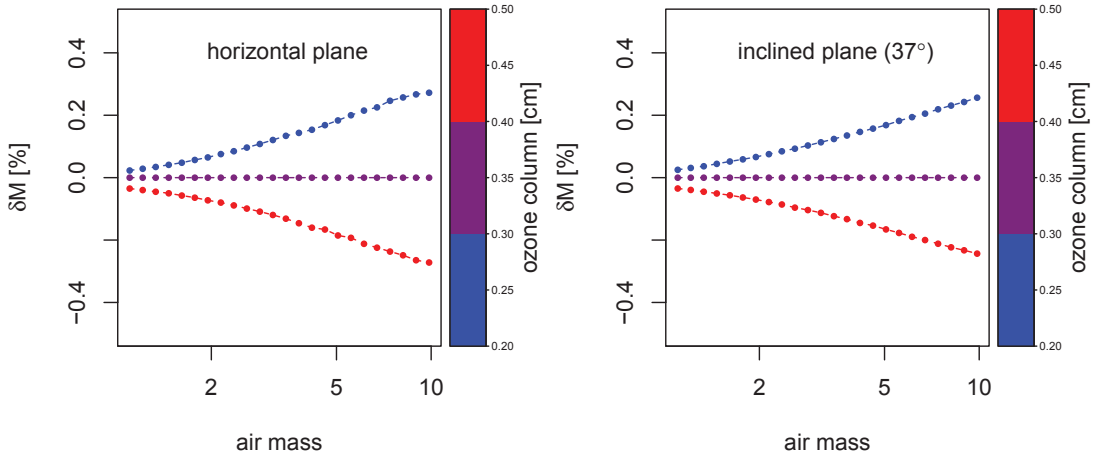

Figure 6.50: Impact of the ozone variations on the relative difference between $M_{specific}$ and $M_{AM1.5}$ for a multi-cSi cell and a mono-cSi reference detector

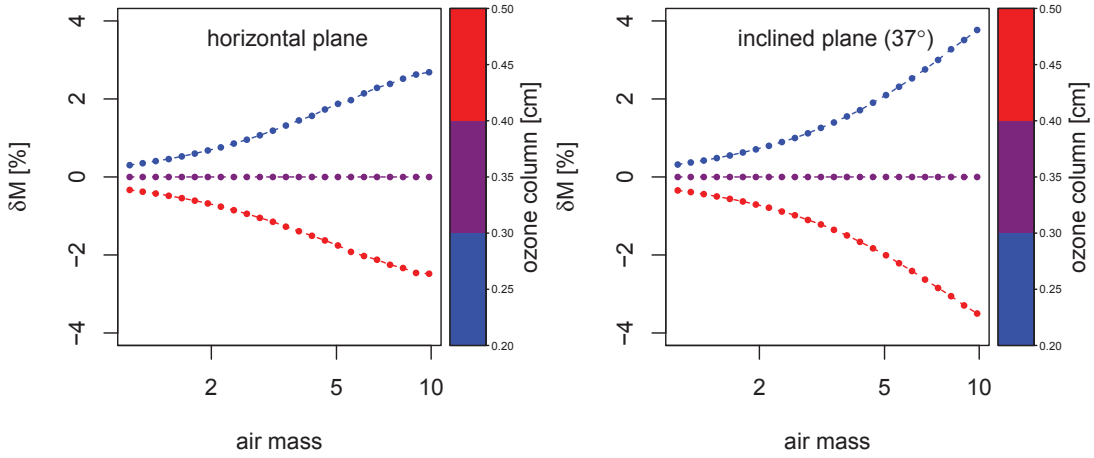

Figure 6.51: Impact of the ozone variations on the relative difference between $M_{specific}$ and $M_{AM1.5}$ for an a-Si cell and a broadband reference detector

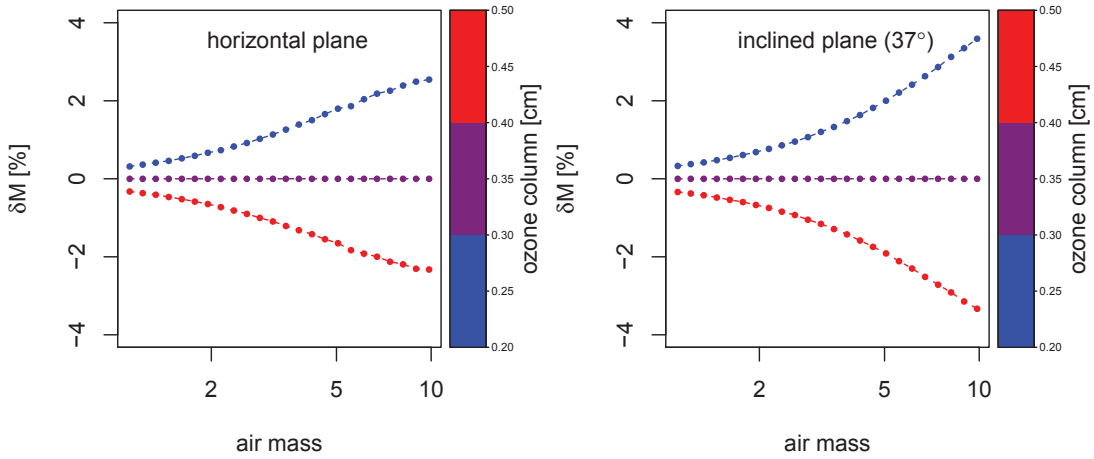

Figure 6.52: Impact of the ozone variations on the relative difference between $M_{specific}$ and $M_{AM1.5}$ for an a-Si cell and a mono-cSi reference detector

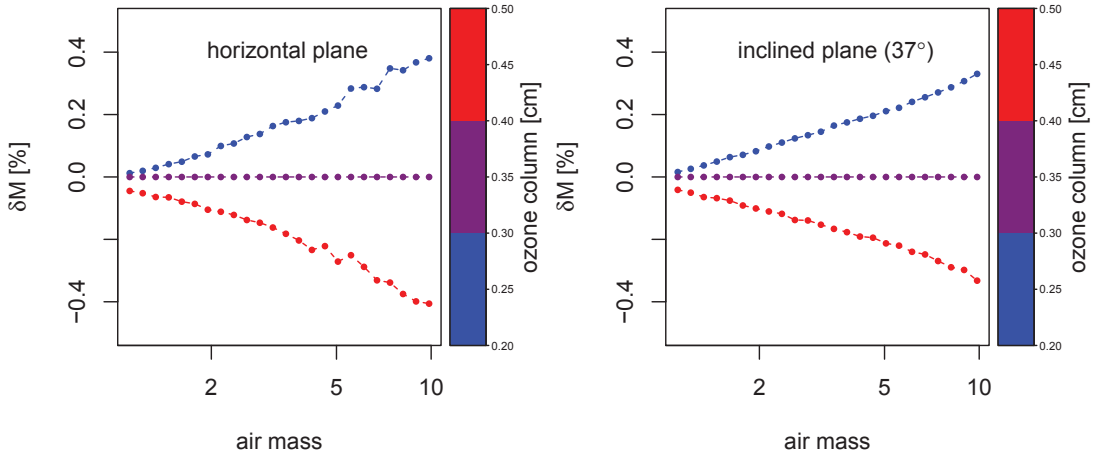

Figure 6.53: Impact of the ozone variations on the relative difference between $M_{specific}$ and $M_{AM1.5}$ for a CIS cell and a broadband reference detector

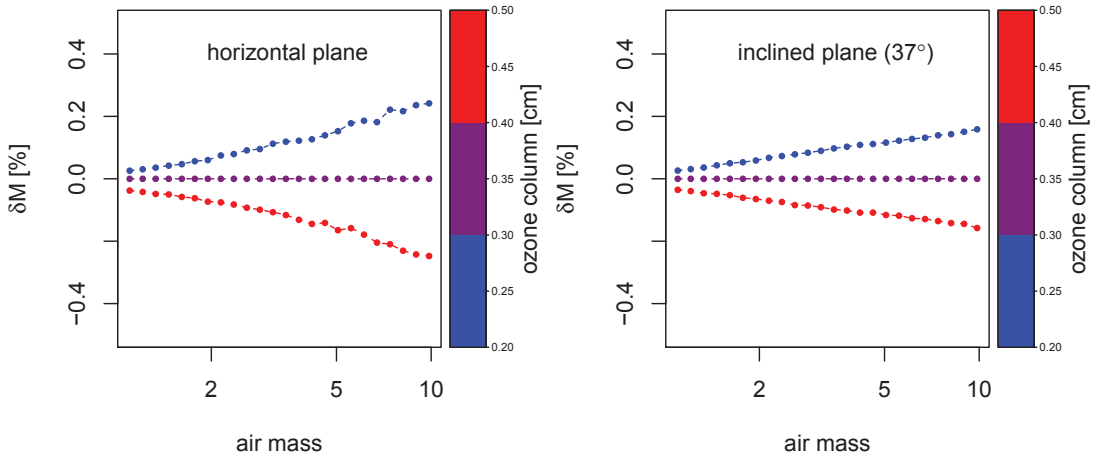

Figure 6.54: Impact of the ozone variations on the relative difference between $M_{specific}$ and $M_{AM1.5}$ for a CIS cell and a mono-cSi reference detector

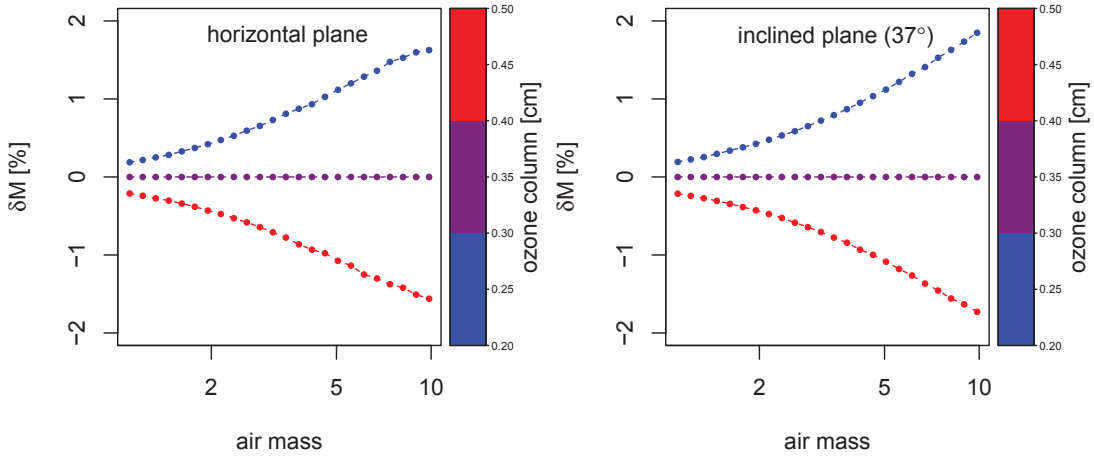

Figure 6.55: Impact of the ozone variations on the relative difference between $M_{specific}$ and $M_{AM1.5}$ for a CdTe cell and a broadband reference detector

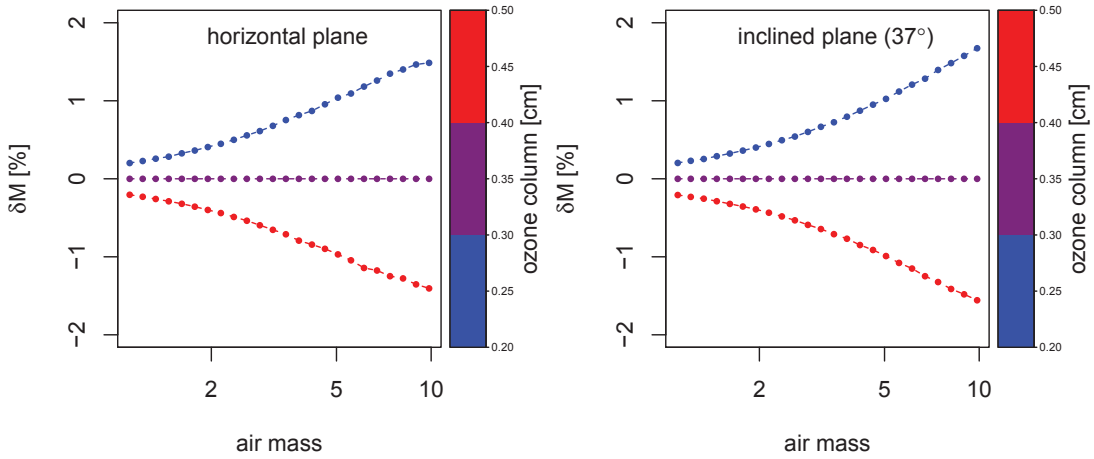

Figure 6.56: Impact of the ozone variations on the relative difference between $M_{specific}$ and $M_{AM1.5}$ for a CdTe cell and a mono-cSi reference detector

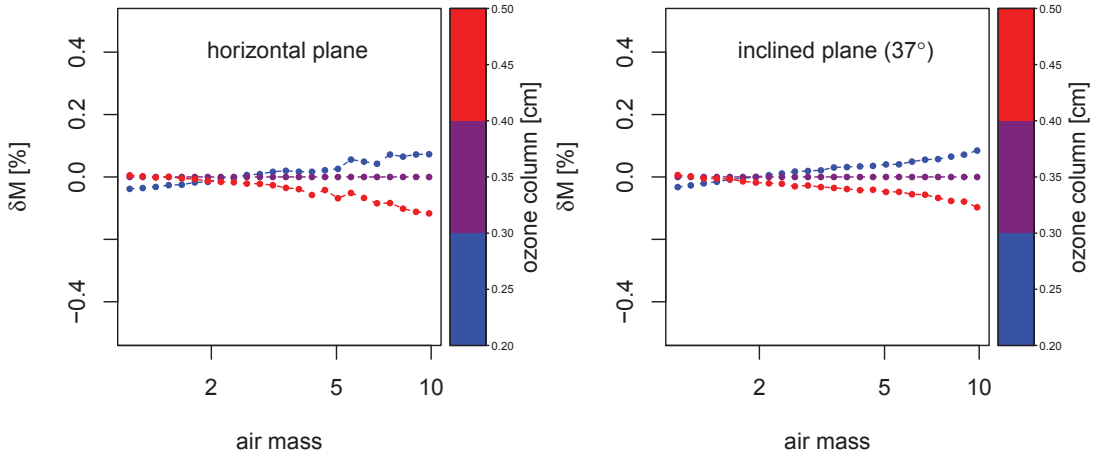

Figure 6.57: Impact of the ozone variations on the relative difference between $M_{specific}$ and $M_{AM1.5}$ for a HIT cell and a broadband reference detector

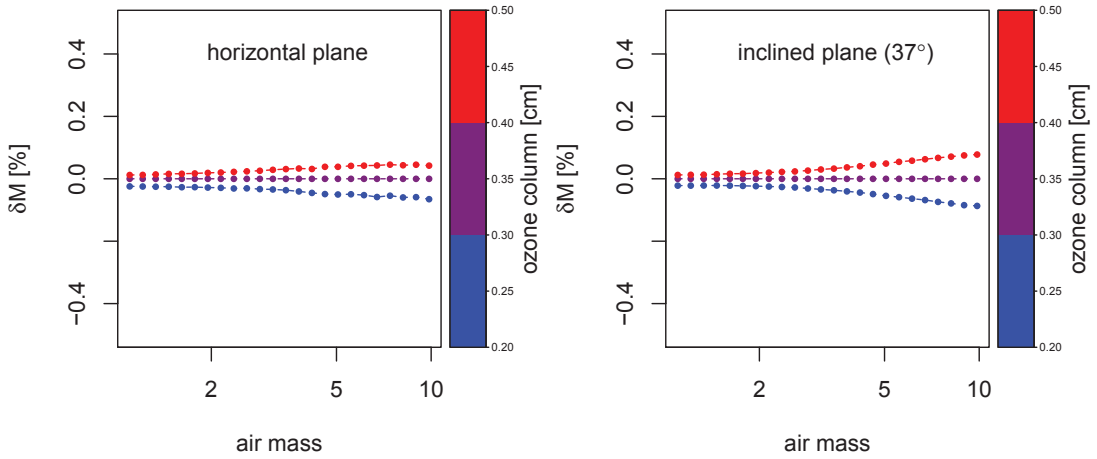

Figure 6.58: Impact of the ozone variations on the relative difference between $M_{specific}$ and $M_{AM1.5}$ for a HIT cell and a mono-cSi reference detector

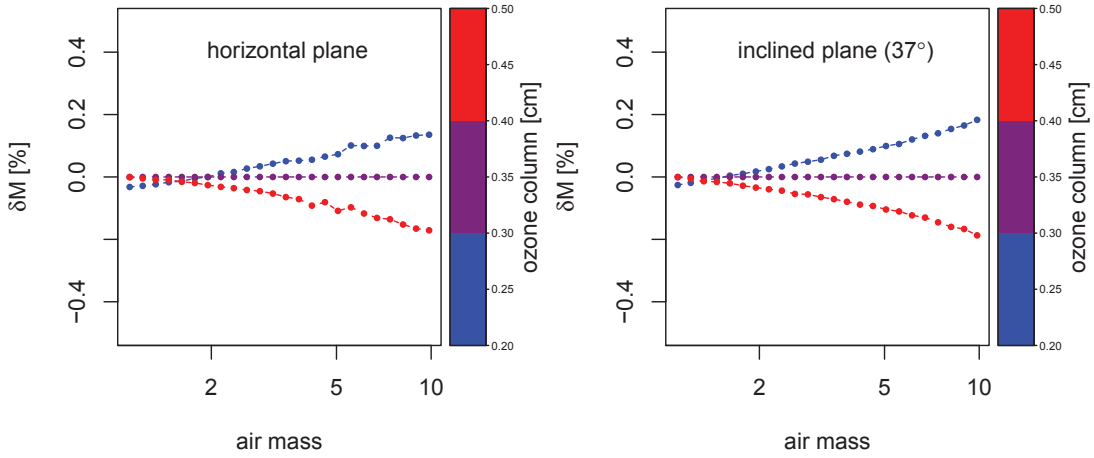

Figure 6.59: Impact of the ozone variations on the relative difference between $M_{specific}$ and $M_{AM1.5}$ for a mono-cSi cell and a broadband reference detector

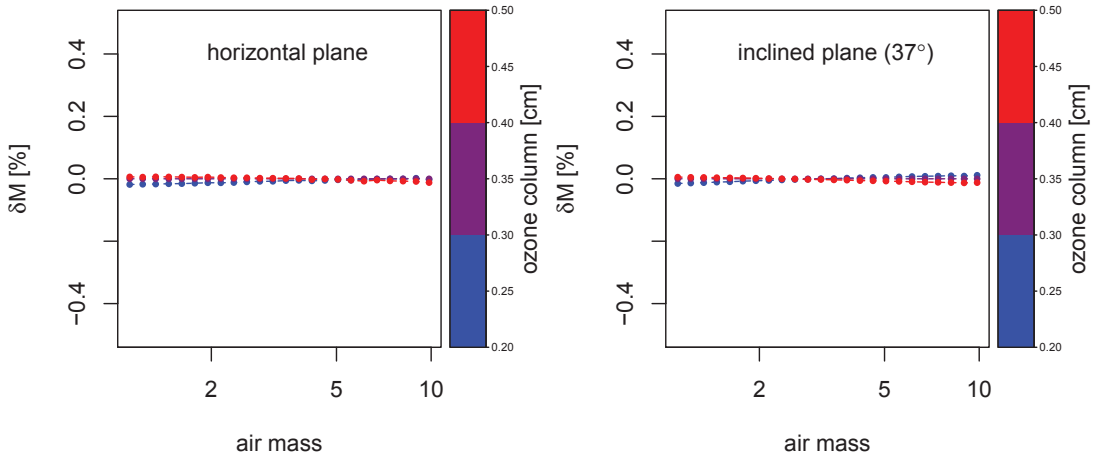

Figure 6.60: Impact of the ozone variations on the relative difference between $M_{specific}$ and $M_{AM1.5}$ for a mono-cSi cell and a mono-cSi reference detector

6.3.4.4 Atmospheric pollution

The main atmospheric pollutant responsible for absorption in the visible range of the spectrum is nitrogen dioxide. Its absorption band covers the range from 250 to 600 nm. Natural sources of nitrogen oxides include: intrusion of stratospheric nitrogen oxides, bacterial and volcanic action, and lightning [106]. In most ambient situations, nitric oxide is emitted and transformed into nitrogen dioxide in the atmosphere. Natural sources of nitrogen dioxide are evenly distributed which effectively causes its low concentrations. By contrast, anthropogenic nitrogen dioxide is generated within specific locations, and relates to the process of combustion of fossil fuels. Nitrogen dioxide can be observed as brown smog over cities. Four levels of nitrogen dioxide pollution were set in SMARTS : pristine (no pollutions), light (standard), moderate and severe. Figures 6.61 to 6.72 present the impact of nitrogen dioxide on the difference in response from a variety of photovoltaic cells and reference detectors.

In case of pristine, light and moderate pollution levels, an observed impact of nitrogen dioxide pollution on the relative mismatch difference stayed below 1%. Only for severe pollutions, was the observed impact significant. The most sensitive to nitrogen dioxide pollution was a-Si cell, where differences in the range -4% to -15% were observed. Other cells exhibited differences in the range of: 2%-4% for crystalline silicon, 6%-8% for CIS, 1.5% to -3% for the CdTe and 3% - 5% for the HIT for severe pollution levels. It is worth noting, that these effects were present starting from low levels of air mass. Severe level of atmospheric pollution is most frequently a localised phenomenon therefore this factor will have an impact only on photovoltaics installed in highly polluted urban areas and in heavily industrialised zones. In case of severe pollution levels, its impact on photovoltaics becomes significant and should not be ignored. Utilisation of a mono-cSi cell instead of broadband reference detector gave significant improvements in case of multi-cSi, HIT, CIS and mono-cSi cells. Even for mono-cSi reference, CIS cell response still differs by 4% from the reference. Once again, a-Si and CdTe cells were proven to be the most susceptible to the impact of the atmospheric pollutions. In these two cases the difference in response did not improve or slightly worsened for a mono-cSi cell in comparison to broadband reference.

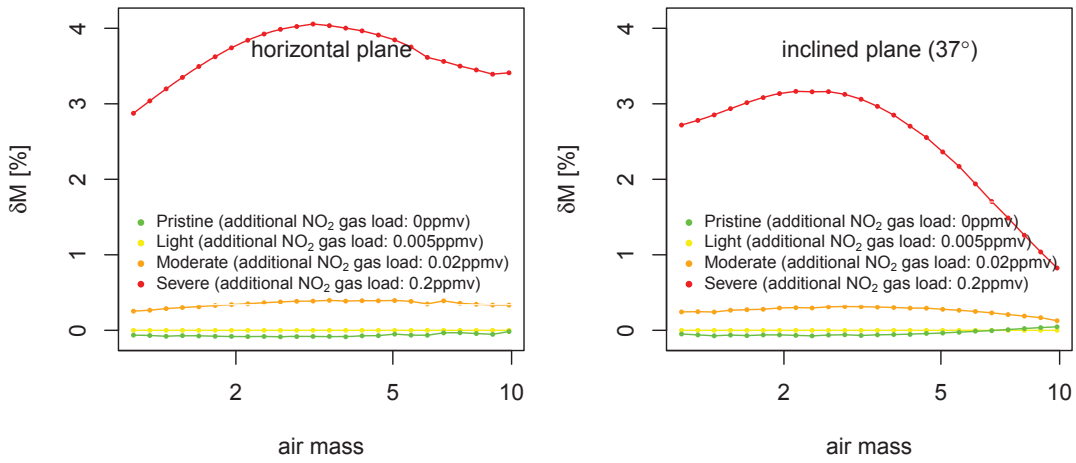

Figure 6.61: Impact of atmospheric pollution variations on the relative difference between $M_{specific}$ and $M_{AM1.5}$ for a multi-cSi cell and a broadband reference detector

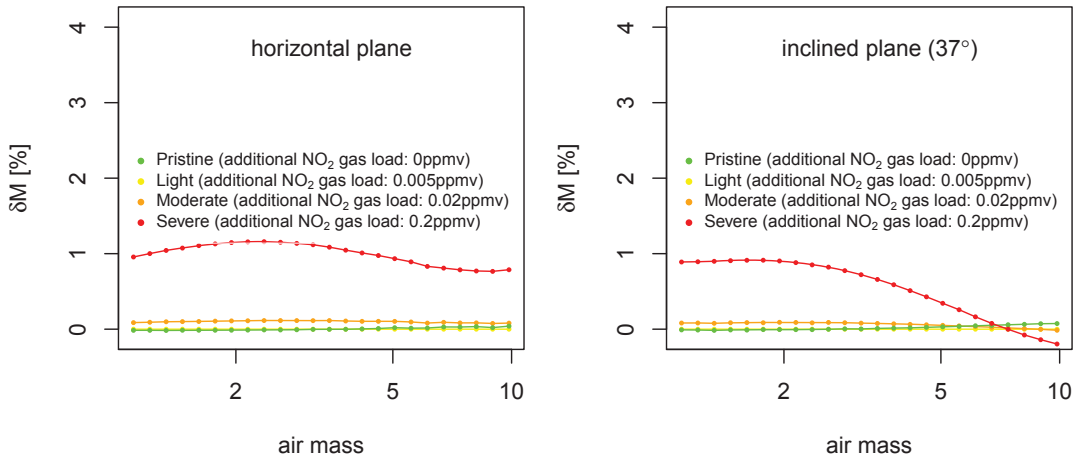

Figure 6.62: Impact of atmospheric pollution variations on the relative difference between $M_{specific}$ and $M_{AM1.5}$ for a multi-cSi cell and a mono-cSi reference detector

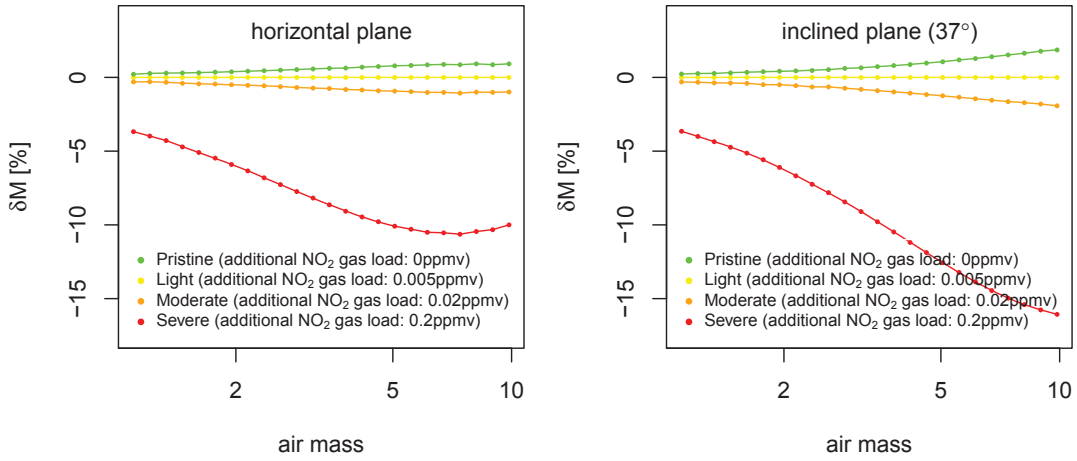

Figure 6.63: Impact of atmospheric pollution variations on the relative difference between $M_{specific}$ and $M_{AM1.5}$ for an a-Si cell and a broadband reference detector

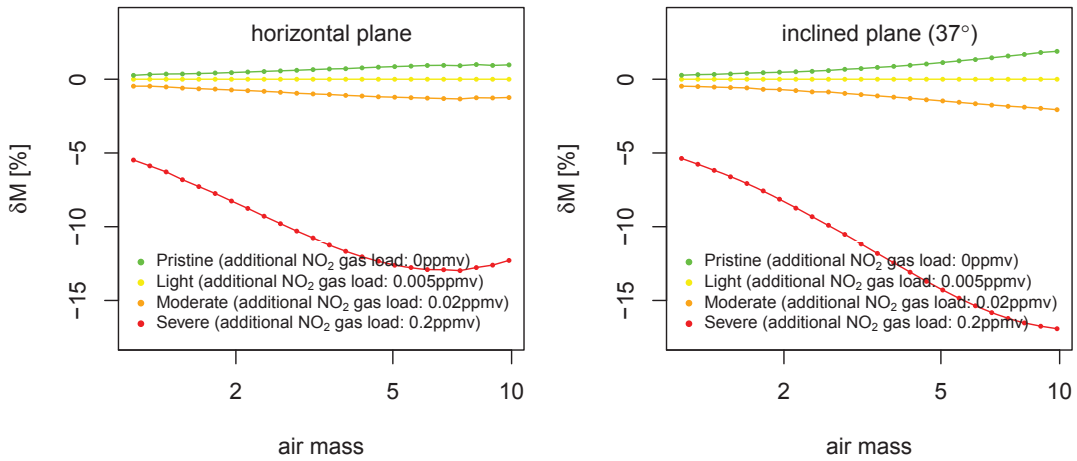

Figure 6.64: Impact of atmospheric pollution variations on the relative difference between $M_{specific}$ and $M_{AM1.5}$ for an a-Si cell and a mono-cSi reference detector

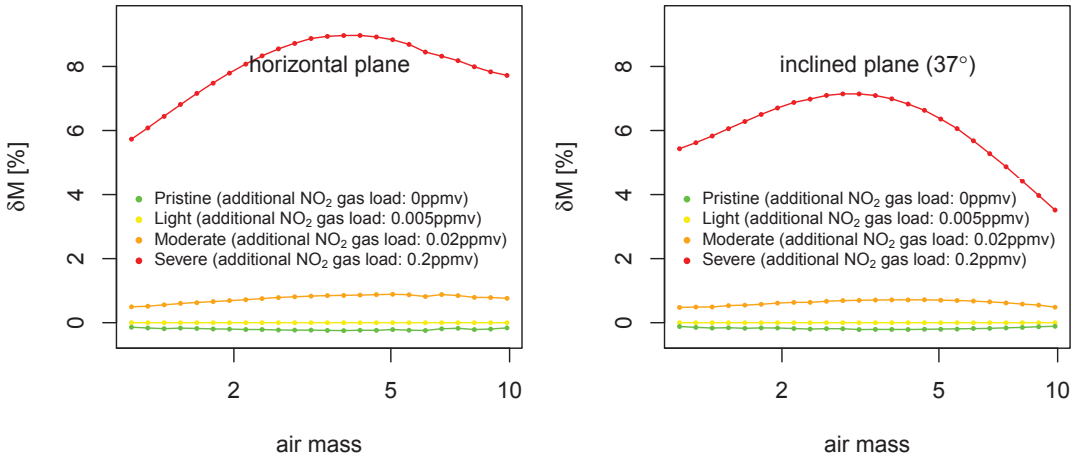

Figure 6.65: Impact of atmospheric pollution variations on the relative difference between $M_{specific}$ and $M_{AM1.5}$ for a CIS cell and a broadband reference detector

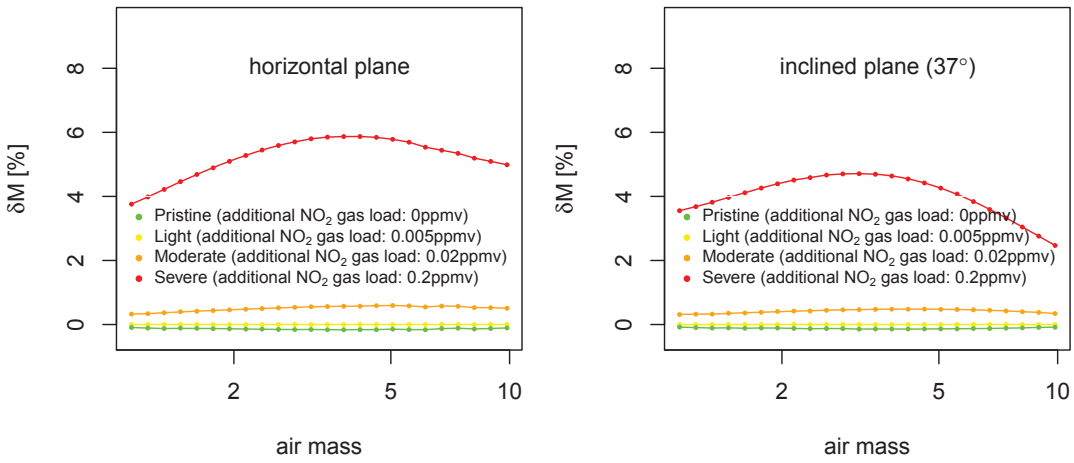

Figure 6.66: Impact of atmospheric pollution variations on the relative difference between $M_{specific}$ and $M_{AM1.5}$ for a CIS cell and a mono-cSi reference detector

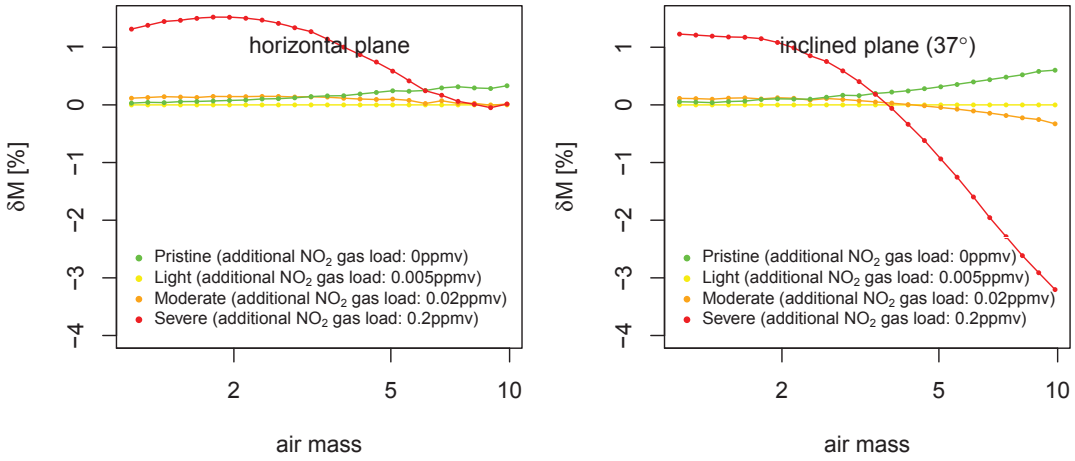

Figure 6.67: Impact of atmospheric pollution variations on the relative difference between $M_{specific}$ and $M_{AM1.5}$ for a CdTe cell and a broadband reference detector

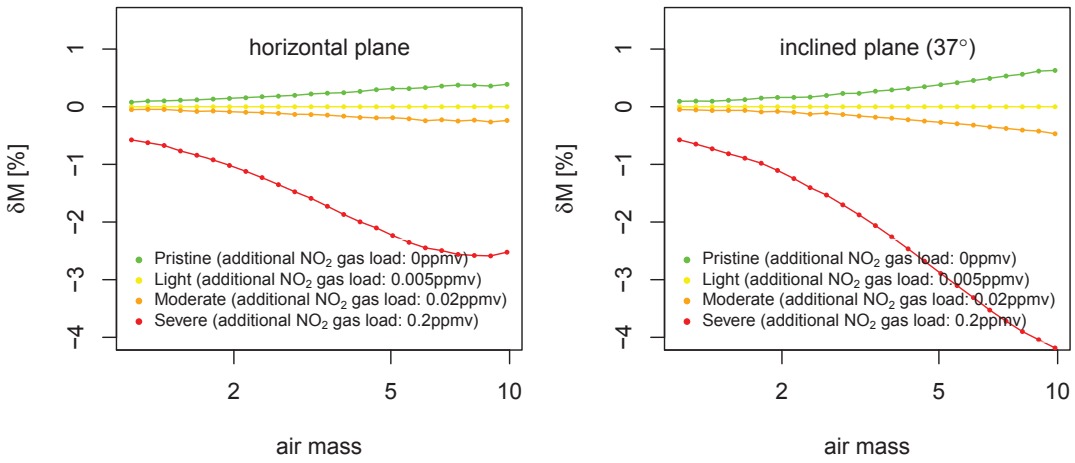

Figure 6.68: Impact of atmospheric pollution variations on the relative difference between $M_{specific}$ and $M_{AM1.5}$ for a CdTe cell and a mono-cSi reference detector

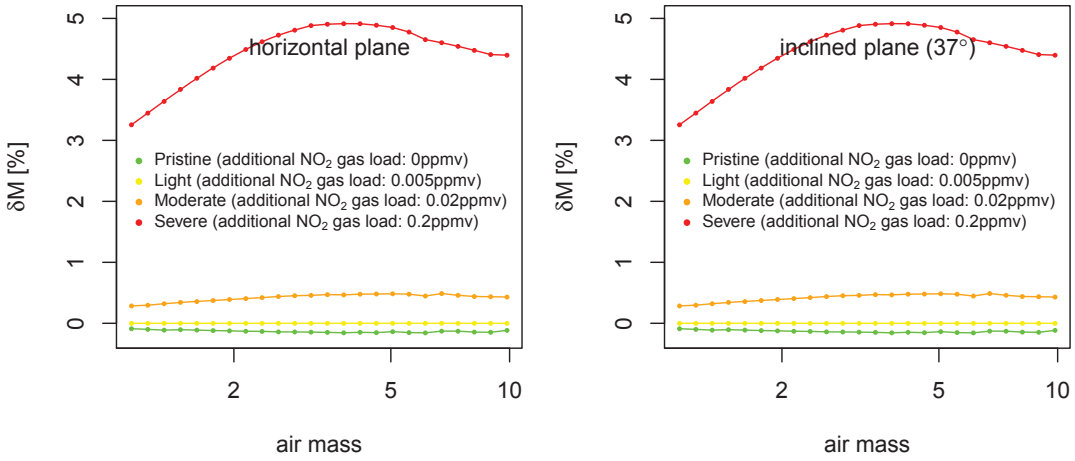

Figure 6.69: Impact of atmospheric pollution variations on the relative difference between $M_{specific}$ and $M_{AM1.5}$ for a HIT cell and a broadband reference detector

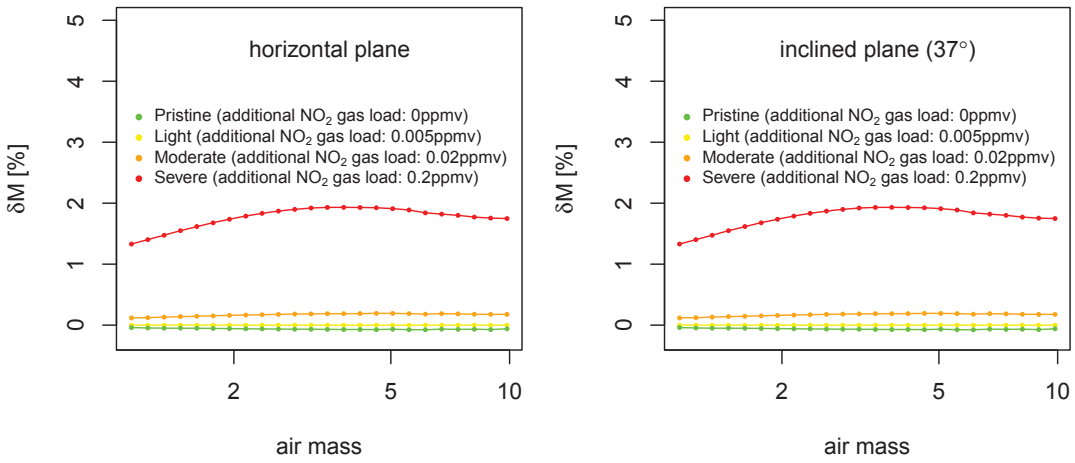

Figure 6.70: Impact of atmospheric pollution variations on the relative difference between $M_{specific}$ and $M_{AM1.5}$ for a HIT cell and a mono-cSi reference detector

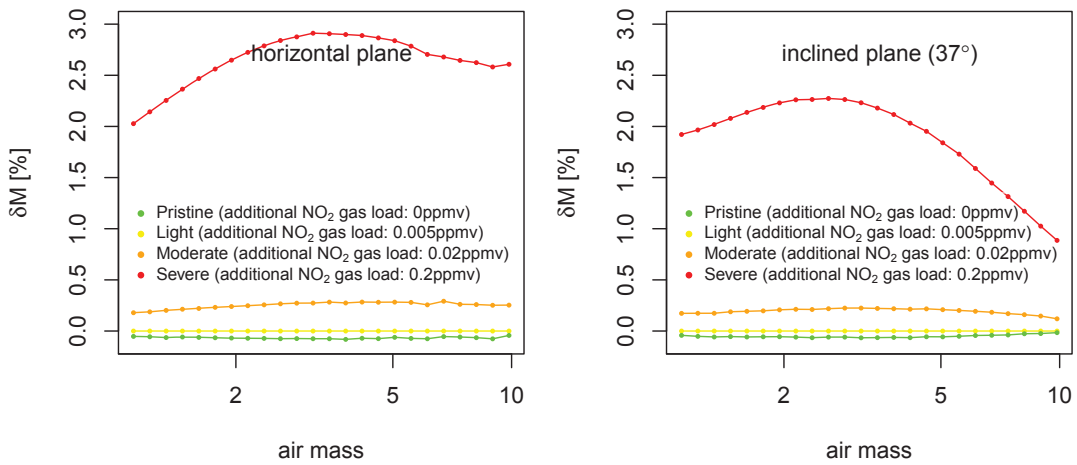

Figure 6.71: Impact of atmospheric pollution variations on the relative difference between $M_{specific}$ and $M_{AM1.5}$ for a mono-cSi cell and a broadband reference detector

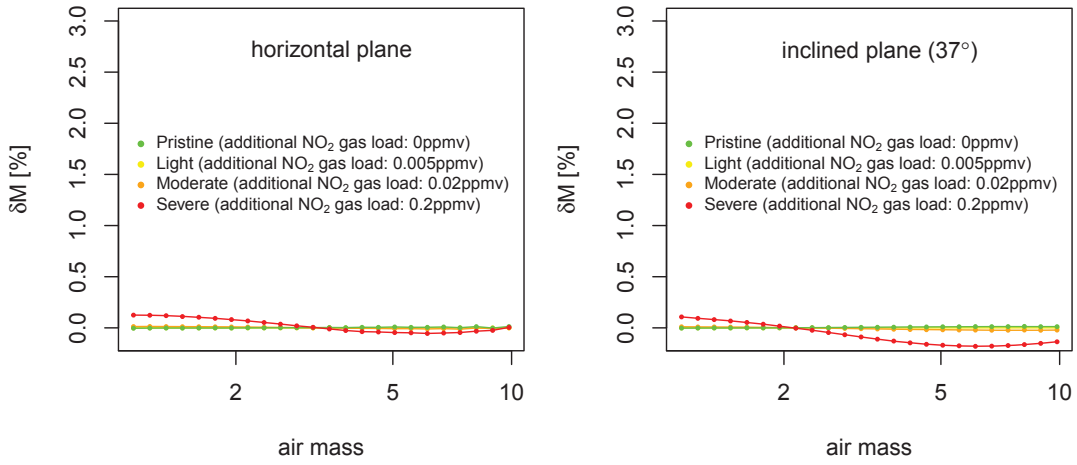

Figure 6.72: Impact of atmospheric pollution variations on the relative difference between $M_{specific}$ and $M_{AM1.5}$ for a mono-cSi cell and a mono-cSi reference detector

6.3.4.5 Spectral Albedo

Albedo defines how much of an incident irradiance is being reflected back towards the space from the surface of the earth. In many cases the albedo of a given surface varies with the wavelength. In such cases spectral albedo should be used for analysis. A fraction of reflected irradiance can be backscattered by the atmosphere or reflected by the clouds towards the earth surface. The case considered takes into account clear sky (backscattering effects) only. Zonal albedo (resulting from the irradiance directly reflected towards the module/reference radiometer) in not consider. Figures 6.73 to 6.84 present the impact of a variety of spectral albedos on the current generation efficiency of the incident irradiance

For most surfaces the impact of spectral albedo on relative mismatch difference was lower than 1%. The only exception from this is fresh snow, for which observed differences varied from -4% for CIS cells up to 3% for a-Si cells. Use of a mono-cSi reference cell improved the accuracy of reference irradiance measurements in the case of multi-cSi, mono-cSi, HIT and CIS cells. The most significant differences between cell generation efficiency and reference irradiance detector generation efficiency were observed for the snow.

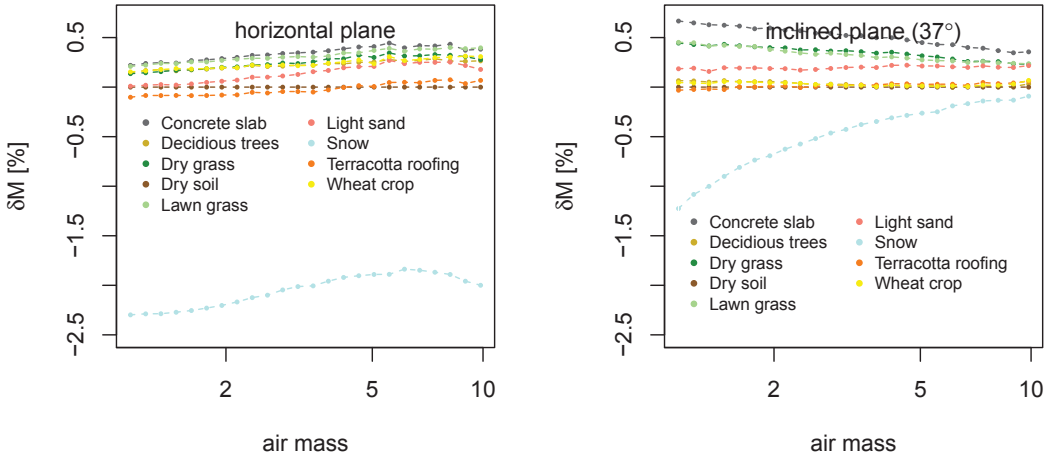

Figure 6.73: Impact of zonal spectral albedo on the relative difference between $M_{specific}$ and $M_{AM1.5}$ for a multi-cSi cell and a broadband reference detector

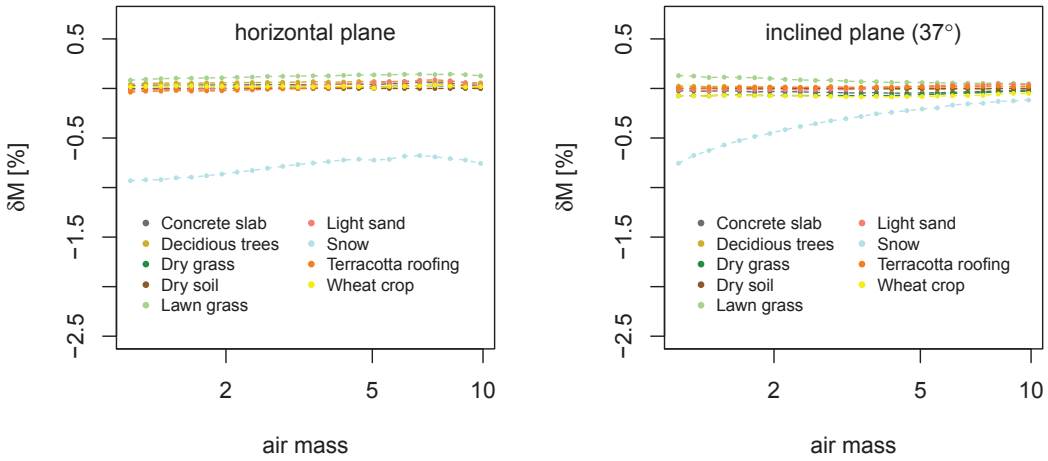

Figure 6.74: Impact of zonal spectral albedo on the relative difference between $M_{specific}$ and $M_{AM1.5}$ for a multi-cSi cell and a mono-cSi reference detector

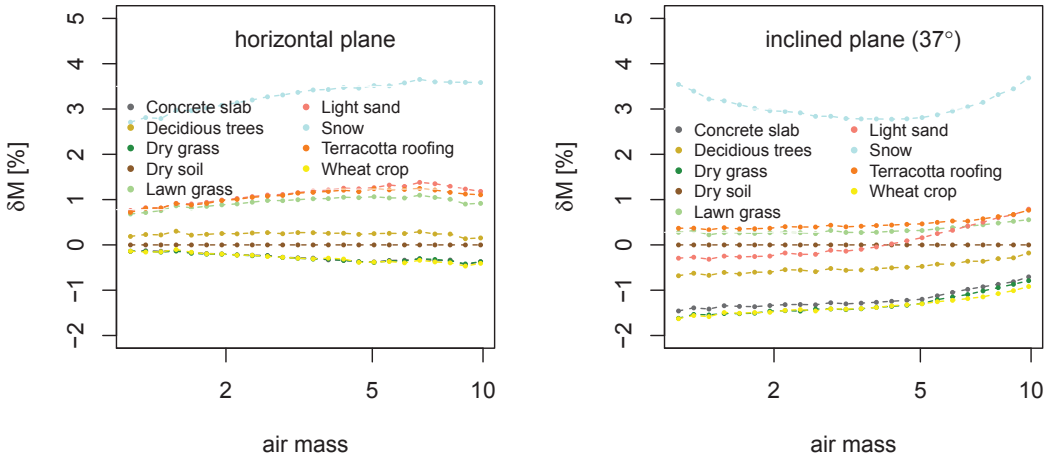

Figure 6.75: Impact of zonal spectral albedo on the relative difference between $M_{specific}$ and $M_{AM1.5}$ for an a-Si cell and a broadband reference detector

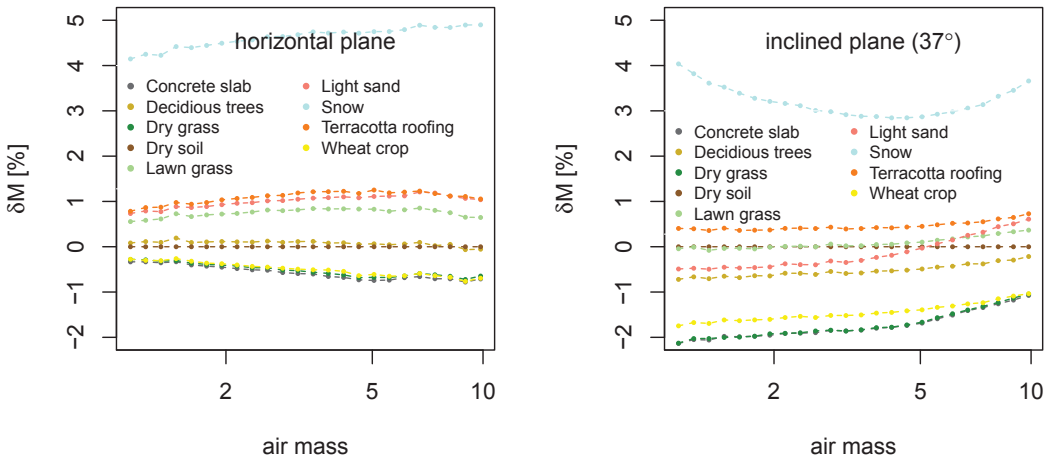

Figure 6.76: Impact of zonal spectral albedo on the relative difference between $M_{specific}$ and $M_{AM1.5}$ for an a-Si cell and a mono-cSi reference detector

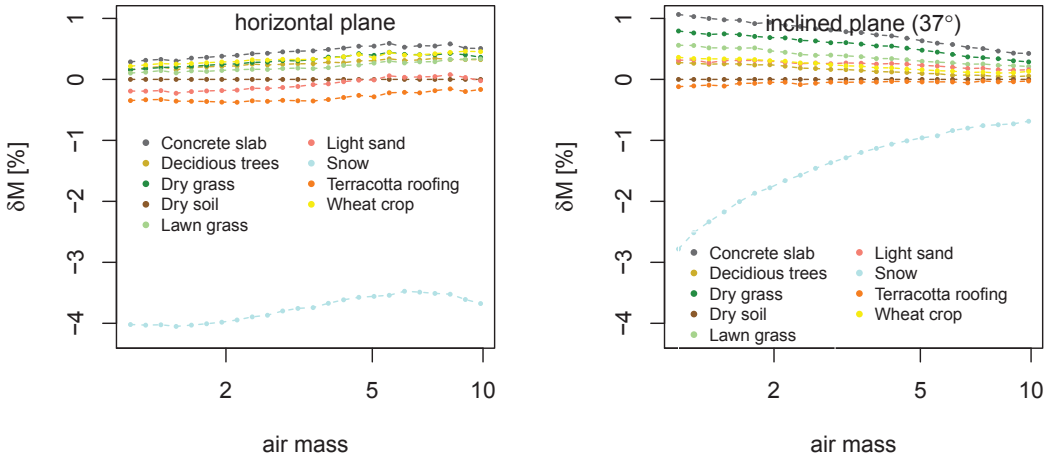

Figure 6.77: Impact of zonal spectral albedo on the relative difference between $M_{specific}$ and $M_{AM1.5}$ for a CIS cell and a broadband reference detector

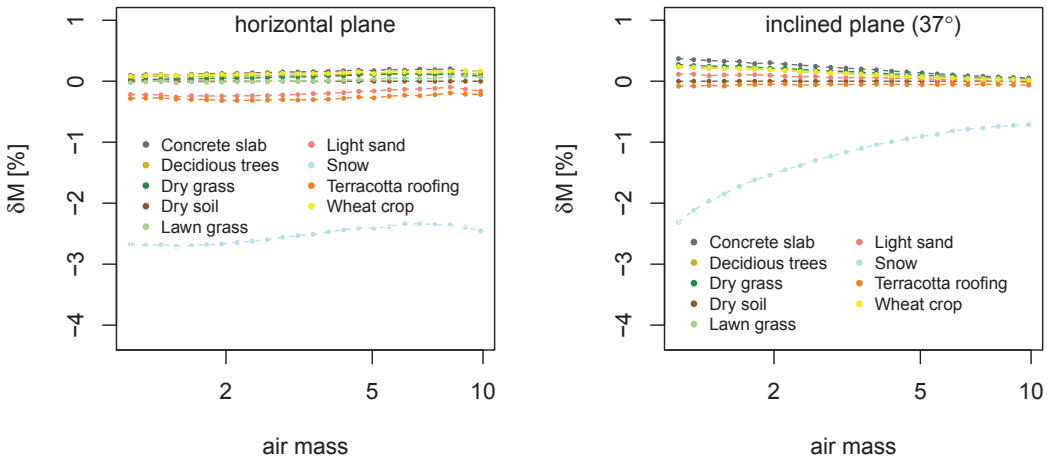

Figure 6.78: Impact of zonal spectral albedo on the relative difference between $M_{specific}$ and $M_{AM1.5}$ for a CIS cell and a mono-cSi reference detector

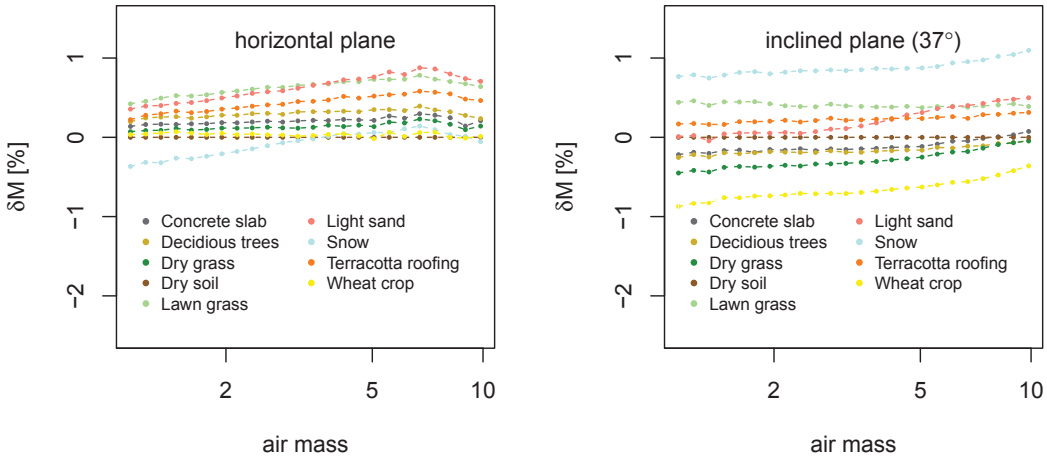

Figure 6.79: Impact of zonal spectral albedo on the relative difference between $M_{specific}$ and $M_{AM1.5}$ for a CdTe cell and a broadband reference detector

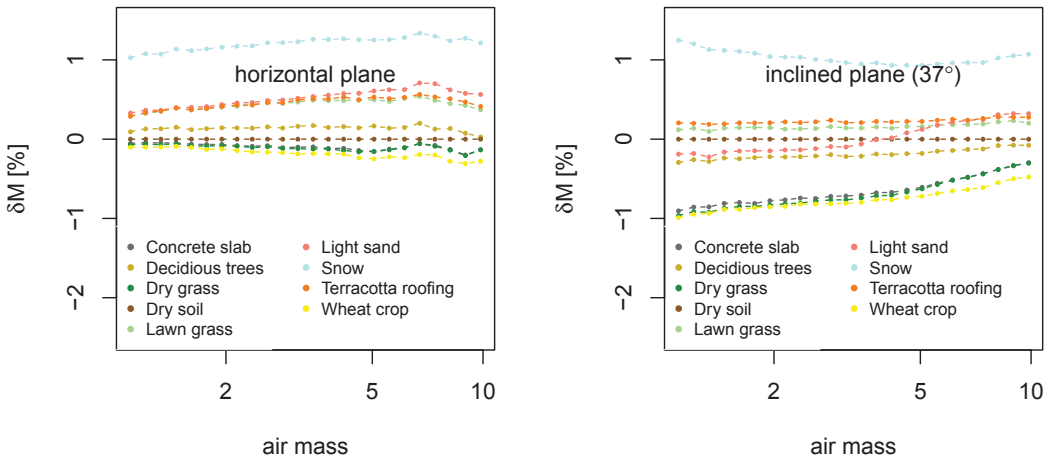

Figure 6.80: Impact of zonal spectral albedo on the relative difference between $M_{specific}$ and $M_{AM1.5}$ for a CdTe cell and a mono-cSi reference detector

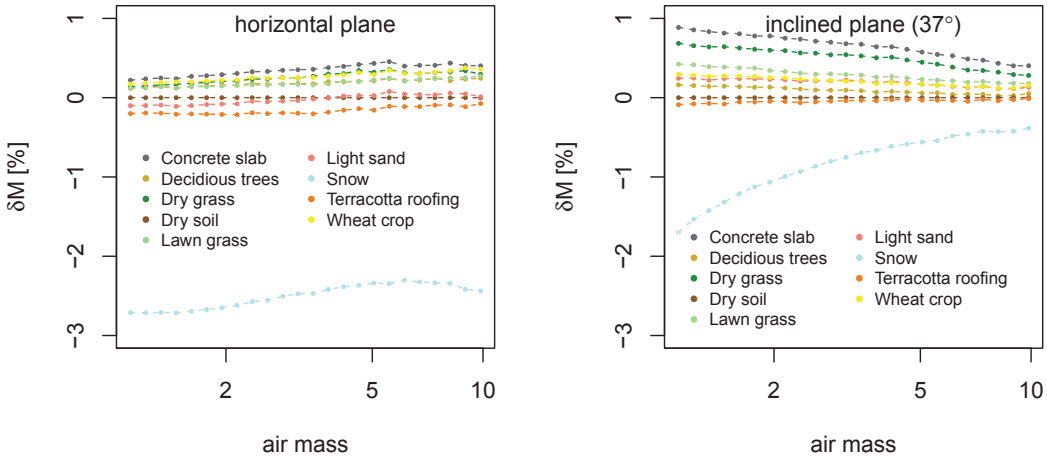

Figure 6.81: Impact of zonal spectral albedo on the relative difference between $M_{specific}$ and $M_{AM1.5}$ for a HIT cell and a broadband reference detector

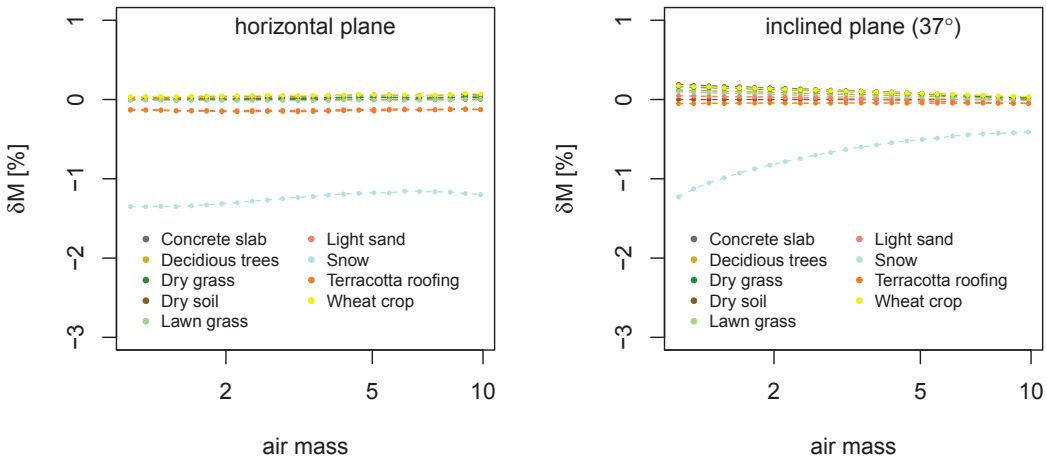

Figure 6.82: Impact of zonal spectral albedo on the relative difference between $M_{specific}$ and $M_{AM1.5}$ for a HIT cell and a mono-cSi reference detector

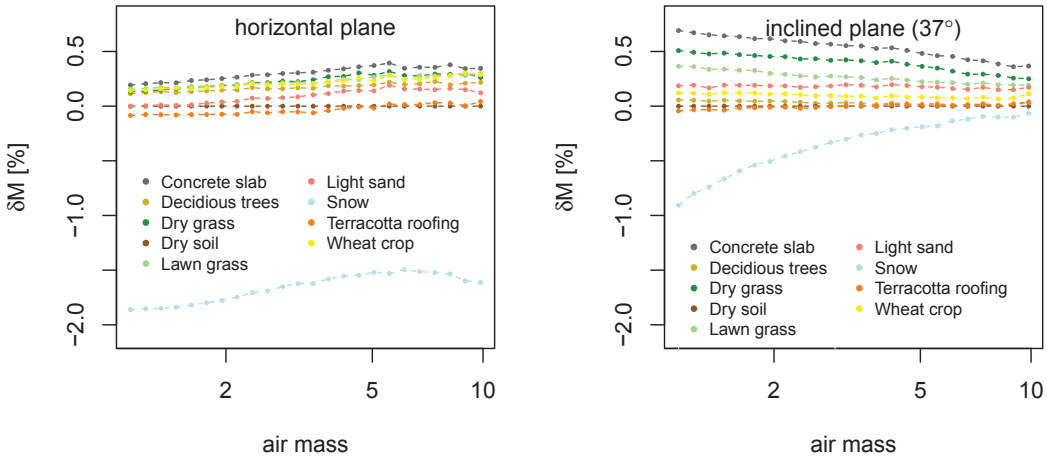

Figure 6.83: Impact of zonal spectral albedo on the relative difference between $M_{specific}$ and $M_{AM1.5}$ for a mono-cSi cell and a broadband reference detector

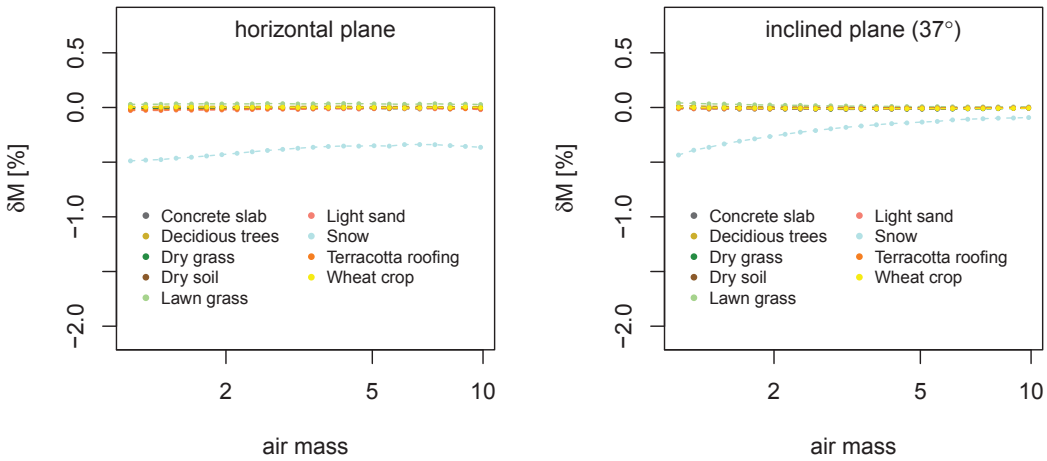

Figure 6.84: Impact of zonal spectral albedo on the relative difference between $M_{specific}$ and $M_{AM1.5}$ for a mono-cSi cell and a mono-cSi reference detector

.

6.4 Summary

Summary of the impact of atmospheric constituents on the relative mismatch between a specific photovoltaic cell technology and the reference detector (broadband and mono-cSi) are presented in Figures 6.85 ,6.86 ,6.87 and 6.88.

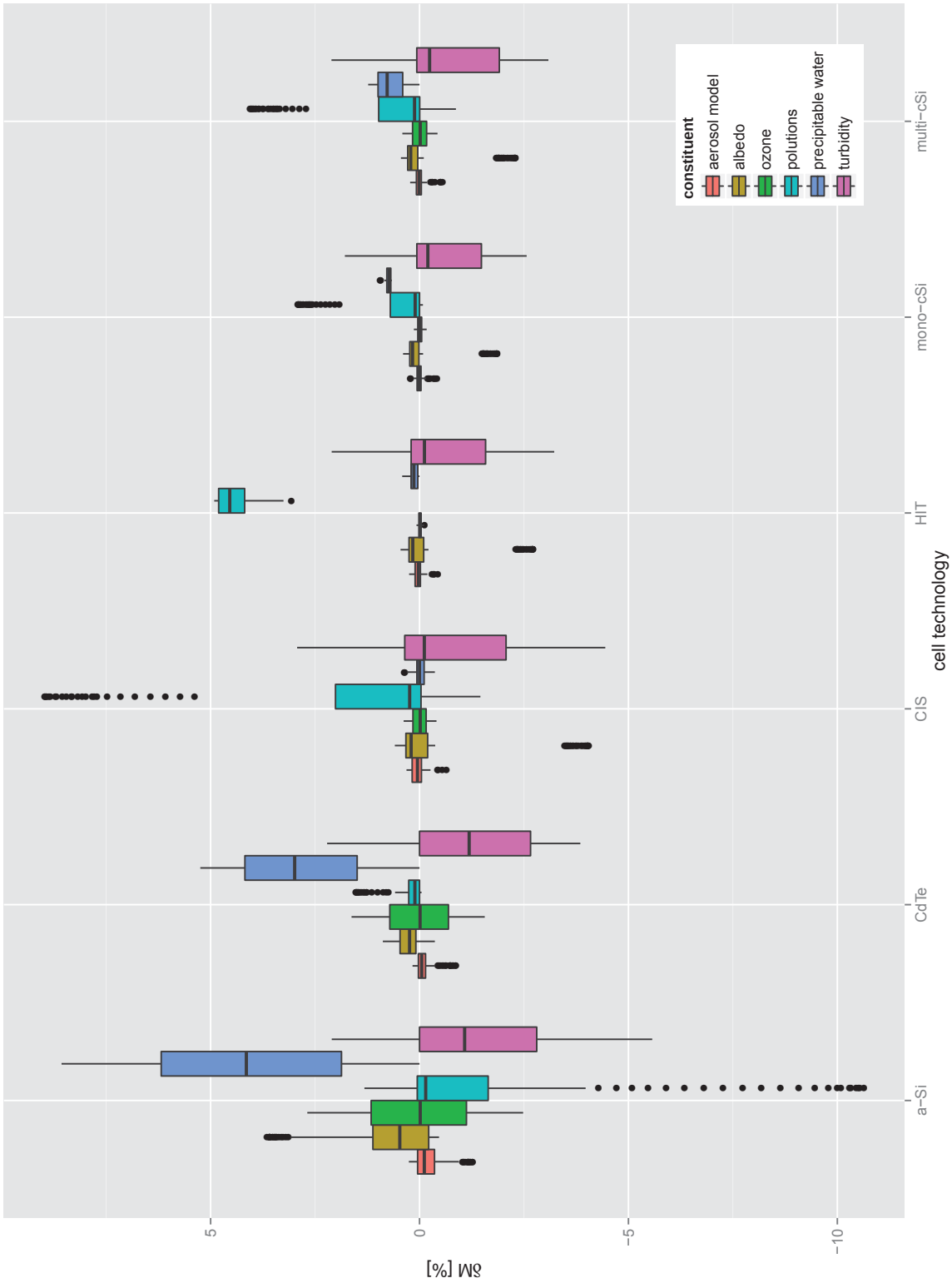

Figure 6.85: Summary - broadband reference detector at the horizontal plane

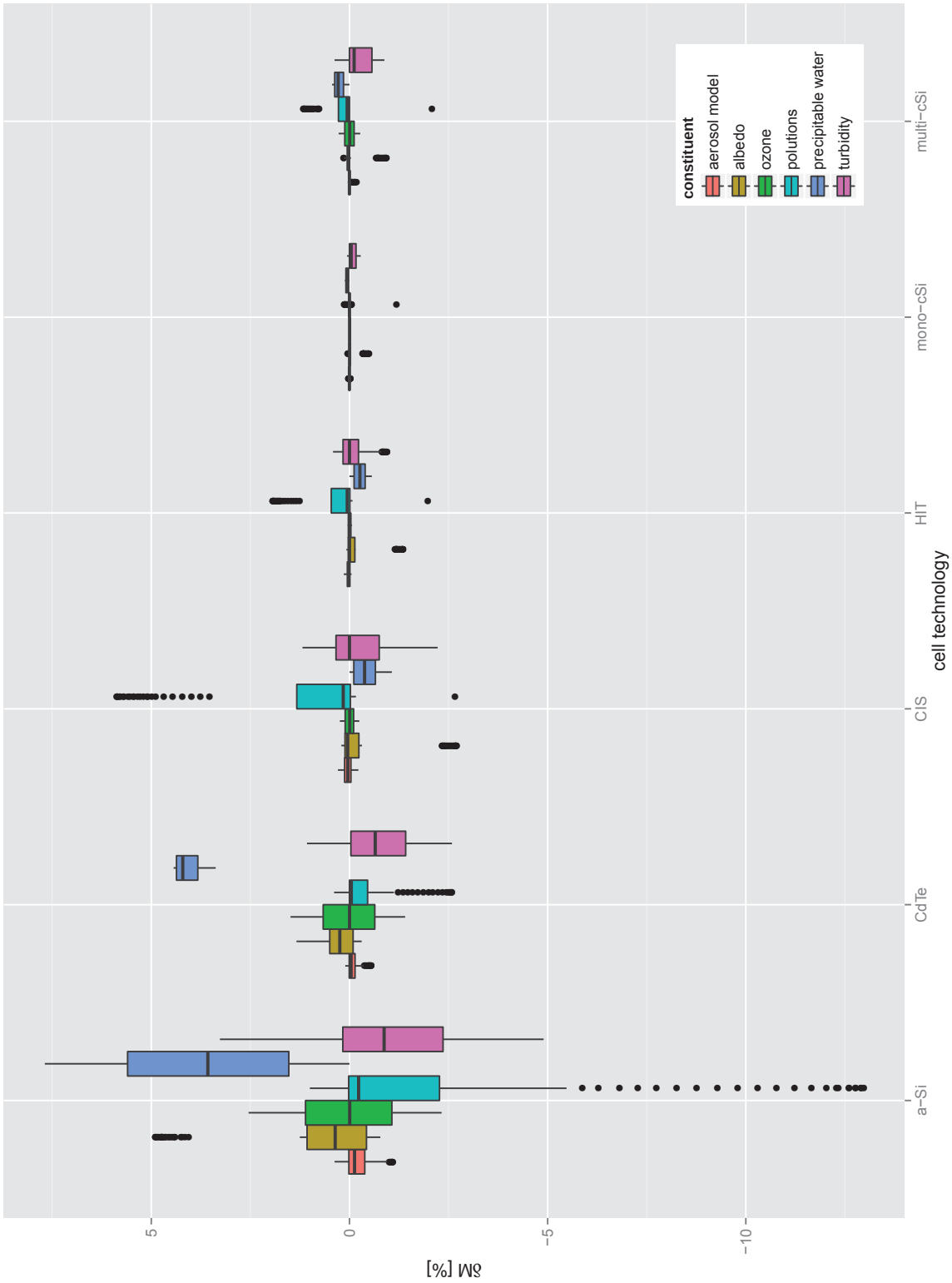

Figure 6.86: Summary - broadband reference detector at the 37° incline plane

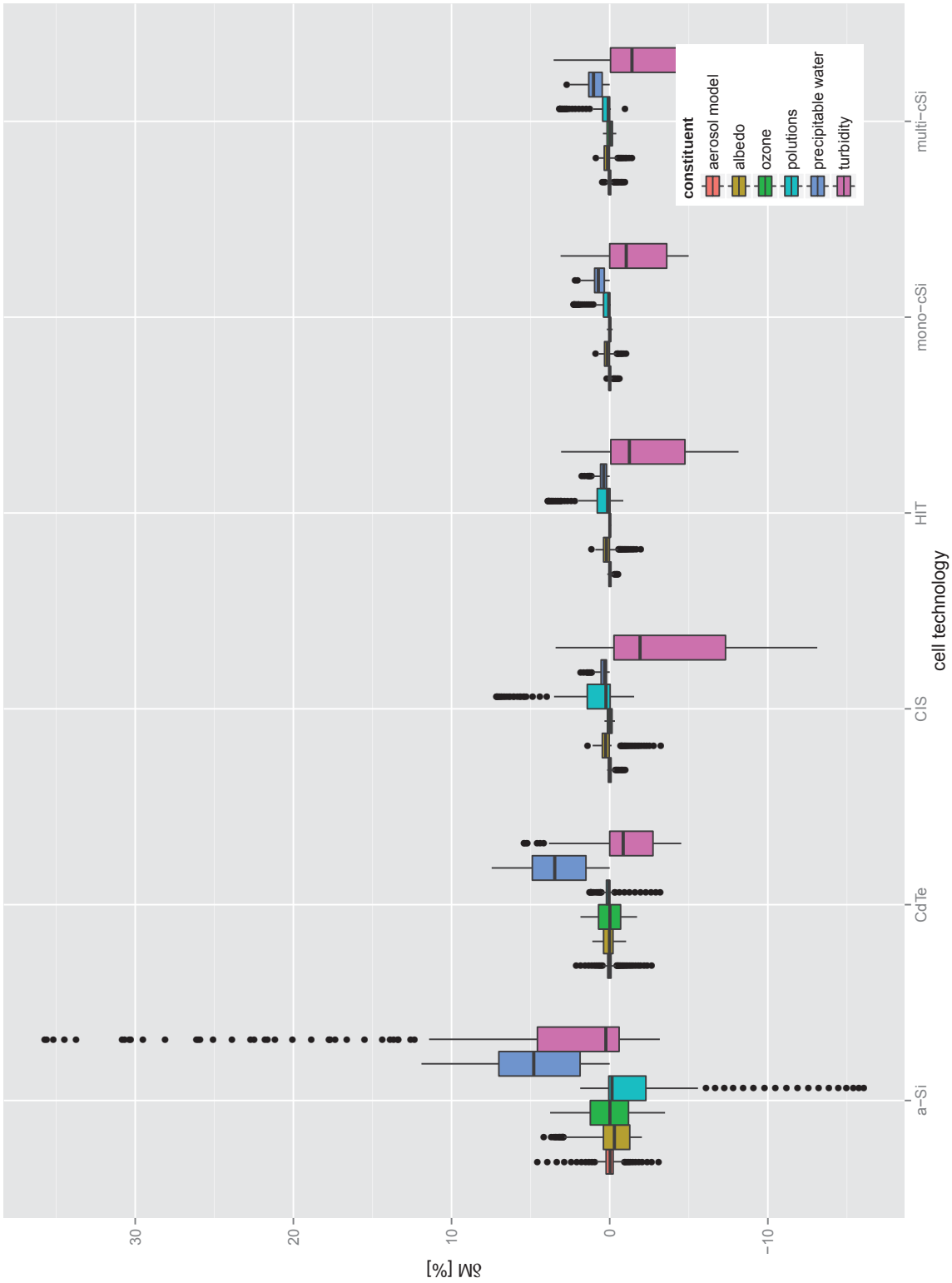

Figure 6.87: Summary - mono-cSi reference detector at the horizontal plane

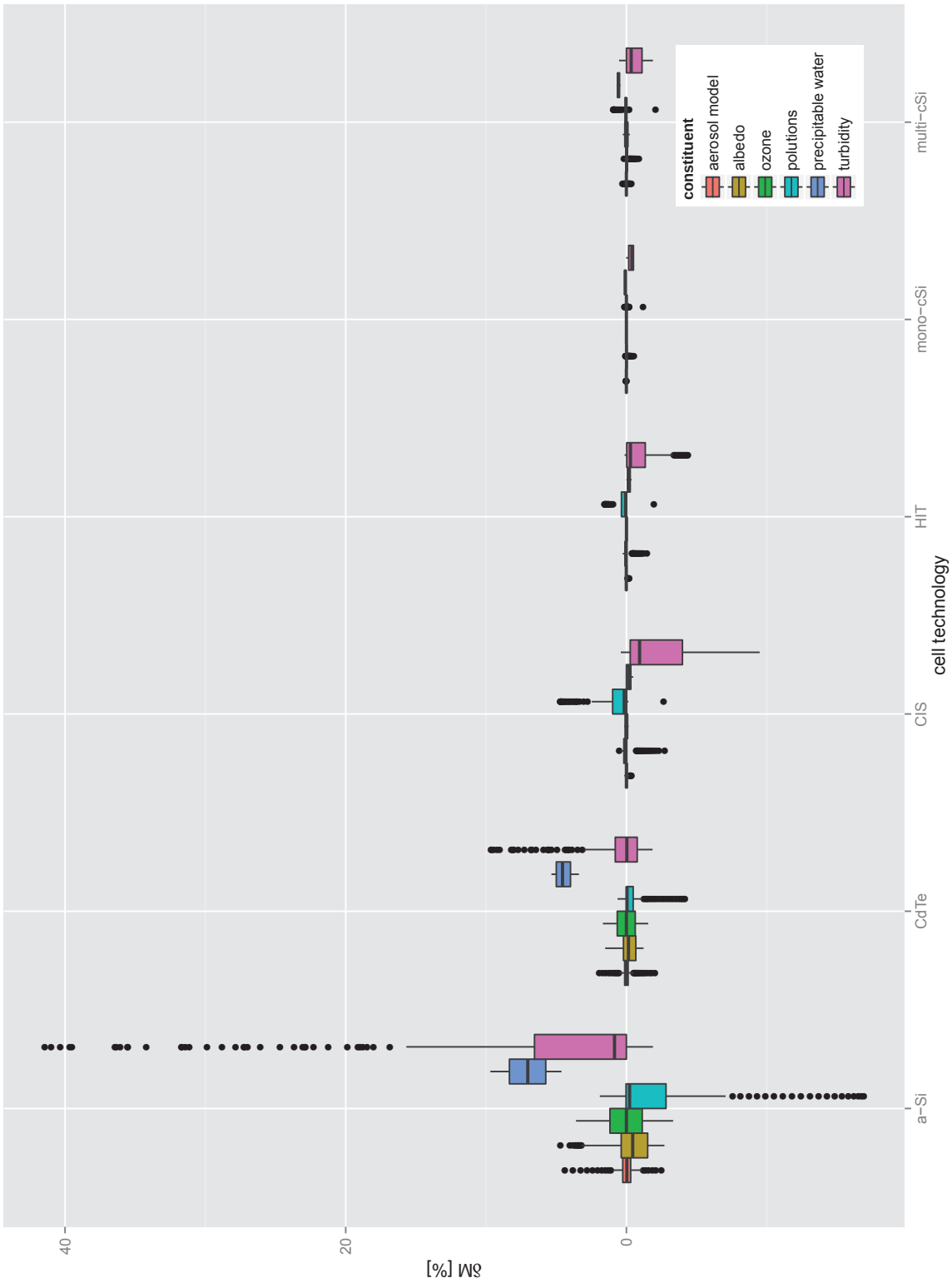

Figure 6.88: Summary - mono-cSi reference detector at the 37° incline plane

6.5 Conclusions

The impact of spectral irradiance variations on the accuracy of reference irradiance measurement was investigated in the context of various photovoltaic device and reference detector technologies. The response from the photovoltaic device and the reference irradiance detector is not proportional if both devices are not spectrally matched. This situation is not optimal as an excessive systematic error is being introduced.

The work presented has proven that the accuracy of the reference irradiance measurements can be significantly degraded by spectral mismatch between the monitored photovoltaic device and the reference detector. What's more, it was shown that the effects caused by spectral mismatch can be suppressed or amplified by the distribution of the incident spectral irradiance and the inclination of the observation plane. The characteristic and the scale of the observed "effective mismatch" depends on a specific combination of these three factors.

One type of reference irradiance detector cannot offer an optimal measurements for all kind of module technologies. Relevant correction coefficients were proposed as a partial remedy to this problem. Proposed correction coefficients, however, are only valid for the standard atmospheric conditions.

It was demonstrated that the plane of observation has a significant impact on the spectral characteristic of irradiance. Therefore, the accuracy of the reference irradiance is affected differently depending on the inclination of the observation plane. An optimal tilt angle for the photovoltaic module differs with respect to the geographic location. This observation suggests, that a specific type of the reference detector may be better suited for a given geographic location, whereas it won't be the best choice for another. Differences in spectral irradiance distributions related to the observation plane should be considered to be significant in the case of irradiance translation models. As these models predict inclined irradiance from horizontal plane measurements, ignoring spectral effects will compromise their accuracy.

It was shown that the use of a thermopile pyranometer can introduce a significant systematic error to the reference irradiance measurements for photovoltaic applications. A mono-crystalline reference cell improves the accuracy of reference

measurements in the case of photovoltaic devices with similar spectral response. However for a-Si devices there is still a significant difference in yielded results and for CdTe devices a pyranometer produces more accurate reference measurements. The accuracy of the pyranometer response is heavily affected by variations in the precipitable water content of the atmosphere. Besides the precipitable water, the accuracy of reference irradiance measurements is also significantly affected by aerosol concentration and atmospheric pollution.

Chapter 7

Conclusions

The presented thesis concentrated on the topics of solar spectral irradiance, its metrology, spectroradiometer calibration, calibration transfer standards, spectral irradiance variations and their impact on photovoltaics, and the effects of irradiance sensor spectral mismatch on accuracy of reference irradiance measurements.

The very first findings during the course of the work was a significant inconsistency between the manufacturer and in-house calibration of tested spectroradiometers. Observed initial calibration errors significantly exceeded a level which could have been considered as an acceptable considering stated uncertainty. This situation can be partially explained by the lack of standardised procedures for spectroradiometer calibration applicable to the manufacturers practice, leading to the conclusion that this requires the attention of national and international standards bodies. To support this claim, calibration of standardised broadband thermophile pyranometers was proven to be significantly more accurate. Work exploring possible standardisable methods employed a Langley outdoor calibration method as an alternative method for spectroradiometer calibration. This exercise has shown that spectroradiometer calibration can be achieved also without highly specialised equipment, under clear sky conditions, even without exporting the spectroradiometer to high altitude locations. During the outdoor campaign it was proven that semiconductor spectroradiometers should be calibrated separately for each shutter time to assure the linearity of the spectroradiometer response. Appropriate linearity calibration is especially important in the case of a semiconductor spectroradiometer.

Uncertainty of a spectroradiometer calibration heavily depends on the uncertainty of a transferred calibration standard. Spectral irradiance transfer standard is realised with a tungsten halogen FEL bulb. At this point the question arises whether a simplified characterisation technique of a FEL bulb can produce acceptable calibration of a working standard. It has been proved in this thesis, that even simplified characterisation of a bulb, which takes into consideration only temperature and active filament area can produce repeatable bulb calibration with deviation from the mean lower than ±5%. The proposed technique also considers continuous monitoring of output intensity and spectrum of the reference bulb. This way, stability of the bulb output can be improved and a correctness of the operational conditions can be assured. The only existing normative documents defining standards for spectral irradiance originate with NIST (USA). There are no european standards regulating this domain. Given that solar technologies became ubiquitous over the past years and spectral radiation measurements are a significant domain of science, adequate and proportional effort should be undertaken to provide industry with an affordable spectral irradiance standards the industry could comply with.

Long term terrestrial solar spectral irradiance is one of the rarest type of environmental observations. In this thesis, a dedicated spectral irradiance metrological station has been developed and equipped with state-of-the-art radiometers. Spectral irradiance measurements were collected for a period of more than 4 years, creating a unique set of spectral irradiance data . Analysis of this data has extracted additional knowledge about solar spectral irradiance and its variations in the natural environment. Comparison of an observed long term average spectral irradiance with an AM1.5 standard spectrum has shown that there is a substantial difference between observations and the AM1.5 standard. It also was proven that the observed long term average spectral irradiance stayed in a closer relation to yearly averaged 10 minutes SMARTS modelled clear sky irradiance. This allows the conclusion that SMARTS simulations for clear sky conditions can produce a long term average spectrum closer to the results of the observations, than can the AM1.5 standard. Variability of spectral irradiance has been measured and its impact on various photovoltaic devices has been investigated. It has been shown that the spectral characteristic of the solar irradiance is impacted

not only by the air mass, but also by the cloudiness. Further analysis has shown that clouds, besides their neutral spectral characteristic in the VIS spectrum, can increase the level of diffuse irradiance through the back scattering mechanism. Achieved results allow for application of appropriate corrective coefficients to PV device efficiency, based on the cloud coverage. The scale of such a correction varies in the range of 0.5% to 4%, in comparison with the clear sky spectrum. These findings can be applied in energy yield modelling tools to improve the accuracy of expected yield.

It has been shown in field operation that the actual efficiency of photovoltaic devices can be affected by a spectral variations of solar irradiance. The composition of the spectral irradiance also affects the accuracy of reference irradiance measurements. The response from a photovoltaic device and from a reference irradiance sensor is not proportional if the sensors are not spectrally matched. This situation is not optimal as an excessive systematic error is being introduced. The impact of spectral irradiance variations on the accuracy of a reference sensor response was investigated, in the context of various photovoltaic device technologies. Two types of reference sensors were investigated: broadband (thermophile pyranometer) and mono-crystalline silicone. It was demonstrated that none of the sensors were capable of providing spectral-effects-free response for a whole variety of cell technologies. Furthermore, it was shown that the use of a thermophile pyranometer introduces a significant systematic error to the reference irradiance measurements for photovoltaic applications. A mono-crystalline reference cell improves the accuracy of reference measurements in the case of photovoltaic devices with similar spectral response. However for a-Si devices there is still a significant difference in responses and for CdTe devices a pyranometer produces more accurate reference measurements. Appropriate correction coefficients were proposed to account for spectral mismatch between the sensor and the cell technologies. The proposed coefficients are valid only for AM1.5 sky conditions, so the impact of various atmospheric and environmental factors on the differences between reference sensor and photovoltaic cell response were also investigated. One of the most interesting conclusions is that the accuracy of the pyranometer response was heavily affected by variations of the precipitable water content of the atmosphere. Observed effects clearly demonstrate how the atmospheric con-

stituent, which only marginally affects irradiance within an a-Si spectral range, can have a strong impact on the accuracy of reference irradiance measurements. Besides the precipitable water, the accuracy of reference irradiance measurements is also significantly affected by aerosols concentration and atmospheric pollution. The presented results can be used for a partial correction of a spectral mismatch. Pyranometers, despite some advantages, are not always the best possible solution for a reference irradiance sensor in photovoltaic systems. However, the reference cells available on the market are not always a better choice and the conclusion here is that the selection of an optimal reference sensor should be based on a specific system design.

The investigations undertaken analysed a variety of aspects of spectral irradiance: starting from validation of the spectroradiometer calibration, through the spectral irradiance transfer standards, impact of spectral irradiance variations on efficiency of photovoltaic device and ending on the impact of spectral mismatch between the reference irradiance sensor and the monitored photovoltaic devices.

List of Publications

M. Krawczynski, M.B. Strobel, and R. Gottschalg, Intercomparison of pyranometers for distributed measurements system, In Photovoltaic Science Application and Technology Conference, Wrexham, UK, April 2009. The Solar Energy Society

M. Krawczynski, M.B. Strobel and R. Gottschalg, Intercomparison of spectroradiometers for outdoor performance monitoring, In Proceedings of the 24th European Photovoltaic Solar Energy Conference and Exhibition, pages 3406 3408, Hamburg, Germany, September 2009. WIP Wirtschaft und Infrastruktur GmbH

M. Krawczynski, M.B. Strobel, T.R. Betts and R. Gottschalg, Spectral influences on estimations of useful irradiance for different pv technologies. In Photovoltaic Science Application and Technology Conference, Southampton, UK, March 2010. The Solar Energy Society

M. Krawczynski, M.B. Strobel, B. Goss, N. Bristow, M. Bliss, T.R. Betts, and R. Gottschalg, Large scale pv system monitoring - modules technology intercomparison. In Photovoltaic Specialists Conference, pages 002295 002300, Hawai, USA, June 2010. IEEE

M. Krawczynski, M.B. Strobel, C. J. Hibberd, T. R. Betts, and R. Gottschalg, Influence of spectral irradiance measurements on accuracy of performance ratio estimation in large scale pv systems, In Proceedings of the 25th European Photovoltaic Solar Energy Conference and Exhibition, pages 4710 4714, Valencia, Spain, December 2010. WIP Wirtschaft und Infrastruktur GmbH

M. Zehner, M. Hartmann, J. Weizenbeck, T. Gratzl, T. Weigl, Mayer B., G. Wirth, M. Krawczynski, T.R. Betts, R. Gottschalg, A. Hammer, B. Giesler, G. Becker and O. Mayer, Systematic analysis of meteorological irradiation effects. In Proceedings of the 25th European Photovoltaic Solar Energy Conference and Exhibition, pages 4545 4548, Valencia, Spain, September 2010. WIP Wirtschaft und Infrastruktur GmbH

M. Krawczynski, M.B. Strobel, T.R. Betts, and R. Gottschalg, Spectral irradiance measurements for photovoltaic systems in maritime climates. In Photovoltaic Science Application and Technology Conference, Edinburgh, UK, April 2011. The Solar Energy Society

M. Krawczynski and R. Gottschalg, Wireless supervisory control and data acquisition system for photovoltaic installations. In Proceedings of the 26th European Photovoltaic Solar Energy Conference and Exhibition, pages 4281 4282, Hamburg, Germany, September 2011. WIP Wirtschaft und Infrastruktur GmbH

Appendix A

Composition of the atmosphere

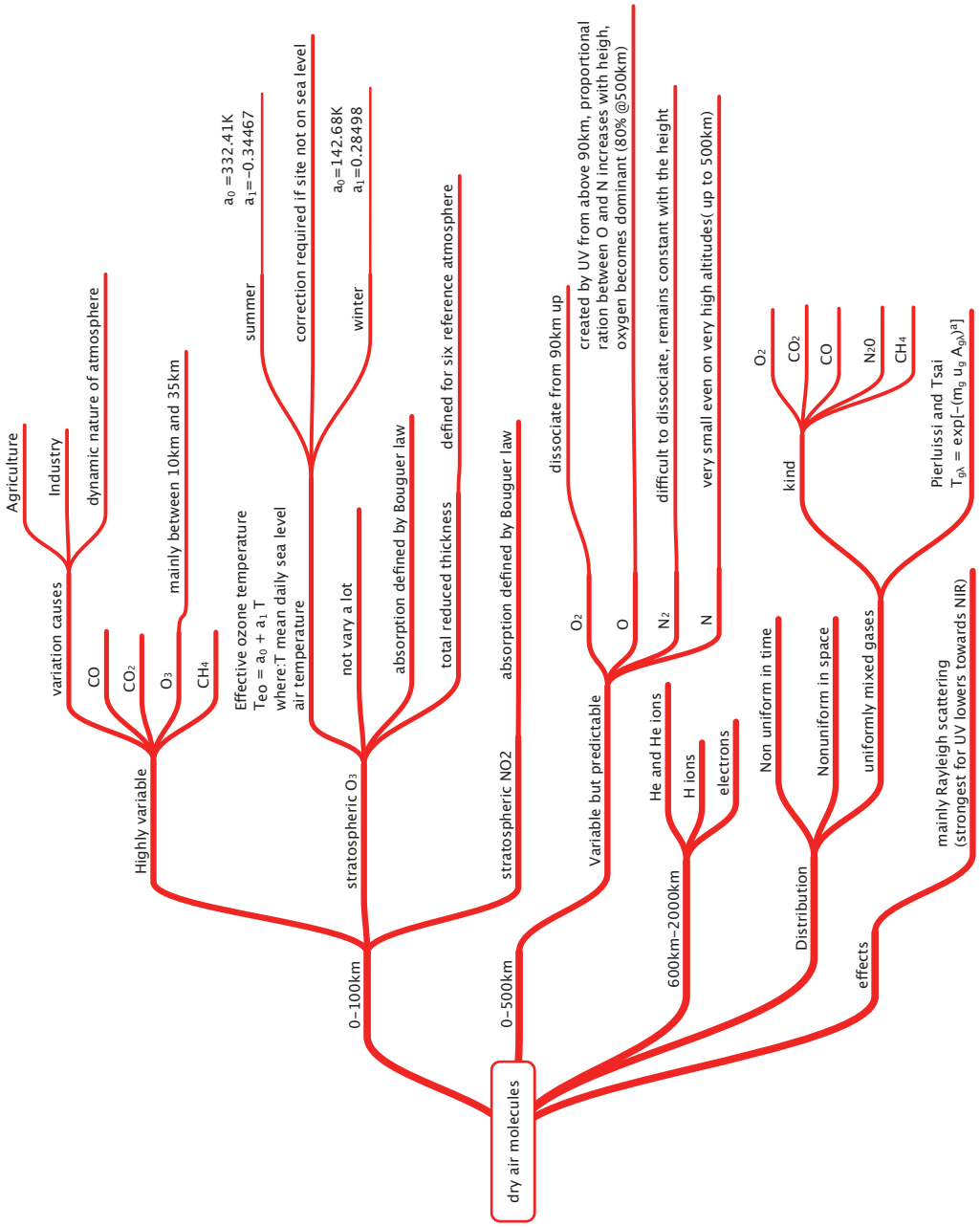

Figure 7.1: Dry air molecules in the atmosphere.

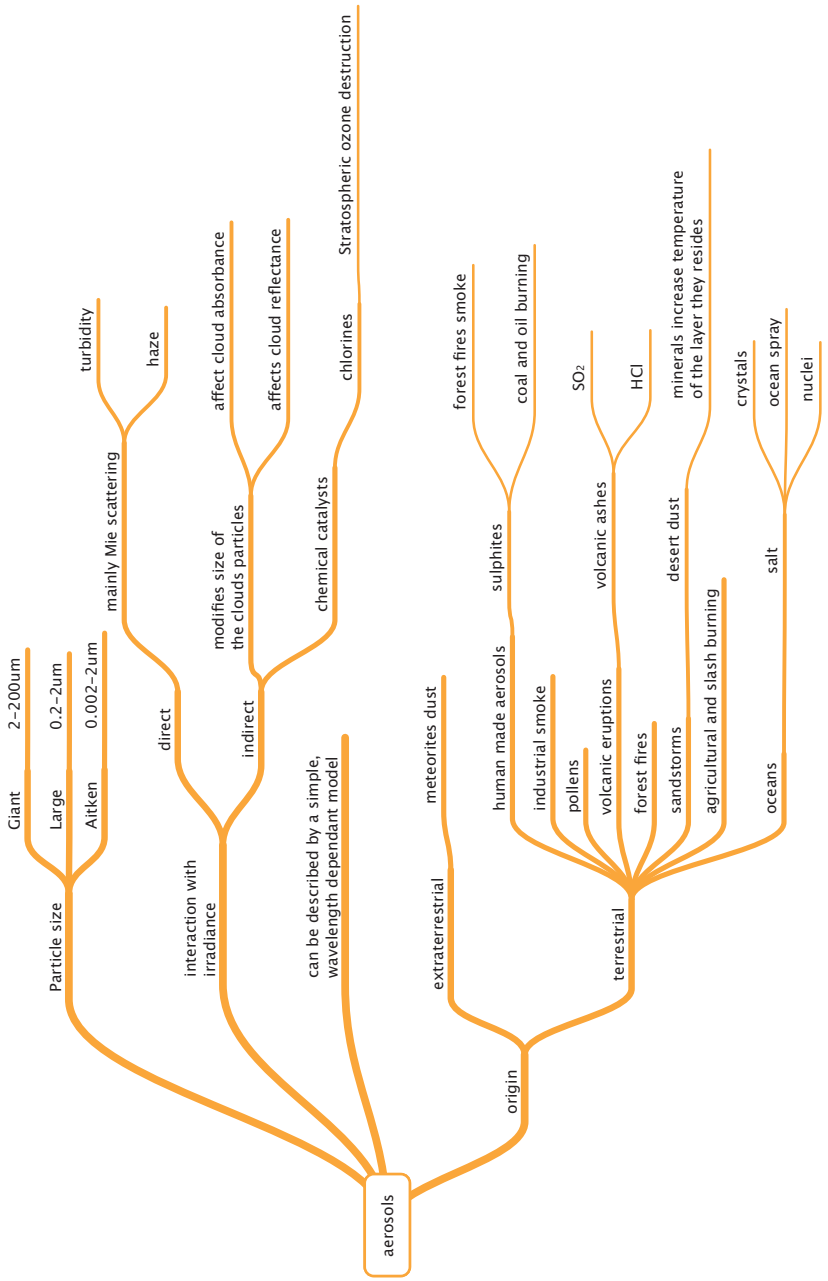

Figure 7.2: Aerosols in the atmosphere.

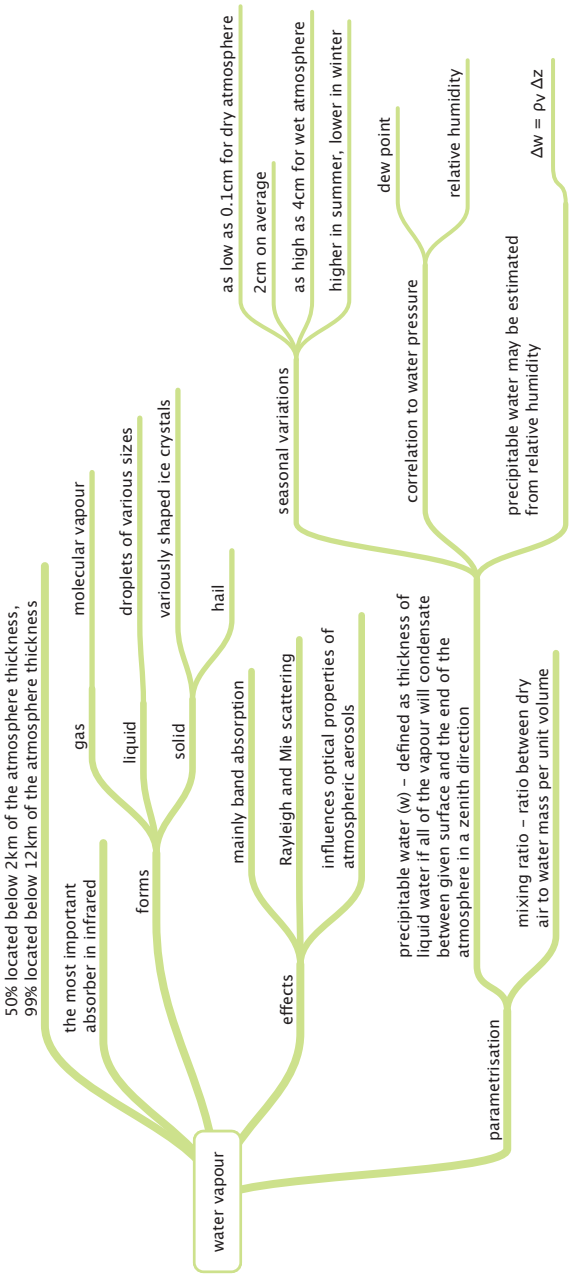

Figure 7.3: Water vapour in the atmosphere.

Appendix B

Data Logging System (Met Box)

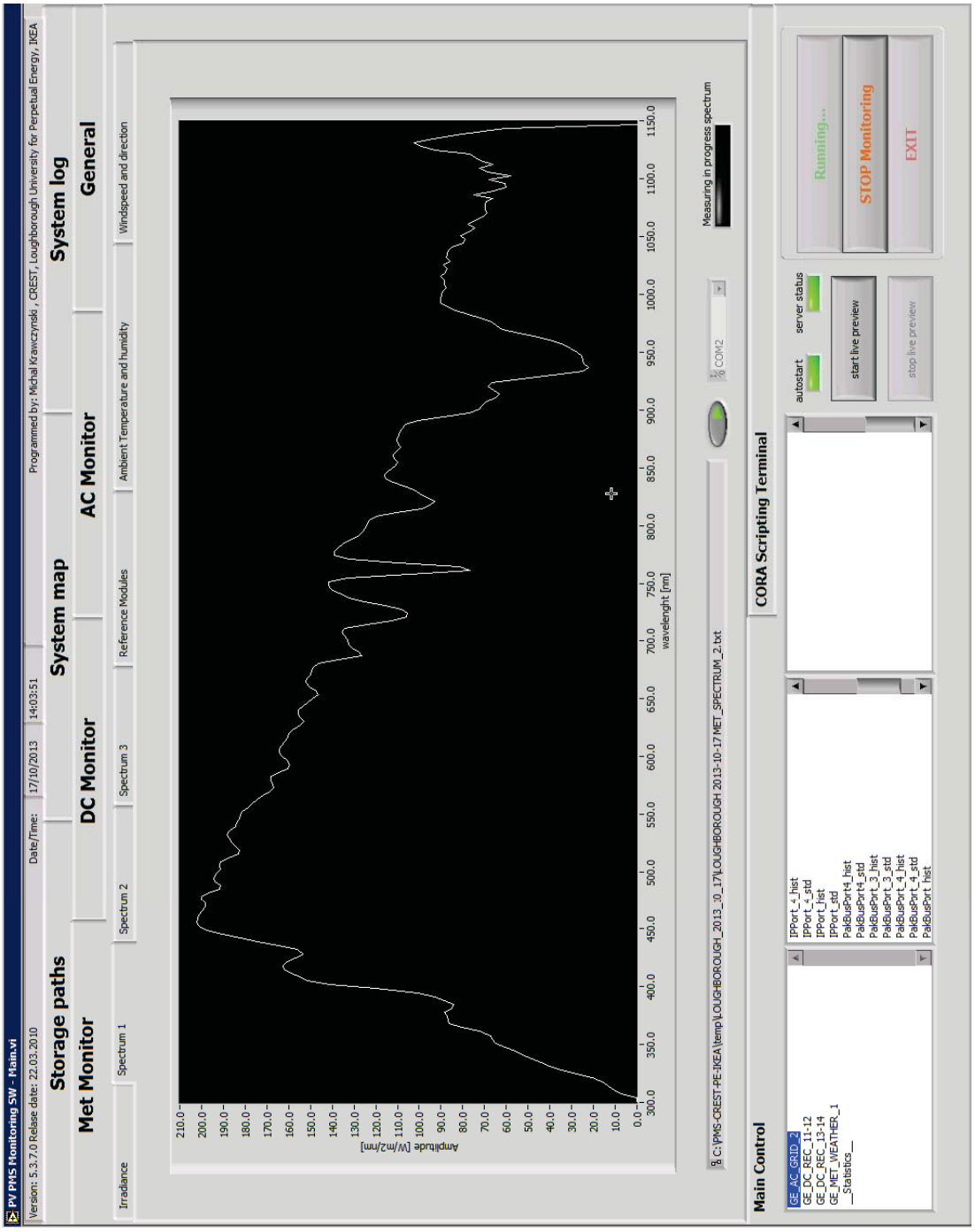

Figure 7.4: Data Logging System - spectral measurements

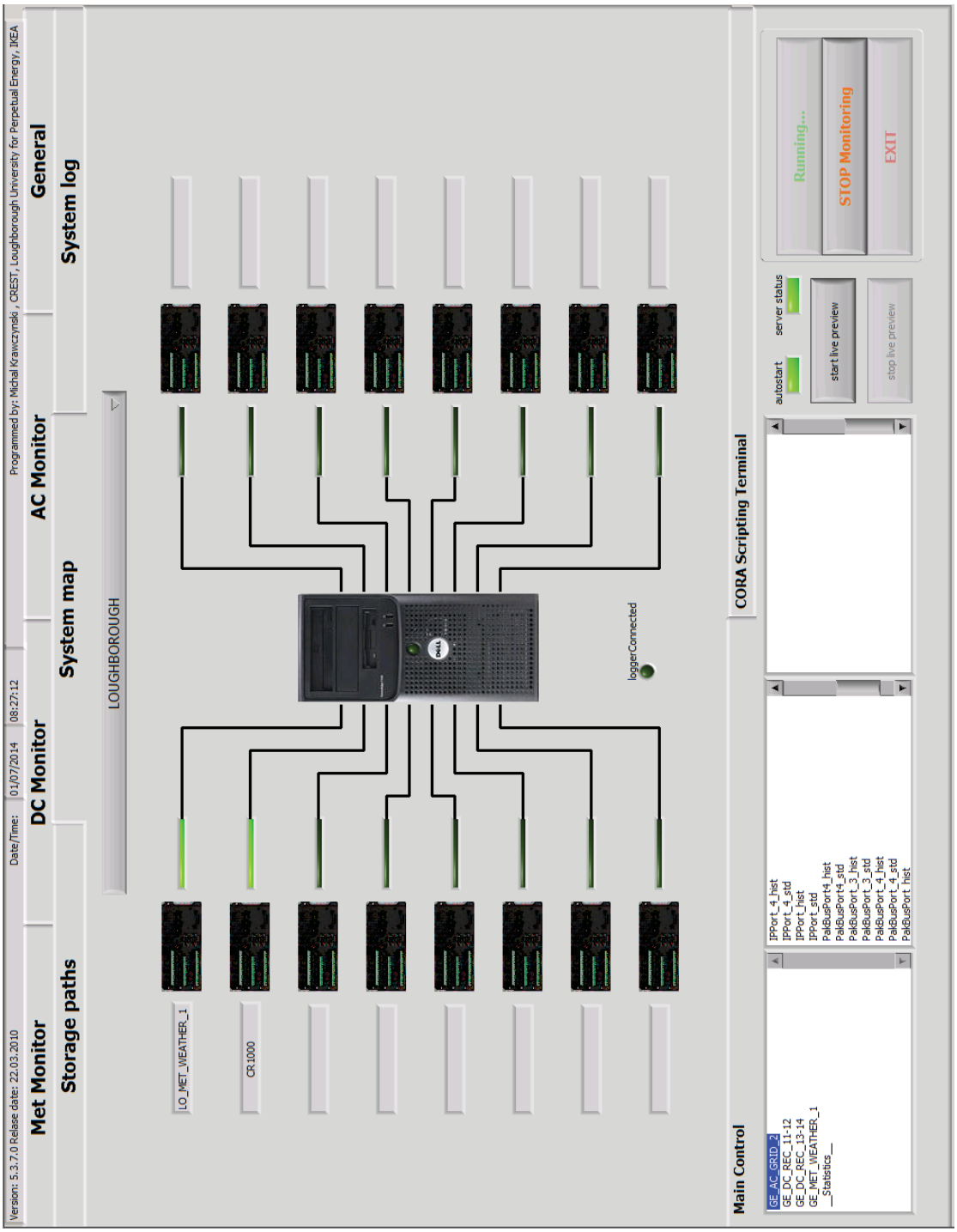

Figure 7.5: Data Logging System - block diagram

Appendix C

Data acquisition system

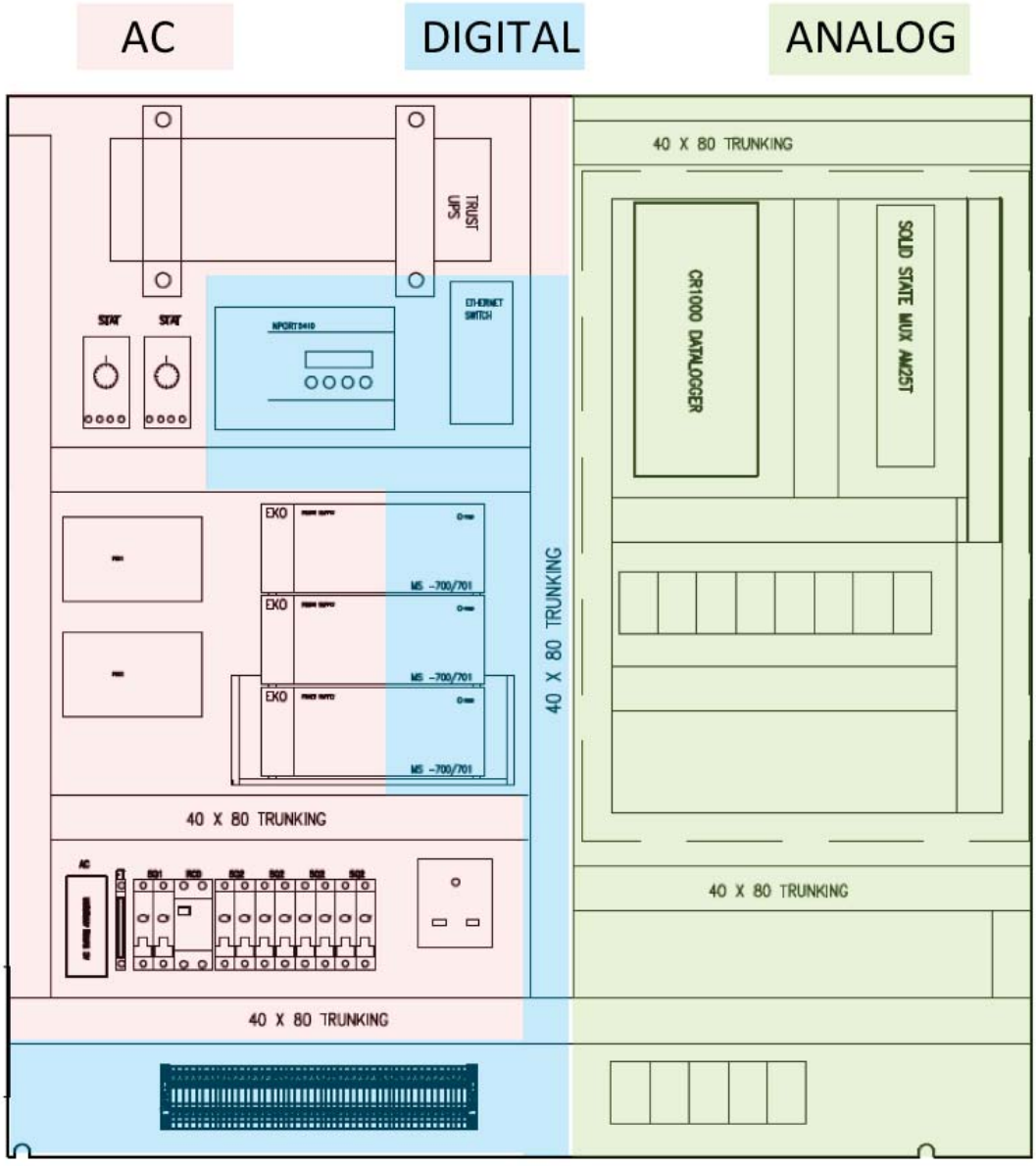

Figure 7.6: Data acquisition system - internal layout

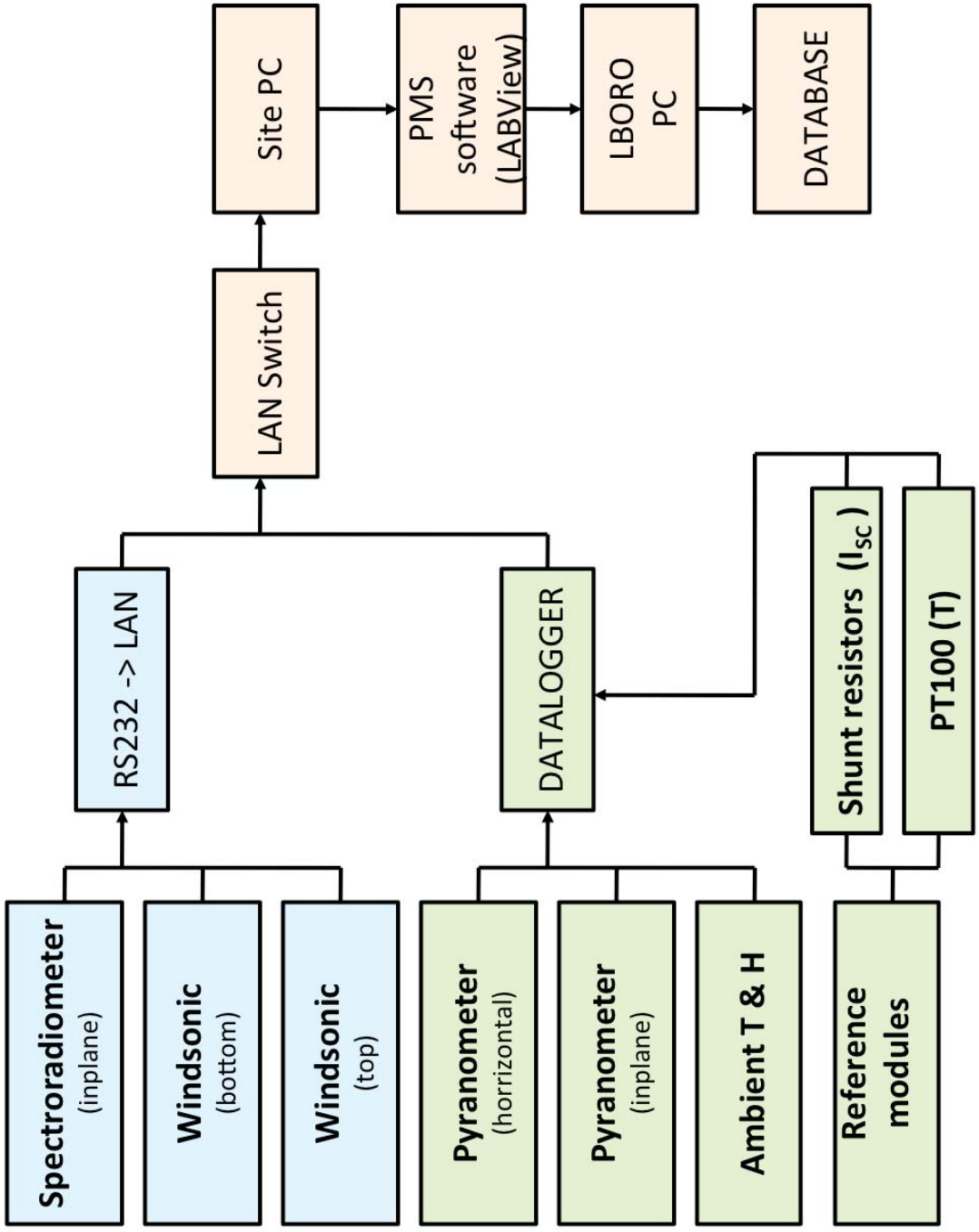

Figure 7.7: Data acquisition system - block diagram

Appendix D

SMARTS batch processing software

To model spectral irradiance under various atmospheric conditions author developed dedicated batch processing software. Developed software utilises SMARTS model engine to generate spectral irradiance under various atmospheric conditions within boundaries defined by the user. It also allows to calculate output of a specific photovoltaic cell technology under simulated conditions. Software interface was organised in a following set of tabs:

- Model parameters (see figure 7.8 for more details)
- Output setup (see figure 7.9 for more details)
- Output (see figure 7.11 for more details)
- SR (see figure 7.12 for more details)
- Batch processing (see figure 7.10 for more details)
- Help

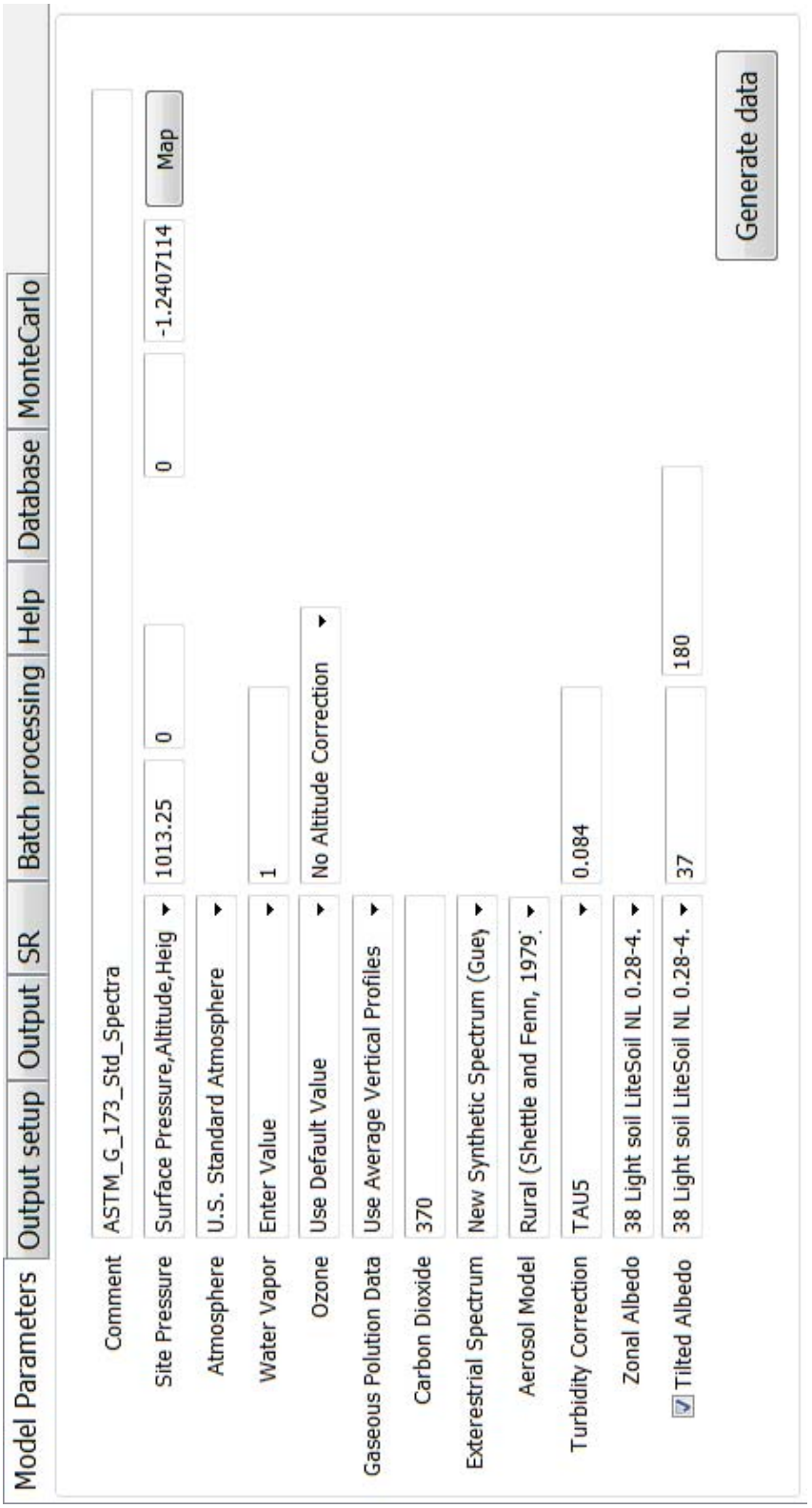

Figure 7.8: SMARTS model - input parameters tab

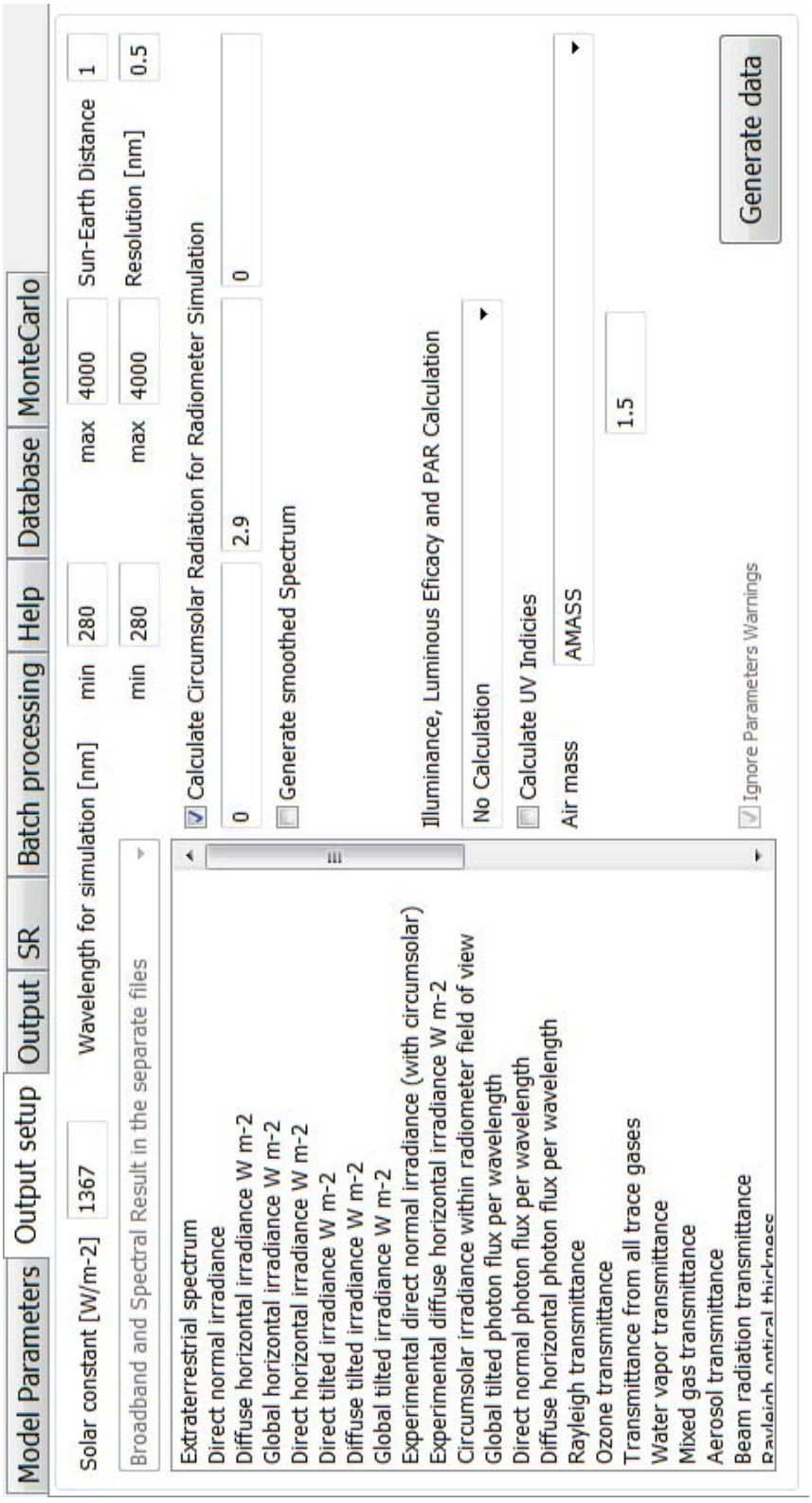

Figure 7.9: SMARTS model - output parameters tab

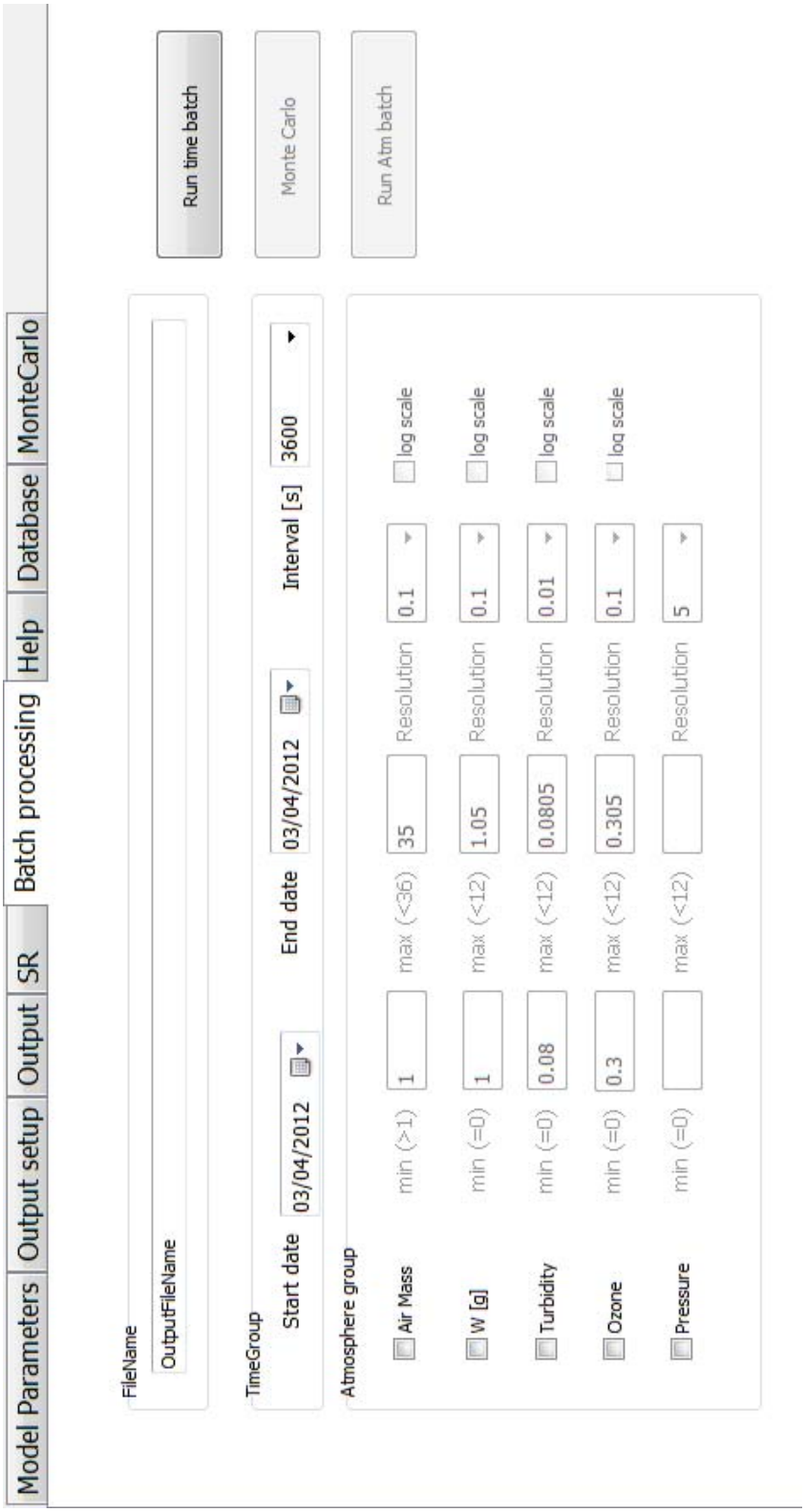

Figure 7.10: SMARTS model - batch processor

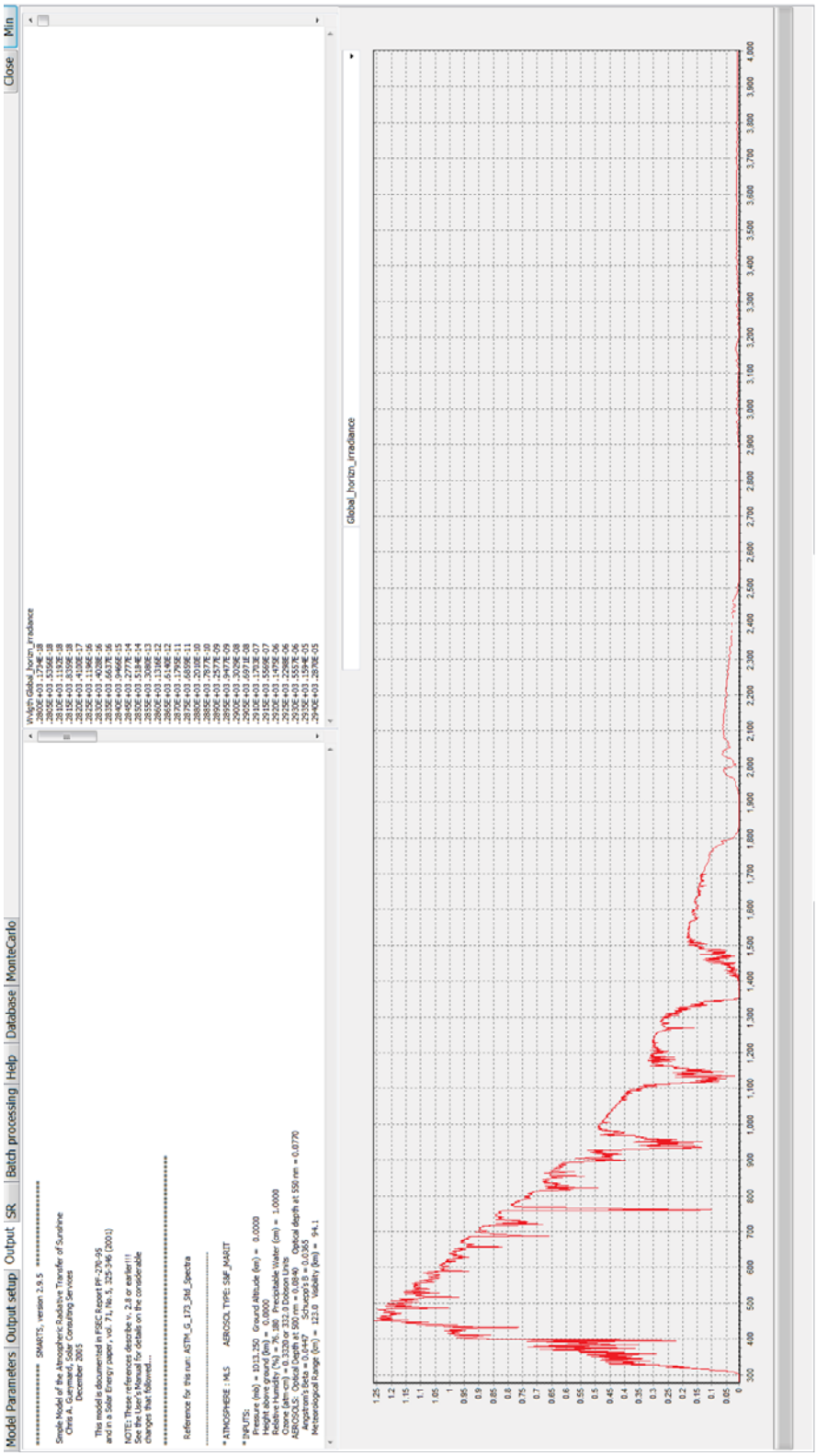

Figure 7.11: SMARTS model - irradiance results tab

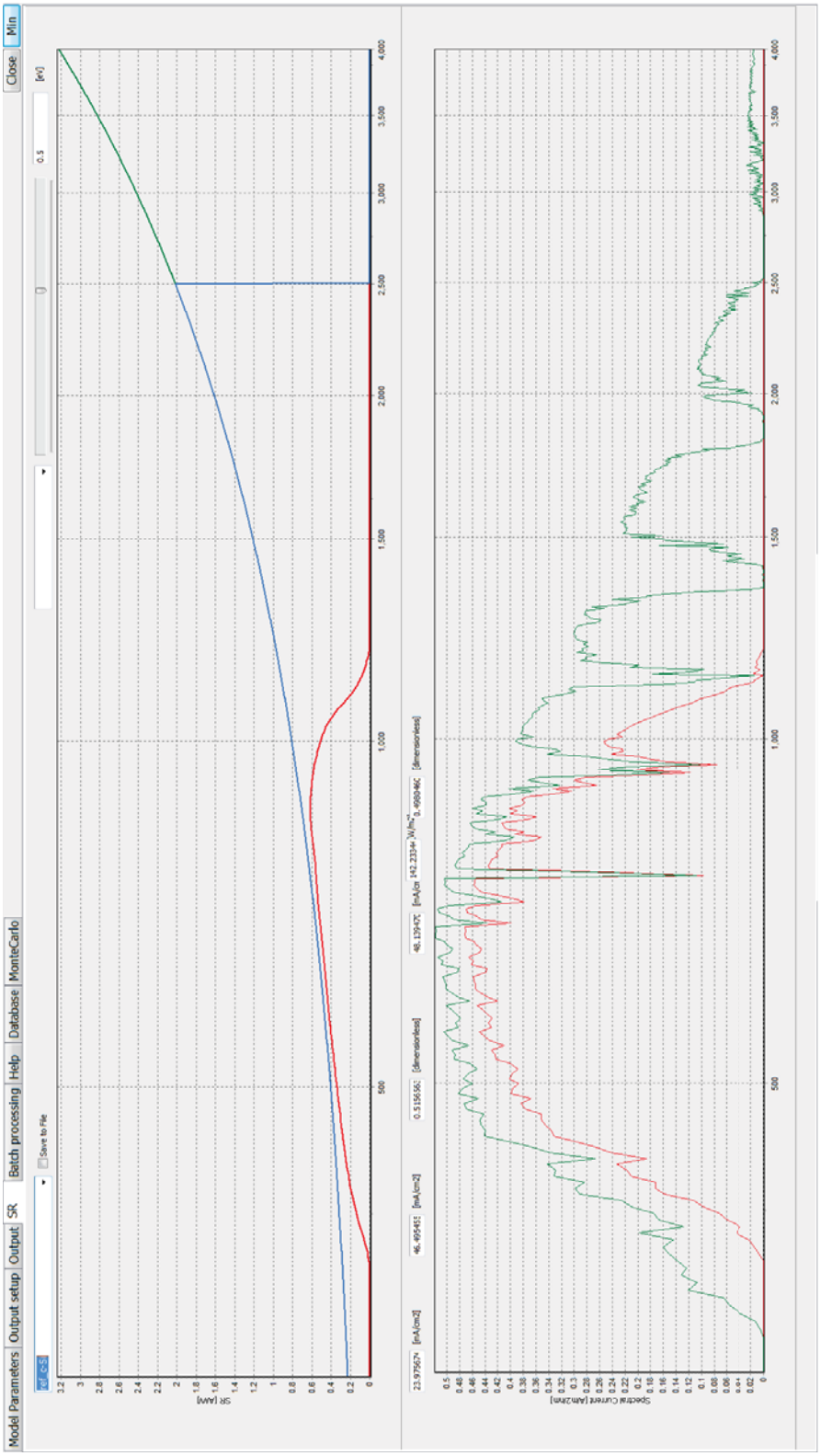

Figure 7.12: SMARTS model - photovoltaic device output

References

[1] NREL. Best research-cell efficiencies, 2013. URL http://www.nrel.gov/ncpv/images/efficiency_chart.jpg. viii, 12

[2] Central operation of resources for educators. The National Aeronautics and Space Administration, 2012. viii, 35

[3] Switzerland ISO, Geneva. Standard atmosphere, May 1975. viii, 39

[4] P.B. Russell, J.M. Livingston, B. Schmid, J. Redemann, and J. Eilers. Ames airborne tracking sunphotometer, AATS-14, 2002. ix, 39

[5] Vaisala Oyj. Humidity conversion formulas:calculation formulas for humidity, 2013. ix, 42

[6] S. Barbaro, G. Cannata, S. Coppolino, C. Leone, and E. Sinagra. Correlation between relative sunshine and state of the sky. *Solar Energy*, 26(6): 537–550, 1981. xxii, 43

[7] M. Iqbal. *An introduction to solar radiation*. Academic Press,Orlando, FL, 1983. xxii, 44

[8] EIA. Sectoral approaches in electricity: Building bridges to a safe climate, 2009. 1

[9] P. Taylor, O. Lavagne d'orTigue, N. Trudeau, and M. Francoeur. Energy efficiency indicators for public electricity production from fossil fuels. OECD/IEA, July 2008. 1

[10] U.S. Energy Information Administration. International energy outlook 2011, 2011. 1

[11] U.S. Energy Information Administration. International energy outlook 2014, 2014. 1

[12] U.S. Energy Information Administration. International energy outlook 2011, 2010. 1

[13] A.E. Becquerel. Recherches sur les effets de la radiation chimique de la lumiere solaire au moyen des courants electriques. *Comptes Rendus de LAcademie des Sciences*, 9:145–149, 1839. 2, 9

[14] EPIA. Global market outlook for photovoltaics until 2014-2018, May 2014. 2, 3

[15] U.S. Energy Information Administration. Annual energy outlook 2012, June 2012. 2

[16] Euclid. Optics. Manusctipt, 300BC. 6

[17] C. Maxwell. A dynamical theory of the electromagnetic field. *Philosophical Transactions of the Royal Society*, 155:459–512, 1865. 6

[18] M. Planck. On the law of distribution of energy in the normal spectrum. *Annalen der Physik*, 4:553, 1901. 7

[19] M. Planck. On an improvement of wien's equation for the spectrum. *German Physical Society*, 1900. 7

[20] G.N. Lewis. The conservation of photons. *Nature*, 118:874–875, 1926. 7

[21] Switzerland ISO, Geneva. Optics and photonics - spectral bands, August 2007. 8

[22] W.G. Adams and R.E. Day. The action of light on selenium. *Proceedings of the Royal Society*, A25:113, 1877. 10

[23] C.E. Fritts. On a new form of selenium photocell. *Procedings of the American Association for the Advancement of Science*, 33:97, 1883. 17

[24] L. Bergmann. Uber eine neue selen- sperrschicht photozelle. *Physikalische Zeitschrift*, 32:286, 1931.

[25] L.O. Grondahl. The copper-cuprous-oxide rectifier and photoelectric cell. *Review of Modern Physics*, 5:141, 1933.

[26] F.C. Nix and A.W. Treptwo. A thallous sulphide photo emf cell. *Journal Opt. Society of America*, 29:457, 1939. 10

[27] R. Ohl. Light-sensitive electric device including silicon, 1941. 10

[28] R. Ohl. US Patent 2402662, June 1946. 10

[29] J. Czochralski. Kristallisationsgeschwindigkeit der metalle. *Zeitschrift für Physikalische Chemie*, 92:219–221, 1918. 16

[30] J. Czochralski and W. Garlicka. Crystallization rate of sodium and the crystallization rate of sodium and the relations between atomic heat of solidification and crystallization rate. *Wiadomosci Instytutu Metalurgii i Metaloznawstwa*, 3:39–41, 1936. 16

[31] D. M. Chapin, C. S. Fuller, and G. L. Pearson. A new silicon p-n junction photocell for converting solar radiation into electrical power. *Journal of Applied Physics*, 25(5):676–677, 1954. doi: 10.1063/1.1721711. 16

[32] J. Zhao, A. Wang, M.A. Green, and F. Ferrazza. Novel 19.8% efficient 'honeycomb' textured multicrystalline and 24.4% monocrystalline silicon solar cells. *Applied Physics Letters*, 73:1991–1993, 1998. 16

[33] O. Schultz, S.W. Glunz, and G.P. Willeke. Multicrystalline silicon solar cells exceeding 20% efficiency. *Progress in Photovoltaics: Research and Applications*, 12:553–558, 2004. 16

[34] J.J. Loferski. Theoretical considerations governing the choice of the optimum semiconductor for photovoltaic solar energy conversion. *Journal of Applied Physics*, 27(7):777–784, July 1956. 17

[35] D. de Nobel. Electronic properties of materials: A guide to the literature, 1959. 17

[36] J. Parkes, R.D. Tomlinson, and M.J. Hampshire. Electrical properties of CuInSe2 singlecrystals. *Solid-State Electronics*, 16:773–777, 1954. 17

[37] S. Wagner, J. Shay, P. Migliorato, and H. Kasper. CuInSe2/CDs heterojunction photovoltaic detectors. *Applied Physics Letters*, 25:434–435, 1974. 17

[38] D.E. Carlson and C.R. Wronski. Amorphous silicon solar cells. *Applied Physics Letters*, 28:671–673, 1976. 17

[39] European Photovoltaic Industry Association. Solar photovoltaic electricity empowering the world. Solar generation 6 report, 2011. 18

[40] BSi. Procedures for temperature and irradiance corrections to measured i-v characteristics. British Standards, 3 2010. 30

[41] R. M. Smith, D. C. Jordan, and S. R. Kurtz. Outdoor pv module degradation of current-voltage parameters. 2012. 31

[42] K.M. Broek, I.J. Bennett, M.J. Jansen, N.J.C.M. Borg, and W. Eerenstein. Light and current induced degradation in p-type multi-crystalline cells and development of an inspection method and a stabilization method. *Solar Energy*, 2011:2010, September 2012.

[43] R. Feist, M. Mills, S. Rozeveld, C. Wood, and K. Thompson. Thermal degradation and light capture performance of CuInGaSe(CIGS) and c-Si photovoltaic devices. In *Photovoltaic Specialists Conference (PVSC), 2010 35th IEEE*, pages 003411–003416. IEEE, 2010.

[44] E. L. Meyer and E E. van Dyk. Assessing the reliability and degradation of photovoltaic module performance parameters. *Reliability, IEEE Transactions on*, 53(1):83–92, 2004. 31

[45] G. Makrides, B. Zinsser, A. Phinikarides, M. Schubert, and G.E. Georghiou. Temperature and thermal annealing effects on different photovoltaic technologies. *Renewable Energy*, 43(0):407 – 417, 2012. ISSN 0960-1481. doi: 10.1016/j.renene.2011.11.046. URL http://www.sciencedirect.com/science/article/pii/S0960148111006483. 31

[46] BSi. Photovoltaic system performance monitoring. guidelines for measurement, data exchange and analysis photovoltaic system performance monitoring. guidelines for measurement, data exchange and analysis photovoltaic system performance monitoring — guidelines for measurement, data exchange and analysis. British Standards, 12 1998. 32, 34

[47] B. Marion, J. Adelstein, and K. Boyle. Performance parameters for grid-connected pv systems. In *National Renewable Energy Laboratory 31st IEEE Photovoltaics Specialists Conference and Exhibition*, Lake Buena Vista, Florida, January 2005. 32

[48] A.Einstein. Does the inertia of a body depend upon its energy content? *Annalen der Physik*, 4(18):639–641, 1905. 34

[49] ASTM International. Standard solar constant and zero air mass solar spectral irradiance tables, 2000. 35, 36

[50] C. Wehrli. Extraterrestrial solar spectrum, 1985. 36, 84, 92

[51] A. T. Young. Air mass and refraction. *Applied Optics*, 33(6):1108–1110, Feb 1994. doi: 10.1364/AO.33.001108. URL http://ao.osa.org/abstract.cfm?URI=ao-33-6-1108. 41

[52] B.E. Schaefer. To the visual limits: How deep can you see? Sky & Telescope, 1998.

[53] K. A. Pickering. The southern limits of the ancient star catalog. *DIO*, 12:1: 3–27, 2002. 41

[54] F. Kasten and A.T. Young. Revised optical air mass tables and approximation formula. *Applied Optics*, 28(22):4735–4738, Nov 1989. doi:

10.1364/AO.28.004735. URL http://ao.osa.org/abstract.cfm?URI=ao-28-22-4735. 41

[55] F. Kasten. A simple parameterization of the pyrheliometric formula for determining the linke turbidity factor. *Meteorologische Rundschau*, 33:124–127, 1980. 45

[56] F. Kasten and G. Czeplak. Solar and terrestrial radiation dependent on the amount and type of cloud. *Solar energy*, 24(2):177–189, 1980.

[57] J. A. Davies and D.C. McKay. Estimating solar irradiance and components. *Solar Energy*, 29(1):55–64, 1982.

[58] V. Badescu. Verification of some very simple clear and cloudy sky models to evaluate global solar irradiance. *Solar Energy*, 61(4):251–264, 1997 .

[59] L. Robledo and A. Soler. Luminous efficacy of global solar radiation for clear skies. *Energy Conversion and Management*, 41(16):1769–1779, 2000.

[60] P. Ineichen and R. Perez. A new airmass independent formulation for the linke turbidity coefficient. *Solar Energy*, 73:151–157, 2002. 45

[61] R. Perez, P. Ineichen, R. Seals, and A. Zelenka. Making full use of the clearness index for parameterizing hourly insolation conditions. *Solar Energy*, 45(2):111–114, 1990. 45

[62] D. Thevenard and A. Brunger. Typical weather years for international locations. *ASHRAE Report No. RP-1015*, 2001. 46

[63] P. Ineichen. Comparison of eight clear sky broadband models against 16 independent data banks. *Solar Energy*, 80(4):468–478, 2006. 46

[64] S. Younes and T. Muneer. Clear-sky classification procedures and models using a world-wide data-base. *Applied energy*, 84(6):623–645, 2007. 46

[65] L.J.B. McArthur. Baseline surface radiation network operations manual, April 2005. 47

[66] World Meteorological Organization. Guide to meteorological instruments and methods of observation, 2008. 47

[67] Switzerland ISO, Geneva. Specification and classification of instruments for measuring hemispherical solar and direct solar radiation, 1990. 47, 68

[68] M. Zehner, T. Weigl, S. Thaler, O. Schrank, M. Czakalla, B. Mayer, T.R. Betts, R. Gottschalg, K. Behrens, G. Koenig Langlo, B. Giesler, G. Becker, and O. Mayer. Energy loss due to irradiance enhancement, 2011. 48

[69] T.R. Betts, R. Gottschalg, and D.G. Infield. Spectral irradiance correction for pv system yield calculations. In *Proceedings of the 19th European Photovoltaic Solar Energy Conference, Paris*, 2004. 49

[70] Switzerland ISO, Geneva. Solar energy - reference solar spectral irradiance at the ground at different receiving conditions - part 1: Direct normal and hemispherical solar irradiance for air mass 1,5, 1992. 49

[71] ASTM G173-03(2012). Standard tables for reference solar spectral irradiances: Direct normal and hemispherical on 37° tilted surface. ASTM International, 2012. 49, 180

[72] International Electrotechnical Commission. Photovoltaic devices measurement principles for terrestrial photovoltaic (PV) solar devices with reference spectral irradiance data, January 2009. 49

[73] ISO Gum. Guide to the expression of uncertainty in measurement. *BIPM, IEC, IFCC, ISO, IUPAP, IUPAC, OIML*, 1995. 50

[74] OptronicsLabolatories. OL FEL High-accuracy irradiance standard. URL `http://www.olinet.com/content/file/1208372889B053_FEL_3-07.pdf`. 60

[75] J.H. Walker, R.D. Saunders, J.K. Jackson, and D.A. McSparron. Nbs measurement services: Spectral irradiance calibrations. *National Bureau of Standards Special Publication*, 250:1, 1987. 62

[76] P.W. Kiedron, J.J. Michalsky, J.R. Berndt, and L.C. Harrison. Comparison of spectral irradiance standards used to calibrate shortwave radiometers and spectroradiometers. *Applied Optics*, 38(12):2432–2439, April 1999. doi: 10.1364/AO.38.002432. URL http://ao.osa.org/abstract.cfm?URI=ao-38-12-2432. 62, 81, 82

[77] *Spectral Irradiance*. Newport Inc., Stratford, CT, 2013. 62

[78] Switzerland ISO, Geneva. Solar energy - calibration of a pyranometer using a pyrheliometer, 1993. 68

[79] Switzerland ISO, Geneva. Solar energy - calibration of field pyranometers by comparison to a reference pyranometer, 1992.

[80] Switzerland ISO, Geneva. Solar energy - calibration of field pyrheliometers by comparison to a reference pyrheliometer, 1990. 68

[81] C.G. Abbot and L.B. Aldrich. The pyranometer: An instrument for measuring sky radiation. *Proceedings of the National Academy of Sciences of the United States of America*, 2(6):333, 1916. 68

[82] A. Fehlmann, G. Kopp, W. Schmutz, R. Winkler, W. Finsterle, and N. Fox. Fourth world radiometric reference to si radiometric scale comparison and implications for on-orbit measurements of the total solar irradiance. *Metrologia*, 49(2):S34, 2012. URL http://stacks.iop.org/0026-1394/49/i=2/a=S34. 82

[83] S. M. Adler-Golden and J. R. Slusser. Comparison of plotting methods for solar radiometer calibration. *Journal of Atmospheric and Oceanic Technology*, 24(5):935–938, 2013/10/02 2007. doi: 10.1175/JTECH2012.1. URL http://dx.doi.org/10.1175/JTECH2012.1. 84

[84] F. Kasten and A.T. Young. Revised optical air mass tables and approximation formula. *Appllied Optics*, 28(22):4735–4738, Nov 1989. doi: 10.1364/AO.28.004735. URL http://ao.osa.org/abstract.cfm?URI=ao-28-22-4735. 84

[85] P. Russell, J. Livingston, B. Schmid, J. Eilers, R. Kolyer, J. Redemann, S. Ramirez, J.-H. Yee, W. Swartz, R. Shetter, C. Trepte, A. Risley Jr., B. Wenny, J. Zawodny, W. Chu, M. Pitts, J. Lumpe, M. Fromm, C. Randall, K. Hoppel, and R. Bevilacqua. Aerosol optical depth measurements by airborne sun photometer in solve ii: Comparisons to sage iii, poam iii and airborne spectrometer measurements. *Atmospheric Chemistry and Physics*, 5(5):1311–1339, 2005. doi: 10.5194/acp-5-1311-2005. URL http://www.atmos-chem-phys.net/5/1311/2005/. 86

[86] N.R. Draper and H. Smith. *Applied regression analysis*. John Wiley & Sons, 2014. 86

[87] C. Gueymard. A simple model of the atmospheric radiative transfer of sunshine: Algorithms and performance assessment, 1995. 89, 180

[88] M. Ojanen, P. Kärhä, S. Nevas, A. Sperling, H. Mäntynen, and E. Ikonen. Double-coiled tungsten filament lamps as absolute spectral irradiance reference sources. *Metrologia*, 49(2):S53, 2012. 103

[89] H.W. Yoon and C.E. Gibson. NIST measurement services: spectral irradiance calibrations. *NIST Special Publication*, pages 250–89. 104

[90] K.D. Stock, K.H. Raatz, P. Sperfeld, J. Metzdorf, T. Kübarsepp, P. Kärhä, E. Ikonen, and L. Liedquist. Detector-stabilized FEL lamps as transfer standards in an international comparison of spectral irradiance. *Metrologia*, 37(5):441, 2000. URL http://stacks.iop.org/0026-1394/37/i=5/a=21. 117

[91] T.R. Betts, R. Gottschalg, and D.G. Infield. Aspire - a tool to investigate spectral effects on pv device performance. In *Photovoltaic Energy Conversion, 2003. Proceedings of 3rd World Conference on*, volume 3, pages 2182 –2185 Vol.3, May 2003. 130

[92] N. Pooltananan, P. Sripadungtham, A. Limmanee, and E. Hattha. Effect of spectral irradiance distribution on the outdoor performance of photovoltaic modules. In *Electrical Engineering/Electronics Computer Telecom-*

munications and Information Technology (ECTI-CON), 2010 International Conference on, pages 71 –73, May 2010.

[93] T.R. Betts, R. Gottschalg, and D.G. Infield. Modelling spectral irradiation effects on single- and multijunction amorphous silicon photovoltaic devices. In *Photovoltaic Specialists Conference, 2002. Conference Record of the Twenty-Ninth IEEE*, pages 1242 – 1245, May 2002. doi: 10.1109/PVSC.2002.1190833.

[94] M. Bliss, T.R. Betts, and R. Gottschalg. Performance measurements at varying irradiance spectrum, intensity and module temperature of amorphous silicon solar cells. In *Photovoltaic Specialists Conference (PVSC), 2010 35th IEEE*, pages 002660 –002665, June 2010. doi: 10.1109/PVSC.2010.5617110. 130

[95] M. Ibañez, W.A. Beckman, and S.A. Klein. Frequency distributions for hourly and daily clearness indices. *Journal of Solar Energy Engineering*, 124 (1):28–33, 07 2001. URL http://dx.doi.org/10.1115/1.1445443. 152

[96] B.C. Kindel, K.S. Schmidt, P. Pilewskie, B.A. Baum, P. Yang, and S. Platnick. Observations and modeling of ice cloud shortwave spectral albedo during the tropical composition, cloud and climate coupling experiment (tc4). *Journal of Geophysical Research: Atmospheres (1984–2012)*, 115 (D10), 2010. 168

[97] A. Kokhanovsky. Optical properties of terrestrial clouds. *Earth-Science Reviews*, 64(3):189–241, 2004.

[98] G.W. Paltridge. Spectral and total albedo to solar radiation of ice and water clouds-experimental results from aspire. *Atmósfera*, 1(1):5–16, 1988. 168

[99] A. Berk, L.S. Bernstein, and D.C. Robertson. Modtran: A moderate resolution model for lowtran. Air Force Geophysics Laboratory, 1986. 180

[100] A.K. Ångström. Techniques of determinig the turbidity of the atmosphere. *Tellus*, 13(2):214–223, 1961. ISSN 2153-3490. doi: 10.1111/j.2153-3490.

1961.tb00078.x. URL http://dx.doi.org/10.1111/j.2153-3490.1961.tb00078.x. 189

[101] A.K. Ångström and A.J. Drummond. Basic concepts concerning cutoff glass filters used in radiation measurements. *Journal of Meteorology*, 18(3):360–367, 2013/10/29 1961. doi: 10.1175/1520-0469(1961)018⟨0360:BCCCGF⟩2.0.CO;2. URL http://dx.doi.org/10.1175/1520-0469(1961)018<0360:BCCCGF>2.0.CO;2.

[102] J. McCartney. *Optics of the Atmosphere: Scattering by Molecules and Particles*. Pure and Applied Optics Series. London ; Sydney ; Toronto : John Wiley & Sons, 1976. ISBN 9780471015260. URL http://books.google.co.uk/books?id=NMIRAQAAIAAJ. 189

[103] A.K. Ångström. The parameters of atmospheric turbidity. *Tellus*, 16(1):64–75, 1964. ISSN 2153-3490. doi: 10.1111/j.2153-3490.1964.tb00144.x. URL http://dx.doi.org/10.1111/j.2153-3490.1964.tb00144.x. 189

[104] B.N. Holben, T.F. Eck, I. Slutsker, D. TanrÃ©, J.P. Buis, A. Setzer, E. Vermote, J.A. Reagan, Y.J. Kaufman, T. Nakajima, F. Lavenu, I. Jankowiak, and A. Smirnov. AERONET- A federated instrument network and data archive for aerosol characterization. *Remote Sensing of Environment*, 66(1):1 – 16, 1998. ISSN 0034-4257. doi: http://dx.doi.org/10.1016/S0034-4257(98)00031-5. URL http://www.sciencedirect.com/science/article/pii/S0034425798000315. 189

[105] S.E. Tuller. World distribution of mean monthly and annual precipitable water. *Monthly Weather Review*, 96(11):785–797, 2013/10/23 1968. doi: 10.1175/1520-0493(1968)096⟨0785:WDOMMA⟩2.0.CO;2. URL http://dx.doi.org/10.1175/1520-0493(1968)096<0785:WDOMMA>2.0.CO;2. 208

[106] World Health Organization et al. WHO Air quality guidelines for particulate matter, ozone, nitrogen dioxide and sulfur dioxide: global update 2005: summary of risk assessment. 2006. 225